

EXHUMATION AND COOLING HISTORY OF THE MIDDLE EOCENE
ANACONDA METAMORPHIC CORE COMPLEX,
WESTERN MONTANA

By

WARREN CALHOUN GRICE, JR.

A THESIS PRESENTED TO THE GRADUATE SCHOOL
OF THE UNIVERSITY OF FLORIDA IN PARTIAL FULFILLMENT
OF THE REQUIREMENTS FOR THE DEGREE OF
MASTER OF SCIENCE

UNIVERSITY OF FLORIDA

2006

Copyright 2006

by

WARREN CALHOUN GRICE, JR.

Dedication: To my family for their never ending support and inspiration.

ACKNOWLEDGMENTS

I would like to thank David Foster, my advisor, for his guidance and patience while working with me on this study over the past few years. I thank Tom Kalakay for introducing me to geology and for instilling in me great passion and motivation for the subject; I also thank Kalakay for his essential guidance in the field during the 2004 field season. I am greatly appreciative of Jim Vogl, Phil Neuoff, Paul Mueller, Matt Smith, and Mike Perfit for their assistance and guidance with several aspects of the study. I thank George Kamenov, Sam Coyner, and Tom Beasley who helped make the analytical aspects of the study possible. I thank Dan Gorman for help with sample preparation. I would also like to thank Michaela Speirs, Heather Bleick, Syklar Pauli, and Mike McTeague for their assistance in the field; I also thank McTeague for sharing my joy for geology over the past several years and for many interesting geologic discussions.

Financial support for the field aspect of this study was supplied by grants obtained by author from the Tobacco Root Geological Society, the Geological Society of America, and the Belt Association. Funding for the analytical portion of the study was supplied by a USGS EDMAP grant obtained by Tom Kalakay and by grants obtained by David Foster. The study would not have been possible without this funding.

TABLE OF CONTENTS

	<u>page</u>
ACKNOWLEDGMENTS	iv
LIST OF TABLES	ix
LIST OF FIGURES	x
ABSTRACT	xiv
CHAPTERS	
1 INTRODUCTION	1
2 REGIONAL GEOLOGIC BACKGROUND	9
Pre-Mesozoic History	9
Mesozoic History	13
Crustal Shortening along the Lewis and Clark Line during the Late Cretaceous	14
Late Cretaceous Magmatism	16
High Grade Metamorphism during the Cretaceous	19
Eocene History	20
Regional Transtension and Large-scale Crustal Extension along the Lewis and Clark Line	21
3 THE ANACONDA METAMORPHIC CORE COMPLEX	23
Structural-metamorphic Domains of the Anaconda Metamorphic Core Complex: ...	23
The Lower Plate	23
The Detachment Fault Zone	29
The Upper Plate	33
Description of the Lake of the Isle Shear Zone	35
Description and Distribution of Metamorphic and Structural fabrics	36
Metamorphic foliations and gneissic banding	36
Mesoscopic-scale folds	41
Mesoscopic-scale boudins	42
Shear sense	45
Description and Distribution of Metamorphic Phase Assemblages and Textures	45

	Metamorphic phase assemblages and textures in the meta-Greyson Formation.....	46
	Relict and fresh kyanite in the upper Meta-Ravalli Group	50
	Spatial Relationship Between the Lake of the Isle Shear Zone and Late Cretaceous Intrusions	53
4	U-PB ZIRCON GEOCHRONOLOGY	58
	Purpose and Strategy	58
	Relevant Previous U-Pb Zircon Geochronology	59
	U-Pb Zircon Geochronology Results.....	59
	WG04-114 (Storm Lake Stock Granodiorite)	60
	Ug-1 (The Deformed Quartz Diorite Sill)	61
	WG05-02 (Leucosome from the Meta-Greyson Paragneiss)	70
5	THERMOBAROMETRY	76
	Purpose and Strategy	76
	ME-231 (Migmatitic Meta-Greyson Formation Paragneiss).....	77
	Relevant Previous Pressure-temperature Constraints.....	78
	Thermobarometry Results	80
	Electron Microprobe Analyses	80
	Garnet	80
	Biotite	86
	Plagioclase.....	86
	Cordierite.....	86
	Mineral End Member Activity Calculations made using AX	87
	Pressure-temperature Estimates using THERMOCALC	87
	Pressure-temperature Estimates using Geothermobarometry (GTB).....	93
6	⁴⁰ AR/ ³⁹ AR THERMOCHRONOLOGY	95
	Purpose and Strategy	95
	Previous Thermochronology	96
	⁴⁰ Ar/ ³⁹ Ar Thermochronology Results	104
	Argon Closure Temperature	105
	Biotite	122
	Muscovite	125
	Hornblende	128
	K-feldspar	131
	⁴⁰ Ar/ ³⁹ Ar Thermochronology From Outside the Lower Plate Transect	133
7	DISCUSSION.....	136
	Origin of the Lake of the Isle Shear Zone	136
	Age Constraints	137
	Pressure-temperature History	140
	Kinematic Interpretation.....	144

Strain localization and ductile attenuation of metasedimentary strata in the LISZ	145
Strain classification	146
Structural Interpretation	146
Eocene Exhumation and Cooling History of the Anaconda Metamorphic Core	
Complex defined by ⁴⁰ Ar/ ³⁹ Ar Thermochronology	147
Lower Plate Cooling History	148
Constraints on the Timing of the Onset of Extension	154
Constraints on the Duration of Extension	159
Constraints on the Detachment Slip Rate	161
Constraints on the Original Detachment Geometry	169
Magnitude of Offset on the Detachment	177
 8 CONCLUSIONS	 183
Age and Pressure-temperature Constraints on High Grade Metamorphism in the ACC lower plate: Origin of the Lake of the Isle Shear Zone.....	183
Exhumation and Cooling History of the Middle Eocene Anaconda Metamorphic Core Complex:	183
Regional Tectonic Context	188
 APPENDIX	
 A METHODOLOGIES	 191
Field Mapping and Sampling Methods.....	191
⁴⁰ Ar/ ³⁹ Ar Thermochronology Methods.....	192
Thermobarometry	195
U-Pb Geochronology	196
Major and Trace Element Geochemistry	203
 B ACC LOWER PLATE LITHOLOGIC UNIT DESCRIPTIONS AND DISTRIBUTION	 205
General Statement.....	205
Belt Supergroup-equivalent Metasedimentary Strata	206
Middle Cambrian-equivalent Metasedimentary Strata.....	210
Late Cretaceous Intrusions	212
The Storm Lake Stock	212
The Deformed Quartz Diorite Sill.....	216
Eocene Intrusions.....	217
 C DESCRIPTION OF SAMPLE ME-231	 224
 D MAJOR AND TRACE ELEMENT GEOCHEMISTRY	 229
Purpose	229
Major and Trace Element Analytical Results	230

Major Element Analyses	231
Trace Element Analyses	231
E THERMOCALC AND AX OUTPUT FILES	240
F GEOLOGIC MAP OF THE ANACONDA METAMORPHIC CORE COMPLEX LOWER PLATE	245
REFERENCES CITED	247
BIOGRAPHICAL SKETCH	261

LIST OF TABLES

<u>Table</u>	<u>page</u>
3-1. Description and distribution of key mineral phases and textures in the metamorphosed Greyson Formation.	54
4-1. U-Pb LA-MC-ICP-MS analytical results for WG04-114	62
4-2. U-Pb LA-MC-ICP-MS analytical results for Ug-1	66
4-3. U-Pb LA-MC-ICP-MS analytical results for WG05-02	68
5-1. Results from electron microprobe mineral analyses.	81
5-2. Averaged ME-231 electron microprobe analyses used in thermobarometry	88
6-1. Summary of relevant previous thermochronology.....	98
6-2. Summary of $^{40}\text{Ar}/^{39}\text{Ar}$ thermochronology from the Anaconda metamorphic core complex.	106
D-1. Results from major and trace element analyses	232

LIST OF FIGURES

<u>Figure</u>	<u>page</u>
1-1. Regional geologic map of the North American Cordillera. Emphasis is placed on major igneous and tectonic features.	2
1-2. Tectonic map of northwestern United States and southern Canada showing major structures related to Tertiary extension.	4
2-1. Regional geologic map of the major Archean basement provinces and Proterozoic suture zones of the North American Cordillera in the western United States and southern Canada.	10
2-2. Simplified tectonic map of Belt Basin in the Mesoproterozoic. Map shows the major normal faults active during deposition of the Belt-Purcell Supergroup.	12
2-3. Tectonic map of the North American Cordillera of western Montana, northern Idaho, northeastern Washington, and southern Canada during the Late Cretaceous.	15
2-4. Geologic map of western Montana, south of the Lewis and Clark line.	18
3-1. Geological Map of the Anaconda metamorphic core complex (ACC) in western Montana.	25
3-2. Geologic cross section of the Anaconda metamorphic core complex, western Montana.	26
3-3. Photomosaic of the Anaconda metamorphic core complex.	32
3-4. Greenschist facies mylonites.	33
3-5. Outcrop photos of late listric-shaped brittle normal faults in the greenschist facies mylonite zone.	34
3-6. Outcrop photograph showing the strong gneissic banding of the metamorphosed Greyson Formation in the LISZ.	39
3-7. Outcrop photographs of gneissic banding commonly observed in the LISZ.	40
3-8. Photomicrograph of the Missoula Group-equivalent calc-silicate paragneiss.	41

3-9. Outcrop photograph of the deformed quartz diorite sill in the center of the LISZ.	43
3-10. Outcrop photographs of mesoscopic-scale folds found in Belt equivalent metasedimentary strata deformed in the LISZ.	44
3-11. Outcrop photographs of mesoscopic-scale folds found in Belt-equivalent metasedimentary strata deformed in the LISZ.	46
3-12. Outcrop photographs of mesoscopic boudins in the LISZ.	47
3-13. Outcrop photographs of shear sense indicators in the meta-Greyson Formation deformed in the LISZ.	49
3-14. Outcrop photographs of meta-Greyson migmatitic paragneiss showing granitic leucosome commonly found in pressure shadows between quartzite boudins.	51
3-15. Photomicrographs of thin sections of the meta-Greyson migmatitic paragneiss exhibiting granitic leucosome (sample ME-231).	52
3-16. Simplified geologic sketch map of the ACC lower plate exposed in the current study area showing the metamorphic mineral/textural zones 1, 2, and 3 mapped in the meta-Greyson Formation adjacent to the deformed quartz diorite sill.	55
3-17. Kyanite pseudomorphs in the upper meta-Ravalli Group. A) Outcrop photograph of kyanite pseudomorphs.	56
3-18. Photomicrograph showing fresh kyanite in the upper meta-Ravalli Group.	57
4-1. Tera-Wasserburg plot and $^{206}\text{Pb} / ^{238}\text{U}$ weighted mean zircon age plot for Storm Lake Stock granodiorite sample WG04-114.	70
4-2. Tera-Wasserburg plot and $^{206}\text{Pb} / ^{238}\text{U}$ weighted mean zircon age plot for the deformed quartz diorite sill sample Ug-1.	71
4-3. Conventional U-Pb concordia plots for zircons for leucosome sample WG05-02 collected from the meta-Greyson migmatitic paragneiss in the central LISZ.	74
4-4. $^{207}\text{Pb}/^{206}\text{Pb}$ age density plot for the WG05-02 leucosome zircons. $^{207}\text{Pb}/^{206}\text{Pb}$ ages range from ~1525-3004 Ma.	75
5-1. Phase diagrams showing PT estimates for ME-231, migmatitic Greyson paragneiss from the Lake of the Isle shear zone.	91
5-2. Phase diagram showing phase equilibria used by THERMOCALC to calculate the average PT estimate for sample ME-231.	93
6-1. Geologic map of Anaconda metamorphic core complex (ACC), western Montana and vicinity showing location of previous thermochronology.	102

6-2.	Geologic sketch map showing mineral cooling ages from samples collected along the ACC lower plate transect using $^{40}\text{Ar}/^{39}\text{Ar}$ thermochronology.....	109
6-3.	$^{40}\text{Ar}/^{39}\text{Ar}$ mineral age spectra obtained for samples collected from the Anaconda metamorphic core complex using $^{40}\text{Ar}/^{39}\text{Ar}$ thermochronology.....	110
7-1.	Phase diagram showing the Late Cretaceous PT history of the Lake of the Isle shear zone (LISZ).....	142
7-2.	Geologic sketch map showing the mineral cooling ages obtained by $^{40}\text{Ar}/^{39}\text{Ar}$ thermochronology from samples collected along the ACC lower plate transect in this study..	149
7-3.	Mica cooling age contour map constructed from biotite and muscovite cooling ages obtained $^{40}\text{Ar}/^{39}\text{Ar}$ thermochronology from samples collected along the ACC lower plate transect in this study.....	150
7-4.	Temperature-time cooling diagram showing the cooling history of the ACC lower plate.....	151
7-5.	Age vs. distance in slip direction diagram and lower plate transect sketch map..	159
7-6.	Slip rate calculations.....	166
7-7.	Paleoisootherm contour map. Paleoisotherms refer to estimated temperatures of the ACC lower plate directly beneath the detachment at the onset of extension at ~53 Ma.....	174
7-8.	Distance in slip direction vs. paleodepth diagram showing geometries for the detachment at the onset of extension at ~53 Ma.....	175
7-9.	Distance in slip direction vs. paleodepth diagram showing magnitude of offset on the detachment with variable slip rate from ~53-40 Ma with a geothermal gradient of 35°C/km.....	181
7-10.	Geologic map of the ACC showing structural pinning points used to constrain the maximum amount of displacement facilitated by the Anaconda detachment..	182
D-1.	Major element Harker variation diagrams for samples Ug-1, WG04-114, and DF02-114.....	236
D-2.	REE trend and trace element spider diagrams for samples Ug-1, WG04-114, and DF02-114.....	239

OBJECT LIST

<u>Object</u>	<u>page</u>
F-1. Geologic map of the Anaconda metamorphic core complex lower plate (AMCCfinalmap.pdf, 22 mb).....	246

Abstract of Thesis Presented to the Graduate School
of the University of Florida in Partial Fulfillment of the
Requirements for the Degree of Master of Science

EXHUMATION AND COOLING HISTORY OF THE MIDDLE EOCENE
ANACONDA METAMORPHIC CORE COMPLEX, WESTERN MONTANA

By

Warren Calhoun Grice, Jr.

August 2006

Chair: David A. Foster

Major: Department: Geological Sciences

New $^{40}\text{Ar}/^{39}\text{Ar}$ thermochronology, U-Pb geochronology, and thermobarometry define the tectonic exhumation and cooling history of the Middle Eocene Anaconda metamorphic core complex (ACC) of western Montana. Mica $^{40}\text{Ar}/^{39}\text{Ar}$ cooling ages obtained from the ACC lower plate (footwall): (1) constrain the age of the onset of extension in the ACC to ~53 Ma; (2) constrain the duration of extension to at least ~53-39 Ma; (3) define a lateral cooling age gradient, where mica cooling ages decrease to the ESE across the ACC lower plate confirming top-to-the-ESE directed unroofing of the lower plate; (4) constrain the original geometry of the Anaconda detachment at ~53 Ma to a listric-shaped normal fault comprised of a steep portion (~54-70°) in the upper brittle crust and a sub-horizontal portion (~7-12°) in the middle crust; and (5) constrain the rate of slip on the detachment to ~0.9 km/Myr during the time interval of ~53-39 Ma. Reconstruction of similar Late Cretaceous granodiorite plutons in the detached ACC upper plate (hanging wall) and lower plate indicate ~25-28 km of (horizontal)

displacement occurred on the detachment during the Eocene. Thermobarometry and U-Pb zircon geochronology from the Lake of the Isle shear zone (LISZ, named herein), structurally beneath the detachment, show that uppermost-amphibolite facies metamorphism (at ~3.2-5.3 kbar and ~750-850°C) ended in the Late Cretaceous (at ~75-74 Ma). Pressure constraints from the thermobarometry indicate the lower plate was exhumed from a maximum crustal depth of ~10-16 km.

The results from this study show the exhumation and cooling histories of the ACC and the Bitterroot metamorphic core complex (BCC), located ~70 km west of the ACC, are remarkably similar. Therefore, the ACC and BCC represent one continuous and integrated extensional system that accommodated large-scale extension in easternmost Idaho and western Montana during the Eocene. Extension in the ACC and BCC was linked to regional dextral transtension along the Lewis and Clark Line (LCL), a major strike-slip fault zone located to the north of these metamorphic core complexes. Extension in the ACC and BCC, combined with extension in several other metamorphic core complexes north of the LCL, is responsible for the initial collapse of the previously thickened Sevier hinterland beginning in the early to middle Eocene immediately following (~1-3 Ma) the end of crustal shortening in the foreland fold-and-thrust-belt to the east. Regional dextral transtension, large-scale extension, and exhumation of metamorphic core complexes in the northwestern United States and southern British Columbia were likely driven by traction caused by increased obliquity of convergence at the western margin of the North American Plate beginning in the early to middle Eocene.

CHAPTER 1 INTRODUCTION

Metamorphic core complexes are regional extensional structures characterized by large-scale crustal extension and tectonic exhumation of mid-crustal metamorphic and plutonic rocks along low-angle normal brittle-ductile detachment fault zones (e.g., Davis and Coney, 1979; Coney, 1980). More than thirty metamorphic core complexes have now been documented throughout the North American Cordillera and comprise a relatively narrow and sinuous belt stretching from southern British Columbia into northern Mexico (Coney, 1980; Armstrong and Ward, 1991). These metamorphic core complexes formed during early to middle Tertiary time following a long period of crustal accretion, shortening, and thickening caused by convergence along the western margin of North America during the Mesozoic (Burchfiel et al., 1992; Wernicke, 1992). With the exception of the southernmost metamorphic core complexes, all the core complexes formed in the previously thickened Mesozoic Sevier hinterland, west of the Sevier thin-skinned foreland fold-and-thrust belt and Laramide-style basement-involved foreland uplifts (Fig. 1-1; Coney and Harms, 1984; Wernicke, 1992). Large-scale extension in metamorphic core complexes occurred before widespread Basin-and-Range-style extension affected the North American Cordillera (Liu, 2001). Therefore, metamorphic core complexes are responsible for the initial extensional collapse of the previously thickened Cordilleran crust during the Tertiary (Coney and Harms, 1984; Wernicke, 1992; Foster et al., 2001; Vanderhaeghe et al., 2003).

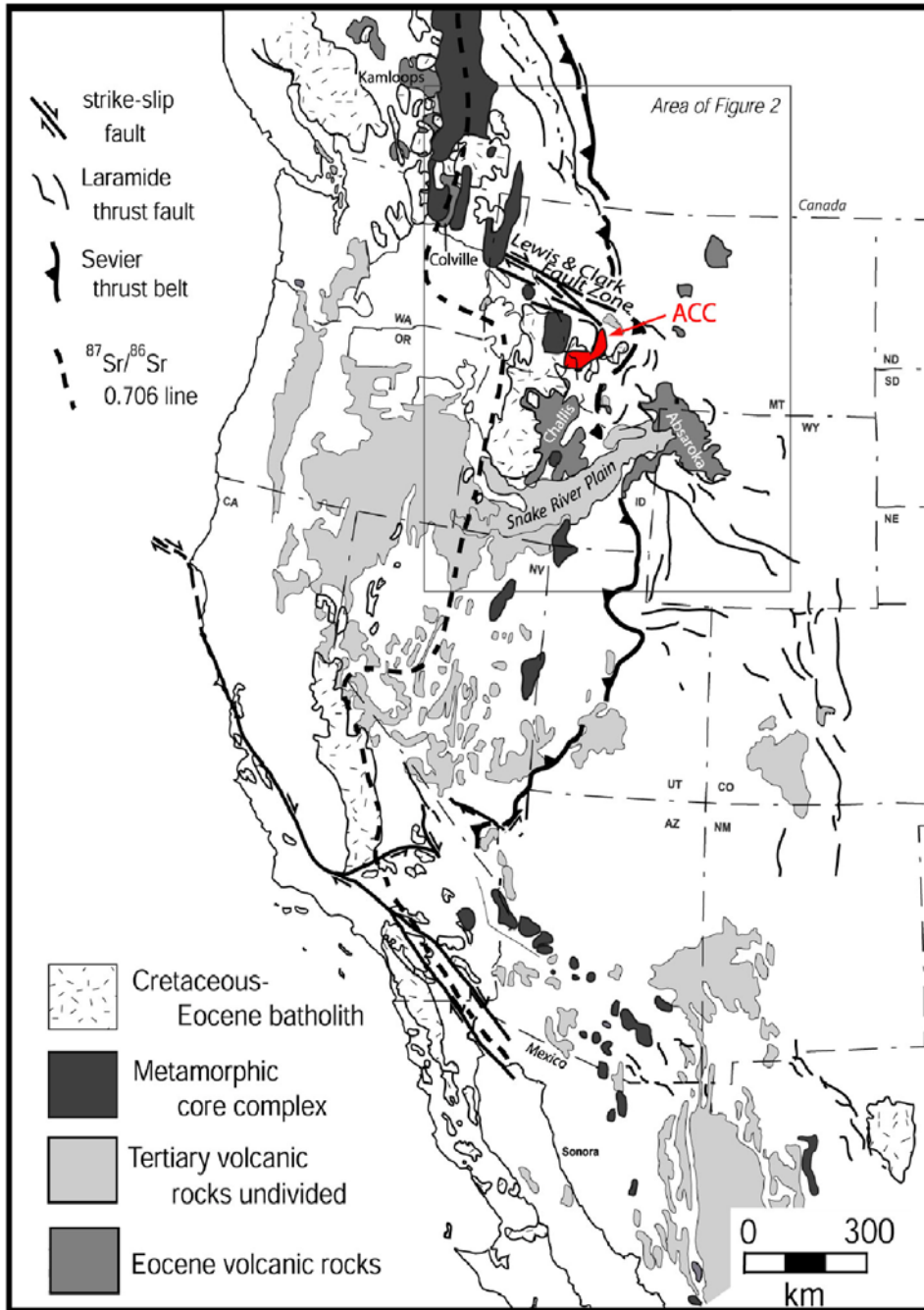


Figure 1-1. Regional geologic map of the North American Cordillera. Emphasis is placed on major igneous and tectonic features. Note the location of the Cordilleran metamorphic core complexes located west of the Sevier fold-and-thrust-belt. The Anaconda metamorphic core complex (ACC) is located south of the Lewis and Clark line in western Montana. Note the Lewis and Clark Fault Zone = the Lewis and Clark Line. (Modified from Coney, 1980, and Foster et al., 2006a).

Large-scale extension and exhumation of mid-crustal metamorphic and plutonic rocks in metamorphic core complexes in the northwestern United States was linked to regional dextral transtension along the Lewis and Clark line (LCL) during the Eocene (Doughty and Sheriff, 1992; Yin and Oertel, 1995; Foster et al., 2006a). The LCL is a northwest-west-trending ~40-80 km wide zone of steeply-dipping strike-slip, oblique-slip, and dip-slip faults that reaches from northeastern Washington to west-central Montana. Many faults of the LCL accommodated repeated displacement during multiple tectonic reactivations since the inception of the line in the Mesoproterozoic or earlier (Wallace et al., 1990; Sears and Hendrix, 2004). During the Late Cretaceous to early Eocene (~88-55 Ma) the LCL accommodated sinistral displacement and regional transpression related to crustal shortening and thickening in the Sevier fold-and-thrust belt of southern Alberta and western Montana. Beginning in the early Eocene (~54-52 Ma), the LCL was reactivated as a regional dextral transfer structure related to large-scale extension and exhumation of several metamorphic core complexes in the Sevier hinterland, west of the fold-and-thrust belt (Fig. 1-1 and 1-2, Sears and Hendrix, 2004; Foster et al., 2006a).

South of the LCL, in eastern Idaho and western Montana, large-scale Eocene extension may have been accommodated by exhumation of both the Bitterroot and Anaconda metamorphic core complexes (Fig. 1-2, Foster et al., 2006a). The timing and kinematics of Eocene extension in the Bitterroot metamorphic core complex (BCC), the more westerly of the two core complexes, is well constrained (e.g., Hyndman, 1980; House and Applegate, 1993; House and Hodges, 1994; Foster and Fanning, 1997; Foster, 2000; Foster et al., 2001; House et al., 2002; Foster and Raza, 2002). Extension in the

BCC began at ~53 Ma and continued to ~25 Ma (based on a large U-Pb geochronology, $^{40}\text{Ar}/^{39}\text{Ar}$, and fission track thermochronological data set from the exhumed footwall,

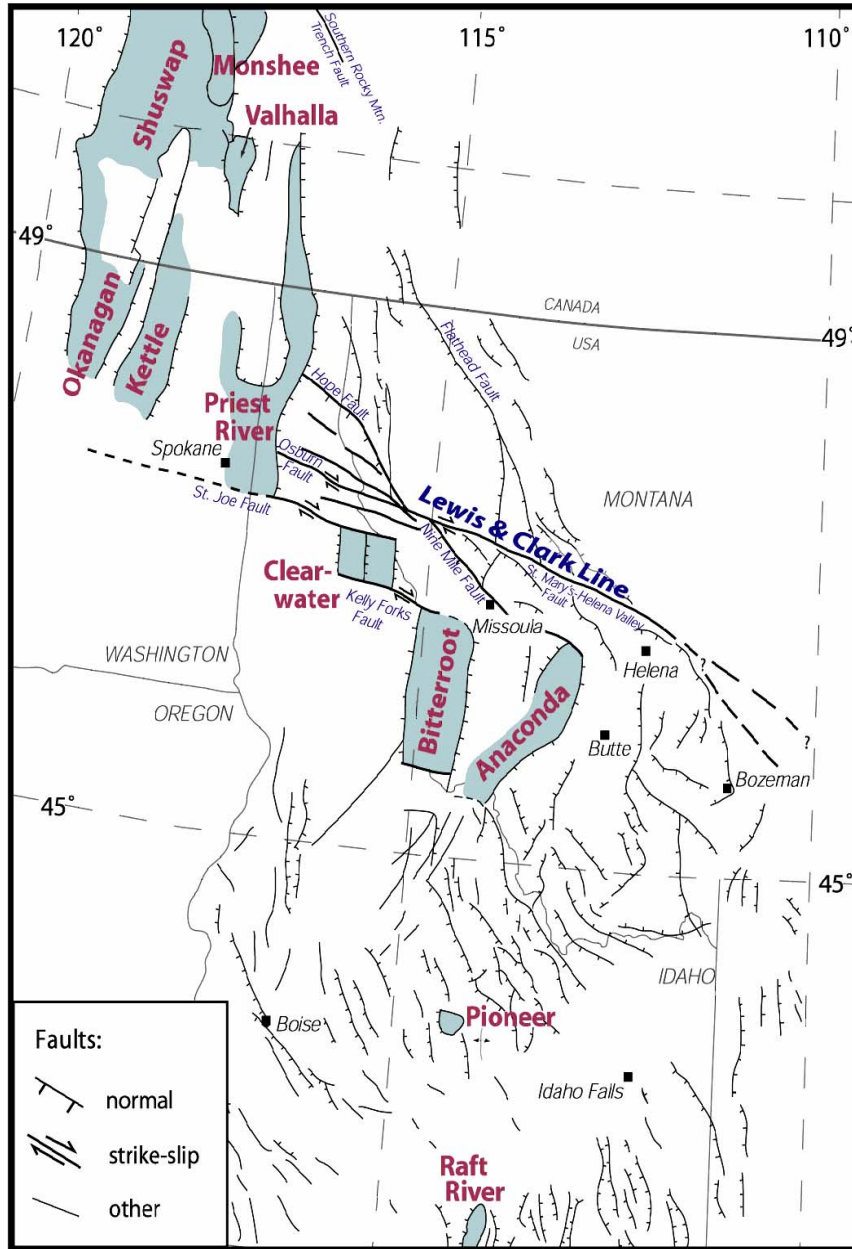


Figure 1-2. Tectonic map of northwestern United States and southern Canada showing major structures related to Tertiary extension. The Bitterroot and Anaconda metamorphic core complexes are located south of the Lewis and Clark Line (LCL). The LCL was active as a regional dextral transfer structure between extension north and south of the line during the Eocene (Modified from Foster et al., 2006a).

Foster et al., 2001; Foster and Raza, 2002; Foster et al., 2006a). During this time, the BCC lower plate was exhumed from beneath a single east-dipping upper-amphibolite facies mylonitic shear zone and overprinting brittle normal detachment fault system by top-to-the-east-southeast directed ($110\text{-}100^\circ$) detachment of the hanging wall (constrained by a large thermochronology data set from the footwall and kinematic indicators and mineral stretching lineations from the mylonites, Foster, 2000; Foster, et al., 2001; House et al., 2002; Foster and Raza, 2002). Early extension in the BCC was accompanied by upper-amphibolite facies metamorphism at $\sim 6\text{-}8$ kbar and $\sim 650\text{-}750^\circ\text{C}$ and localized decompressional anatexis (partial melting) based on thermobarometry and U-Pb geochronology from migmatites directly beneath the mylonitic shear zone in the eastern parts of the footwall (House et al., 1997; Foster et al., 2001; Foster and Raza, 2002). The thermobarometric data show that the eastern BCC was exhumed from lower to mid-crustal depths of $\sim 20\text{-}25$ km (Foster and Raza, 2002; Foster et al., 2006a). Total (horizontal) displacement on the detachment in the BCC is estimated to be $\sim 40\text{-}50$ km, based on reconstruction of Cretaceous dioritic plutons in the detached hanging wall with similar dioritic plutons in western footwall (Foster et al., 2006a).

Extension in the Anaconda metamorphic core complex (ACC, O'Neill, et al., 2002; Kalakay and Lonn, 2002; Kalakay et al., 2003; O'Neill et al., 2004), located $\sim 70\text{-}80$ km east of the BCC, is not well constrained, but apparently remarkably similar (Fig. 1-2). Limited U-Pb geochronological and thermochronological data suggest extension in the ACC began at ~ 53 Ma, coincident with the onset of extension in the BCC, and continued until at least ~ 47 Ma (O'Neill et al., 2004; Foster et al., 2006a). As in the BCC, the ACC lower plate (footwall) appears to have been exhumed along a single east-dipping

mylonitic shear zone and overprinting brittle detachment fault system which now bounds its eastern side (Kalakay et al., 2003; O'Neill et al., 2004). Kinematic indicators and mineral stretching lineations from the mylonites suggest top-to-the-east-southeast (102-108°) directed detachment of the ACC upper plate (hanging wall) exhumed the ACC lower plate (Kalakay et al., 2003). However, a rather large thermochronological data set is needed from across the ACC to definitely prove east-southeast directed detachment of the upper along an east-dipping detachment system (e.g., Foster and John, 1999).

Metamorphosed Lower Belt Supergroup pelitic strata exposed directly beneath the mylonitic shear zone and brittle detachment system in the ACC are migmatitic and show evidence for upper-amphibolite facies metamorphism and anatexis during high temperature ductile deformation (T. Kalakay, per comm.). However, the metamorphic grade, age, and relationship of these migmatites to Eocene extension in the ACC have not been established. Geochronological and thermobarometric data are needed from the lower plate migmatites. Within these data, the amount of exhumation in the ACC can not be quantified. In addition, the total amount of displacement facilitated by the ACC detachment during the Eocene has not been established.

The apparent similarities in the timing and kinematics of Eocene extension in the BCC and ACC has led some workers to propose the two metamorphic core complexes were part of a continuous integrated extensional system that together accommodated large-scale extension south of the LCL during the Eocene (Doughty and Sheriff, 1992; O'Neill et al., 2004, Foster et al., 2006a). Following this idea, the BCC and ACC would have been exhumed along separate synthetic (parallel) east-dipping mylonitic shear zones and brittle detachment systems that would have been active at the exact same time. In

this tectonic model a “nested” more shallow position for ACC mylonitic shear zone and brittle detachment is proposed (D. Foster, per. comm.; O’Neill et al., 2004, their Fig. 8).

The primary aim of this study is to test the idea that the BCC and ACC metamorphic core complexes represent a single integrated extensional system responsible for large-scale Eocene extension south of the LCL as has been suggested. In order to test the proposed tectonic model, Eocene extension in the ACC must be constrained. In this study a combination of $^{40}\text{Ar}/^{39}\text{Ar}$ thermochronology, U-Pb geochronology, thermobarometry, major-trace element geochemistry, and field mapping are used to provide a detailed exhumation and cooling history for the ACC. In particular, this study will: (1) confirm the age of the onset extension in the ACC; (2) provide constraints on the duration of extension in the ACC (i.e., did extension in the ACC continue after ~47 Ma?); (3) constrain the Late Cretaceous to Late Eocene cooling history for the ACC lower plate; (4) confirm top-to-the-east-southeast directed tectonic unroofing (detachment) of the ACC upper plate as in the BCC; (5) constrain on the original geometry of ACC detachment to confirm an original east-dipping detachment synthetic to the BCC detachment; (6) constrain the slip rate and magnitude of slip on the ACC detachment system; (7) constrain metamorphic pressure and temperature conditions and age of upper-amphibolite facies metamorphism in the ACC lower plate; these metamorphic pressure constraints are used to (8) constrain the maximum amount of exhumation in the ACC. The metamorphic pressure constraints are also used to (9) determine the maximum depth of the ACC detachment in the Eocene to test its proposed “nested” geometry relative to the BCC detachment.

If the proposed tectonic model for large-scale Eocene extension in the BCC and ACC is substantiated then the structural style of extension south of the LCL differed significantly from Eocene extension in and north of the LCL in northern Idaho, northeastern Washington, and southern British Columbia; as all of these core complexes were exhumed by paired east and west-dipping detachment systems (e.g., the Shuswap metamorphic core complex), not by single asymmetric detachments (e.g., the BCC). An improved and more complete understanding of Eocene extension in the northwestern United States, south of the LCL, is a critical contribution for defining the role of plate margin forces, mantle upwelling, and extensional (orogenic) collapse which apparently caused the destruction of an Andean-style orogen that existed in the North American Cordillera from Cretaceous to early Eocene time (e.g., Coney and Harms, 1984, Foster et al., 2001; Foster et al., 2006a).

CHAPTER 2 REGIONAL GEOLOGIC BACKGROUND

Pre-Mesozoic History

Archean (≥ 2.5 Ga) and Paleoproterozoic basement underlie western Montana (Foster et al., 2006b). In northwestern Montana the basement is comprised of the Medicine Hat Block of the southern Archean Hearne Province, which extends beneath southernmost British Columbia, Alberta and Saskatchewan. To the south, the underlying basement consists of the Archean Wyoming Province. These two Archean Provinces are separated by the linear northeast-trending Great Falls tectonic zone (GFTZ) which stretches from eastern Idaho to the northeast into Saskatchewan (O'Neill and Lopez, 1985). The GFTZ is mostly Paleoproterozoic in age and has been interpreted to represent the final suturing of the Archean Wyoming Province and Medicine Hat Block at ca. ~ 1.9 - 1.8 Ga (based on U-Pb zircon crystallization ages, Mueller et al., 2003). The Wyoming-Medicine Hat suture (the GFTZ), along with several other north to northeast-trending Paleoproterozoic collisional belts within the Canadian shield (e.g., the Trans-Hudson orogen) were responsible for the assemblage of the Laurentia cratonic core from ~ 2.0 - 1.8 Ga (Hoffman, 1988).

The Mesoproterozoic Belt Basin is superimposed of the western edge of the Archean-Paleoproterozoic basement in western Montana and also extends into northern Idaho, northeastern Washington, and southern Alberta (Fig. 2-1). The Belt Basin contains a thick (up to ~ 18 km) sequence of fine-grained quartzites, red to green-colored argillites, argilleous carbonates, and dark-grey well laminated argillites and quartzites

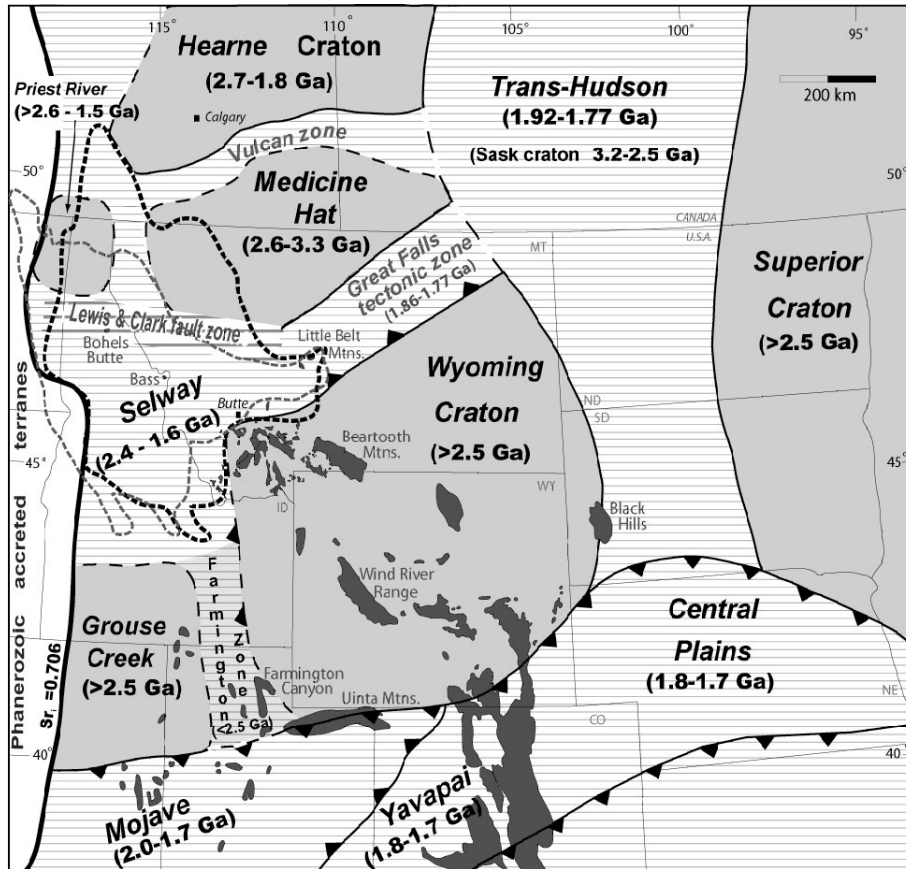


Figure 2-1. Regional geologic map of the major Archean basement provinces and Proterozoic suture zones of the North American Cordillera in the western United States and southern Canada. The map also shows the position of the Belt-Purcell Basin superimposed (dark dashed outline) on the western edge of the Precambrian basement provinces in northwestern Washington, northern Idaho, western Montana, and southern Canada. Darkened shapes represent subaerial exposes of Precambrian basement. The $Sr_i = 0.706$ line represents the western edge of Precambrian basement (from Foster et al., 2006).

(Winston and Link, 1993). In the northwestern United States this immense sequence of sedimentary strata is referred to as the Belt Supergroup and in Canada as the Purcell Supergroup. The timing of deposition of the Belt Supergroup sedimentary strata is now well constrained to the interval of ~1.47-1.40 Ga by U-Pb zircon crystallization ages from intercalated syn-depositional mafic sills and volcanic tuffs, a large detrital zircon U-Pb age dataset, and detrital muscovite $^{40}\text{Ar}/^{39}\text{Ar}$ cooling ages (Ross and Villeneuve, 2003; and references therein). The origin and Mesoproterozoic tectonic setting of the Belt

Basin is still controversial (see Winston and Link, 1993 for review). There is increasing evidence and a general consensus among many workers for an extensional rift-related intracratonic basin setting for the Belt Basin, where the subsiding basin was in part, if not fully isolated from an adjacent seaway to the western or northwest (e.g., Winston, 1986; Winston and Link, 1993; Lyons et al., 2000; Ross and Villeneuve, 2003).

In western-central Montana the Belt Basin narrows significantly to form a prominent east-west-trending structural embayment referred to as the Helena embayment (Fig. 2-1 and 2-2). The Helena embayment formed when several major syn-depositional steep normal faults down-dropped the embayment separate from the rest of the Belt basin to the west during the Mesoproterozoic (Winston and Link, 1993). The southern margin of the Helena embayment was bound and down-dropped by the east-west-trending Perry Line/Willow Creek fault zone. As a result, the Dillon block of the Archean Wyoming Province was first uplifted along the up-thrown (southern) side of the fault zone (Winston and Link, 1993). The northern margin of the Helena embayment was bound and down-dropped along a series of high-angle northwest-west-trending faults which comprised the eastern continuation of the proto-Lewis and Clark line (see below, e.g., Wallace et al., 1990; Sears and Hendrix, 2004). Other major faults also active along the eastern segment of the Lewis and Clark line during the Mesoproterozoic may have included the inferred east-west-trending Jocko and Garnet lines and the Volcanic Valley fault zone (Fig. 2-2, Winston and Link, 1993). The geometry of the Helena embayment, as defined by the Early bounding fault system, had a major influence on subsequent tectonism in western Montana (especially during the Late Mesozoic to Early Cenozoic, Winston et al., 1986; Foster et al., 2001, 2006; Sears and Hendrix, 2004).

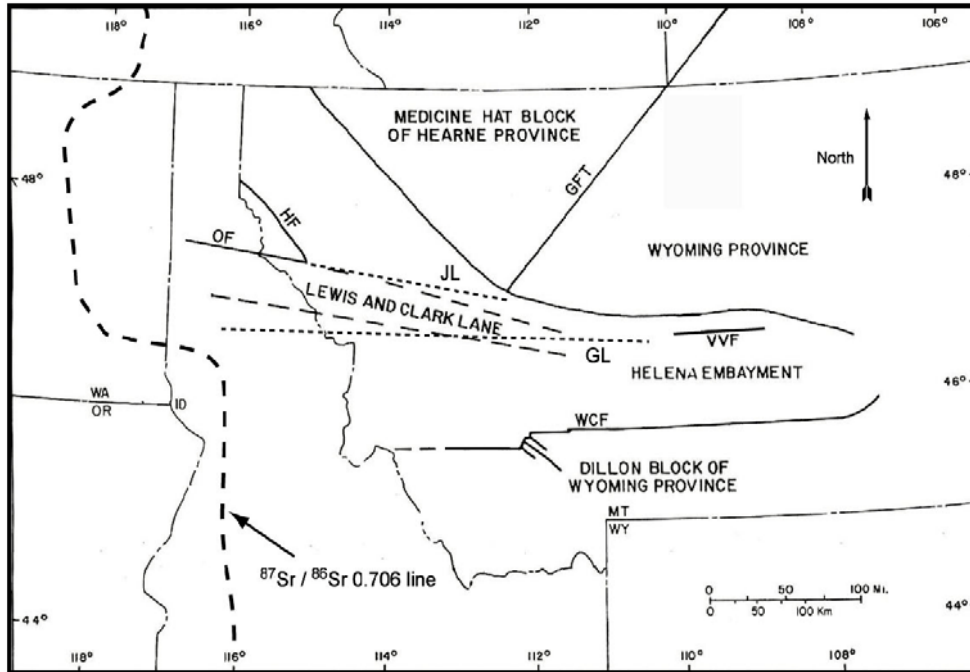


Figure 2-2. Simplified tectonic map of Belt Basin in the Mesoproterozoic. Map shows the major normal faults active during deposition of the Belt-Purcell Supergroup. The early Lewis and Clark likely included the Osborn Fault (OF), the Hope Fault (HF), the Jocko Line (JL), and Garnet Line. The JL and GL are inferred (see Winston and Link, 1993). The Volcano Valley Fault (VVF) and the Willow Creek Fault Zone (WCF) were responsible for down-dropping the Helena Embayment during deposition of the Belt-Purcell Supergroup. The $^{87}\text{Sr}/^{86}\text{Sr} = 0.706$ line from Sears and Hendrix (2004) and represents the western edge of known Precambrian basement. The Great Falls Tectonic Zone (GFT) was not active during deposition of the Belt-Purcell Supergroup Mesoproterozoic (Modified from Winston and Link, 1993).

Following the deposition of the Belt Supergroup sedimentary strata, during the Late Neoproterozoic (ca. ~800-700 Ma), a major rift zone developed along the entire western margin of Laurentia as the proposed pre-Gondwanan supercontinent Rodinia began to break apart (e.g., Meert and Torsvik, 2003). As a result, the western side of the Belt Basin was truncated as the adjacent landmass rifted away (the identity of the western landmass is highly controversial; see Karlstrom et al., 2001 for review). As rifting continued, a paleo-Pacific Ocean opened and a passive margin sequence was deposited beginning with the deposition of the Late Neoproterozoic to Early Cambrian-aged

Windermere deep-water sequence along the entire western margin of Laurentia but mainly outboard (west) of the Belt Basin in western Montana (Burchfiel et al., 1992; Winston and Link, 1993).

During the Middle Cambrian, a thick miogeoclinal sequence (continental shelf deposits) was deposited over the eastern Windermere sequence and further inboard onto the craton during a major transgression (Burchfiel et al., 1992). In western Montana, the earliest phase of this transgression is represented by the Middle Cambrian Flathead Sandstone which lies unconformably over upper Belt Supergroup strata in much of western Montana (Emmons and Calkins, 1913; Winston and Link, 1993).

Mesozoic History

Beginning in the Early Triassic, an active convergent margin developed along the western margin of Laurentia (Burchfiel et al., 1992). With continued convergence, from the Early Triassic to Early Cretaceous, several exotic terranes (including a number of volcanic arc complexes) were accreted to the western edge of Laurentia (e.g., the Wrangellia terrane and the Wallowa-Seven Devils terrane adjacent to the Western Idaho Suture, Hamilton, 1978). Despite the major contractional deformation associated with convergence at this time, the Belt Basin and its Paleozoic miogeoclinal sedimentary cover sequence remained largely stable until the Late Early to Late Cretaceous (Burchfiel et al., 1992).

By the Late Early to Late Cretaceous, crustal shortening and thickening related to the ongoing convergence along the western margin of Laurentia migrated eastward into present-day northeastern Idaho and western Montana. Thrust faulting began first in eastern Idaho at ~105 Ma and moved progressively eastward into western Montana before ending at ~55 Ma (Hyndman, et al., 1988; Constenius, 1996; Sears and Hendrix,

2004). In western Montana, the east-directed crustal shortening and thickening was facilitated predominately by low-angle “thin-skinned” basement-detached Sevier-style thrust faulting superimposed on the Mesoproterozoic Belt Basin (Allmendinger, 1992; Winston and Link, 1993); this deformation was part of the Sevier orogen which stretches from British Columbia into southern Nevada (Burchfiel et al., 1992). As a result, many thin-skinned thrusts in western Montana involve thick sequences of Belt Supergroup and Paleozoic sedimentary strata thrust eastward over younger Belt, Paleozoic, and Mesozoic sedimentary strata (Winston, 1986; Foster et al., 2001). In addition, because thrusting was superimposed on the Belt Basin, a prominent east-directed structural bulge formed in the thrust belt in the original Helena embayment referred to as the Helena thrust salient (Fig. 1-2 and 2-3; Winston, 1986).

Crustal Shortening along the Lewis and Clark Line during the Late Cretaceous

Thin-skinned Sevier-style thrusting in western Montana was accommodated by the eastward displacement of three major thrust slabs (or plates) along the Lewis and Clark Line (LCL): 1) the Lewis-Eldorado-Hoadley (LEH) slab in northwestern Montana and the 2) Sapphire and 3) Lombard slabs in southwestern Montana (Constenius, 1996; Sears and Hendrix, 2004). The LCL, a complex zone of west-to-northwest-trending steeply dipping strike-slip, dip-slip and oblique slip faults, separates the LEH slab in the north from the Sapphire and Lombard slabs to the south (Fig. 2-3, Wallace et al., 1990). As noted above, some faults within the LCL likely originated during subsidence of the Belt Basin in the Mesoproterozoic. However, several workers show evidence for reactivation of these old faults as well as inception of younger faults along the LCL during the Mesozoic (e.g., Harrison et al., 1972; Hyndman et al., 1988; Wallace et al., 1990; Stewart and Crowell, 1992; Sears and Hendrix, 2004). Most recently, Sears and

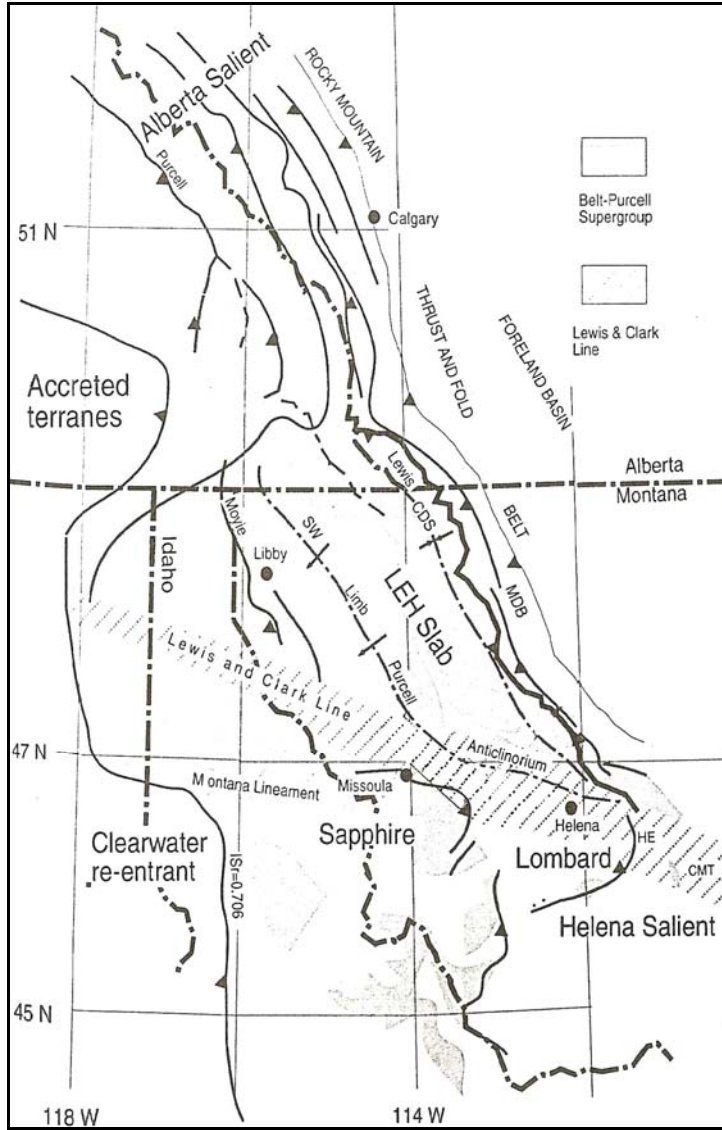


Figure 2-3. Tectonic map of the North American Cordillera of western Montana, northern Idaho, northeastern Washington, and southern Canada during the Late Cretaceous. Major thrust slabs in western Montana were comprised of the Sapphire and Lombard slabs south of the Lewis and Clark Line and the Lewis-Eldorado-Hoadley slab to the north. Note the eastward budge in the fold-and-thrust directly east of the Sapphire and Lombard slabs referred to as the Helena Salient. The $ISr = 0.706$ line represents the western edge of Precambrian basement (Modified from Sears and Hendrix, 2004).

Hendrix (2004) show that the LCL was reactivated as a major left-Lateral transpressional shear zone from the Late Cretaceous to the Early Eocene (~88-55 Ma). In their model, left-Lateral motion along the LCL accommodated clock-wise rotation and eastward displacement of the LEH, Sapphire, and Lombard thrust slabs in western Montana from

Late Cretaceous to Early Eocene time. In addition, Sears and Hendrix (2004) attribute development of the Helena and Alberta (southern Alberta and northwestern Montana) thrust salients to clock-wise rotation of these major thrust slabs along the LCL during this time.

Late Cretaceous Magmatism

Voluminous magmatism was broadly synchronous with crustal shortening and thickening in eastern Idaho and western Montana. In eastern Idaho and westernmost Montana the Bitterroot lobe (~14,000 km²) of the Idaho-Bitterroot Batholith was emplaced into the accreted Seven Devils-Wallow terrane and Belt Supergroup largely from ~120-52 Ma (see Fig. 1-1, Bickford et al., 1981; Hyndman, 1984; Foster and Fanning, 1997; Foster et al., 2001). Early (~120-70 Ma) “deep level” quartz diorite and tonalite plutons of the western Bitterroot lobe were emplaced at crustal depths up to ~25 km (Hyndman et al., 1988; Foster et al., 2001). In the central and eastern Bitterroot lobe “main phase” granodiorites and two-mica granites were emplaced at progressively shallower crustal depths to the east (~25-10 km) between 65-52 Ma. In addition, several younger alkali-feldspar granite plutons were emplaced in the older batholith intrusions from ~50-46 Ma at very shallow crustal depths ranging from ~7-1.5 km (Foster et al., 2001).

East of the Bitterroot lobe of the Idaho-Batholith Batholith several smaller batholiths, stocks, and plutons were emplaced into the Sapphire and Lombard thrust slabs from ~80-65 Ma at relatively shallow crustal depths (~1-15 km, Hyndman et al., 1988; Kalakay et al., 2001). Major intrusions in this region include the Sapphire Batholith, the Chief Joseph Batholith, the Flint Creek plutons, and the Boulder Batholith (Fig. 2-4).

The Boulder Batholith, the largest of these intrusions (~4,000 km²), intruded its own volcanic cover (the Elkhorn Mountains Volcanics) indicating a very shallow emplacement depth, probably on the order of ~1-10 km (Tilling et al., 1968). Individual plutons and stocks within these large intrusions often exhibit a close spatial and temporal relationship with thrust faulting in the Sapphire and Lombard thrust slabs. In several places within the Flint Creek and Anaconda-Pintlar Ranges (i.e., the Sapphire thrust slab) Late-Cretaceous plutons were preferentially emplaced along thrust faults ramps (Hyndman et al., 1975; Kalakay et al., 2001). Older plutons commonly exhibit strong solid-state deformation while slightly younger plutons emplaced along the thrusts (some cross-cutting the thrusts) are undeformed; this relationship indicates the older plutons were probably emplaced during thrusting while emplacement of the younger plutons post-dated the thrusting (e.g., Hyndman et al. 1975; Hawley, 1975; Wallace et al., 1992; Kalakay et al., 2001). Kalakay et al. (2001) reports similar relationships between Late-Cretaceous plutons and thrust faulting in eastern Pioneer Batholith along the eastern front of the Grasshopper thrust slab located directly south of the Sapphire thrust slab in southwestern Montana. Similarly, the Boulder Batholith was emplaced into a major thrust fault ramp system within the Lombard thrust slab in the Helena thrust salient at ~80-75 Ma (Fig 4., based on SHRIMP U-Pb zircon crystallization ages, Lund et al., 2002). Lageson et al. (2001) suggest that emplacement of the Boulder Batholith (and the Elkhorn Mountains Volcanics) at this time created a supercritical taper geometry in the Lombard thrust slab facilitating further east-directed displacement of the slab.

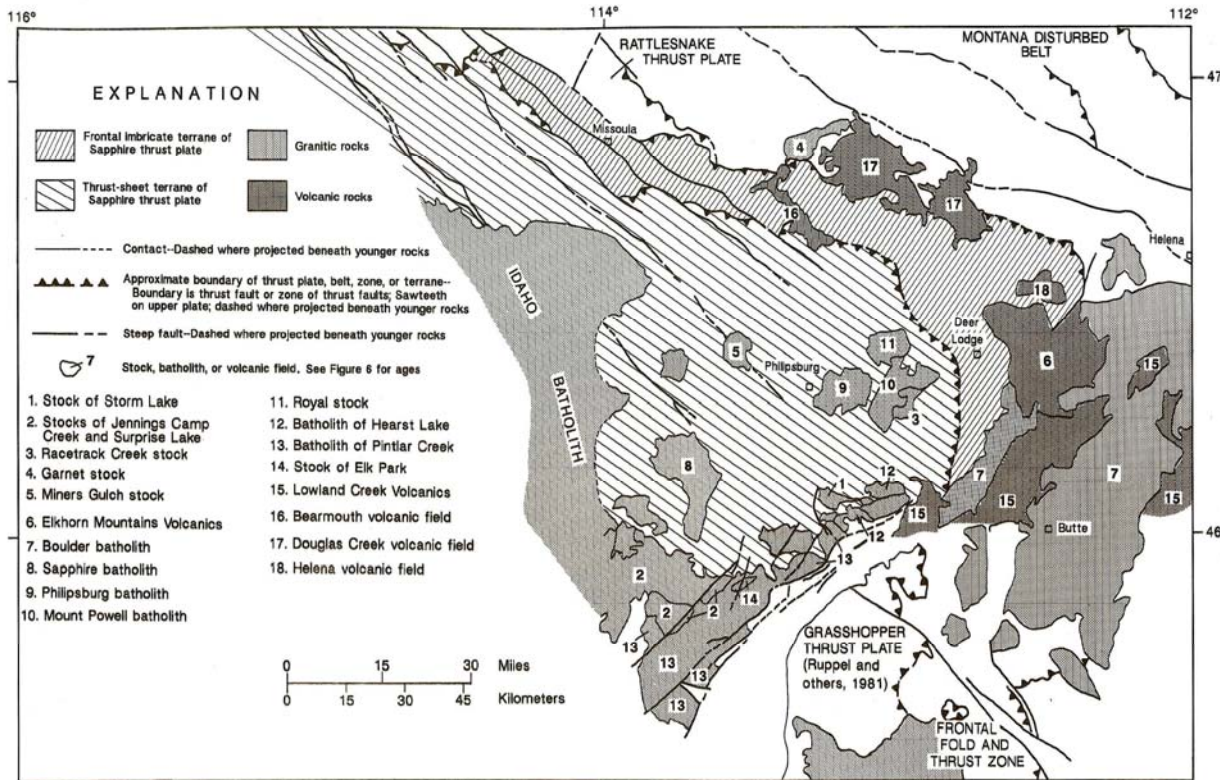


Figure 2-4. Geologic map of western Montana, south of the Lewis and Clark line. Emphasis is on the location and names of Late Cretaceous through middle Eocene granitic batholiths, stocks, plutons, and volcanic fields in the Sapphire thrust plate and the frontal imbricate thrust zone which lies to the east (from Wallace et al., 1992).

High Grade Metamorphism during the Cretaceous

Grover et al. (1992) and House et al. (1997) document three major metamorphic events that affected the areas adjacent to the Bitterroot lobe of the Idaho-Bitterroot Batholith during the Late Early to Late Cretaceous. (1) Regional prograde metamorphism at ~100-80 Ma was synchronous with crustal shortening and partly coincident with emplacement of deep level plutons in the western Bitterroot lobe (~120-70 Ma, Foster et al., 2001). Pressure and temperature conditions during this metamorphism have been estimated (based on phase assemblages and quantitative thermobarometry) to be at Middle-amphibolite facies conditions, ~5-6 kbar and ~500-600°C (House et al., 1997 and references therein). (2) Upper-amphibolite facies metamorphism occurred synchronous to emplacement of main phase plutons in the Bitterroot lobe at ~64-53 Ma. Metamorphic grade decreases from upper-amphibolite facies conditions (peak metamorphic conditions at ~6-8 kbar and ~650-750°C) directly adjacent to the batholith to lower greenschist facies conditions at a distance of ~30 km (House et al., 1997; Foster et al., 2001). Local anatexis accompanied the upper-amphibolite facies metamorphism near the batholith. Anatexis of Belt-equivalent quartz-two feldspar gneisses was facilitated by the breakdown (dehydration) of muscovite within underlying semi-pelitic schist under sillimanite-zone conditions (Foster et al., 2001). (3) Later relatively low pressure (~4-6 kbar) high temperature upper-amphibolite facies metamorphism and anatexis during isothermal decompressional accompanied exhumation of the Bitterroot metamorphic core complex at ~53-48 Ma (see below, House et al., 1997; Foster et al., 2001).

Quantitative thermobarometric data were not available from areas east of the Bitterroot-Idaho Batholith prior to this study. Some workers provide broad pressure-

temperature estimates based on the metamorphic phase assemblages of metasedimentary strata adjacent to plutons. These estimates indicate localized low pressure Middle to upper-amphibolite facies metamorphism at ~1-4 kbar and ~500-700°C accompanied emplacement of the plutons during the Late Cretaceous (~80-70 Ma, Hyndman, 1988, see previous pressure-temperature constraints summarized in a Later section).

Eocene History

An episode of large-scale extension began in the Early to Middle Eocene with inception of numerous metamorphic core complexes along the previously thickened Sevier hinterland, north of the Snake River Plain (SRP) in present-day southern British Columbia, northeastern Washington, northern Idaho, and western Montana (Foster et al., 2001, Foster et al., 2006a). The large-scale core-complex related extension immediately followed the end of crustal shortening (ca. ~55 Ma) in the fold-and-thrust belt located directly to the east of the hinterland (Fig. 1-2, Constenius, 1996; Foster et al., 2001; Sears and Hendrix, 2004). Large-scale extension in these metamorphic core complexes was facilitated by displacement along low-angle brittle/ductile normal-sense detachment fault zones comprised of a brittle upper crustal portion rooted to a mid-crustal ductile portion; the mid-crustal portion of these detachments are characterized by mylonitic shear zones (Coney, 1980; Lister and Davis, 1989; Wernicke, 1992; Foster et al., 2001).

Early extension in the metamorphic core complexes of southern British Columbia and the northwestern United States was accompanied by the voluminous Kamloops-Colville-Challis-Absaroka (KCCA) magmatism in the back-arc region, ~500-1000 km inboard of the convergent plate margin (Armstrong and Ward, 1991; Morris et al., 2000; Breitsprecher et al., 2003). The (KCCA) magmatism is expressed by a belt of calc-alkaline and alkaline volcanic rocks extending from British Columbia into northwestern

Wyoming and roughly overlaps with areas affected by extension in the metamorphic core complexes. The exhumed lower plates of many of the Eocene metamorphic core complexes in southern British Columbia and the northwestern United States are characterized by voluminous granitic plutons the same age as the (KCCA) volcanic rocks (Armstrong and Ward, 1991; Foster et al., 2006a).

Regional Transtension and Large-scale Crustal Extension along the Lewis and Clark Line

Large-scale crustal extension in the metamorphic core complexes of northeastern Washington, northern Idaho, and western Montana was linked kinematically to regional dextral transtensional along the Lewis and Clark line during the Eocene (LCL, Doughty and Sheriff, 1992; Yin and Oertel, 1995; Foster et al., 2006a). The LCL is comprised of a northwest-west trending ~40-80 km wide zone of steeply-dipping strike-slip, oblique-slip, and dip-slip faults that stretches from northeastern Washington into west-central Montana (a distance greater than 800 km). Several major faults along the LCL have accommodated repeated displacement during tectonic reactivations since inception of the line during the Mesoproterozoic or earlier (Wallace et al., 1990; Sears and Hendrix, 2004). Regional dextral transtension and development of metamorphic core complexes along the LCL began in Early to Middle Eocene time (at. ~54-52 Ma) after a long-lived episode of sinistral transpressional during the Late Cretaceous to early Eocene (ending at ~55 Ma) associated with east-directed crustal shortening in the fold-and-thrust-belt of western Montana (Foster et al., 2001; Sears and Hendrix, 2004; Foster et al., 2006a). The detachment fault zone of the metamorphic core complexes along the LCL are structurally linked to one another via strike-slip and/or oblique-slip splay faults of the LCL; these

splay faults exhibit major Eocene aged dextral offset (Fig. 1-2, Hendrix and Sears, 2004; Foster et al., 2006a).

Although the timing of large-scale Eocene extension in metamorphic core complexes along the LCL is very similar, there are some significant differences in the kinematics of extension in these metamorphic core complexes north and south of the LCL. To the north, metamorphic core complexes were exhumed by paired (or symmetric) east and west dipping detachment fault zone by ENE-WSW directed tectonic unroofing (Fig. 1-2; e.g., Okanagan, Kettle, and the Priest River metamorphic complexes). To the south, the BCC was exhumed by a single (or asymmetric) east dipping detachment fault zone by ESE directed unroofing (Foster et al., 2006a). It has been proposed that the ACC was exhumed along east-dipping detachment fault zone by ESE directed unroofing as well (Kalakay et al., 2003; O'Neill et al., 2004, Foster et al., 2006a). The Clearwater metamorphic core complexes is located within the LCL and occupies a relay between two major strike-slip faults which link the Priest River metamorphic core complex and the BCC (Fig. 1-2). The Clearwater metamorphic core complexes was exhumed along single east-dipping detachment fault zone by top-to-the-east directed unroofing, similar to the BCC (Foster et al., 2006a).

CHAPTER 3
THE ANACONDA METAMORPHIC CORE COMPLEX

Structural-metamorphic Domains of the Anaconda Metamorphic Core Complex:

The Anaconda metamorphic core complex (ACC) is located within the collapsed Sevier hinterland province in western Montana, south of the Lewis and Clark line, east of the Bitterroot metamorphic core complex, and west of the Boulder Batholith, and Helena salient of the fold-and-thrust belt (Fig. 1-1 and 1-2). As in other Cordilleran metamorphic core complexes (e.g., Coney, 1980), the ACC is subdivided into three structural-metamorphic domains: (1) the high grade metamorphic and plutonic lower plate (footwall), (2) the unmetamorphosed or low-grade metamorphic, brittle faulted upper plate (hanging wall), and (3) the detachment fault zone which juxtaposes and separates the upper and lower plates.

In this chapter general descriptions are provided for each of the three structural-metamorphic domains of the ACC. Detailed descriptions are provided for the Lake of the Isle shear zone, a km-scale upper-amphibolite facies ductile shear zone mapped in the northeastern Anaconda-Pintlar Range during this study. Detailed descriptions of the individually mapped ACC lower plate units and a new 1:24,000 scale geologic map of the study area are provided in Appendix B and D, respectively.

The Lower Plate

Rocks of the ACC lower plate are partly exposed in the cores of two broad antiformal flexures, or domes, in the Flint Creek and northern Anaconda-Pintlar Ranges that lie structurally beneath the detachment. These two antiforms are separated by a

synformal trough west of Anaconda, MT where upper plate rocks partly cover the lower plate rocks (Fig. 3-1, O'Neill et al., 2004). Lower plate rocks in the Flint Creek and Anaconda-Pintlar Ranges are comprised partly of metamorphic equivalents to the Mesoproterozoic Belt Supergroup, Middle Cambrian, and in some areas, to Devonian to Lower Cretaceous sedimentary strata. All of these metasedimentary strata were intruded by multiple generations of Late Cretaceous to early-middle Eocene batholiths, plutons, stocks, dikes, and sills (Fig. 3-1 and 3-2, Emmons and Calkins, 1913; Csejtey, 1963; Stuart, 1966; Desmarais, 1983; Heise, 1983; Wallace et al., 1992; Lonon et al., 2003). A new 1:24000 scale geologic map was produced from the ACC lower plate located in the field area of this study. The map and a detailed description of the mapped lower plate units are included in Appendix F and B, respectively.

In the Flint Creek Range, the intrusive rocks comprise epizonal biotite-hornblende granodiorite and granitic plutons of the Late Cretaceous Mount Powell and Philipsburg Batholiths and the Royal Stock which intrude mostly Cambrian and Lower Cretaceous-equivalent metasedimentary strata and Belt-equivalent metasedimentary strata in a few areas (Fig. 3-1, Allen, 1966; Stuart, 1966; Hyndman et al., 1972; Lonon et al., 2003). In the Anaconda-Pintlar Range, both Late Cretaceous and early to middle Eocene intrusive rocks intrude mostly Belt and middle Cambrian-equivalent metasedimentary strata (Desmarais, 1983; Wallace, et al., 1992; Lonon et al., 2003). The early to middle Eocene intrusive rocks are much more voluminous and form a southward widening belt of biotite granodiorite, biotite granite, and two-mica granite batholiths, stocks, and plutons along the entire length of the Anaconda-Pintlar Range (Fig. 3-2, Desmarais, 1983; Wallace et al., 1992).

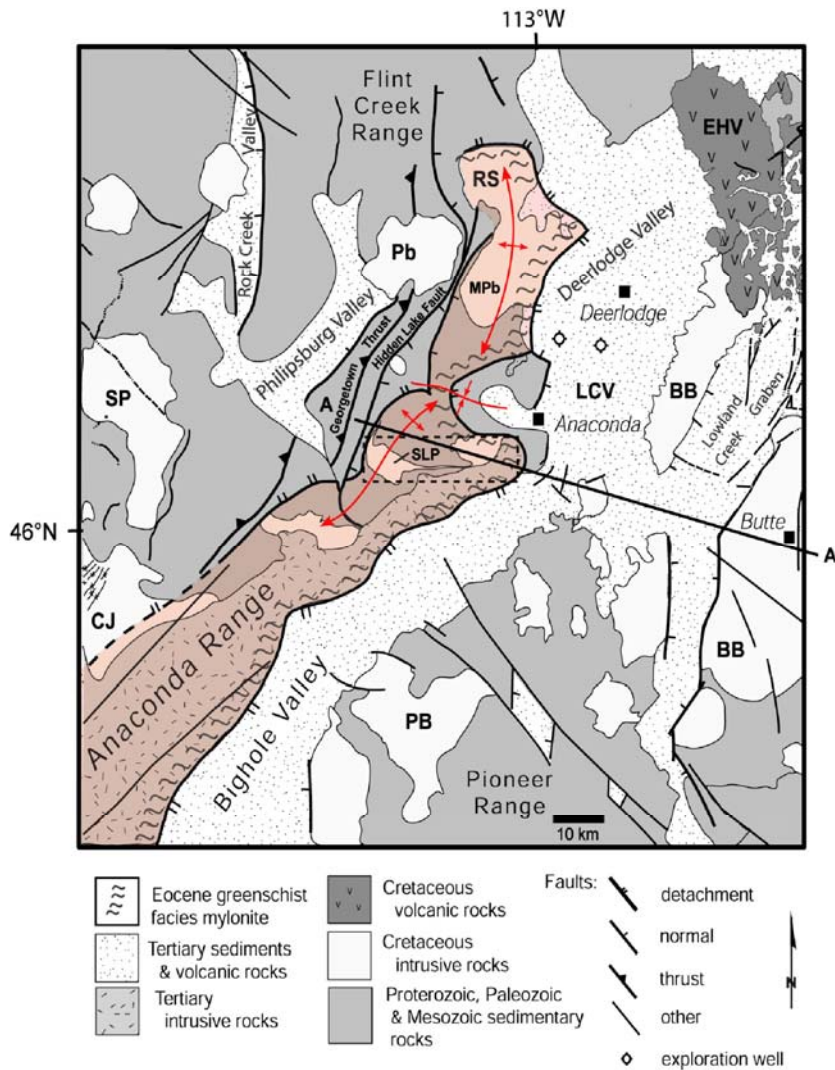


Figure 3-1. Geological Map of the Anaconda metamorphic core complex (ACC) in western Montana. The exhumed ACC lower plate (footwall) highlighted in red is exposed in the Anaconda-Pintlar eastern Flint Creek Ranges. The detachment zone bounds the eastern side of the lower plate and consists of the Eocene greenschist facies mylonite and overprinting brittle detachment. The ACC upper plate (hanging wall) lies mostly east of the lower plate and detachment zone with limited exposes just west of Anaconda, MT between the Anaconda-Pintlar and Flint Creek Ranges. RS = Royal Stock, Pb = Philipsburg Batholith, MPb = Mt. Powell Batholith, SLP = Storm Lake Stock pluton, SP = Sapphire Batholith, CJ = Chief Joseph Batholith, PB = Pioneer Batholith, BB = Boulder Batholith, LCV = Lowland Creek Volcanic Field, EHV = Elkhorn Mountains Volcanic Field. The current study area is marked by the dashed box (Modified from Foster et al., 2006a).

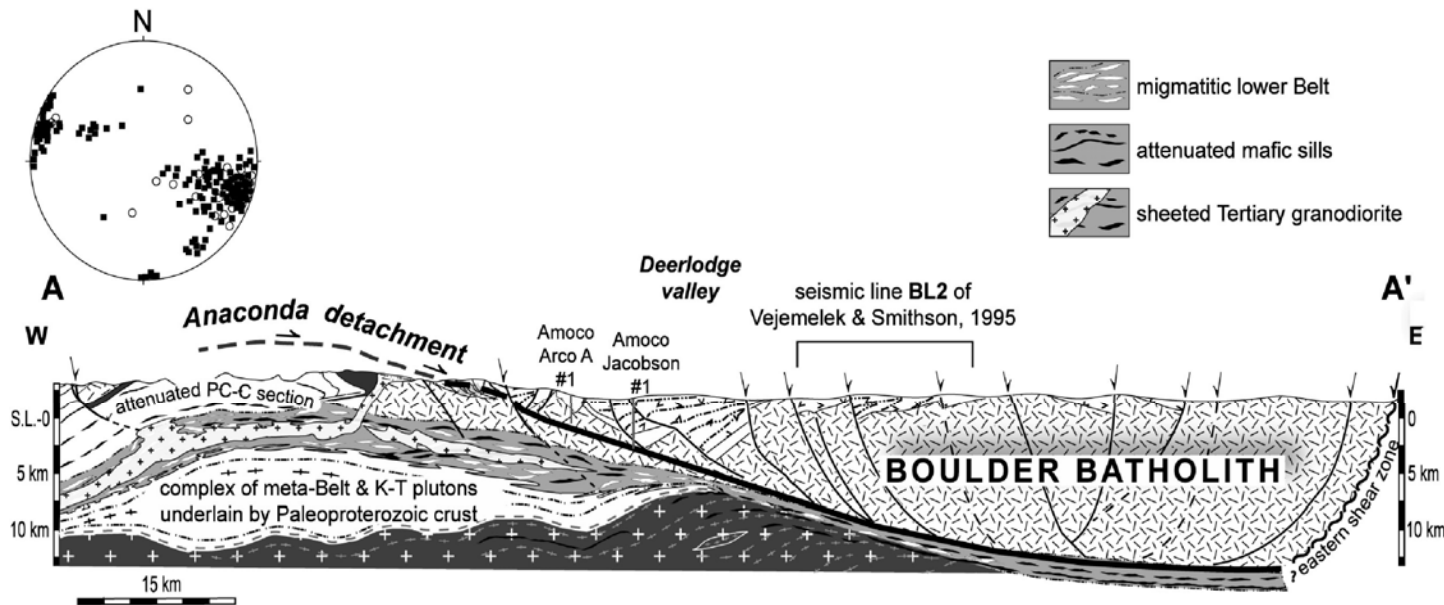


Figure 3-2. Geologic cross section of the Anaconda metamorphic core complex, western Montana. The Eocene mylonite and brittle detachment dip gently to the east beneath the Deerlodge Valley and project beneath the Boulder Batholith as indicated by Amoco exploration wells and seismic reflection data (see text for details). Equal-area stereonet projection shows the orientation of mylonite stretching lineations (solid squares) and fault slickenlines (open circles) from the detachment zone (Stereonet data and cross section from courtesy of Kalakay).

Major structures exposed with the ACC lower plate include numerous folds and low-angle thrust faults related to crustal shortening along the eastern edge of the Sapphire (Skalkaho) thrust plate during the Late Cretaceous (Hyndman, 1975; Hyndman et al., 1988; Wallace et al., 1992; Sears and Hendrix, 2004). The Georgetown thrust (Emmons and Calkins, 1913), the largest of the thrust fault structures, places metamorphosed Helena Formation (middle Belt Carbonate-equivalent) over Devonian, Pennsylvanian, and Mississippian metasedimentary strata (>7000 m of stratigraphic offset) and marks the western margin of the ACC lower plate from central Anaconda-Pintlar Range to the northern Flint Creek Range (Fig. 3-2, Wallace et al., 1992; O'Neill et al., 2004). The northern end of this thrust is cut by the Philipsburg Batholith in the western Flint Creek Range which yielded concordant hornblende and biotite K-Ar cooling ages of ~77-72 Ma (Hyndman et al., 1972). Several other thrust faults and related folds involving Belt-equivalent through Cretaceous metasedimentary strata have been documented in throughout the Flint Creek and Anaconda-Pintlar Ranges (e.g., Emmons and Calkins, 1913; McGill, 1959; Flood, 1974; Heise, 1983; Baken, 1984; Wallace et al., 1992; Lonn et al., 2003). A common characteristic in both the Anaconda-Pintlar and Flint Creek Ranges is the close spatial and temporal relationship between thrusting and emplacement of Late Cretaceous plutons (e.g., the Philipsburg Batholith and Georgetown thrust, Emmons and Calkins, 1913; Wallace et al., 1992).

Other structures found within the ACC lower include high-angle, sometimes listric-shaped, normal faults associated with the brittle detachment found mostly along the eastern flanks of the Flint Creek and Anaconda-Pintlar Ranges (see below). The largest normal fault exposed in the ACC lower plate is the Hidden Lake-Dry Creek fault zone

(HLCDFZ), a large east-dipping, listric-shaped, locally ductile normal fault zone that strikes parallel to and lies directly east of the Georgetown thrust (Fig. 3-1, 3-2). The HLDCF shows >450 m of offset in some areas and may have been active in the Late-Cretaceous during intrusion of the Dora Thorn pluton of the Philipsburg Batholith (Buckley, 1990) and during the Eocene, as listric splays of the HLDCF form ductile shear zones in the middle Eocene Pintlar Creek Batholith in the northern Anaconda-Pintlar Range (Wallace et al., 1992). The shallow portion of these splay faults may have been part of the original east-dipping detachment breakaway zone or an east-dipping brittle normal fault synthetic to the basal detachment (O'Neill et al., 2004).

The Mesoproterozoic Belt through Cretaceous-equivalent metasedimentary strata exposed in the ACC lower plate have been subjected to at least two major episodes of high grade metamorphism: (1) pervasive regional metamorphism that predated the emplacement of voluminous epizonal Late Cretaceous to Middle Eocene intrusions and (2) high temperature, lower pressure contact metamorphism associated with the emplacement of the Late Cretaceous to Middle Eocene (Emmons and Calkins, 1913; Csejtey, 1963; Stuart, 1966; Desmarais, 1983; Heise, 1983; Hyndman et al., 1988; Wallace et al., 1992; Kalakay et al., 2003; Grice et al., 2005). In the Flint Creek Range, a pervasive regional upper-amphibolite facies cordierite-bearing assemblage, found mostly within pelitic Cretaceous-equivalent phyllite, is overprinted by andalusite-bearing assemblages in contact aureoles surrounding the Late Cretaceous intrusions (Stuart, 1966; Buck, 1990). The earlier regional metamorphic assemblages show an overall increase in metamorphic grade from greenschist to upper-amphibolite facies from west to east across the Flint Creek Range (Stuart, 1966). In the Anaconda-Pintlar Range, upper-amphibolite

facies sillimanite-cordierite bearing assemblages are common in Lower Belt-equivalent pelitic metasedimentary strata (Greyson Fm.) surrounding Late Cretaceous granodiorite and quartz diorite plutons and sills. These metasedimentary strata are locally migmatitic and characterized by granitic leucosome, abundant sillimanite, cordierite, garnet, K-feldspar, biotite, and no primary muscovite (Desmarais, 1983; Grice et al., 2005). This phase assemblage overprints an earlier higher pressure kyanite-bearing assemblage in the current study area in the northeastern Anaconda Pintlar Range (see description of the LISZ below, Kalakay et al., 2003; Grice et al., 2005). In addition, andalusite-bearing assemblages overprint cordierite-sillimanite-bearing assemblages in some pelitic metasedimentary strata adjacent to early to middle Eocene intrusions in the northern Anaconda Pintlar Range (Emmons and Calkins, 1913). Andalusite assemblages were not documented in the contact aureoles of Late Cretaceous intrusions in the current study area. As in the Flint Creek Range, the regional metamorphic grade shows a general increase from middle to uppermost amphibolite facies from west to east across the Anaconda-Pintlar Range (Kalakay et al., 2003). A summary of previous pressure-temperature estimates from the lower plate, along with new thermobarometry from LISZ in this study, are provided in chapter 5.

The Detachment Fault Zone

The high grade metamorphic and plutonic rocks of the lower plate and unmetamorphosed upper plate rocks of the ACC are juxtaposed and separated by an east-dipping low-angle brittle detachment that exhibits significant top-to-the-east-southeast displacement (Fig. 3-1 and 3-2, O'Neill et al., 2002; Kalakay et al., 2003; O'Neill et al., 2004). The detachment was first recognized and mapped by Emmons and Calkins (1913) who noted its striking similarities with the “great Bitterroot fault,” which was later

defined to be the low-angle detachment that bounds the Bitterroot metamorphic core complex to the west (Hyndman, 1980). The detachment now has a documented strike length of >100 km stretching from the northern flank of the Flint Creek Range south to the Bighole Valley along the eastern flanks of the southern Anaconda-Pintlar Range (Kalakay et al., 2003; O'Neill et al., 2004). In the north, the detachment terminates into steeply-dipping strike-slip and oblique-slip splay faults of the Ninemile fault, part of the greater Lewis and Clark line (Foster et al., 2006a). The southern termination of the brittle-ductile detachment has not been well established. Along the eastern flanks of the Flint Creek and Anaconda-Pintlar Ranges the detachment dips gently ($\sim 10\text{-}30^\circ$) beneath the Deerlodge Valley; the gentle dip of the detachment is collaborated by industry exploration wells that intersected greenschist mylonites at the base of the Tertiary basin fill in the western Deerlodge Valley at depths of ≤ 5 km (Fig 3-2, McLeod, 1987). In addition, the downward projection of the detachment aligns well with sub-horizontal seismic reflectors beneath the Boulder Batholith, suggesting the detachment flattens with depth and continues to the east (Fig. 3-2, Vejmelek and Smithson, 1995; Foster et al., 2006a). The detachment is not well exposed along the western margin of the ACC; however, it is inferred in several places by the juxtaposition of brittlely faulted upper plate rocks with ductily deformed metamorphic rocks and plutonic rocks. The western part of the detachment probably originated as a series of east-dipping listric-shaped normal faults east of a breakaway zone, which is inferred to be directly east of the Georgetown thrust (O'Neill et al., 2004; Foster et al., 2006a).

In the northeastern Anaconda-Pintlar Range, within the current study area, the brittle detachment overprints a $\sim 300\text{-}500$ m thick greenschist facies mylonitic shear zone

comprised mostly of stretched two-mica granite, biotite granite, and granodiorite and minor micaeous quartzite (Fig. 3-3, Emmons and Calkins, 1913; Kalakay et al., 2003; Appendix D). Strain is heterogeneous in the granitoid mylonites and distributed into numerous 1-2 m thick ultramylonite zones separated by 5-15 m thick zones of mylonite and protomylonite (Foster et al., 2006a). The metamorphic grade of the granitoid mylonites is indicated by brittle fractured feldspar porphyroclasts surrounded by a matrix of plastically deformed quartz (Kalakay et al., 2003). In addition, micaeous quartzite mylonites exhibit unannealed quartz grains with well-developed undulatory extension in thin section (Fig. 3-4a); these features are indicative of lower to middle greenschist facies metamorphism at temperatures < 400-450°C (Wells et al., 2000). In addition, the greenschist mylonites contain kinematic indicators and shallow plunging mineral stretching lineations that show top-to-the-east-southeast sense of movement; mineral lineations in both the granitoid and micaeous quartzite mylonites are comprised of stretched quartz ribbons (Fig 3-4a and 4b, 102-108°, Kalakay et al., 2003; O'Neill et al., 2004).

The greenschist facies mylonites exposed in the Mill and Clear Creek drainages are cut by series of closely spaced (~0.1-1 km) east-dipping listric-shaped normal faults that commonly become sub-horizontal with depth and tangential to the highly strained ultramylonite zones in the mylonites (Kalakay et al., 2003). In some places, the deeper portions of these brittle faults terminate into the detachment (O'Neill et al., 2004). Good examples of these faults are found on the western walls of the Clear Creek drainage and along the continental divide separating the Mill and Tenmile Lake drainages (Fig. 7-5, Appendix D). Slickenline striations on these fault surfaces indicate top-to-the-east-

southeast (100-110°) slip, consistent with motion in the greenschist mylonites (Kalakay et al., 2003; Foster et al., 2006a).

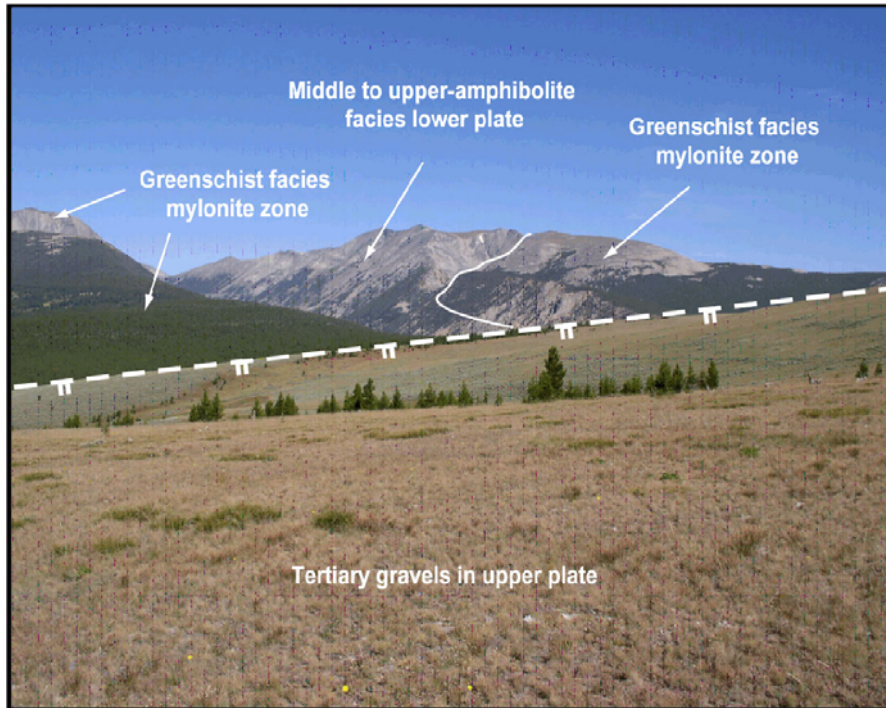


Figure 3-3. Photomosaic of the Anaconda metamorphic core complex. Photo directed to the northwest showing the brittle detachment (dashed and barbed line) which juxtaposes unmetamorphosed Tertiary upper plate rocks with the Eocene greenschist facies mylonite zone and high grade lower plate rocks.

To the north, along the eastern flank of the Flint Creek Range, Eocene mylonites formed in the eastern parts of the Mount Powell Batholith and Royal Stock, both comprised mostly of Late Cretaceous granodiorite and granite plutons (Allen, 1966; Lonon et al., 2003; O'Neill et al., 2004). These mylonites are cut by high-angle normal faults similar to those exposed in the Clear and Mill Creek drainages in the northeastern Anaconda-Pintlar Range (O'Neill et al., 2004). To the south, along the eastern flanks of the central and southern Anaconda-Pintlar Range, Wallace et al. (1992) mapped and described low grade mylonites in two mica granites and granodiorites of the Middle Eocene Pintlar Creek Batholith. These mylonites are cut by a series of northeast-trending

steeply-dipping normal faults related to the detachment that juxtapose the mylonites with unmetamorphosed Tertiary fluvial deposits.

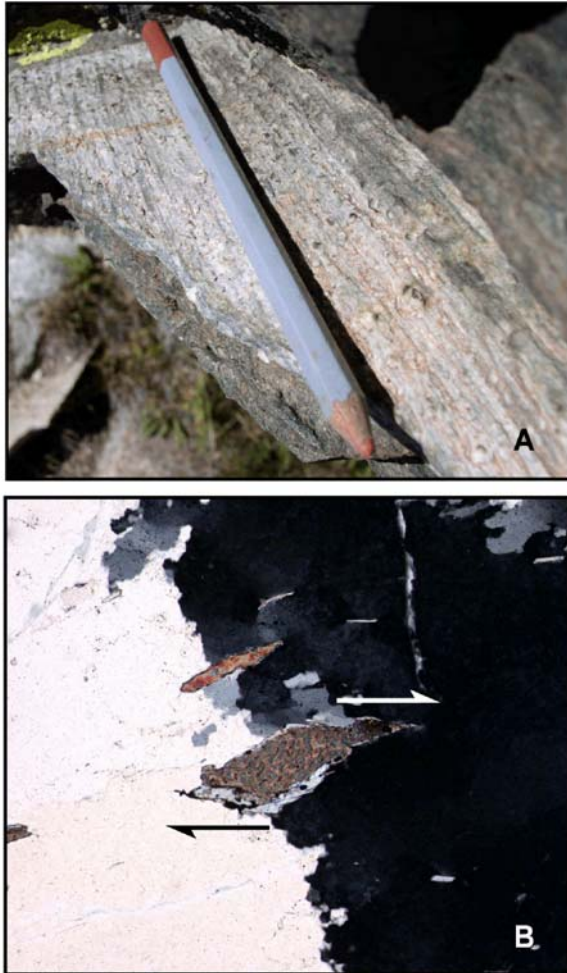


Figure 3-4. Greenschist facies mylonites. A) Outcrop photo of stretched granodiorite with greenschist facies mylonitic fabric, upper Clear Creek drainage. Pencil is oriented parallel to the stretching lineation ($T/P = 100^\circ/10^\circ$). B) Photomicrograph of mylonitic micaeous quartzite, Short Peak, right is to the ESE. Asymmetric mica fish with top-to-the-ESE sense of shear. Note undulatory extinction in the large deformed quartz grains. Cross polar light; field of view is ~ 2 mm.

The Upper Plate

Structurally above the high grade metamorphic-plutonic lower plate, greenschist facies mylonitic shear zone, and brittle detachment, the eastern ACC upper plate is mostly composed of an array of asymmetrical fault-bound basins filled with

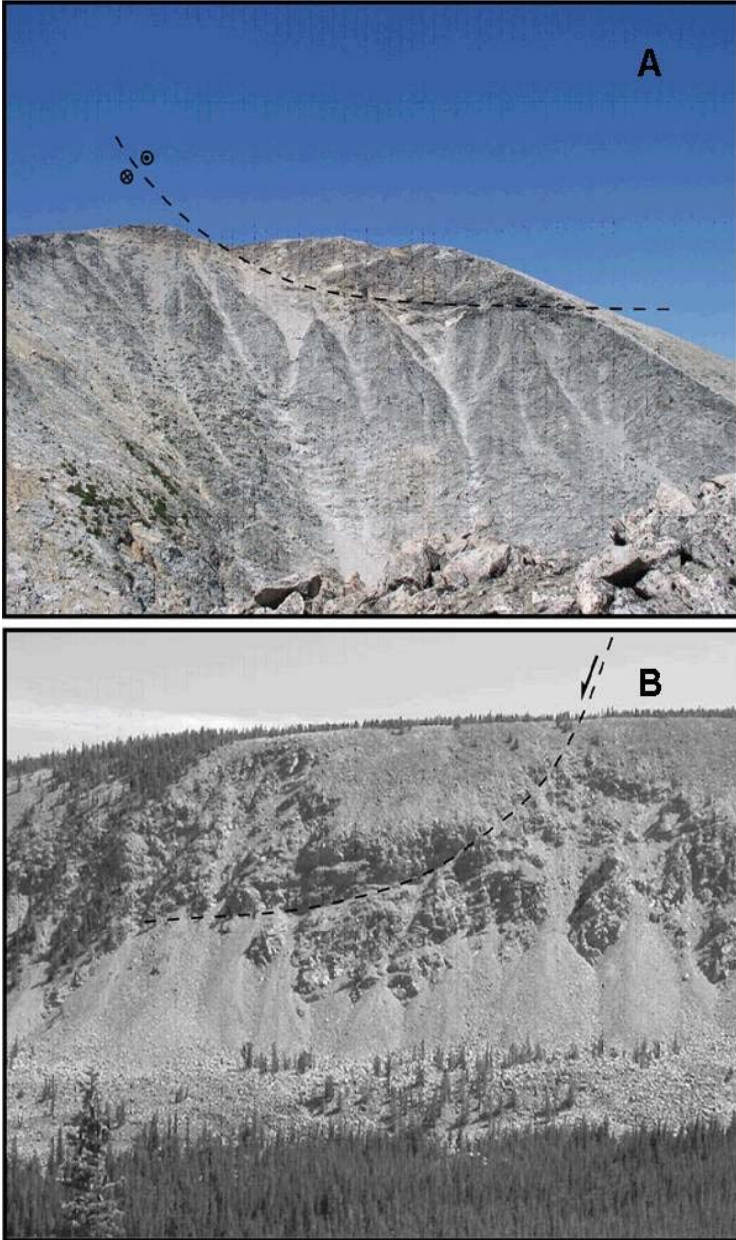


Figure 3-5. Outcrop photos of late listric-shaped brittle normal faults in the greenschist facies mylonite zone. A) Photo taken from the southeastern flank of Short Peak looking towards the northwest showing a listric-shaped brittle fault that juxtaposed mylonitic micaeous quartzite with biotite granodiorite. Symbols: Dot within the circle indicates previous fault motion out-of-the-page and X within the circle indicates previous fault motion “into-the-page.” B) Photo taken from eastern side of the upper Clear Creek drainage looking south showing an east-dipping listric-shaped brittle fault cutting greenschist facies two-mica granite mylonite (photo in B is courtesy of David Foster).

unmetamorphosed syn-extensional Tertiary sedimentary, volcanoclastic, and volcanic rocks (Fig. 3-1, 3-2). The faults that bound the basins are listric-shaped and sometimes

sole into the low-angle detachment at depth. In the Deerlodge Valley, the stratigraphically lowest rocks in the basins consists of moderately west tilted ($\sim 50\text{-}60^\circ$), poorly sorted, and poorly consolidated conglomerates, sandstones, breccias and mega-breccias (Kalakay et al., 2003; O'Neill et al., 2004). These strata grade upwards into progressively less tilted ($\sim 0\text{-}25^\circ$) volcanic lava flows, volcanic tuffs, and volcanoclastic units that are correlated with the early to middle Eocene Lowland Creek Volcanic (LCV) sequence ($\sim 54\text{-}48$ Ma, based on $^{40}\text{Ar}/^{39}\text{Ar}$ cooling ages from the volcanic units by Isoplatov, 1997; Lewis, 1990; Kalakay et al., 2003). The significant upward decrease in tilt of the basin fill strata indicates deposition during brittle extension of the ACC upper plate in the early to middle Eocene (Kalakay et al., 2003). Clasts of greenschist facies two-mica granite and granodiorite mylonite were found in stratigraphically high volcanoclastic lahar deposits in the upper plate, directly south of the current study area. However, the age or volcano-stratigraphic correlation of these volcanoclastic deposits is not yet well established (Kalakay et al., 2003; Foster, per comm.).

Description of the Lake of the Isle Shear Zone

A sinuous, km-scale ductile shear zone was documented and mapped in the ACC lower plate within the northeastern Anaconda-Pintlar Range during this study. The ductile shear zone strikes approximately east-west and outcrops over a broad area from immediately west of Storm Lake ~ 15 km to the east near the base of Mount Haggin in the upper Mill Creek drainage. In the Mount Haggin area, the easternmost part of the ductile shear zone is truncated by granitoids and greenschist mylonites associated with the Eocene detachment. The ductile shear zone has been named the Lake of the Isle shear zone (LISZ) herein after a small lake in the central part of the shear zone (see Appendix D).

Mesoproterozoic Belt Supergroup and Middle Cambrian-equivalent

metasedimentary in the LISZ have been subjected to pervasive ductile deformation under middle to upper-amphibolite facies conditions and exhibit a well-developed transposed metamorphic foliation throughout the structure; the dip of the foliation varies from gentle to moderate in east and west and is sub-vertical in the central LISZ (Appendix F). As a result, the metasedimentary strata deformed in the LISZ are strongly attenuated (ductily thinned) and characterized by dramatically reduced original stratigraphic thicknesses, common mesoscopic boudins, and recumbent, locally isoclinal mesoscopic folds. Late Cretaceous and early to middle Eocene plutons, dikes, and sills intrude the LISZ along its entire length. The spatial relationship between these intrusions and the LISZ is described below along with several aspects of the ductile deformation and high grade metamorphism that were briefly summarized here.

Description and Distribution of Metamorphic and Structural fabrics

Metamorphic foliations and gneissic banding

Metasedimentary strata deformed and metamorphosed in the LISZ are correlated with metamorphosed Mesoproterozoic Belt Supergroup and Middle Cambrian sedimentary strata (Appendix B). Belt Supergroup-equivalent metasedimentary strata mapped in the LISZ include the metamorphosed Greyson Formation (Lower Belt), Ravalli Group, Helena Formation (Middle Belt Carbonate), and Missoula Group. Middle Cambrian-equivalent metasedimentary strata mapped include the metamorphosed Flathead Formation, Silver Hill Formation, and Hasmark Formation.

All of the meta-Belt and meta-Cambrian metasedimentary strata in the LISZ exhibit a metamorphic foliation and/or gneissic (compositional) banding. The pelitic schist correlated with Greyson Formation (Lower Belt) shows a strongly developed foliation

defined by the parallel alignment of abundant coarse-grained biotite with less abundant fine-grained sillimanite fibrolite. Some exposures of the meta-Greyson pelitic schist in the southern study area have a foliation comprised of biotite + sillimanite fibrolite + muscovite. In the central and eastern study area the pelitic schist grades to a pelitic paragneiss (also correlated with the metamorphosed Greyson Fm.) characterized by a distinct gneissic banding. The gneissic banding in these strata is defined by alternating quartzite and pelitic layers, both typically ranging from ~1-20 cm in thickness. The quartzite layers of the gneissic banding are comprised of medium to coarse-grained light-to-dark grey quartzite with minor biotite. The pelitic layers are medium to coarse-grained and comprised largely of (in increasing relative abundance) cordierite + garnet + plagioclase + biotite + K-feldspar + quartz + sillimanite fibrolite. Within the pelitic layers very abundant sillimanite fibrolite and much less abundant biotite (note the lack of muscovite) comprise a strongly developed foliation parallel to the gneissic banding (Fig. 7-6).

The biotite quartzite paragneiss (metamorphosed Ravalli Group) often exhibits a moderately to strongly developed gneissic banding. This gneissic banding is defined by alternating quartzite and more pelitic layers, both ranging in thickness from a few centimeters to a few meters in some places. The quartzite layers are composed of light to medium-grey medium-grained quartzite with minor biotite. The more pelitic layers are typically medium-grained and largely comprised of (in increasing relative abundance) K-feldspar + biotite (commonly chloritized) + plagioclase + quartz ± muscovite. In both the quartzite and more pelitic layers aligned biotite defines a weakly to moderately developed foliation parallel to the gneissic banding (Fig. 7-7a). In addition, in some exposures the

foliation in the more pelitic layers is comprised of aligned biotite + sillimanite fibrolite ± muscovite.

The calc-silicate paragneisses correlated with the metamorphosed Helena Formation and Missoula Group (middle and upper Belt, respectively) are also commonly characterized by a prominent gneissic banding. Within these calc-silicate paragneisses, gneissic banding is defined by alternating light-grey to light-green and dark-green layers. The light-grey to light-green layers are mostly composed of quartz + calcite ± chlorite while the dark-green layers are comprised of diopside + calcite + quartz ± chlorite ± tremolite ± sericite white mica. Light-grey to light-green and dark-green layers are both fine-grained and typically range in thickness from ≤ 1 mm to ~ 10 cm (Fig. 7-7b). Aligned chlorite defines a moderately developed foliation in both of these layer types which is oriented parallel to the gneissic banding. A thin section prepared from the dark green layering in the Missoula Group-equivalent calc-silicate paragneiss exhibits highly altered tremolite phenocrysts surrounded by a matrix rich in clinopyroxene (Fig. 8). Near the base of both the Helena Formation and Missoula Group the calc-silicate paragneisses grade into layers of alternating biotite schist and biotite-rich quartzite where biotite ± chlorite define a moderate to strongly developed foliation parallel to gneissic banding.

The metamorphosed middle Cambrian-equivalent strata within the LISZ lack gneissic banding but do exhibit variably developed metamorphic foliations. The white to pink coarse-grained quartzite correlated with metamorphosed Flathead Formation shows a weakly to moderately developed foliation in some areas defined solely by the parallel alignment of muscovite. Fine-grained biotite schist correlated with metamorphosed

Silver Hill Formation exhibits a moderately developed foliation composed of aligned biotite \pm sillimanite. The white coarse-grained marble correlated with the Hasmark

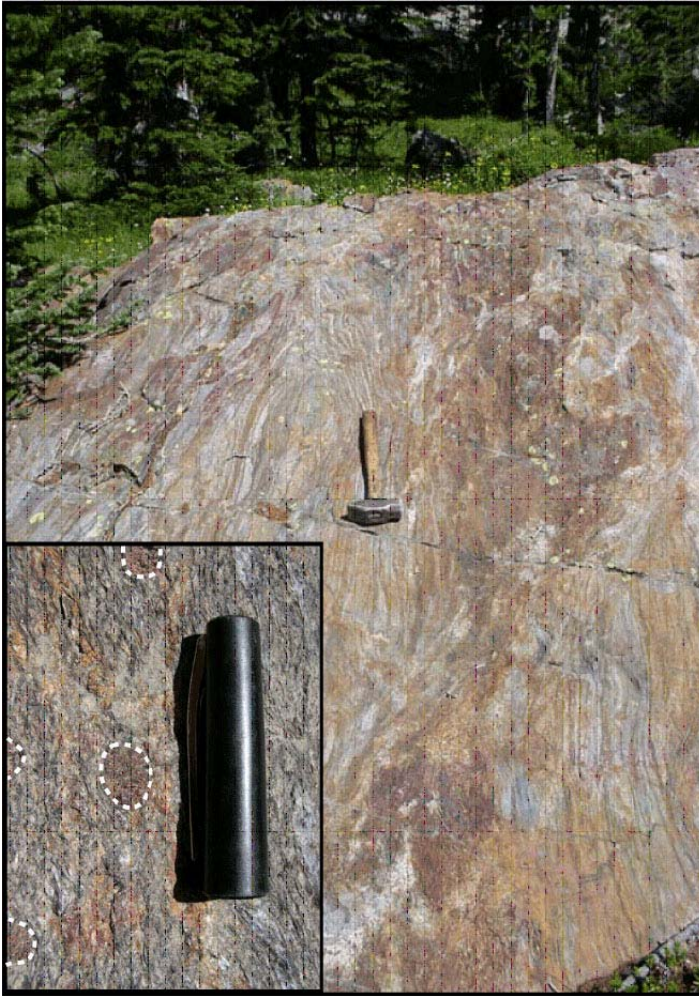


Figure 3-6. Outcrop photograph showing the strong gneissic banding of the metamorphosed Greyson Formation in the LISZ. The inset shows a close up of the outcrop exhibiting large garnet porphyroblasts encased by a metamorphic foliation comprised of abundant sillimanite fibrolite with less biotite. Photograph is directed to the east.

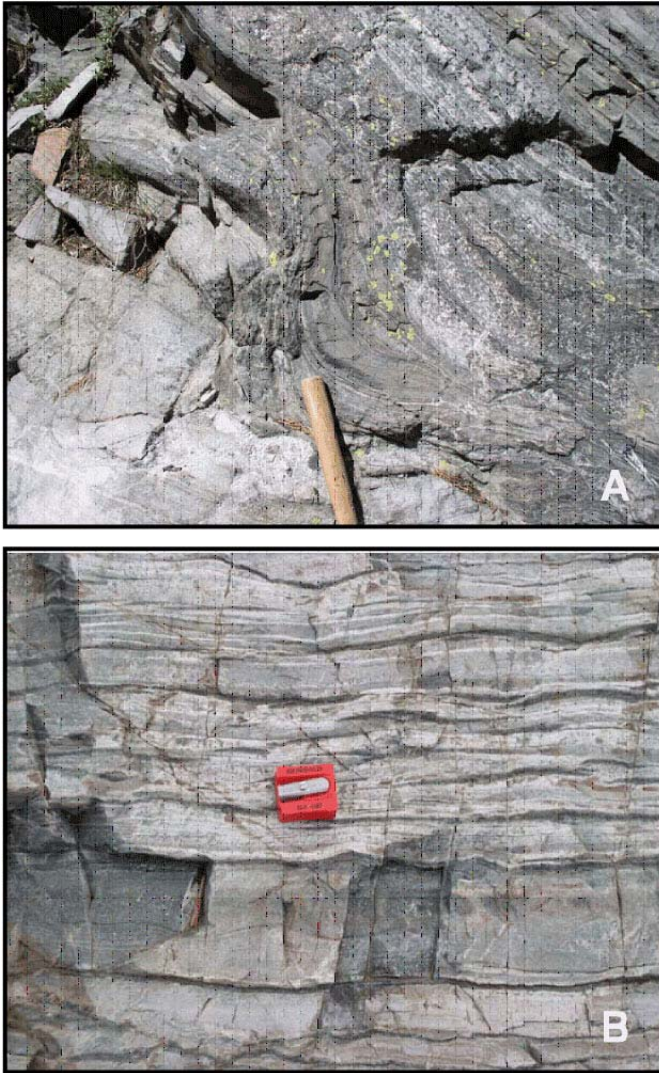


Figure 3-7. Outcrop photographs of gneissic banding commonly observed in the LISZ. A) Gneissic banding common in the metamorphosed Ravalli Group. Rock hammer handle for scale. B) Gneissic banding common in the metamorphosed Missoula Group. The pencil sharpener is for scale.

Formation lacks a visible foliation in most places observed. However, a few outcrops exhibit a weak foliation defined by the parallel alignment of sparse chlorite.

In the central and eastern study area, a prominent deformed quartz diorite sill is emplaced within Belt and Middle Cambrian-equivalent metasedimentary strata and

exhibits a moderately to strongly developed solid-state foliation. The solid-state foliation is defined by the parallel alignment of elongate hornblende, K-feldspar, plagioclase, and

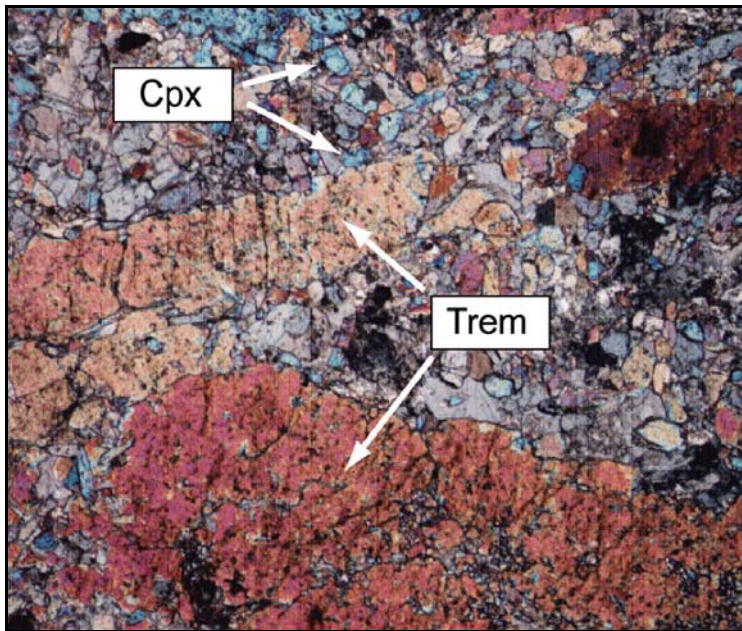


Figure 3-8. Photomicrograph of the Missoula Group-equivalent calc-silicate paragneiss. Note large altered tremolite grains surrounded by fine-grained clinopyroxene in the matrix. Photomicrograph was taken in cross polar light. Trem = Tremolite, cpx = Clinopyroxene. Field of view is ~3 mm.

quartz (Fig. 3-9). This foliation is concordant to (parallel with) the metamorphic foliations and gneissic banding in the adjacent attenuated Belt and middle Cambrian-equivalent metasedimentary strata.

Mesoscopic-scale folds

Mesoscopic-scale folds are found in both the meta-Belt and meta-Cambrian metasedimentary strata in the LISZ, but especially in meta-Belt metasedimentary strata. These mesoscopic folds typically have geometries that range from open (60-120° interlimb angles) to isoclinal (0-10° interlimb angle). The hinge lines of the folds are oriented parallel to the strike of the metamorphic foliation (and/or gneissic banding) in the metasedimentary strata and their plunges vary from steep to shallow. The orientation

of the axial plane with respect to the foliation ranges from upright (70-90°) to recumbent (0-10°) (e.g., Van Der Pluijm and Marshak, 2004, p. 243-247). In addition, the style of mesoscopic folding in the LISZ ranges from parallel (Class 1B, constant layer thickness maintained) to Class 3 type folding (significant thickening in fold hinge region and thinning in the limbs, see Ramsay, 1967 for fold classification). Figures 3-10 and 3-11 displays common mesoscopic fold geometries found in the Belt metasedimentary strata of the LISZ.

It is important to note here that the overall geometry of the mesoscopic folds markedly changes across the east-west striking LISZ (and the contact with the deformed quartz diorite sill). Near the center of the LISZ, directly adjacent to the deformed quartz diorite sill, mesoscopic folds are tight to isoclinal and almost exclusively recumbent. This fold geometry is especially common in the Greyson pelitic paragneiss adjacent to the sill where the folds so flattened and transposed it is often difficult to distinguish the folds from the planar gneissic banding. Away from the deformed quartz diorite the mesoscopic folds become progressively more open and are typically not recumbent.

Mesoscopic-scale boudins

Mesoscopic boudins are also common in the Belt-equivalent metasedimentary strata within the LISZ. In the Greyson Formation and Ravalli Group-equivalent metasedimentary strata these boudins are found in quartzite layers. In the calc-silicate paragneisses correlated with the metamorphosed Helena Formation and Missoula Group the boudins are found within the lighter-colored more quartz-rich layers. Boudins within the Belt-equivalent metasedimentary strata are blocky to tablet or lozenge-shaped and range in length and width from ~5 cm to 1-1.5 m and ~5-25 cm, respectively. In addition, when asymmetrical the longer axes of the boudins are usually oriented parallel

sub-parallel to the metamorphic foliation (and/or gneissic banding) in the metasedimentary strata.

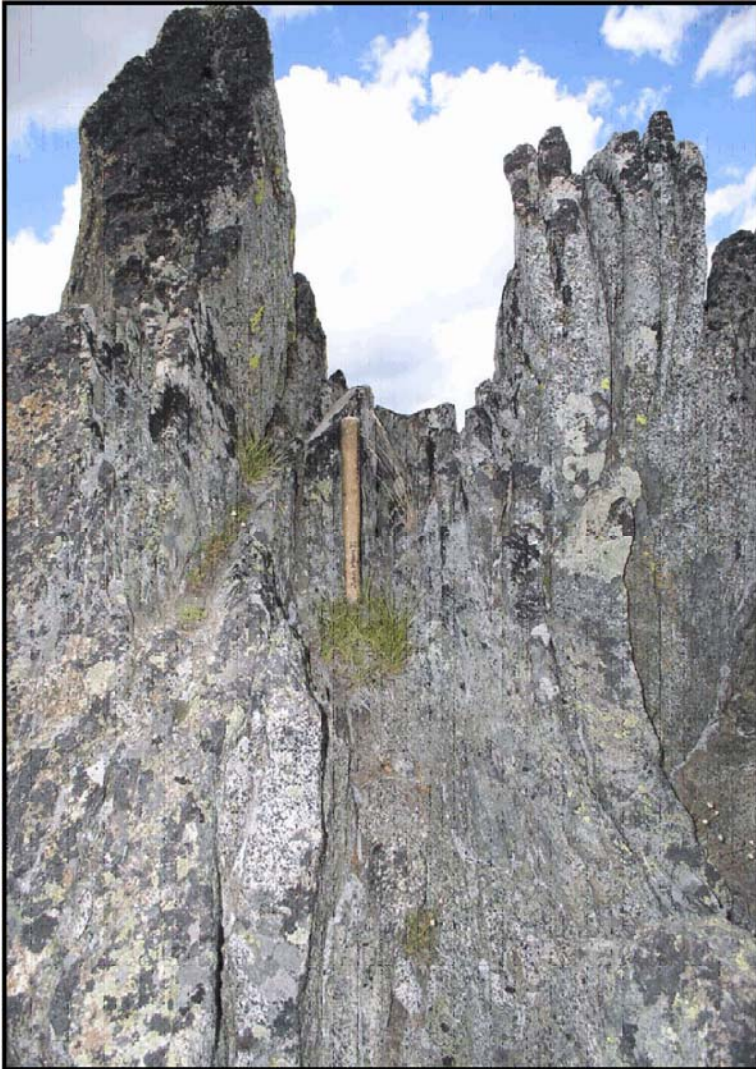


Figure 3-9. Outcrop photograph of the deformed quartz diorite sill in the center of the LISZ. The sill exhibits a strong solid-state foliation (sub-vertical in photograph) concordant to metamorphic foliation in the adjacent metasedimentary country rocks. This relationship indicates the sill was emplaced into the LISZ prior to or during some phase of solid-state deformation. The photo is directed to the west. Rock hammer handle for scale.

As in the case of the mesoscopic folds, the overall geometries of the mesoscopic boudins change in a direction perpendicular to the overall strike of the LISZ. In the

central LISZ, adjacent to the deformed quartz diorite sill, the boudins are more flattened, lozenge-shaped, and are characterized by large aspect ratios (i.e., length to width ratio; Fig. 3-12a). However, away from the central LISZ and deformed quartz diorite sill the mesoscopic boudins are typically block-shaped and shorter, having smaller aspect ratios (Fig. 3-12b).



Figure 3-10. Outcrop photographs of mesoscopic-scale folds found in Belt equivalent metasedimentary strata deformed in the LISZ. A) Nearly isoclinal class 3 folds in meta-Greyson Formation paragneiss. B) Mesoscopic folds in the meta-Ravalli Group biotite quartzite gneiss.

Shear sense

The sense of shear for the LISZ is shown by shear-sense indicators found mostly in the meta-Greyson pelitic schist and paragneiss and the deformed quartz diorite sill in the central part of the shear zone. In the meta-Greyson, large garnet and cordierite porphyroblasts with pressure shadows “tails” form these shear-sense indicators. Flattened plagioclase and K-feldspar porphyroclasts form the shear-sense indicators in the deformed quartz diorite sill. In most observations, the porphyroblasts of the meta-Greyson and porphyroclasts of the deformed quartz diorite sill formed approximately symmetric sigma-type shear-sense indicators with pressure shadow tails aligned with the median line of the porphyroblast (the median bisects the porphyroblast) indicative of pure (or flattening) shear (Fig. 3-13a, Passchier et al., 1990). However, in a few observations outcrops located directly east and west of the Lake of the Isle show garnet porphyroblasts that form asymmetric sigma-type shear indicators (with offset pressure shadow tails) showing evidence for left-lateral simple shear (Fig. 3-13b).

Description and Distribution of Metamorphic Phase Assemblages and Textures

All Belt and Middle Cambrian-equivalent metasedimentary strata in the LISZ bear middle to upper-amphibolite facies phase assemblages. The phase assemblages were briefly summarized above in the descriptions of the metamorphic fabrics. Note that a description of these phase assemblages can be found in Appendix B. Here, descriptions and distributions of key or “index” metamorphic phase assemblages and important textural features are summarized to facilitate a later discussion concerning the PT history of the LISZ during the Late Cretaceous.

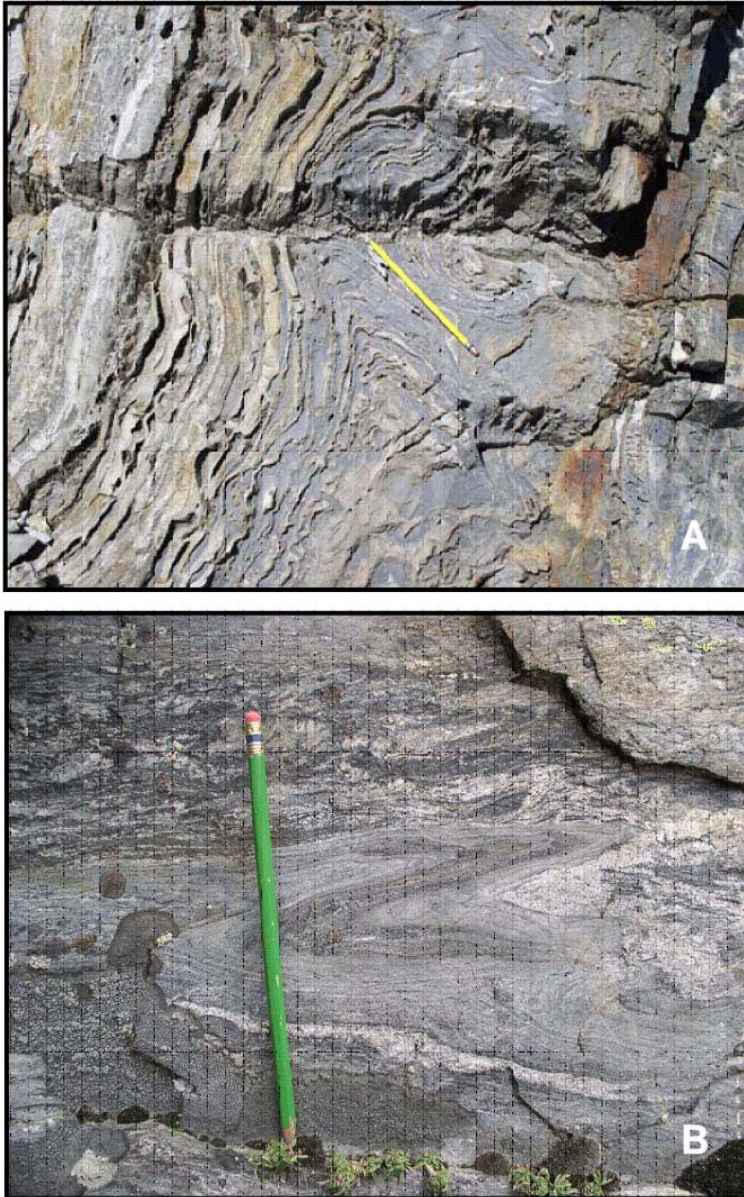


Figure 3-11. Outcrop photographs of mesoscopic-scale folds found in Belt-equivalent metasedimentary strata deformed in the LISZ. A) Mesoscopic folds in meta-Helena Formation calc-silicate gneiss on the eastern Flank of Mount Tiny. Pencil is for scale. B) Mesoscopic Z-fold found in the meta-Ravalli Group biotite quartzite gneiss. Pencil is for scale.

Metamorphic phase assemblages and textures in the meta-Greyson Formation

Pelitic strata correlated with the Greyson Formation exhibit significant changes in metamorphic phases and textures along a transect perpendicular to the strike of the LISZ

and to the contact with the deformed quartz diorite sill. These changes are summarized in the Table 3-1 which includes brief descriptions of the metamorphic phase assemblages and important textures for six samples collected from the metamorphosed Greyson.

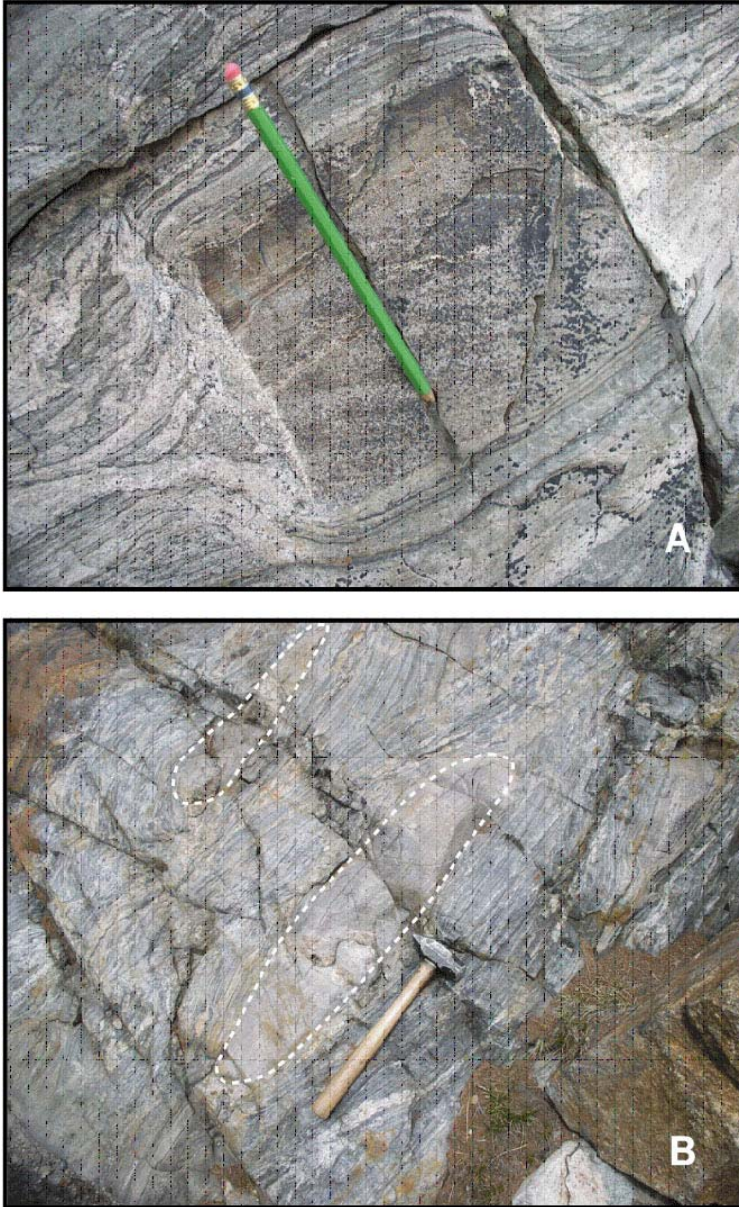


Figure 3-12. Outcrop photographs of mesoscopic boudins in the LISZ. A) In the outer parts of the shear zone, away from the contact with deformed quartz diorite sill, mesoscopic boudins are commonly blocky. B) In the center of the LISZ, near the contact with the deformed quartz diorite sill boudins are more flat and ellipsoidal.

Samples listed in Table 3-1 are arranged in order of decreasing distance from the contact with the deformed quartz diorite sill in the central LISZ. Sample localities are shown in Figure 3-16.

In the southernmost part of the study area, away from the contact with quartz diorite sill and the central LISZ, the pelitic Greyson-equivalent schist bears abundant coarse-grained biotite, relatively small euhedral garnets (~1-5 mm in diameter), K-feldspar, fine-grained sillimanite fibrolite, and primary muscovite (e.g., WG04-108, Table 3-1). This phase assemblage and general textural features are maintained within the pelitic Greyson schist north towards the central LISZ until ~1 km from contact with the deformed quartz diorite sill. Here, the pelitic schist grades to the pelitic paragneiss as described above. At this distance from the sill, the pelitic paragneiss contains much less abundant biotite, relatively large (~5-10 mm in diameter) inclusion-rich subhedral garnets, K-feldspar, relatively coarser-grained sillimanite fibrolite, and no primary muscovite (e.g., WG04-026, Table 3-1).

Further north, at a distance of ~0.5 km from the contact with the deformed quartz diorite sill, some significant changes occur in the phase assemblage and texture of the pelitic paragneiss. Here, the pelitic paragneiss contains much less biotite, relatively large inclusion-rich subhedral to anhedral garnets, K-feldspar, very abundant relatively coarse-grained sillimanite fibrolite, large sigmoidal-shaped cordierite porphyroblasts, and no primary muscovite (e.g., ME-231, Table 3-1). In addition, at this distance from the deformed quartz diorite sill, and closer, the pelitic paragneiss is migmatitic and contains granitic leucosome comprised of (in increasing relative abundant) K-feldspar, quartz, and albite. This leucosome is commonly found in boudin necks within boudinaged quartzite

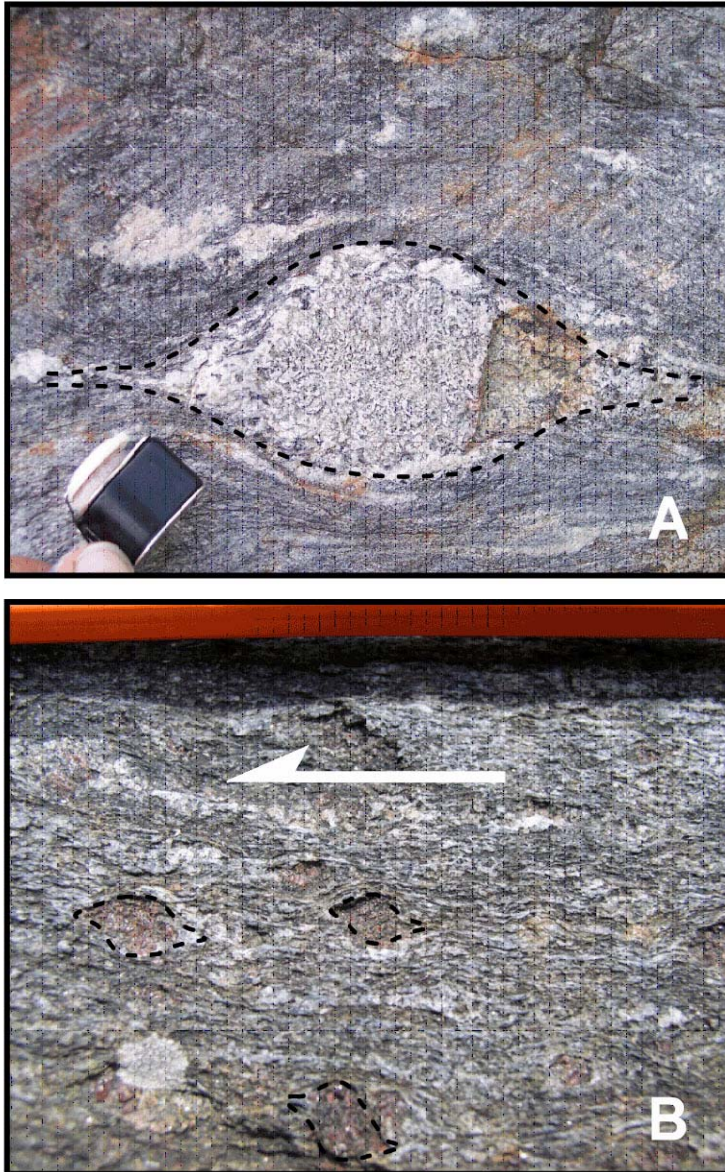


Figure 3-13. Outcrop photographs of shear sense indicators in the meta-Greyson Formation deformed in the LISZ. A) Symmetric porphyroblast shear sense indicator showing pure (flattening) shear. Hand lens for scale, photograph courtesy of Heather Bleick. B) Asymmetric sigma-type garnet porphyroblast shear sense indicator showing left lateral simple shear sense. Pencil is for scale. Note symmetric shear sense indicators such as shown in A were observed much more frequently than left lateral sense of shear indicator as shown in B.

horizons and as thin elongate pods within the metamorphic foliation and/or gneissic banding of the pelitic paragneiss (Fig. 3-14). In thin section, the leucosome is found within the pressure shadows of garnet and cordierite porphyroblasts and as thin elongate

pods or lenses within the sillimanite fibrolite-biotite foliation (Fig. 3-15a). In addition, the leucosome is found in thin section as thin “fingers” or veinlets cross-cutting garnet porphyroblasts extending into the sillimanite fibrolite-biotite foliation (see the detailed description of ME-231 included in Appendix C).

Based on the information summarized above and several other field observations three major mineral/textural zones have been mapped within the pelitic schist and paragneiss correlated with the metamorphosed Greyson Formation. These three zones are shown on a simplified geologic sketch map in Figure 3-16. Zone 1 corresponds to pelitic schist that contains abundant coarse-grained biotite, fine-grained sillimanite fibrolite, relatively small euhedral garnets, and primary muscovite. Zone 2 corresponds to pelitic paragneiss containing, less abundant biotite, fine-grained sillimanite fibrolite, larger inclusion-rich subhedral to anhedral garnets, and no primary muscovite. Zone 3 represents pelitic paragneiss that contain little biotite, relatively abundant coarse-grained sillimanite fibrolite, large inclusion-rich subhedral to anhedral garnets, large cordierite porphyroblasts, and no primary muscovite. K-feldspar is found in all three mineral-textural zones within the meta-Greyson.

Relict and fresh kyanite in the upper Meta-Ravalli Group

The uppermost ~100-200 m section of Ravalli Group-equivalent metasedimentary strata mapped is more pelitic than the rest of the section. These more pelitic strata are well exposed near a small unnamed lake at the head of the Twin Lakes Creek drainage in the western LISZ, southwest of Storm Lake, just north of the continental divide (Appendix D). Here, the more pelitic upper Ravalli metasedimentary strata contain abundant white to light cream-colored pseudomorphs. In outcrop, these pseudomorphs form elongate blade-shape cross-sections when cut parallel to their longer axes. These

elongated pseudomorph cross-section range in length and width from ~1-4 cm and ~2-5 mm, respectively. When cut perpendicular to their longer axes, the pseudomorphs form diamond-shaped cross-sections typically ranging from ~3-10 mm in the longer dimension (Fig. 3-17a).

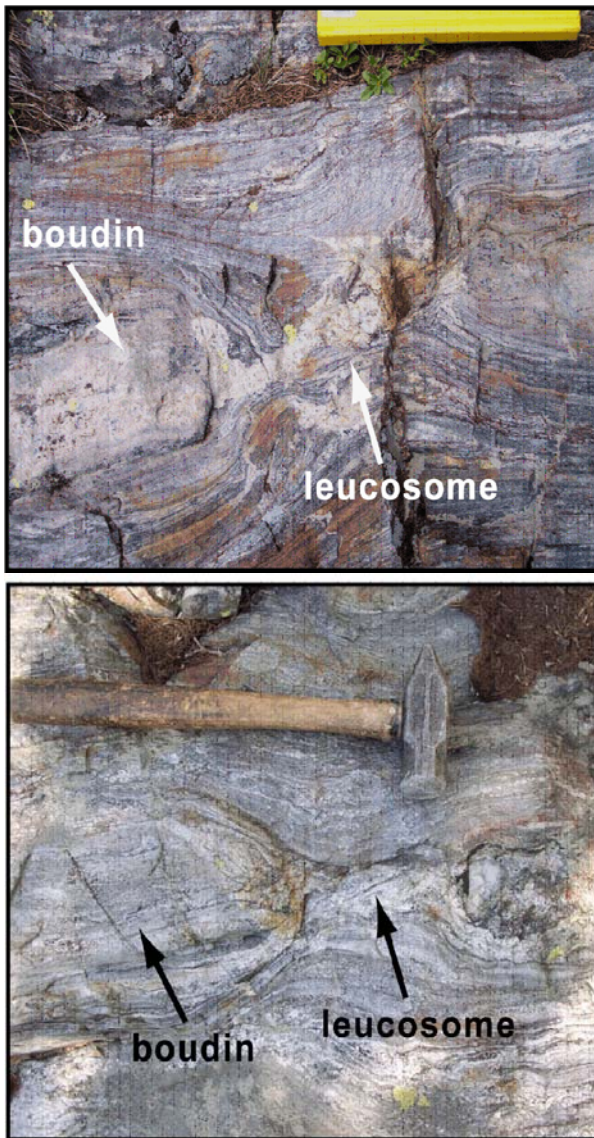


Figure 3-14. Outcrop photographs of meta-Greyson migmatitic paragneiss showing granitic leucosome commonly found in pressure shadows between quartzite boudins. Upper: Field notebook for scale; upper photograph is courtesy of Heather Bleick. Lower: Rock hammer is for scale.

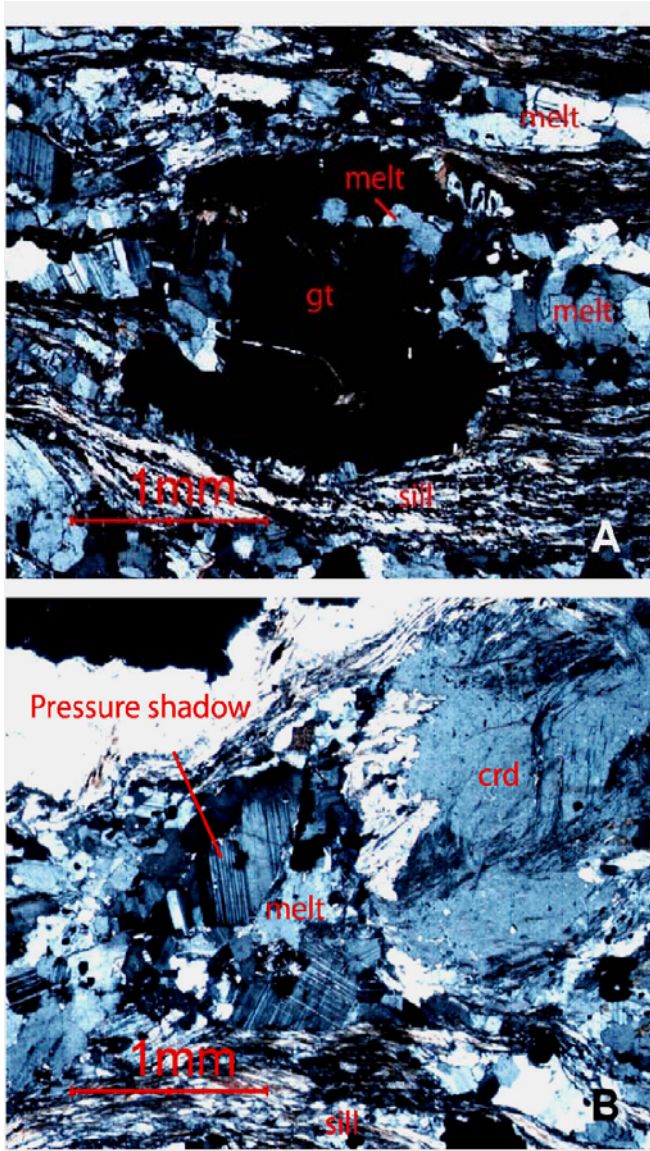


Figure 3-15. Photomicrographs of thin sections of the meta-Greyson migmatitic paragneiss exhibiting granitic leucosome (sample ME-231). A) The leucosome cross-cuts garnet porphyroblast. B) The leucosome is also found in the pressure shadows of large cordierite porphyroblasts. Note the similar placement of the leucosome in pressure shadows at both the outcrop and thin section scale. gt = garnet, crd = cordierite, sill = sillimanite. Photomicrographs were taken in cross polar light.

In thin section, the pseudomorphs are almost entirely composed of fine-grained sericite white mica (Fig. 3-17b). Relatively coarse-grained muscovite laths commonly form corona structures around the pseudomorphs. Small relicts of the original mineral

remain within the pseudomorphs as moderately to highly altered, but high relief fragments that are typically ≤ 0.5 mm in diameter or longest dimension (Fig. 3-17b). Based on the blade-shape form (when cut parallel to their longer axes), the high relief of the internal relict mineral material, and muscovite corona structures the pseudomorphs exposed at this locality likely replace kyanite. In addition, small (≤ 1 mm) blade-shaped mineral grains are found scattered throughout the matrix between large kyanite pseudomorphs (Fig. 3-18). The small blade-shaped grains found in the matrix between the large pseudomorphs are also kyanite, but apparently less altered (Nesse, 1991).

Spatial Relationship Between the Lake of the Isle Shear Zone and Late Cretaceous Intrusions

The spatial relationship between major Late Cretaceous intrusions and the LISZ is described in some detail in Appendix B. Here, a brief summary is given for the important spatial relationships. The LISZ was intruded by four major Late Cretaceous intrusions (see map in Appendix F). In the west, the LISZ was intruded by the quartz diorite and granodiorite plutons of the SLS. Both of these intrusions are undeformed and cross-cut the high grade and deformed meta-Belt and meta-Cambrian metasedimentary strata of the LISZ indicating a post-kinematic relationship to the shear zone. In the east, a quartz diorite pluton (similar to the quartz diorite of the SLS) cross-cuts the Mill Creek nappe indicating a post-kinematic relationship to the LISZ as well. Between these two areas, a quartz diorite sill was emplaced into the deformed metasedimentary strata of the central LISZ. The quartz diorite sill is highly deformed and exhibits a well-developed foliation in many places that is concordant to the foliation in the adjacent metasedimentary country rocks indicating a pre or syn-kinematic relationship to the shear zone (see Appendix B and F).

Table 3-1. Description and distribution of key mineral phases and textures in the metamorphosed Greyson Formation.

Sample	Distance from deformed qd sill (km)	Key phases	Mineral/textural zone (Fig. 3-16)	Textures
WG04-108	4.0	bt, grt, kfs, ms, sill	1	bt is very abundant and fresh; grt is euhedral, no embayments; no cordierite; fine-grained sill fibrolite
WG04-095	1.2	bt, grt, kfs, ms, sill	1	possible kyanite relicts; fine-grained sill fibrolite; grt is v. euhedral; v. abundant ms
WG04-101b	1.2	bt, grt, kfs, ms, sill	1	ms present; little sill, but fine-grained variety; bt is v. abundant
WG04-099	1.2	bt, grt, kfs, ms, sill	1	little sill, fine-grained fibrolite; possible kyanite pseudomorphs; very abundant ms; rock is coarse grained; bt is most abundant; smaller garnets <3 mm in diameter
WG04-026	0.8	bt, grt, kfs, sill	2	grt is subhedral and inclusion rich; coarser sill fibrolite; lacks ms
ME-231	0.4	bt, grt, kfs, sill, crd, leuco	3	bt less abundant and is altered; coarser sill fibrolite is very abundant; larger grt and large crd; crd have abundant fine-grained sill fibrolite inclusions; lacks ms; abundant leuco

Note: qd = quartz diorite, bt = biotite, grt = garnet, ms = muscovite, kfs = K-feldspar, sill = sillimanite, crd = cordierite, and leuco = granitic leucosome.

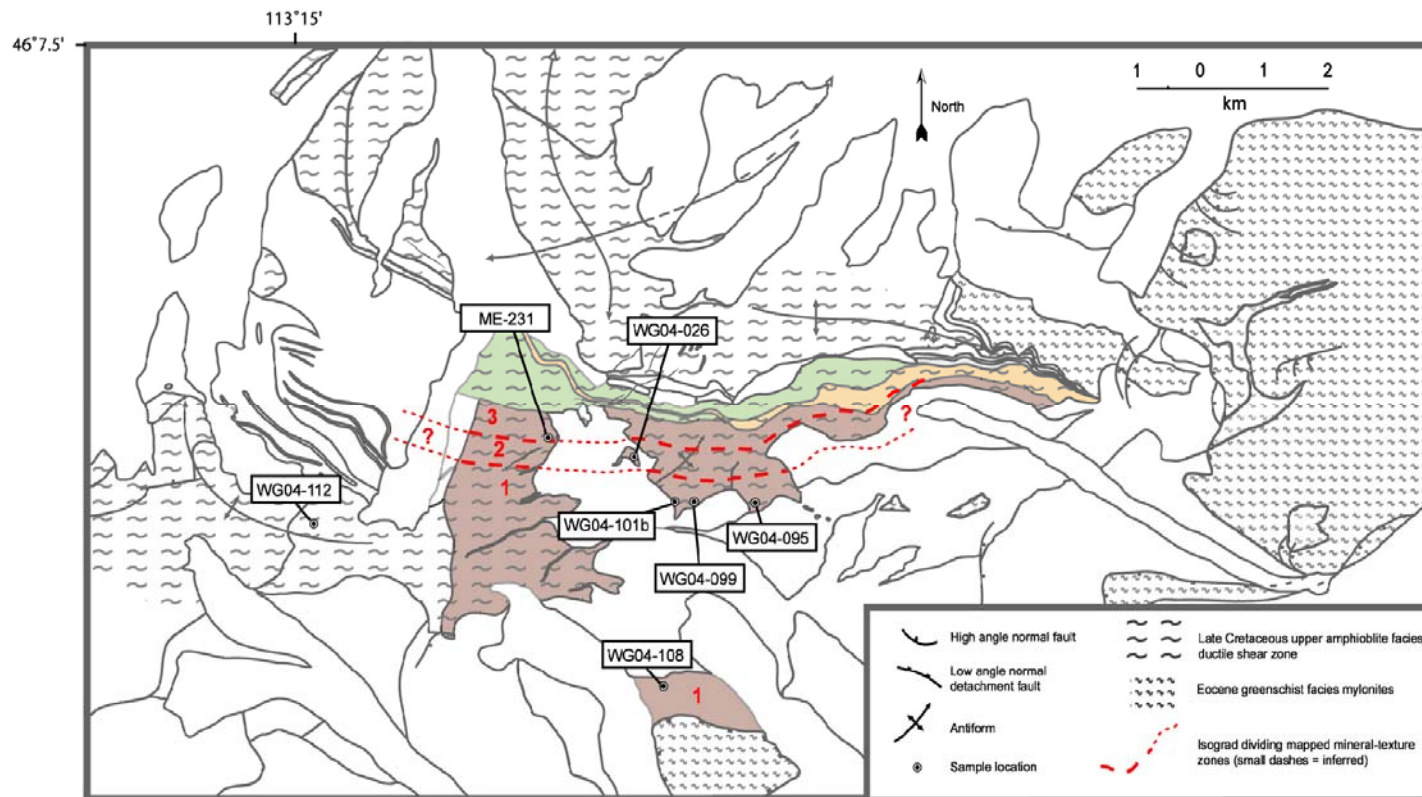


Figure 3-16. Simplified geologic sketch map of the ACC lower plate exposed in the current study area showing the metamorphic mineral/textural zones 1, 2, and 3 mapped in the meta-Greyson Formation adjacent to the deformed quartz diorite sill. The meta-Greyson Formation is brown, the sill is green, and uncorrelated Lower Belt pelitic rocks are light tan. Note the localities of samples discussed in the text and described in Table 3-1 (see text for details).

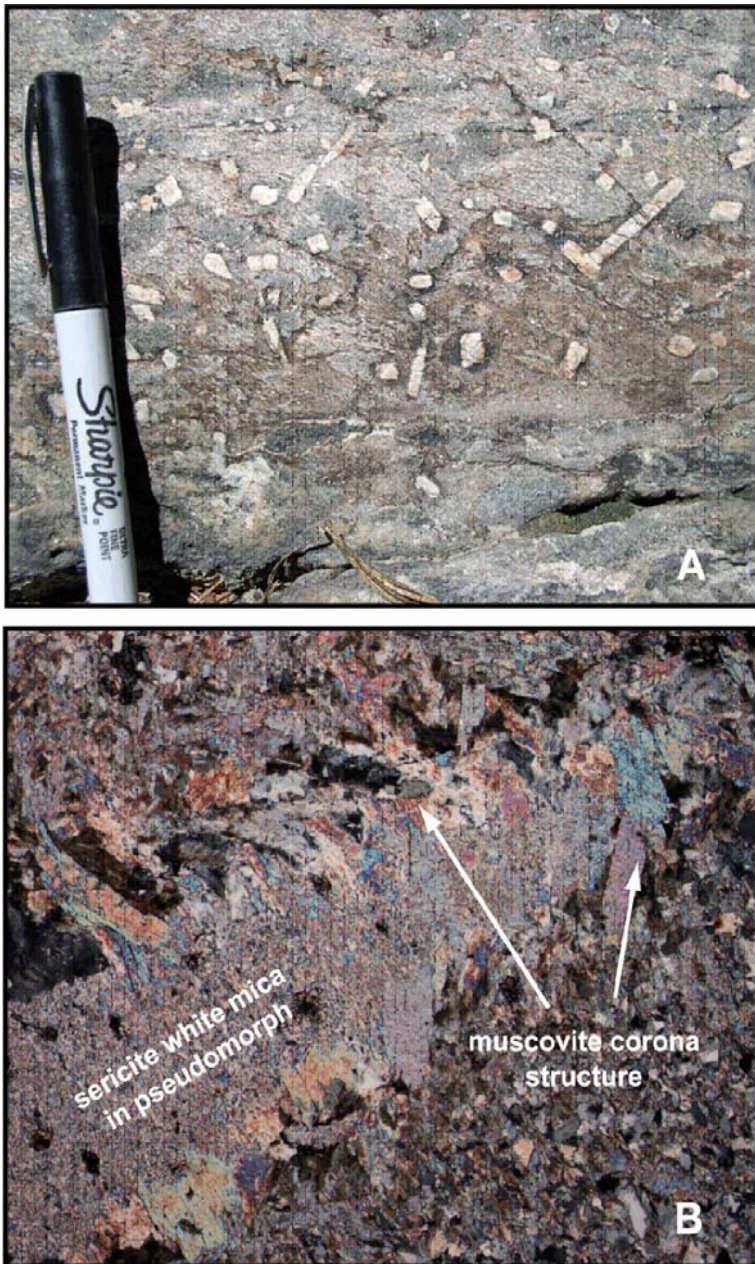


Figure 3-17. Kyanite pseudomorphs in the upper meta-Ravalli Group. A) Outcrop photograph of kyanite pseudomorphs. This outcrop is located in the western LISZ (see Fig. 3-16 and sample locality for sample WG04-113). Pen for is scale. B) Photomicrograph from a thin section of meta-Ravalli Group sample WG04-113 showing large kyanite pseudomorph made of fine-grained sericite white mica surrounded by relatively coarse-grained muscovite corona structure. Photomicrograph was taken in cross polar light. Field of view is ~3 mm.



Figure 3-18. Photomicrograph showing fresh kyanite in the upper meta-Ravalli Group. Thin section of WG04-112 shows fine-grained fresh kyanite scattered through the matrix of between large kyanite pseudomorphs. Field of view is ~3 mm.

CHAPTER 4 U-PB ZIRCON GEOCHRONOLOGY

Purpose and Strategy

U-Pb zircon geochronology was employed in this study to provide age constraints on upper-amphibolite facies metamorphism, anatexis, and ductile deformation in the Lake of the Isle shear zone (see Chapter 3). Three samples were chosen from the geochronology. WG04-114 was collected from the undeformed granodiorite of the Storm Lake Stock (SLS) in the western LISZ (Appendix F). Here, the undeformed granodiorite obliquely crosscuts the deformed metasedimentary strata of the western LISZ, indicating that emplacement of the intrusion postdated upper-amphibolite facies metamorphism and ductile deformation in the LISZ. A U-Pb zircon crystallization age from WG04-114 would provide a minimum age limit for upper-amphibolite metamorphism and ductile deformation in the LISZ. Ug-1 was collected from a quartz diorite sill in the central LISZ where the sill is emplaced within a sequence of upper-amphibolite grade meta-Belt and meta-Cambrian metasedimentary strata. The quartz diorite sill is deformed and exhibits a well-developed solid-state foliation concordant with the foliation in the adjacent metasedimentary country rocks. Such a relationship indicates (1) emplacement of the sill predated upper-amphibolite metamorphism and ductile deformation in the LISZ or (2) the sill was emplaced synkinematic to these events. A U-Pb zircon crystallization age from the deformed quartz diorite sill sample Ug-1 would provide an upper age limit or direct age constraint for upper-amphibolite facies metamorphism and ductile deformation in the LISZ. Finally, sample WG05-02

was also collected from granitic leucosome found in the migmatitic pelitic paragneiss (metamorphosed Greyson Fm., Lower Belt) in the central LISZ. Here there is evidence for anatexis during the upper-amphibolite facies metamorphism and ductile deformation (see Chapter 3). A reliable U-Pb zircon crystallization age from the leucosome sample WG05-02 would provide a direct age constraint on upper-amphibolite facies metamorphism, anatexis, and ductile deformation of metasedimentary strata in the LISZ.

Relevant Previous U-Pb Zircon Geochronology

Prior to this study, there were no U-Pb geochronological data available to provide age constraints for the upper-amphibolite facies metamorphism and ductile deformation in the LISZ. However, Desmarais (1983) reported U-Pb geochronological data from two deformed granodiorite intrusions in the southern Anaconda-Pintlar Range which exhibit solid-state foliations concordant with foliations in metasedimentary country rocks. U-Pb zircon $^{207}\text{Pb} / ^{235}\text{U}$ and $^{206}\text{Pb} / ^{238}\text{U}$ ages from these deformed intrusions were discordant with upper and lower concordia intersects at $\sim 1780\text{-}1890$ and $\sim 78\text{-}77$ Ma, respectively. Desmarais attributed the discordance nature of the zircons to inheritance from Proterozoic cores and he interpreted the lower intersect ages to be minimum ages for emplacement for the intrusions.

U-Pb Zircon Geochronology Results

Zircons were extracted from samples WG04-114, Ug-1 and, WG05-02 using standard rock crushing, density, and magnetic separation techniques. Select zircons were subsequently analyzed along with FC-1 standard zircons (in house $^{207}\text{Pb} / ^{206}\text{Pb}$ age = 1086.9 ± 5.3 , $^{207}\text{Pb} / ^{235}\text{U}$ age = 1091.5 ± 13.4 , and $^{206}\text{Pb} / ^{238}\text{U}$ age = 1096.7 ± 21.7 Ma) at the University of Florida using laser ablation multi-collector inductively coupled

plasma mass spectrometry (LA-MC-ICP-MS). Sample preparation, LA-MC-ICP-MS analytical techniques, and data reduction are summarized in Appendix A.

A common lead correction was applied to the drift and fractionation corrected U-Pb zircon data obtained from zircons of samples WG04-114, Ug-1, and WG05-02 to evaluate the need for the correction (Appendix A). In the case of WG04-114 and Ug-1, individual U-Pb ages calculated from uncorrected and corrected isotopic data were within analytical error indicating negligible concentrations of common lead in these zircons; a common lead correction was deemed unnecessary for these analyses. For WG05-02, a common lead correction is necessary due to the antiquity of the zircons and because all of these zircon gave discordant $^{207}\text{Pb} / ^{235}\text{U}$ and $^{206}\text{Pb} / ^{238}\text{U}$ ages.

WG04-114 (Storm Lake Stock Granodiorite)

Twenty-eight spot analyses were taken from twenty-two euhedral and inclusion free zircons from sample WG04-114 (average size = 200-300 μm), including five paired core and rim analyses from a few larger zircons. Individual U-Pb ages for the WG04-114 zircons are summarized in Table 4-1. $^{207}\text{Pb} / ^{206}\text{Pb}$, $^{207}\text{Pb} / ^{235}\text{U}$, and $^{206}\text{Pb} / ^{238}\text{U}$ ages are reported for the older zircons. $^{206}\text{Pb} / ^{238}\text{U}$ ages are given for younger zircons. Core analyses are indicated by the subscript “c” in Table 4-1. All ages in Table 4-1 are reported with 2σ errors. Three zircon analyses from WG04-114 yielded anomalously old ages (SLS-7c-c, SLS-8a, and SLS-17b-c). These zircons gave discordant $^{207}\text{Pb} / ^{235}\text{U}$ and $^{206}\text{Pb} / ^{238}\text{U}$ ages ranging from ~1189-239 Ma and ~599-88 Ma, respectively. However, the $^{207}\text{Pb} / ^{206}\text{Pb}$ ages are more consistent and range from ~2502-2243 Ma indicating a Paleoproterozoic or Archean component to these zircons. The remaining twenty-five analyses from WG04-114 gave fairly consistent Late Cretaceous $^{206}\text{Pb} / ^{238}\text{U}$ ages ranging from ~80-71 Ma and are interpreted to represent a single magmatic zircon population

related to emplacement of the SLS granodiorite (Table 4-1). Select zircons were (n= 22) are shown plotted on a Tera-Wasserburg diagram and $^{206}\text{Pb} / ^{238}\text{U}$ weighted mean zircon age plot in Figure 4-1. Sixteen of these WG04-114 zircons have similar $^{206}\text{Pb} / ^{238}\text{U}$ ages and correspond to a $^{206}\text{Pb} / ^{238}\text{U}$ weighted mean age of 74.6 ± 0.8 Ma (MSWD = 0.34, 2σ). This age is interpreted to be the age of emplacement for the SLS granodiorite.

Ug-1 (The Deformed Quartz Diorite Sill)

A total of twenty-four spot analyses were taken from twenty-four individual euhedral and inclusion free Ug-1 zircons (average size = 200-300 μm); core and rim zircon analyses were not distinguished during the analyses. Individual U-Pb ages for the Ug-1 zircons are summarized in Table 4-2. As the case of WG04-114, $^{207}\text{Pb} / ^{206}\text{Pb}$, $^{207}\text{Pb} / ^{235}\text{U}$, and $^{206}\text{Pb} / ^{238}\text{U}$ ages are reported for older zircons and only $^{206}\text{Pb} / ^{238}\text{U}$ ages are given for younger zircons. All ages in Table 4-2 are reported with 2σ errors. Two Ug-1 zircons yield anomalously old ages (Ug-01_9 and Ug-01_11). These two zircon analyses gave discordant $^{207}\text{Pb} / ^{235}\text{U}$ and $^{206}\text{Pb} / ^{238}\text{U}$ that range from ~ 510 - 471 Ma and ~ 299 - 109 Ma, respectively. The remaining twenty-two Ug-1 zircon analyses yield Late Cretaceous $^{206}\text{Pb} / ^{238}\text{U}$ ages of ~ 77 - 71 Ma. These zircons are interpreted to be of a single magmatic population which crystallized during the emplacement of the quartz diorite sill. The twenty-two Late Cretaceous aged Ug-1 analyses are shown plotted on a Tera-Wasserburg diagram and $^{206}\text{Pb} / ^{238}\text{U}$ weighted mean zircon age plot in figure 4-2. Sixteen of these zircons correspond to a $^{206}\text{Pb} / ^{238}\text{U}$ weighted mean age of 75.0 ± 0.8 Ma (MSWD = 0.54, 2σ). This age is interpreted to represent the age of emplacement for the quartz diorite sill.

Table 4-1. U-Pb LA-MC-ICP-MS analytical results for WG04-114

Grain spot	Radiogenic ratios						e.c.
	$\frac{^{207}\text{Pb}}{^{206}\text{Pb}}$	\pm	$\frac{^{207}\text{Pb}}{^{235}\text{U}}$	\pm	$\frac{^{206}\text{Pb}}{^{238}\text{U}}$	\pm	
SLS-1	0.0573	0.0025	0.0987	0.0066	0.0121	0.0005	0.08
SLS-2	0.0572	0.0009	0.1026	0.0051	0.0121	0.0005	0.11
SLS-3	0.0566	0.0006	0.0891	0.0045	0.0119	0.0005	0.12
SLS-4	0.0546	0.0008	0.0992	0.0062	0.0119	0.0005	0.09
SLS-5a	0.0572	0.0014	0.0930	0.0047	0.0116	0.0005	0.11
SLS-5b-c	0.0550	0.0017	0.0979	0.0054	0.0118	0.0005	0.10
SLS-6	0.0739	0.0032	0.1225	0.0071	0.0118	0.0005	0.07
SLS-7a	0.0614	0.0022	0.0975	0.0068	0.0118	0.0005	0.08
SLS-7b-c	0.0604	0.0021	0.1051	0.0072	0.0114	0.0005	0.07
SLS-7c-c	0.1648	0.0011	2.2235	0.0975	0.0975	0.0045	0.05
SLS-8a	0.1415	0.0064	0.2654	0.0206	0.0137	0.0006	0.03
SLS-8b-c	0.0877	0.0064	0.1434	0.0141	0.0117	0.0005	0.04
SLS-9-c	0.0554	0.0009	0.0809	0.0051	0.0115	0.0005	0.10
SLS-10	0.0517	0.0012	0.0904	0.0047	0.0119	0.0005	0.11

Table 4-1. Continued.

Grain spot	Ages (Ma)					
	$\frac{^{207}\text{Pb}}{^{206}\text{Pb}}$	\pm	$\frac{^{207}\text{Pb}}{^{235}\text{U}}$	\pm	$\frac{^{206}\text{Pb}}{^{238}\text{U}}$	\pm
SLS-1					77.4	3.4
SLS-2					77.8	3.5
SLS-3					76.5	3.3
SLS-4					76.3	3.4
SLS-5a					74.5	3.3
SLS-5b-c					75.4	3.3
SLS-6					75.8	3.3
SLS-7a					75.4	3.3
SLS-7b-c					73.1	3.2
SLS-7c-c	2502	11	1,188.5	30.2	599.9	26.4
SLS-8a	2243	76	239.0	16.4	88.0	3.9
SLS-8b-c					74.9	3.3
SLS-9-c					73.9	3.3
SLS-10					76.5	3.3

Table 4-1. Continued.

Grain spot	Radiogenic ratios						
	$\frac{^{207}\text{Pb}}{^{206}\text{Pb}}$	\pm	$\frac{^{207}\text{Pb}}{^{235}\text{U}}$	\pm	$\frac{^{206}\text{Pb}}{^{238}\text{U}}$	\pm	e.c.
SLS-11	0.0562	0.0013	0.0944	0.0057	0.0114	0.0005	0.09
SLS-12	0.0514	0.0010	0.1056	0.0068	0.0117	0.0005	0.08
SLS-13	0.0515	0.0009	0.0955	0.0052	0.0114	0.0005	0.10
<i>SLS-14a</i>	<i>0.0517</i>	<i>0.0010</i>	<i>0.0914</i>	<i>0.0058</i>	<i>0.0111</i>	<i>0.0005</i>	<i>0.08</i>
<i>SLS-14b</i>	<i>0.0519</i>	<i>0.0009</i>	<i>0.0973</i>	<i>0.0058</i>	<i>0.0124</i>	<i>0.0005</i>	<i>0.10</i>
SLS-15	0.0535	0.0011	0.0820	0.0048	0.0115	0.0005	0.11
SLS-16	0.0798	0.0029	0.1478	0.0117	0.0116	0.0005	0.04
SLS-17a	0.0849	0.0063	0.1548	0.0164	0.0117	0.0005	0.03
<i>SLS-17b-c</i>	<i>0.1502</i>	<i>0.0031</i>	<i>0.2996</i>	<i>0.0195</i>	<i>0.0140</i>	<i>0.0006</i>	<i>0.03</i>
SLS-18	0.0593	0.0032	0.0970	0.0096	0.0117	0.0005	0.05
SLS-19	0.0598	0.0020	0.0970	0.0056	0.0117	0.0005	0.09
<i>SLS-20</i>	<i>0.0515</i>	<i>0.0014</i>	<i>0.0880</i>	<i>0.0061</i>	<i>0.0117</i>	<i>0.0005</i>	<i>0.09</i>
<i>SLS-21</i>	<i>0.0540</i>	<i>0.0019</i>	<i>0.0931</i>	<i>0.0072</i>	<i>0.0120</i>	<i>0.0005</i>	<i>0.07</i>
<i>SLS-22</i>	<i>0.1104</i>	<i>0.0034</i>	<i>0.2049</i>	<i>0.0215</i>	<i>0.0123</i>	<i>0.0006</i>	<i>0.03</i>

Table 4-1. Continued.

Grain spot	Ages (Ma)					
	$\frac{^{207}\text{Pb}}{^{206}\text{Pb}}$	\pm	$\frac{^{207}\text{Pb}}{^{235}\text{U}}$	\pm	$\frac{^{206}\text{Pb}}{^{238}\text{U}}$	\pm
SLS-11					73.3	3.3
SLS-12					75.0	3.4
SLS-13					73.2	3.3
<i>SLS-14a</i>					71.2	3.1
<i>SLS-14b</i>					79.5	3.5
SLS-15					73.8	3.3
SLS-16					74.5	3.3
SLS-17a					74.9	3.4
<i>SLS-17b-c</i>	2346	37	266.1	15.1	89.4	3.9
SLS-18					75.1	3.3
SLS-19					75.0	3.3
<i>SLS-20</i>					75.0	3.4
<i>SLS-21</i>					76.7	3.4
<i>SLS-22</i>					78.8	3.6

Note: e.c. = error correlation between $^{207}\text{Pb}/^{235}\text{U}$ and $^{206}\text{Pb}/^{238}\text{U}$ errors. Analyses in italics were excluded from the weighted $^{206}\text{Pb}/^{238}\text{U}$ mean age calculation.

Table 4-2. U-Pb LA-MC-ICP-MS analytical results for Ug-1

Grain spot	Radiogenic ratios						e.c.
	$\frac{^{207}\text{Pb}}{^{206}\text{Pb}}$	±	$\frac{^{207}\text{Pb}}{^{235}\text{U}}$	±	$\frac{^{206}\text{Pb}}{^{238}\text{U}}$	±	
Ug-01_1	0.0429	0.0008	0.0683	0.0029	0.0116	0.0005	0.17
Ug-01_2	0.0331	0.0014	0.0527	0.0030	0.0114	0.0005	0.17
<i>Ug-01_3</i>	<i>0.0445</i>	<i>0.0008</i>	<i>0.0679</i>	<i>0.0030</i>	<i>0.0110</i>	<i>0.0005</i>	<i>0.16</i>
<i>Ug-01_4</i>	<i>0.0506</i>	<i>0.0013</i>	<i>0.0771</i>	<i>0.0036</i>	<i>0.0112</i>	<i>0.0005</i>	<i>0.14</i>
<i>Ug-01_5</i>	<i>0.0564</i>	<i>0.0040</i>	<i>0.0889</i>	<i>0.0076</i>	<i>0.0113</i>	<i>0.0005</i>	<i>0.06</i>
<i>Ug-01_6</i>	<i>0.0529</i>	<i>0.0022</i>	<i>0.0824</i>	<i>0.0047</i>	<i>0.0114</i>	<i>0.0005</i>	<i>0.11</i>
Ug-01_7	0.0482	0.0017	0.0786	0.0041	0.0118	0.0005	0.13
Ug-01_8	0.0590	0.0025	0.0952	0.0054	0.0118	0.0005	0.09
<i>Ug-01_9</i>	<i>0.0912</i>	<i>0.0006</i>	<i>0.5902</i>	<i>0.0250</i>	<i>0.0475</i>	<i>0.0021</i>	<i>0.08</i>
Ug-01_10	0.0616	0.0018	0.0998	0.0053	0.0114	0.0005	0.09
<i>Ug-01_11</i>	<i>0.2825</i>	<i>0.0021</i>	<i>0.6538</i>	<i>0.0284</i>	<i>0.0170</i>	<i>0.0007</i>	<i>0.03</i>
Ug-01_12	0.0490	0.0004	0.0802	0.0033	0.0116	0.0005	0.15
Ug-01_13	0.0678	0.0019	0.1132	0.0061	0.0119	0.0005	0.08
Ug-01_13	0.0789	0.0039	0.1335	0.0087	0.0120	0.0005	0.06
Ug-01_15	0.0565	0.0020	0.0952	0.0054	0.0118	0.0005	0.09
Ug-01_16	0.0560	0.0004	0.0914	0.0039	0.0116	0.0005	0.13
Ug-01_17	0.0947	0.0034	0.1602	0.0089	0.0116	0.0005	0.06
Ug-01_18	0.0754	0.0041	0.1336	0.0103	0.0116	0.0005	0.05
Ug-01_19	0.1107	0.0020	0.1912	0.0087	0.0120	0.0005	0.06
Ug-01_20	0.0607	0.0014	0.1003	0.0051	0.0117	0.0005	0.10
Ug-01_21	0.0951	0.0031	0.1610	0.0086	0.0119	0.0005	0.06
<i>Ug-01_22</i>	<i>0.0561</i>	<i>0.0014</i>	<i>0.0865</i>	<i>0.0041</i>	<i>0.0111</i>	<i>0.0005</i>	<i>0.12</i>
<i>Ug-01_23</i>	<i>0.0679</i>	<i>0.0022</i>	<i>0.1055</i>	<i>0.0056</i>	<i>0.0113</i>	<i>0.0005</i>	<i>0.09</i>
Ug-01_24	0.0798	0.0038	0.1329	0.0090	0.0117	0.0005	0.06

Table 4-2. Continued.

Grain spot	Ages (Ma)					
	$\frac{^{207}\text{Pb}}{^{206}\text{Pb}}$	\pm	$\frac{^{207}\text{Pb}}{^{235}\text{U}}$	\pm	$\frac{^{206}\text{Pb}}{^{238}\text{U}}$	\pm
Ug-01_1					74.1	3.2
Ug-01_2					73.0	3.1
<i>Ug-01_3</i>					70.7	3.0
<i>Ug-01_4</i>					72.1	3.1
<i>Ug-01_5</i>					72.4	3.1
<i>Ug-01_6</i>					72.9	3.1
Ug-01_7					75.8	3.3
Ug-01_8					75.5	3.2
<i>Ug-01_9</i>	1449	13	471.0	15.8	299.1	12.7
Ug-01_10					73.1	3.1
<i>Ug-01_11</i>	3375	12	510.8	17.3	108.7	4.7
Ug-01_12					74.6	3.2
Ug-01_13					76.3	3.3
Ug-01_13					77.0	3.3
Ug-01_15					75.6	3.3
Ug-01_16					74.3	3.2
Ug-01_17					74.4	3.2
Ug-01_18					74.1	3.2
Ug-01_19					76.7	3.3
Ug-01_20					74.8	3.2
Ug-01_21					76.1	3.3
<i>Ug-01_22</i>					71.2	3.1
<i>Ug-01_23</i>					72.2	3.1
Ug-01_24					75.2	3.3

Note: e.c. = error correlation between $^{207}\text{Pb}/^{235}\text{U}$ and $^{206}\text{Pb}/^{238}\text{U}$ errors. Analyses in italics were excluded from the weighted $^{206}\text{Pb}/^{238}\text{U}$ mean age calculation.

Table 4-3. U-Pb LA-MC-ICP-MS analytical results for WG05-02

Grain spot	Radiogenic ratios						
	$\frac{^{207}\text{Pb}}{^{206}\text{Pb}}$	\pm	$\frac{^{207}\text{Pb}}{^{235}\text{U}}$	\pm	$\frac{^{206}\text{Pb}}{^{238}\text{U}}$	\pm	e.c.
L1	0.1027	0.0006	1.2005	0.0601	0.1010	0.0045	0.08
L2	0.1703	0.0012	1.0616	0.0678	0.0588	0.0029	0.04
L3	<i>0.1761</i>	<i>0.0010</i>	<i>6.9862</i>	<i>0.2908</i>	<i>0.3003</i>	<i>0.0131</i>	<i>0.05</i>
L4	0.1308	0.0008	1.8921	0.1317	0.1465	0.0068	0.05
L5	<i>0.1446</i>	<i>0.0009</i>	<i>5.4060</i>	<i>0.2574</i>	<i>0.2714</i>	<i>0.0123</i>	<i>0.05</i>
L6	0.1057	0.0006	3.1837	0.1949	0.2197	0.0126	0.06
L7	0.1367	0.0008	1.4190	0.0740	0.0779	0.0035	0.05
L8	0.0988	0.0007	0.3773	0.0384	0.0498	0.0023	0.06
L9	<i>0.1466</i>	<i>0.0086</i>	-	<i>0.0346</i>	<i>0.0034</i>	<i>0.0007</i>	<i>0.02</i>
L10	<i>0.1708</i>	<i>0.0010</i>	<i>10.4532</i>	<i>0.4889</i>	<i>0.3830</i>	<i>0.0175</i>	<i>0.04</i>
L11	0.1003	0.0006	1.7837	0.0848	0.1118	0.0050	0.06
L12	0.2232	0.0019	4.4270	0.2277	0.1176	0.0056	0.02
L13	0.1074	0.0006	3.3357	0.1581	0.1994	0.0088	0.06
L14	0.1042	0.0008	1.9734	0.1056	0.1215	0.0061	0.06
L15	0.1086	0.0008	1.3191	0.0765	0.0935	0.0042	0.05
L16	<i>0.1870</i>	<i>0.0010</i>	<i>9.9195</i>	<i>0.4345</i>	<i>0.3066</i>	<i>0.0139</i>	<i>0.03</i>
L17	0.1032	0.0006	4.0275	0.1739	0.2247	0.0098	0.06
L18	0.0983	0.0006	1.1089	0.0615	0.0772	0.0036	0.06
L19	0.1597	0.0009	3.4682	0.1518	0.1644	0.0073	0.05
L20	0.1038	0.0006	2.2842	0.1000	0.1636	0.0073	0.07
L21	<i>0.1634</i>	<i>0.0009</i>	<i>6.3418</i>	<i>0.2750</i>	<i>0.2849</i>	<i>0.0129</i>	<i>0.05</i>
L22	0.1016	0.0006	0.8736	0.0482	0.0758	0.0035	0.07
L23	0.0950	0.0006	0.4689	0.0291	0.0451	0.0022	0.08
L24	<i>0.7816</i>	<i>0.0043</i>	-	<i>14.0487</i>	<i>0.0508</i>	<i>0.0242</i>	<i>0.00</i>
L25	0.1014	0.0006	0.9928	0.0487	0.0780	0.0036	0.07

Table 4-3. Continued.

Grain spot	Ages (Ma)					
	$\frac{^{207}\text{Pb}}{^{206}\text{U}}$	\pm	$\frac{^{207}\text{Pb}}{^{235}\text{U}}^{\S}$	\pm	$\frac{^{206}\text{Pb}}{^{238}\text{U}}^{\S}$	\pm
L1	1671	11	800.8	27.4	620.6	26.5
L2	2559	13	734.6	32.9	368.3	17.7
<i>L3</i>	<i>2616</i>	<i>9</i>	<i>2109.7</i>	<i>36.3</i>	<i>1693.0</i>	<i>64.8</i>
L4	2105	11	1078.3	45.2	881.1	38.2
<i>L5</i>	<i>2280</i>	<i>11</i>	<i>1885.8</i>	<i>40.0</i>	<i>1547.7</i>	<i>62.0</i>
L6	1723	11	1453.2	46.2	1280.3	66.1
L7	2184	11	896.9	30.6	483.9	20.9
L8	1601	13	325.1	27.9	313.4	14.4
<i>L9</i>	-	-	-	-	-	-
<i>L10</i>	<i>2564</i>	<i>10</i>	<i>2475.8</i>	<i>42.4</i>	<i>2090.5</i>	<i>80.9</i>
L11	1628	10	1039.5	30.5	683.3	29.1
L12	3004	13	1717.4	41.7	716.9	32.3
L13	1754	11	1489.5	36.4	1172.3	47.3
L14	1698	13	1106.5	35.4	739.0	35.2
L15	1776	13	854.1	33.0	576.4	24.5
<i>L16</i>	<i>2712</i>	<i>9</i>	<i>2427.3</i>	<i>39.6</i>	<i>1723.8</i>	<i>68.3</i>
L17	1680	10	1639.8	34.5	1306.8	51.3
L18	1592	12	757.6	29.2	479.5	21.5
L19	2450	9	1520.0	33.9	981.3	40.5
L20	1689	10	1207.4	30.5	976.7	40.4
<i>L21</i>	<i>2488</i>	<i>9</i>	<i>2024.3</i>	<i>37.3</i>	<i>1616.2</i>	<i>64.5</i>
L22	1651	11	637.5	25.8	471.2	20.8
L23	1525	20	390.4	19.9	284.6	13.8
<i>L24</i>	-	-	-	-	-	-
L25	1647	11	700.1	24.5	484.0	21.3

Note: e.c. = error correlation between $^{207}\text{Pb}/^{235}\text{U}$ and $^{206}\text{Pb}/^{238}\text{U}$ errors. Analyses in italics were excluded from the age calculation shown in Figure 4-3b.

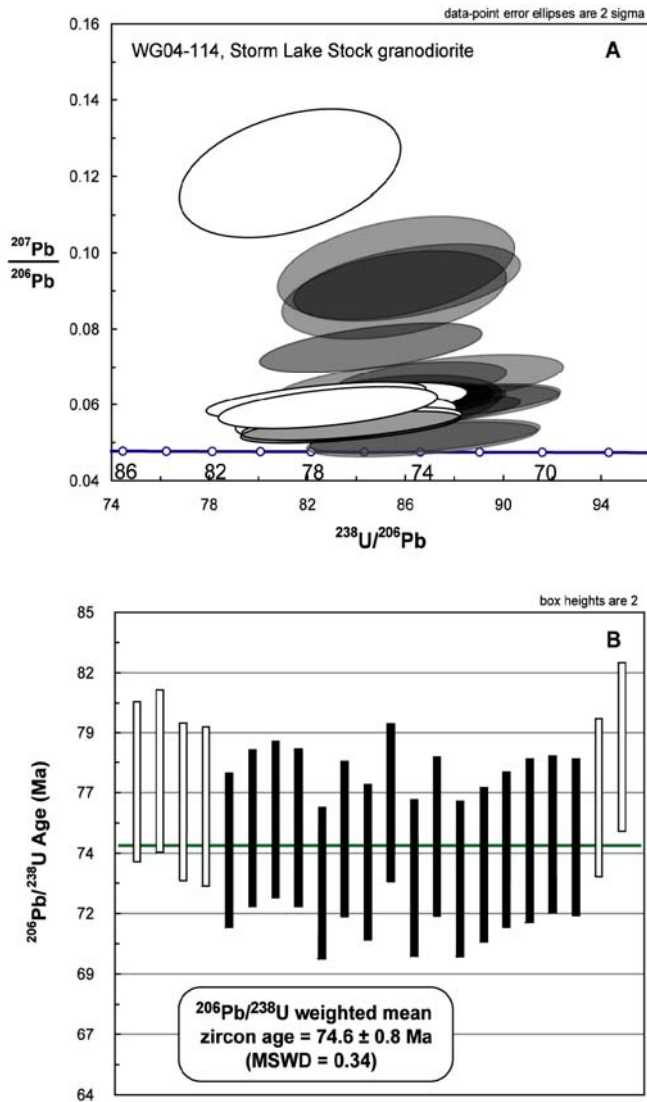


Figure 4-1. Tera-Wasserburg plot and $^{206}\text{Pb} / ^{238}\text{U}$ weighted mean zircon age plot for Storm Lake Stock granodiorite sample WG04-114. Only the zircon analyses represented by the darkened ellipses in A and the darkened boxes in B were used in the weighted mean $^{206}\text{Pb} / ^{238}\text{U}$ zircon age calculation. U-Pb isotopic data were not corrected for common lead (see text).

WG05-02 (Leucosome from the Meta-Greyson Paragneiss)

A total of twenty-five spot analyses were taken from twenty-five individual subhedral and inclusion free zircons of sample WG05-02; because of their small size (average size $<100 \mu\text{m}$), exclusive rim analyses were not made from these zircons.

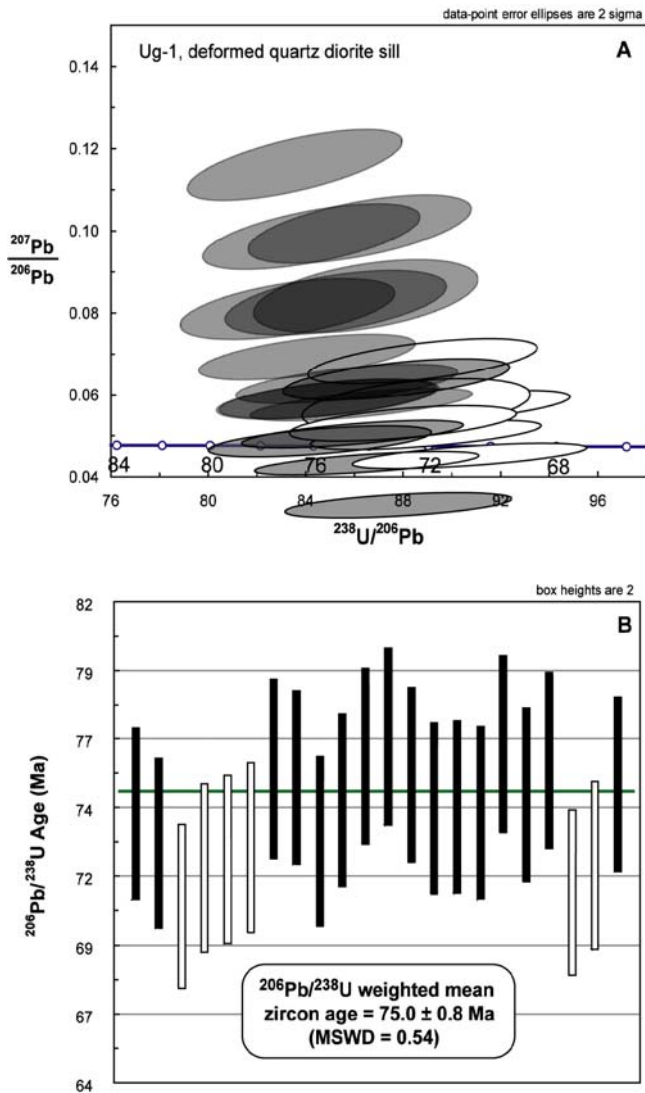


Figure 4-2. Tera-Wasserburg plot and $^{206}\text{Pb}/^{238}\text{U}$ weighted mean zircon age plot for the deformed quartz diorite sill sample Ug-1. Only the zircon analyses represented by the darkened ellipses in A and the darkened boxes in B were used in the weighted mean $^{206}\text{Pb}/^{238}\text{U}$ zircon age calculation. U-Pb isotopic data were not corrected for common lead (see text).

$^{207}\text{Pb}/^{206}\text{Pb}$, $^{207}\text{Pb}/^{235}\text{U}$, and $^{206}\text{Pb}/^{238}\text{U}$ ages are reported for all twenty-five of the WG05-02 zircon analyses in Table 4-3. Ages reported in Table 4-3 are given with 2σ errors. The $^{207}\text{Pb}/^{206}\text{Pb}$ ages range from ~ 1325 - 2804 Ma. However, all the WG05-02 zircon analyses gave discordant $^{207}\text{Pb}/^{235}\text{U}$ and $^{206}\text{Pb}/^{238}\text{U}$ ages except for zircon L8. However, zircon L8 is only concordant because of the large errors associated with the

$^{207}\text{Pb} / ^{235}\text{U}$ and $^{206}\text{Pb} / ^{238}\text{U}$ ages. The other twenty-four WG05-02 zircons yielded discordant $^{207}\text{Pb} / ^{235}\text{U}$ and $^{206}\text{Pb} / ^{238}\text{U}$ ages ranging from ~2476-285 Ma. Figure 4-3a displays a traditional concordia diagram which includes all twenty-five of the WG05-02 zircon analyses. Twelve zircon analyses roughly defined a discordia line (see highlighted ellipses). Figure 4-3b displays this discordia line which intersects concordia at 43 ± 330 Ma and 1736 ± 330 Ma 450 (2σ errors). These intersection ages have large errors because no zircon analyses fall near the intersections themselves.

As noted, all but one of the WG05-02 leucosome zircons (zircon L8) gave discordant $^{207}\text{Pb} / ^{235}\text{U}$ and $^{206}\text{Pb} / ^{238}\text{U}$ ages. There are two possible explanations for the largely discordant nature of the leucosome zircons: (1) One explanation is inheritance of older zircon material from the leucosome zircon cores. Because the WG05-02 zircons are small it is entirely possible that both core and rim regions of the zircons were analyzed simultaneously (with beam diameter of 30-60 μm). As a result, the $^{207}\text{Pb} / ^{235}\text{U}$ and $^{206}\text{Pb} / ^{238}\text{U}$ zircon ages may represent a mixture of two zircon components (i.e., older cores and younger rims). If different proportions of the two components were analyzed from several zircons then a discordia array or mixing line could form when the isotopic data are plotted on a concordia diagram (e.g., Figure 3a). (2) Another explanation for the discordance observed in the WG05-02 leucosome zircons is lead loss from older, probably Proterozoic or Archean zircons. For example, if very old zircons underwent differential lead loss during a younger isotopic disturbance (e.g., subsequent reheating during metamorphism and/or intrusion) these zircons would fall along a discordia line on a concordia diagram. In this case, the two concordia-discordia intersects correspond to

the true age (upper intersect) of the old zircons and the age of younger isotopic disturbance (lower intersect, Faure, 1986; Williams, 1998).

Both of these explanations require the presence of Proterozoic aged or older zircons in the restite from which the WG05-02 leucosome was partially melted (i.e., the meta-Greyson Fm). Ross and Villeneuve (2003) report $^{207}\text{Pb} / ^{206}\text{Pb}$ ages from detrital zircons from unmetamorphosed Lower Belt Greyson-equivalent strata east (in the Helena Salient) and west of the current study area that range from ~1899-1670 Ma; these ages are consistent with the $^{207}\text{Pb} / ^{206}\text{Pb}$ ages for the twelve WG05-02 zircon analyses that define the discordia shown in figures 4-3a and b (~1525-1776 Ma, Fig. 4-4). Therefore, it is possible the WG05-02 leucosome incorporated Mesoproterozoic or Paleoproterozoic detrital zircons from the meta-Greyson Formation during high temperature metamorphism and anatexis in the LISZ. Catholuminescence (CL) imaging of the WG05-02 leucosome zircons is needed to determine which of the two above explanations is correct. CL imaging can be used to determine if the leucosome zircons consist of inherited cores with thin magmatic rims (consistent with explanation 1) or lack younger magmatic rims (consistent with explanation 2). The latter implies that no new magmatic rims grew on the older zircon cores during anatexis and formation of the granitic leucosome.

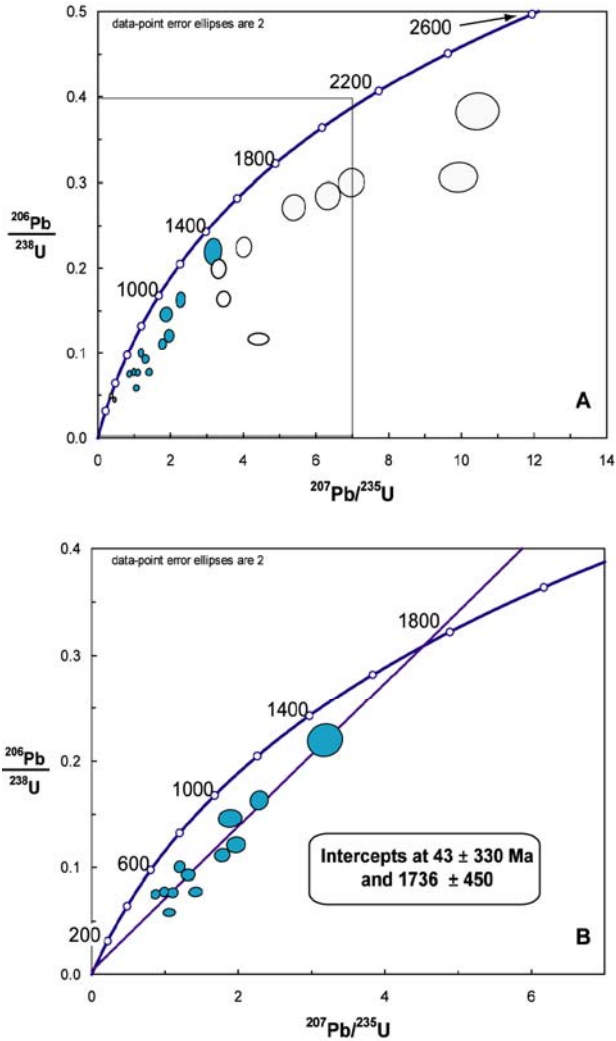


Figure 4-3. Conventional U-Pb concordia plots for zircons for leucosome sample WG05-02 collected from the meta-Greyson migmatitic paragneiss in the central LISZ. A) Most leucosome zircons gave discordance ages with a ^{204}Pb common lead correction. B) Twelve leucosome zircon analyses fall along a discordia that intersects concordia at 1736 ± 450 Ma and 43 ± 330 . The discordia is most likely the result of variable lead loss in Paleoproterozoic zircons inherited from the meta-Greyson Formation protolith. Lead loss likely occurred during anatexis and formation of the leucosome itself.

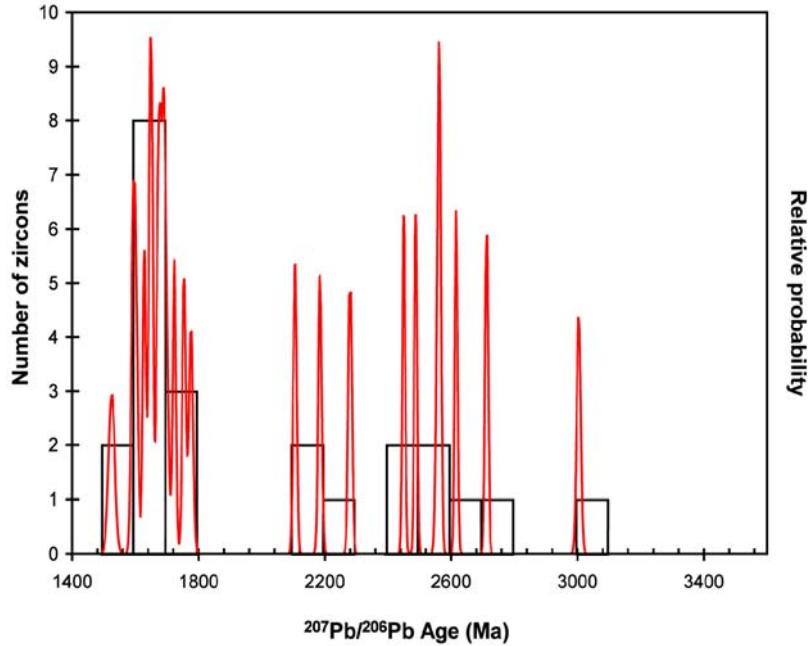


Figure 4-4. $^{207}\text{Pb}/^{206}\text{Pb}$ age density plot for the WG05-02 leucosome zircons. $^{207}\text{Pb}/^{206}\text{Pb}$ ages range from ~1525-3004 Ma. The leucosome zircons fall into two main age groups: (1) a Mesoproterozoic to Paleoproterozoic group (~1525-1776 Ma) and an (2) Archean group (~2105-3004 Ma). The zircons that form the discordia line shown in figures 3-4a and b are part of the Mesoproterozoic to Paleoproterozoic group.

CHAPTER 5 THERMOBAROMETRY

Purpose and Strategy

As described above, the Lake of the Isle shear zone (LISZ) is a sinuous, middle to upper-amphibolite facies ductile shear zone that stretches across the exhumed lower plate of the ACC within the current study area (see Appendix F and description of the LISZ above). Within the LISZ, Mesoproterozoic Belt Supergroup and middle Cambrian-equivalent metasedimentary strata have undergone major ductile attenuation (thinning) during upper amphibolite facies metamorphism. As a result, the deformed metasedimentary strata of the LISZ exhibit a strongly transposed metamorphic foliation and common mesoscopic foliation-parallel boudins and near isoclinal folds.

In the central LISZ, in the vicinity of the Lake of the Isle, migmatitic pelitic paragneiss (correlated with metamorphosed Greyson Fm, Lower Belt) bears an uppermost-amphibolite facies phase assemblage and shows evidence for anatexis during the ductile deformation. In this part of the LISZ granitic leucosome is commonly found in boudin necks and as isolated thin and elongate pods within the transposed foliation indicating upper-amphibolite facies metamorphism and anatexis accompanied ductile attenuation of Belt Supergroup and middle Cambrian-equivalent metasedimentary strata in the central LISZ.

In the eastern part of the study area the LISZ is overprinted by the Eocene Anaconda mylonite and several listric brittle normal faults related to the now largely eroded brittle detachment system (Appendix F). Here, lower to middle greenschist facies

fabrics of the Anaconda granitoid mylonites contrast sharply with the plastically deformed upper-amphibolite facies metasedimentary strata of the LISZ which lie structurally beneath the mylonites. This structural relationship indicates that the LISZ predated development of the Anaconda mylonite and brittle detachment system which later facilitated the exhumation of the ACC lower plate. U-Pb geochronological and $^{40}\text{Ar}/^{39}\text{Ar}$ thermochronological data obtained from the LISZ in this study give a Late Cretaceous age for the shear zone (ca. ~75-74 Ma, see Chapter 4 and 6). These age constraints indicate that upper-amphibolite facies metamorphism in the LISZ predated tectonic exhumation of the ACC lower plate by probably no less than ~23 Ma. The structural relationship between the Anaconda greenschist facies mylonite zone and the LISZ in the eastern study area also shows that the LISZ was exhumed from beneath the brittle detachment fault system and ACC upper plate along with the greenschist mylonites during the Eocene.

In this study, thermobarometric data were obtained from pelitic strata in the LISZ to constrain the peak pressure-temperature associated with upper-amphibolite metamorphism, local anatexis, and ductile attenuation of metasedimentary strata in the shear zone. Because of the structural relationship between the LISZ and the greenschist mylonites pressure constraints from the LISZ can be used to constrain the maximum amount of exhumation facilitated by extension in the ACC.

ME-231 (Migmatitic Meta-Greyson Formation Paragneiss)

Sample ME-231 was selected for the thermobarometry needed in this study. ME-231 was collected from cordierite-bearing migmatitic pelitic paragneiss (meta-Greyson) exposed in the central part of the LISZ, just southwest of the Lake of the Isle (Appendix F). Upper-amphibolite facies metamorphism was most intense here and the meta-

Greyson strata bear a phase assemblage of (in increasing relative abundance) cordierite + garnet + K-feldspar + albite plagioclase + biotite + quartz + sillimanite fibrolite. This metamorphic assemblage is indicative of uppermost amphibolite facies in the second sillimanite-K-feldspar zone (Spear, 1993). A detailed description of ME-231 is included in Appendix C.

Relevant Previous Pressure-temperature Constraints

Prior to this study, quantitative thermobarometric data were not available from the metasedimentary strata deformed in the LISZ or any other part of the Anaconda-Pintlar and Flint Creek Ranges. A few previous studies do document amphibolite facies regional metamorphism of metasedimentary rocks in the ACC lower plate. The observations and pressure-temperature estimates made in these studies are important to later discussion of regional metamorphism in the ACC lower plate.

Desmarais (1983) described amphibolite facies pelitic and calc-silicate schists and paragneisses in ACC lower plate exposed in the southern Anaconda-Pintlar Range, southwest of the current study area. He described pelitic strata with an upper-amphibolite facies assemblage of quartz + biotite + plagioclase + K-feldspar + sillimanite ± muscovite. Desmarais correlated these strata with the Mount Shields Formation (middle Missoula Group equivalent, upper Belt). He also observed migmatitic paragneisses in some areas suggesting that local anatexis accompanied upper-amphibolite facies metamorphism. Based on these observations, Desmarais estimated peak metamorphic conditions in the southern Anaconda-Pintlar range reached pressures of ~3.0-7.0 kbar and temperatures of ~600-700°C.

Flood (1974) mapped and described the Fishtrap Creek nappe, a large west-verging recumbent nappe fold structure exposed in the southern Anaconda-Pintlar Range. The

Fishtrap Creek nappe is comprised of metasedimentary strata he correlated with (from structurally lowest to highest) the Prichard Formation (Greyson Fm. equivalent), Ravalli Group, and the Wallace Formation (Helena Fm. equivalent). Flood described these meta-Belt units as biotite-muscovite schist, quartzite, and calc-silicate schist, respectively. Flood (1974) also documented and measured well-developed metamorphic foliation throughout the Fishtrap Creek nappe and common mesoscopic-scale folds. Based on the metamorphic assemblages of these Belt-correlated metasedimentary strata Flood estimated that peak metamorphic conditions in the southernmost Anaconda-Pintlar Range reached pressures of ~2-4 kbar and temperatures of ~550-650°C.

Stuart (1966) mapped and described metasedimentary strata adjacent to the Late Cretaceous Royal Stock granodiorite in the northeastern Flint Creek Range, north of the current study area. He described a somewhat narrow contact aureole surrounding the Royal Stock superimposed on more widespread and regional metamorphic fabrics. Within the Royal Stock contact aureole he notes randomly oriented andalusite porphyroblasts overprinting the regional metamorphic fabric. Outside the contact aureole, Stuart documented highly deformed metasedimentary strata comprised of muscovite + biotite + quartz + cordierite rather than andalusite. In thin section, he noted large sigmoidal shaped cordierite porphyroblasts with their long axes oriented parallel to the pervasive regional metamorphic foliation. These observations indicate an earlier regional metamorphic event at middle to upper-amphibolite facies followed by a lower pressure event associated with the intrusion of the Royal Stock. Notably, Stuart also documented a general increase in the regional metamorphic grade west to east across the northern Flint Creek Range, ranging from greenschist to upper-amphibolite facies.

Thermobarometry Results

Pressure-temperature estimates were obtained from polished thin sections prepared from sample ME-231 by electron microprobe analyses and subsequent thermodynamic calculations made using the computer programs AX (activity-composition) by Holland and Powell (2000) and THERMOCALC v. 3.21 by Powell et al. (1998). For comparison, a pressure-temperature estimate for ME-231 was also made using the computer program Geothermobarometry (GTB) v. 2.1 by Spear and Kohn (1999). Sample preparation, microprobe instrumentation and analytical procedures are summarized in Appendix A. Thermodynamic calculations made using AX, THERMOCALC, and GTB are discussed below.

Electron Microprobe Analyses

Major elemental compositions were obtained from individual mineral phases in sample ME-231 using a JOEL Superprobe electron microprobe at Florida International University. The results from the analyses of garnet, biotite, albite plagioclase and cordierite are summarized in Table 5-1. Each mineral analysis is reported in elemental oxide weight percent and element oxide totals from each analysis are shown in the far right column of the table. Garnet and cordierite analyses labeled with the suffixes “c” and “r”, indicate mineral core and rim analyses, respectively. Garnet and cordierite analyses without these suffixes were taken from intermediate spots on the mineral, between the rim and core region. All biotite and plagioclase analyses from sample ME-231 are rim analyses.

Garnet

A total of thirty-five spot analyzes were taken from large and small garnet porphoroblasts. Most of these analyses gave elemental oxides totals of 100 ± 1 weight

Table 5-1. Results from electron microprobe mineral analyses.

Analyses	SiO ₂	TiO ₂	Cr ₂ O ₃	Na ₂ O	K ₂ O	Al ₂ O ₃	MnO	FeO	MgO	CaO	Total
<u>Garnet</u>											
PMT-2-1-gt1c	36.94	0.23	0.17	0.32	0.10	21.29	1.06	36.93	2.54	1.02	100.60
PMT-2-1-gt2	37.36	0.15	0.17	0.37	0.10	21.46	1.29	36.18	2.97	1.03	101.06
PMT-2-1-gt3	37.02	0.12	0.14	0.33	0.10	21.33	1.28	36.30	2.99	1.09	100.70
PMT-2-1-gt4	37.00	0.23	0.25	0.31	0.11	21.50	1.04	36.62	2.99	0.94	100.97
PMT-2-1-gt5	36.72	0.21	0.15	0.28	0.11	21.29	0.58	37.85	2.24	1.14	100.57
PMT-2-3-gt1	36.68	0.05	0.06	0.01	0.01	21.05	0.33	37.72	2.47	1.22	99.61
PMT-2-3-gt2	36.42	0.07	0.07	0.00	0.01	21.29	0.44	37.50	2.56	0.90	99.26
PMT-2-3-gt3	36.51	0.00	0.06	0.02	0.00	21.19	0.40	36.59	2.50	1.12	98.40
PMT-2-3-gt4	36.41	0.00	0.05	0.00	0.01	21.36	0.36	36.86	2.55	0.95	98.54
PMT-2-6-gt1	36.37	0.00	0.04	0.00	0.00	21.08	0.29	38.31	2.13	0.82	99.03
PMT-2-6-gt2	36.12	0.00	0.02	0.00	0.00	21.13	0.49	34.29	2.25	1.19	95.50
PMT-2-6-gt3	36.79	0.00	0.00	0.00	0.01	21.07	0.49	37.68	2.18	1.00	99.21
PMT-3-1-gt1	36.81	0.13	0.15	0.30	0.13	21.57	0.51	38.35	2.91	1.10	101.94
PMT-3-1-gt2	36.73	0.13	0.16	0.31	0.12	21.39	1.13	36.78	3.11	0.95	100.81
PMT-3-1-gt3	36.60	0.18	0.14	0.29	0.13	21.24	1.40	36.75	2.89	1.02	100.64
PMT-3-1-gt4	36.17	0.13	0.16	0.29	0.12	21.14	0.95	36.64	2.94	1.04	99.57
PMT-3-1-gt5	36.58	0.17	0.12	0.29	0.11	21.38	0.49	37.96	2.93	1.26	101.28
PMT-3-1-gt6	36.70	0.21	0.33	0.30	0.11	21.13	0.76	37.25	2.93	1.45	101.16
PMT-3-1-gt7	36.18	0.12	0.34	0.27	0.12	21.17	0.81	36.84	2.54	1.30	99.70
PMT-3-1-gt8	36.37	0.08	0.16	0.29	0.13	20.93	0.63	37.50	2.97	1.25	100.30
PMT-3-1-gt9	36.54	0.19	0.26	0.31	0.12	21.58	0.99	36.94	2.96	1.29	101.17
PMT-3-1-gt10	36.38	0.21	0.21	0.30	0.12	21.13	0.99	37.09	3.01	1.23	100.67

Table 5-1. Continued.

Analyses	SiO ₂	TiO ₂	Cr ₂ O ₃	Na ₂ O	K ₂ O	Al ₂ O ₃	MnO	FeO	MgO	CaO	Total
PMT-3-2-gt1-1	37.87	0.00	0.02	0.00	0.00	21.41	0.37	36.61	2.62	0.97	99.86
PMT-3-2-gt1-2	37.51	0.01	0.01	0.00	0.02	21.34	0.31	37.33	2.54	1.12	100.18
PMT-3-2-gt1-3	37.52	0.02	0.05	0.02	0.00	21.21	0.32	38.36	2.11	1.00	100.60
PMT-3-2-gt2-1	37.82	0.00	0.00	0.03	0.00	20.93	0.38	37.03	2.50	0.93	99.62
PMT-3-2-gt2-2	37.79	0.06	0.00	0.00	0.01	20.88	0.33	36.71	2.37	1.23	99.38
PMT-3-2-gt2-3	37.84	0.00	0.02	0.02	0.00	21.07	0.36	36.83	2.31	1.00	99.45
PMT-3-3-gt1	37.23	0.19	0.18	0.27	0.10	21.19	0.49	37.64	2.90	1.19	101.38
PMT-3-3-gt2	36.47	0.09	0.15	0.31	0.11	21.40	0.50	36.99	2.90	0.97	99.89
PMT-3-3-gt3	36.60	0.18	0.13	0.32	0.10	21.46	0.54	37.41	2.87	1.16	100.76
PMT-3-3-gt4	36.38	0.16	0.19	0.30	0.11	21.52	0.54	37.44	2.90	1.15	100.68
PMT-3-3-gt5	36.84	0.12	0.18	0.29	0.10	21.33	0.46	38.06	2.97	1.05	101.39
PMT-3-3-gt6	36.91	0.12	0.14	0.31	0.11	21.16	0.53	37.57	2.89	0.96	100.69
PMT-3-3-gt7	36.95	0.15	0.21	0.32	0.10	21.32	0.54	37.30	2.90	1.24	101.01
<u>Biotite</u>											
PMT-2-3-bt1	33.48	2.08	0.12	0.16	8.66	20.61	0.00	24.94	4.52	0.00	94.56
PMT-2-3-bt2	32.09	3.48	0.11	0.21	8.54	18.94	0.03	23.47	3.77	0.11	90.75
PMT-2-3-bt3	32.92	3.34	0.14	0.22	8.51	19.86	0.08	24.63	4.41	0.01	94.11
PMT-2-6-bt1	33.71	4.25	0.18	0.27	8.71	19.25	0.00	22.79	5.16	0.00	94.31
PMT-2-6-bt2	33.21	3.74	0.25	0.13	8.52	19.32	0.01	23.39	5.56	0.00	94.12
PMT-2-6-bt3	33.01	3.79	0.10	0.21	8.74	19.50	0.00	22.48	5.19	0.00	93.02
PMT-2-6-bt4	33.01	3.36	0.11	0.23	8.46	18.96	0.00	22.46	4.99	0.01	91.59
PMT-2-6-bt5	32.61	2.55	0.17	0.23	8.07	19.42	0.07	23.02	5.23	0.01	91.38

Table 5-1. Continued.

Analyses	SiO ₂	TiO ₂	Cr ₂ O ₃	Na ₂ O	K ₂ O	Al ₂ O ₃	MnO	FeO	MgO	CaO	Total
PMT-2-6-bt6	32.58	3.92	0.06	0.25	8.47	18.96	0.05	21.25	5.06	0.01	90.61
PMT-2-6-bt7	32.74	4.46	0.10	0.23	7.93	19.29	0.00	22.46	4.82	0.00	92.04
PMT-3-1-bt1	33.50	3.40	0.23	0.43	8.38	19.37	0.12	23.84	5.11	0.15	94.53
PMT-3-1-bt2	32.89	3.80	0.30	0.48	8.43	19.07	0.14	24.43	5.26	0.15	94.95
PMT-3-1-bt3	32.93	3.55	0.20	0.42	8.13	19.28	0.13	23.43	4.98	0.17	93.22
PMT-3-1-bt4	33.87	2.82	0.25	0.43	8.23	19.52	0.16	24.11	5.39	0.16	94.95
PMT-3-1-bt5	33.64	2.62	0.26	0.42	8.05	20.06	0.19	24.15	5.23	0.15	94.77
PMT-3-1-bt6	34.13	3.27	0.24	0.41	8.30	20.03	0.13	23.64	4.81	0.14	95.09
PMT-3-1-bt7	33.37	3.31	0.22	0.47	8.23	19.85	0.21	23.90	5.07	0.16	94.79
PMT-3-1-bt8	33.63	3.58	0.28	0.48	8.10	19.26	0.20	23.23	5.54	0.17	94.45
PMT-3-1-bt9	34.08	3.42	0.28	0.42	8.19	19.50	0.16	23.62	5.85	0.14	95.66
PMT-3-1-bt10	33.30	3.67	0.28	0.40	7.99	19.06	0.14	24.17	5.96	0.15	95.10
PMT-3-2-bt1	33.92	2.02	0.06	0.21	8.70	20.85	0.07	24.19	4.58	0.01	94.60
PMT-3-2-bt2	34.05	2.85	0.15	0.20	8.60	20.05	0.00	24.03	4.55	0.00	94.47
PMT-3-2-bt3	33.78	2.58	0.05	0.18	8.54	19.83	0.07	24.48	4.84	0.01	94.35
PMT-3-2-bt4	33.67	2.84	0.20	0.16	8.93	19.46	0.00	23.56	4.97	0.00	93.81
PMT-3-2-bt5	34.08	2.52	0.13	0.16	8.61	19.72	0.00	23.62	5.07	0.00	93.91
PMT-3-2-bt6	33.58	3.14	0.10	0.19	8.81	19.98	0.02	22.82	5.06	0.01	93.71
PMT-3-3-bt1	33.54	3.22	0.29	0.44	7.97	19.49	0.15	24.40	5.50	0.14	95.14
PMT-3-3-bt2	33.55	3.50	0.25	0.41	8.26	19.32	0.12	23.59	5.29	0.13	94.42
PMT-3-3-bt3	33.42	3.55	0.34	0.50	7.96	19.00	0.11	24.26	5.30	0.16	94.60
PMT-3-3-bt4	34.43	3.03	0.24	0.52	8.18	19.97	0.13	24.65	5.27	0.15	96.58
PMT-3-3-bt5	31.31	2.54	0.19	0.37	6.60	19.80	0.13	25.02	5.59	0.17	91.73

Table 5-1. Continued.

Analyses	SiO ₂	TiO ₂	Cr ₂ O ₃	Na ₂ O	K ₂ O	Al ₂ O ₃	MnO	FeO	MgO	CaO	Total
<u>Plagioclase</u>											
PMT-3-3-bt6	33.74	3.06	0.24	0.39	7.79	20.38	0.11	24.59	5.05	0.15	95.50
PMT-3-3-bt7	34.46	3.47	0.31	0.38	8.06	19.72	0.11	23.09	5.72	0.14	95.46
PMT-3-3-bt8	34.11	2.93	0.36	0.47	7.87	20.17	0.15	24.12	5.95	0.15	96.28
PMT-2-6-pl1	59.96	0.00	0.01	6.28	0.06	24.67	0.00	0.05	0.00	6.07	97.10
PMT-2-6-pl2	60.94	0.02	0.00	5.19	0.08	24.61	0.00	0.03	0.00	5.91	96.77
PMT-2-6-pl3	57.90	0.06	0.00	7.34	0.06	24.80	0.02	0.01	0.00	7.04	97.22
PMT-2-6-pl4	60.05	0.00	0.00	7.04	0.08	24.41	0.00	0.00	0.00	3.85	95.44
PMT-2-6-pl5	59.46	0.03	0.00	6.81	0.06	24.74	0.03	0.00	0.00	6.25	97.38
PMT-3-1-pl1	58.74	0.14	0.18	7.18	0.13	24.76	0.10	0.28	0.26	7.50	99.26
PMT-3-1-pl2	58.57	0.08	0.07	7.18	0.17	24.65	0.11	0.42	0.27	7.58	99.10
PMT-3-1-pl3	59.38	0.19	0.21	7.39	0.14	24.17	0.09	0.32	0.26	7.05	99.18
PMT-3-1-pl4	58.16	0.10	0.18	7.00	0.20	24.70	0.07	0.49	0.28	7.86	99.04
PMT-3-1-pl5	59.02	0.05	0.13	7.12	0.13	24.54	0.10	0.34	0.28	7.38	99.07
PMT-3-1-pl6	59.83	0.11	0.11	7.43	0.15	24.23	0.13	0.31	0.29	7.02	99.61
PMT-3-1-pl7	59.36	0.09	0.09	7.17	0.15	24.79	0.08	0.25	0.27	7.28	99.51
PMT-3-1-pl8	60.35	0.11	0.14	7.63	0.13	23.99	0.09	0.31	0.28	6.53	99.55
PMT-3-2-pl1	61.02	0.00	0.05	7.38	0.06	23.97	0.01	0.23	0.00	6.41	99.12
PMT-3-2-pl2	60.55	0.00	0.00	7.52	0.05	24.11	0.00	0.13	0.00	6.47	98.84
PMT-3-2-pl3	60.94	0.00	0.08	7.70	0.06	23.95	0.00	0.22	0.00	6.40	99.35
PMT-3-2-pl4	61.86	0.00	0.01	5.39	0.05	24.34	0.02	0.18	0.00	6.49	98.35
PMT-3-3-pl1	59.52	0.00	0.10	6.37	0.04	25.47	0.05	0.11	0.00	8.10	99.75
PMT-3-3-pl2	58.89	0.00	0.00	6.12	0.03	25.18	0.03	0.09	0.00	8.30	98.64

Table 5-1. Continued.

Analyses	SiO ₂	TiO ₂	Cr ₂ O ₃	Na ₂ O	K ₂ O	Al ₂ O ₃	MnO	FeO	MgO	CaO	Total
PMT-3-3-pl2	60.77	0.03	0.05	7.66	0.05	24.15	0.00	0.31	0.00	6.52	99.52
PMT-3-3-pl4	58.82	0.00	0.01	6.80	0.03	25.13	0.04	0.29	0.02	8.12	99.26
PMT-3-3-pl5	60.29	0.00	0.00	7.35	0.04	24.21	0.01	0.27	0.00	7.10	99.26
PMT-3-3-pl6	59.55	0.00	0.05	6.87	0.02	24.78	0.00	0.11	0.00	7.78	99.15
PMT-3-3-pl6	59.42	0.00	0.00	6.75	0.03	24.97	0.03	0.12	0.00	7.86	99.18
PMT-3-3-pl7	60.23	0.00	0.00	7.25	0.05	23.69	0.02	0.05	0.00	6.88	98.17
PMT-3-3-pl8	58.87	0.00	0.00	6.86	0.05	24.35	0.01	0.29	0.07	7.07	97.58
PMT-3-3-pl9	58.69	0.04	0.00	5.76	0.05	24.15	0.03	0.44	0.00	6.81	95.97
<u>Cordierite</u>											
PMT-2-3-crd1	47.78	0.04	0.00	0.17	0.00	31.02	0.07	12.16	5.23	0.03	96.50
PMT-2-3-crd2	48.54	0.04	0.00	0.14	0.01	31.35	0.07	11.13	6.29	0.03	97.60
PMT-2-3-crd3	45.90	0.00	0.00	0.16	0.01	32.55	0.00	11.45	6.30	0.02	96.39
PMT-2-8-crd1	47.09	0.09	0.21	0.40	0.09	31.95	0.09	11.48	6.53	0.15	98.08
PMT-2-8-crd2	46.90	0.10	0.10	0.38	0.10	32.28	0.15	10.76	6.84	0.13	97.74
PMT-2-8-crd3	47.02	0.09	0.12	0.35	0.09	31.73	0.09	11.66	6.46	0.13	97.74
PMT-3-4-crd1	49.37	0.13	0.15	0.37	0.08	31.75	0.17	11.05	6.64	0.13	99.85
PMT-3-4-crd2	48.78	0.09	0.09	0.36	0.08	31.32	0.13	11.02	6.91	0.15	98.92
PMT-3-4-crd3	48.98	0.11	0.15	0.34	0.09	31.21	0.16	11.22	6.70	0.15	99.10

Note: gt = garnet, bt = biotite, pl = plagioclase, crd = cordierite. The letter c indicates a core analyses. All analyses are reported in weight percent elemental oxides.

percent, indicating high quality microprobe analyses. Ten garnet analyses did fall slightly outside this range, total to 100 ± 1.5 weight percent. A Fe composition map were made from one large garnet in ME-231 show that ME-231 garnets are Fe-rich and homogeneous with respect to Fe (i.e., no evidence for composition zoning, Appendix F).

Biotite

Thirty-four spot analyses were taken from fine-grained biotite of the ME-231 matrix. On average, these microprobe analyses totaled to 94.1 elemental oxides weight percent. The lower total elemental oxide weight percents of these analyses are probably due to significant quantities of H₂O in the biotites of ME-231. For these analyses the JOEL microprobe was not calibrated to measure H₂O and therefore did not measure H₂O. However, most biotites contain 5-6 weight percent H₂O within their crystalline structures (Deer *et al.*, 1992). Therefore, biotites with element oxide weight percent totals ≥ 94.0 are considered reliable here.

Plagioclase

Fine-grained plagioclase was analyzed from the matrix of ME-231. A total of twenty-seven spot analyses were taken from areas in the polished thin sections with abundant garnet, quartz and sillimanite. Sixteen of these analyses fell within 100 ± 1 total elemental oxide weight percent are considered reliable. The other eleven plagioclase analyses gave total elemental oxide weight percents < 99.0 and are not considered reliable and were not used in subsequent calculations.

Cordierite

Nine spot analyses were taken from three large cordierite porphoroblasts in ME-231. All cordierite analyses totaled to < 100 weight percent elemental oxides. However, two analyses (3-4-crd1 and 3-4-crd3) from one cordierite gave elemental oxides total

weight percents of 100 ± 1 , indicating these were good analyses. The other seven cordierite analyses yielded elemental oxides total weight percent of 96.4-98.9. Lower elemental oxides total weight percents in these analyses may be due to undetected H₂O in the cordierite, as in the case of the biotites (Nesse, 1991). Only cordierite analyses 3-4-cord1 and 3-4-cord3 were used in subsequent thermodynamic calculations.

Mineral End Member Activity Calculations made using AX

A total of six garnet, twenty-two biotite, eighteen albite plagioclase, and two cordierite robust rim microprobe analyses from one of the polished thin sections were individually averaged and then imported into the computer program AX (Table 5-2). The AX program was used to calculate mineral end member activities and to convert the elemental oxide data to cation unit formulas needed for subsequent thermobarometric calculations made using THERMOCALC. End member activities and cation unit formulas were calculated in AX at 4.0 kbar and 800°C, an approximate PT estimate for sample ME-231 based on its metamorphic petrology. End member activities for each mineral phase were calculated using ideal and non-ideal solution mixing models incorporated within AX. Cation unit formulas were calculated with ferric iron (Fe³⁺) estimation. The AX calculated end member activity and cation unit formulas are summarized in the AX output file included in Appendix E. See Holland and Powell (1998) or <http://www.earthsci.unimelb.edu.au/tpg/thermocalc/> for a more detailed description of the computer program AX.

Pressure-temperature Estimates using THERMOCALC

Mineral end member activities calculated in AX were imported into the computer program THERMOCALC to calculate average PT estimates for the ME-231 phase assemblage. THERMOCALC utilizes the internally consistent thermodynamic database

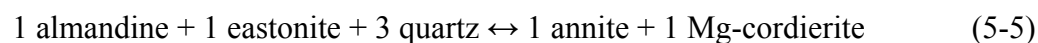
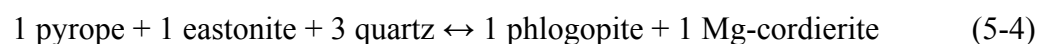
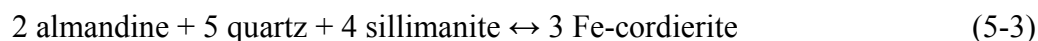
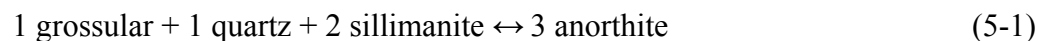
Table 5-2. Averaged ME-231 electron microprobe analyses used in thermobarometry

<u>Mineral</u>	<u>grt rims</u>	<u>bt rims</u>	<u>pl rims</u>	<u>crd rims</u>
n	6	22	18	2
SiO ₂	36.88	33.76	59.62	49.17
TiO ₂	0.14	3.12	0.05	0.12
Al ₂ O ₃	21.32	19.71	24.54	31.48
Cr ₂ O ₃	0.16	0.23	0.08	0.15
Fe ₂ O ₃	2.71	0.00	0.28	1.33
FeO	35.37	23.93	0.00	9.94
MnO	0.50	0.11	0.05	0.17
MgO	2.92	5.24	0.12	6.67
CaO	1.13	0.11	7.29	0.14
Na ₂ O	0.30	0.37	7.15	0.35
K ₂ O	0.11	8.28	0.09	0.09
<u>Totals</u>	101.56	94.88	99.27	99.61
<u>Oxygens</u>	12.00	11.00	8.00	18.00
Si	2.93	2.63	2.68	5.06
Ti	0.01	0.18	0.00	0.01
Al	2.00	1.81	1.30	3.82
Cr	0.01	0.01	0.00	0.01
Fe ³⁺	0.16	0.00	0.01	0.10
Fe ²⁺	2.35	1.56	0.00	0.86
Mn	0.03	0.01	0.00	0.01
Mg	0.35	0.61	0.01	1.02
Ca	0.10	0.01	0.35	0.02
Na	0.05	0.06	0.62	0.07
K	0.01	0.83	0.01	0.01
<u>Cation sum</u>	8.0	7.7	5.0	11.0
	XMg 0.1	XFe 2.6	XNa 1.8	XMg 1.1
	XCa 0.0	XMg 0.4	XCa 0.6	XFe 0.9
	XFe 5.3			
	XMn 0.0			

Note: grt = garnet, bt = biotite, pl = plagioclase, crd = cordierite, n = number of individual analyses averaged.

HP98 to make pressure-temperature estimates for rock phase assemblages based on imported mineral end member activities (e.g., Holland and Powell, 1998). For the ME-

231 phase assemblage PT estimates made here, the activities of sillimanite and quartz were assumed to be 1.0 by convention because these phases are considered pure mineral end members. Using THERMOCALC, a set of five independent reactions was calculated from the imported ME-231 mineral end member activities:



Reaction 5-1 is the “GASP,” geobarometer, which utilizes the equilibrium between garnet, aluminosilicate, quartz, and plagioclase to estimate pressures from pelitic rock phase assemblages (e.g., Koziol and Newton, 1988; Spear, 1993). The GASP geobarometer is a net transfer reaction, which means phases are consumed and produced across the reaction (Spear, 1993). The GASP acts as an adequate geobarometer because it is sensitive to volume change (large ΔV) and less sensitive to temperature (i.e., small ΔS and ΔH). Reactions 5-2, 5-3 and 5-4 are also net transfer reactions that act as geobarometers for the ME-231 phase assemblage. Reaction 5 is an exchange reaction, meaning chemical components are exchanged between the phases across the reaction without net consumption or production of any phases (Spear, 1993). In the case of reaction 5-5, iron and magnesium are exchanged between garnet, biotite and cordierite as a function of temperature.

The five independent reactions calculated in THERMOCALC have uncertainties in PT space, where these uncertainties are a function of the uncertainties in electron

microprobe analyses, calculated mineral end member activities, and modeled thermodynamic data, especially enthalpy (ΔH , Holland and Powell, 1998). THERMOCALC uses the least-squares method (e.g., York, 1969) to vary the positions of the independent reactions in PT space relative to these uncertainties and to reaction correlations (reactions with common end members are correlated in PT space) until a statistical intersection occurs at one point in PT space, the so-called “average PT” (e.g., Powell and Holland, 1994). In the case of ME-231, the five independent reactions intersect at an average PT of 3.8 ± 1.8 kbar and $657 \pm 176^\circ\text{C}$ (errors are 2σ ; also see the THERMOCALC output file in Appendix E).

The average PT estimate is plotted in Figure 5-1a on a phase diagram modified from Spear et al. (1999, see their Fig. 2, p. 19) representing the KFMASH (K_2O - FeO - MgO - Al_2O_3 - SiO_2 - H_2O) chemical system for pelitic rocks. The average PT estimate is marked by the star on the phase diagram in Figure 5-1a. In addition, the pressure and temperature errors associated with the average PT estimate are represented by the two sigma error ellipse shown in figure X; the position and shape of this error ellipse is defined by the statistical intersection of the five independent reactions calculated for the ME-231 phase assemblage in PT space.

The average PT estimate made here provides moderate constraints on the pressure and relatively poor constraints on temperature for the phase assemblage of ME-231 (Fig. 5-1a). Only the high temperature portion of the average PT error ellipse actually falls within the divariant field consistent with the metamorphic petrology of ME-231 (see description of ME-231 in Appendix C). The large uncertainties in the temperature of the average PT estimate can be explained by the relative positions of the five independent

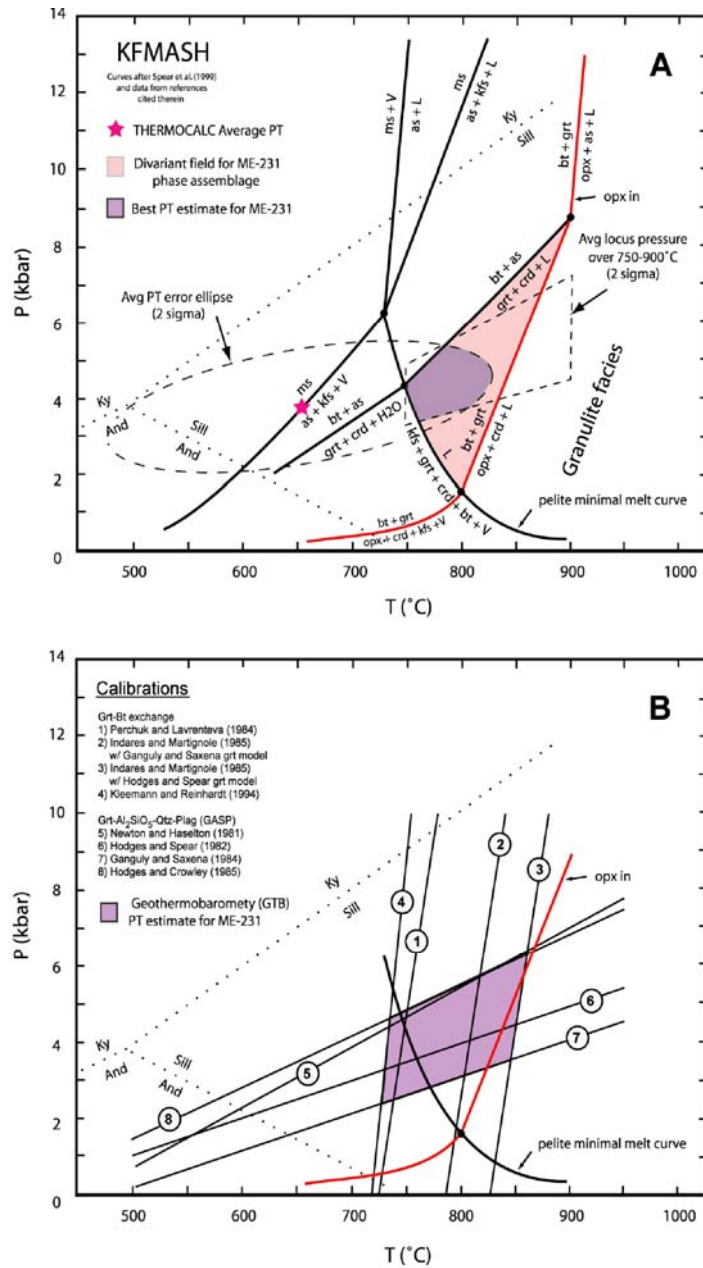


Figure 5-1. Phase diagrams showing PT estimates for ME-231, migmatitic Greyson paragneiss from the Lake of the Isle shear zone. A) THERMOCALC average and locus PT estimates. Uncertainties in the THERMOCALC average and locus PT estimates are represented by the dashed ellipse and box, respectively. The intersection (darkened region) of these two PT calculates is the best PT estimate for ME-231. B) Geothermobarometry (GTB) PT estimate for ME-231. The best GTB PT estimate is defined by intersections of several independently determined garnet-biotite exchange and GASP reaction calibrations. In both A and B Al_2SiO_5 stability fields are from Spear (1993) and univariant reaction curves are taken from Spear et al. (1999).

reactions in PT space. Figure 5-2 displays a pressure-temperature plot showing the five independent reactions calculated from the mineral end member data for ME-231 plotted in PT space. Considerable spread (separation) between the five independent reactions does not permit a well-defined statistical intersection to be made between the reactions. Consequently, a precise average PT estimate cannot be made for the ME-231 using the intersection of these five independent reactions. Figure 5-2 also explains why temperature is less constrained than pressure for the ME-231 phase assemblage. Because all five independent reactions are characterized by gentle to moderate Clapeyron slopes (the reaction curve slope in PT space), the temperature is much less constrained than pressure.

A more accurate PT estimate can be made for the ME-231 phase assemblage using the average “locus” option in THERMOCALC rather than the average PT option (e.g., Powell and Holland, 1994). The average locus option allows the user to calculate pressure or temperature independently from the one another, provided a geologically reasonable range of values can be estimated for one of the unknowns (see Powell and Holland, 1994 for a description of the average PT and locus pressure-temperature estimates). Since the range of possible temperatures consistent with the ME-231 assemblage is fairly well constrained to ~750-900°C (Fig. 5-1a), the average pressure can be calculated in THERMOCALC using the average locus option. Pressures calculated over these temperatures range from 4.6-6.0 kbar; however locus pressures above ~830-900°C fall outside of the divariant field of the ME-231 phase assemblage and are therefore not considered realistic (i.e., these pressures fall within the granulite facies). Notably, locus pressures from ~750-825°C overlap with the high temperature side of the

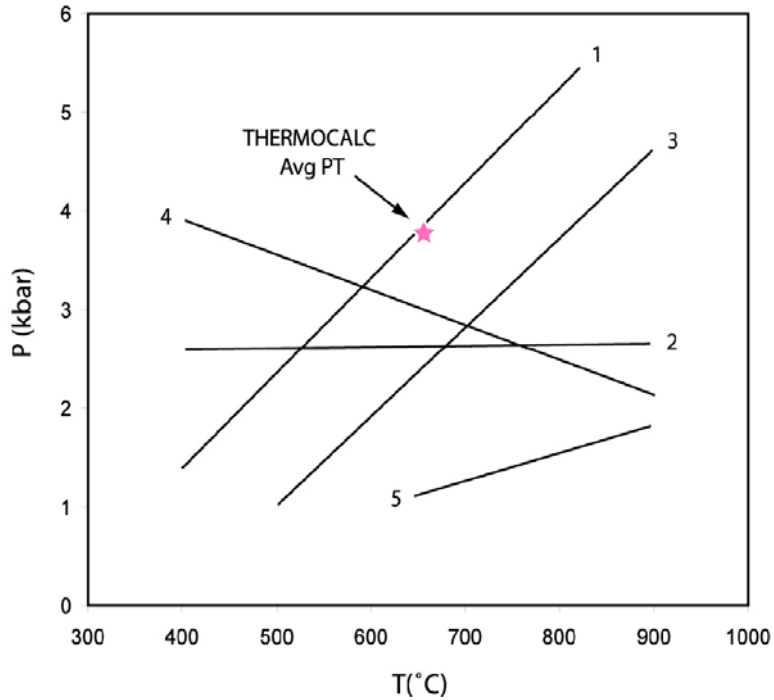


Figure 5-2. Phase diagram showing phase equilibria used by THERMOCALC to calculate the average PT estimate for sample ME-231. The poorly defined intersection between these reactions in PT space resulted in an average PT estimate with large uncertainties, especially in temperature.

average PT error ellipse within the central part of the ME-231 divariant field (Fig. 5-1a).

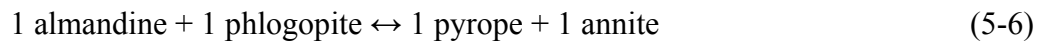
This region of overlap (darkened region) is considered the best (i.e., the most statistically sound) PT estimate for sample ME-231, corresponding to a pressure and temperature of 3.2-5.3 kbar and 750-825°C, respectively.

Pressure-temperature Estimates using Geothermobarometry (GTB)

To obtain a pressure-temperature estimate for ME-231 using GTB, the same averaged weight percent elemental oxide data (see Table 5-2) were first converted to cation unit formulas using the Microsoft Excel based spreadsheet program Formula.xls; this program is available at http://www.earth.ox.ac.uk/~davewa/pt/th_tools.html. The calculated cations for garnet, biotite, and plagioclase were then manually imported into GTB. GTB uses the imported cation data to calculate mineral end member activities then

the positions of several geothermometer and geobarometer reactions in PT space; the intersection of these reactions defines a pressure-temperature estimate. It is important to note GTB uses phase equilibria calibrations from several different sources to make a pressure-temperature estimate (e.g., the geothermometer and geobarometer equilibria are calibrated by different workers, and different thermodynamic data). Therefore, the GTB pressure-temperature estimates are not “internally consistent” as pressure-temperature estimates made using the THERMOCALC.

Figure 5-1b shows the positions of the Fe-Mg garnet-biotite exchange geothermometer:



and the garnet-aluminosilicate-quartz-plagioclase (GASP) geobarometer (see reaction 5-1 above) determined using several different calibrations. The region of intersection between the garnet-biotite exchange geothermometer and GASP geobarometer (darkened region), as defined by the different calibrations, corresponds to a PT estimate for ME-231 of ~3-6 kbar and ~725-850°C (Fig. 5-1b). These GTB pressure-temperature estimate for ME-231 is in good agreement with the THERMOCALC best PT estimate. The GTB pressure-temperature estimate also corresponds to upper-amphibolite conditions up-temperature of the minimal pelite melt curve (Fig. 5-1b).

CHAPTER 6
⁴⁰AR/³⁹AR THERMOCHRONOLOGY

Purpose and Strategy

Mineral cooling ages obtained by ⁴⁰Ar/³⁹Ar thermochronology can be used to constrain the cooling and exhumation histories of highly extended terranes such as metamorphic core complexes (e.g., Foster and John, 1999; Stockli, 2005). Rock samples are typically collected along transects in the lower plate parallel to the direction of slip on the bounding detachment fault zone(s). Apparent cooling ages are then obtained from individual mineral separates extracted from the transect samples using the ⁴⁰Ar/³⁹Ar method. These data can then be used to estimate the timing of the onset and duration of extension, rate(s) of extension (e.g., slip rates on detachment faults), cooling histories for lower plates, detachment geometry, and amounts of vertical and horizontal displacement along detachment fault systems (e.g., Foster et al., 1993; John and Foster, 1993; Scott et al., 1998; Foster and John, 1999; Brichau et al., 2005). In order to constrain such aspects of extension in the ACC a suite of sixteen rock samples was collected for ⁴⁰Ar/³⁹Ar thermochronology along a transect across the lower plate, parallel to the approximate direction of slip (ESE, ~105°) on the east-bounding detachment fault system.

The ⁴⁰Ar/³⁹Ar thermochronology transect of this study was carried out in the northeastern Anaconda-Pintlar Range, southwest of the town of Anaconda, MT. Here, upper plate rocks have been almost entirely removed, exposing the metamorphic-plutonic lower plate of the ACC for a lateral (east-west) distance greater than 20 km. Rock samples collected along the transect were taken from high elevations where possible (i.e.,

closest to the original detachment level as possible) to ensure that cooling ages obtained from the samples would reflect tectonic unroofing and subsequent cooling of the ACC lower plate. Individual samples along the transect were chosen based on their mineral content; samples with multiple argon-bearing minerals (e.g., hornblende, K-feldspar, muscovite, and biotite) were targeted. Rock types sampled along the transect included: micaeous quartzites correlated with the lower Belt Supergroup and middle Cambrian section, undeformed granitoids, and deformed granitoids with greenschist facies mylonitic fabrics from within the mylonite zone in the easternmost part of the study area.

Four other rock samples were collected from areas outside the transect. Two granitoid samples were collected from exposures of the detachment north of the study area, along the eastern flanks of the Flint Creek Range. The other two samples were collected from the detached upper plate within the Deerlodge Valley, east of the study area; these include a large granodiorite block or “mega-clast” and a crystal-lithic rhyolitic tuff unit correlated with the Eocene Lowland Creek Volcanic Sequence (Isopolatov, 1997).

Previous Thermochronology

Previously available thermochronological data relevant to the exhumation and cooling history of the ACC have been compiled and are summarized in Table 6-1. The majority of the previously thermochronology was obtained using the K-Ar method. However, cooling ages reported in some of the more recent studies were obtained by $^{40}\text{Ar}/^{39}\text{Ar}$ and fission-track thermochronology. The relevant previous thermochronology are grouped by geographic location in Table 6-1 (e.g., by name of mountain range or valley) and discussed briefly below. In addition, the previous K-Ar, $^{40}\text{Ar}/^{39}\text{Ar}$ and

fission-track thermochronology summarized in Table 1 are presented on a regional scale geologic map in Figure 6-1.

Four previous studies provide thermochronological data from the Anaconda-Pintlar Range. Desmarais (1983) reports K-Ar cooling ages from granitoids of the Chief Joseph Batholith in the southwestern Anaconda-Pintlar Range. Quartz diorite and granodiorite rocks, some exhibiting strong solid-state deformation, yield hornblende and biotite cooling ages ranging from ~75-60 Ma. Biotite from a biotite granite and dacite dike yield K-Ar cooling ages of 51.3 ± 1.6 and 50.3 ± 2.2 Ma, respectively; these two samples were collected east of the Chief Joseph Batholith. Foster and Raza (2002) report apatite fission-track ages of ~40-30 Ma from granodiorite and quartz diorite rocks of the Chief Joseph Batholith. Wallace et al. (1992) report K-Ar cooling ages from the central and northeastern Anaconda-Pintlar Range; biotite and muscovite from a number of granodiorite samples and a dacite dike within in the central Anaconda-Pintlar Range give cooling ages of ~55-49 Ma. In addition, biotite and hornblende from the Storm Lake Stock granodiorite (sample E1048) within the northeastern Anaconda-Pintlar Range (and within the current study area) yield cooling ages of 78.7 ± 1.6 and 116.4 ± 4.6 Ma, respectively. O'Neill et al. (2004) report a $^{40}\text{Ar}/^{39}\text{Ar}$ cooling age of 47.2 ± 0.3 Ma for muscovite from a mylonitic micaeous quartzite (sample ME-1) of the Sullivan Creek drainage in the northeastern Anaconda Pintlar Range (also within the current study area). Note rock samples were taken from the same localities as samples E1048 and ME1 for $^{40}\text{Ar}/^{39}\text{Ar}$ thermochronology in this study.

Three previous studies provide thermochronology from the Flint Creek Range. Hyndman (1972) and Martin et al. (1989) report hornblende and biotite K-Ar cooling

Table 6-1. Summary of relevant previous thermochronology.

Sample	Rock type	Latitude	Longitude	Mineral	Age (Ma)	Error (+/-)	Method	Source
<u>Northern Flint Creek Range, Royal Stock (1)</u>								
FC-263	porphyritic granite	46°24'30"	113°05'40"	bt	64.7	1.6	K-Ar	Martin et al., 1989
<u>Southern Flint Creek Range, Mt. Powell Batholith (2)</u>								
FC-273	granodiorite	46°18'23"	113°00'16"	ms	61.5	1.0	K-Ar	Martin et al., 1989
<u>Western Flint Creek Range, Phillipsburg Batholith (3)</u>								
BB6	hb bt granodiorite	46°16'19"	113°14'07"	hbl	76.7	2.5	K-Ar	Hyndman et al., 1972
				bt	74.0	2.1	K-Ar	
AA-4	hb bt granodiorite	46°18'21"	113°13'39"	hbl	72.0	2.5	K-Ar	Martin et al., 1989
				bt	73.4	2.1	K-Ar	
FC-271	hbl bt granodiorite	46°18'52"	113°15'00"	bt	77.2	1.9	K-Ar	Martin et al., 1989
FC-272	hbl bt granodiorite	46°16'42"	113°11'17"	bt	73.3	1.8	K-Ar	
98-75	hb bt granodiorite	46°19.1'	113°13.45'	ap	57.0	5.0	fis-tr	Foster and Raza, 2002
<u>Northern Anaconda-Pintlar Range (4)</u>								
E0134	granodiorite	46°2.55'	113°10.51'	ms	50.6	1.0	K-Ar	Wallace et al., 1992
				bt	48.5	1.0	K-Ar	
E1048	hbl bt granodiorite	46°6.10'	113°16.55'	hbl [§]	116.4	4.6	K-Ar	O'Neill et al., 2004
				bt [§]	78.7	1.6	K-Ar	
				bt	53.1	1.6	K-Ar	
ME-1	mylonitic mica quartzite [§]	46°01'16"	113°10'04"	ms	47.2	0.3	Ar-Ar	O'Neill et al., 2004
<u>Sapphire Batholith (5)</u>								
Grouped	granodiorite, granite	-	-	hb, bt	~75-73	-	Ar-Ar	Foster, unpub. data
98-65	granodiorite, granite	46°13.44'	113°43.58'	ap	44.0	3.0	fis-tr	Foster and Raza, 2002
98-66	granodiorite, granite	46°13.64'	113°41.83'	ap	45.0	4.0	fis-tr	

Table 6-1 Continued.

Sample	Rock type	Latitude	Longitude	Mineral	Age (Ma)	Error (+/-)	Method	Source
Chief Joseph Batholith (6)								
ND-80-173	hbl bt granodiorite	46°01'20"	113°49'10"	hbl	74.9	2.6	K-Ar	Desmarais, 1983
				bt	71.3	5.1	K-Ar	
ND-80-298	q diorite ^f	45°56'20"	113°43'30"	hbl	73.4	3.2	K-Ar	
				bt	64.6	2.8	K-Ar	
ND-81-475	q diorite ^f	-	-	hb	72.8	2.5	K-Ar	
				bt	64.1	2.2	K-Ar	
ND-80-14	hbl bt granodiorite ^f	45°53'58"	113°48'56"	hbl	66.8	2.9	K-Ar	
				bt	61.8	1.9	K-Ar	
AP-81-529	bt granodiorite ^f	45°51'19"	113°49'20"	bt	60.2	1.9	K-Ar	Foster and Raza, 2002
Grouped	granodiorite ^f	see map		ap	~40-30	-	fis-tr	
Central and southern Anaconda-Pintlar Range (7)								
ND-80-120	bt granodiorite	45°53'45"	113°54'00"	bt	57.6	2.5	K-Ar	Desmarais, 1983
ND-81-362	biotite granite ^f	45°54'30"	113°53'40"	bt	59.7	2.6	K-Ar	
ND-79-269	two-mica granodiorite	45°31'35"	113°50'58"	ms	58.2	2.1	K-Ar	
				bt	54.8	2.4	K-Ar	
ND-79-89	bt granite	45°46'25"	113°57'25"	bt	51.3	1.6	K-Ar	
AP-81-123	dacitic dike	45°50'33"	113°42'53"	bt	50.3	2.2	K-Ar	Wallace et al., 1992
81642	granodiorite	45°56.04'	113°28.40'	ms	49.9	1.0	K-Ar	
				bt	50.7	1.0	K-Ar	

Table 6-1 Continued.

Sample	Rock type	Latitude	Longitude	Mineral	Age (Ma)	Error (+/-)	Method	Source
81540	granodiorite			ms	54.9	1.2	K-Ar	
81639	granodiorite	45°54.21'	113°31.14'	bt	53.1	1.2	K-Ar	
81640	dacitic dike	45°55.30'	113°30.17'	bt	51.8	1.0	K-Ar	
<u>Pioneer Batholith (8)</u>								
Grouped	q diorite, granodiorite, granite	see map		hb, bt, ms	~80-65	-	K-Ar, Ar-Ar	Snee, 1978, 1982
<u>Boulder Batholith (9)</u>								
Grouped	granodiorite, granite	see map		hb	~76-71	-	K-Ar	Tilling et al., 1968
				bt	~74-70	-	K-Ar	
Grouped	late-stage granitic veins	see map		kfs, bt, ms	~74-59	-	Ar-Ar	Lund et al., 2002
<u>Deerlodge Valley (10)</u>								
LVC-32	rhyolite	46°08'00"	112°56'20"	sd	48.4	0.5	Ar-Ar	Isopolatov, 1997
LVC-6	rhyodacite porphyry	46°01'10"	112°58'50"	hbl	51.7	1.1	Ar-Ar	
				bt [§]	51.5	0.4	Ar-Ar	
LCV-19-3	andesite porphyry	46°03'10"	112°44'30"	pl	^{TF} 52.6	1.9	Ar-Ar	
LCV-15	Dacitic porphyry			pl	49.8	0.5	Ar-Ar	
LCV-18	andesite porphyry	46°03'10"	112°44'30"	pl	^{TF} 50.2	2.1	Ar-Ar	

Table 6-1 Continued.

Sample	Rock type	Latitude	Longitude	Mineral	Age (Ma)	Error (+/-)	Method	Source
95LCV-9	rhyodacite porphyry	46°00'47"	112°44'37"	hbl	52.2	0.4	Ar-Ar	
95LCV-7	rhyolite porphyry	46°00'57"	112°42'11"	hbl	52.6	0.2	Ar-Ar	
95LCV-10A	rhyolite tuff	46°10'20"	112°26'44"	bt	52.4	0.5	Ar-Ar	
00-11	rhyolite tuff	-	-	bt	52.9	0.4	Ar-Ar	Dudas, unpub. data
00-24	rhyolite tuff	-	-	bt	51.5	0.4	Ar-Ar	
BQM-2	rhyodacite porphyry	-	-	bt	51.5	0.2	Ar-Ar	
Elkhorn Mts. Volcanic Fie (11)								
Grouped	varied	-	-	hbl, bt	~81-74	-	K-Ar	Tilling, et al., 1968

Note: q = quartz, bt = biotite, ms = muscovite, hbl = hornblende, kfs = K-feldspar, sd = sanidine, pl = plagioclase, ap = apatite, § = sample also dated in this study, f = moderate to strong solid-state foliation, TF = total fusion age, i = normal isochron age, MSWDp = mean standard weighted deviates for plateau cooling age, PB = Philipsburg Batholith, MPB = Mt. Powell Batholith, RS = Royal Stock, CJ = Chief Joseph Batholith. Number geographic regions correspond to Figure 6.1. All cooling ages are reported with 2 sigma error.

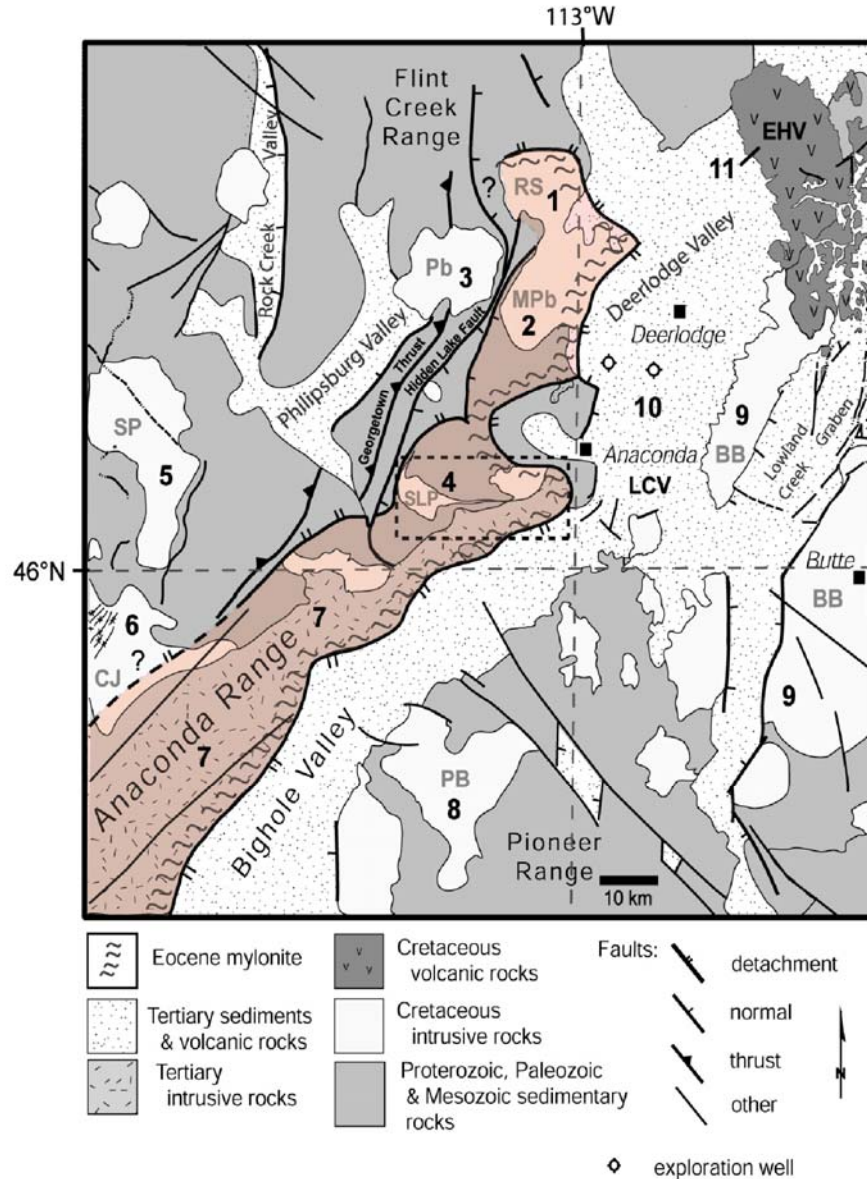


Figure 6-1. Geologic map of Anaconda metamorphic core complex (ACC), western Montana and vicinity showing location of previous thermochronology. See Table 1 for explanation for number regions. RS = Royal Stock, Pb = Philipsburg Batholith, MPb = Mt. Powell Batholith, SLP = Storm Lake Stock pluton, SP = Sapphire Batholith, CJ = Chief Joseph Batholith, PB = Pioneer Batholith, BB = Boulder Batholith, LCV = Lowland Creek Volcanic Field, EHV = Elkhorn Mountains Volcanic Field. The current study area is designated by the dashed box (Modified from Foster et al., 2006a).

ages ranging from ~77-72 Ma for the Philipsburg Batholith, a predominately granodioritic intrusion in the northwestern Flint Creek Range. In addition, Foster and

Raza (2002) report an apatite fission-track cooling age of 57.0 ± 5 Ma for a sample taken from the western part of the Philipsburg Batholith. Marvin et al. (1989) provide biotite and muscovite K-Ar cooling ages of ~65-60 Ma for the Royal Stock (mostly granodiorite) and Mount Powell Batholith (granodiorite and two-mica granite) in the northeastern Flint Creek Range.

Isopolatov (1997) and Dudas (unpublished data) report $^{40}\text{Ar}/^{39}\text{Ar}$ cooling ages from several samples collected from the Lowland Creek Volcanic Field (LCV) located within the Deerlodge Valley, east of the Anaconda-Pintlar and Flint Creek Ranges. Note some of these samples were collected from the western Deerlodge Valley, directly east of the current study area within the detached, brittlely faulted upper plate of the ACC. Biotite, hornblende, plagioclase, and sanidine from rhyolitic lava flows/tuffs and rhyolitic-to-andesitic hypabyssal (very shallow) porphyries of the LCV all report $^{40}\text{Ar}/^{39}\text{Ar}$ cooling ages ranging from ~53-48 Ma. Note that a sample (DF02-113) was collected from the same outcrop as LCV sample LV-6 (of Isopolatov, 1997) for $^{40}\text{Ar}/^{39}\text{Ar}$ thermochronology in this study (Table 6-1).

The cooling histories of the Pioneer, Boulder, and Sapphire Batholiths also bear significant importance on later discussions of the exhumation and cooling history of the ACC. Therefore, a summary of the thermochronology from these batholiths is also included here. Snee (1978, 1982) provides a large K-Ar and $^{40}\text{Ar}/^{39}\text{Ar}$ thermochronological data set for the Pioneer Batholith, a predominately quartz diorite-granodiorite-granite intrusion located southeast of the Anaconda-Pintlar Range and east of the Bighole Valley. Hornblende, biotite and muscovite cooling ages from the Pioneer Batholith reported by Snee range from ~80-65 Ma. The Boulder Batholith is a large

(>6000 km²) intrusion, mostly comprised of a granite phase (previously classified as a quartz monzonite; see Lund et al., 2002) and several smaller granodiorite intrusions that lies directly east of the current study area and east of the Deerlodge Valley (Vejmelek and Smithson, 1995). Tilling et al. (1968) report biotite and hornblende K-Ar cooling ages of ~76-71 Ma for plutons of the Boulder Batholith and ~81-74 Ma for the Elkhorn Mountains Volcanic Field, the volcanic cover for the Boulder Batholith. In addition, Lund et al. (2002) report ⁴⁰Ar/³⁹Ar cooling ages of ~74-59 Ma for late-stage granitic veins intruded within the main phases of the Boulder Batholith. Foster (unpublished data) reports muscovite and biotite ⁴⁰Ar/³⁹Ar cooling ages of ~75-73 Ma from the Sapphire Batholith located west of the current study area and east of the Bitterroot Valley. Foster and Raza (2002) also report apatite fission-track cooling ages of 44.0 ± 3 and 45.0 ± 4 Ma for two samples collected from the Sapphire Batholith.

⁴⁰Ar/³⁹Ar Thermochronology Results

Individual mineral separates (biotite, muscovite, hornblende, and K-feldspar) were obtained from a total of the twenty-two rock samples (twenty lower plate and two upper plate samples) for the ⁴⁰Ar/³⁹Ar thermochronology in this study. These mineral separates were subsequently analyzed during in-vacuo laser and furnace step-heating experiments coupled with mass spectrometry in the noble gas laboratory at the University of Florida. Sample preparation, analytical instrumentation and procedures, and thermochronological data reduction are summarized in Appendix A.

The results from the ⁴⁰Ar/³⁹Ar thermochronology of this study are reported in Table 6-2. These results are organized into two groups; one corresponds to rock samples collected along the lower plate transect described above and the other group to samples collected outside the lower plate transect. Note the results from rock samples collected

along the lower plate transect are listed spatially, from west to east (top to bottom in Table 6-2) according to their relative position along the lower plate transect. Individual $^{40}\text{Ar}/^{39}\text{Ar}$ cooling ages are reported in Table 6-2 according to rock sample name, rock type, sample location, elevation, and mineral dated. Total percent ^{39}Ar gas released during step-heating and MSWD (mean standard weighted deviates) are also reported with weighted plateau cooling ages in Table 6-2. The J-values (from mineral flux monitors) used in individual cooling age calculations are also included in Table 6-2. In addition, mineral cooling ages obtained from samples collected along the lower plate transect are shown with sample localities on a simplified geologic sketch map in Figure 6-2. The individual mineral cooling age spectra are shown in Figure 6-3.

Argon Closure Temperature

Mineral ages obtained using $^{40}\text{Ar}/^{39}\text{Ar}$ thermochronology in this study are cooling ages, not crystallization ages. Therefore, these cooling ages record the time at which a mineral grain (and its host rock) cooled below a certain temperature and when ^{40}Ar , the radiogenic daughter product of ^{40}K , fully ceased to escape (diffuse) from the mineral crystal lattice. This critical temperature is referred to as the “closure temperature,” below which the mineral system is effectively closed to the diffusion of Ar (Dodson, 1973; Harrison and McDougall, 1999). Ar closure temperatures vary between different minerals in a given rock because of significant differences in their crystalline structures and consequently, in Ar diffusion properties. Modeling and experimentation involving Ar diffusion over the past several decades has provided approximate Ar closure temperatures for common K-bearing minerals are: $\sim 300^\circ\text{C}$ for biotite, $\sim 350^\circ\text{C}$ for muscovite, and $\sim 500^\circ\text{C}$ for hornblende (see Harrison and McDougall, 1999 and many references therein). K-feldspar has been shown to have a range of Ar closure.

Table 6-2. Summary of $^{40}\text{Ar}/^{39}\text{Ar}$ thermochronology from the Anaconda metamorphic core complex.

Sample	Rock type	Latitude	Longitude	Elevation (m)	Mineral	Age (Ma)	Errors (+/-)	% $^{39}\text{Ar}_p$	MSWD _p
Samples from the $^{40}\text{Ar}/^{39}\text{Ar}$ transect in the northeastern Anaconda-Pintlar Range									
SL-38 [†]	hbl bt grd	46°6.10'	113°16.55'	2311	bt	79.0	1.2	78	2.02
					hbl	^U 102.5	12.8	65	144.50
					kfs	^{LT} 56.9	1.6	9	4.98
WG04-114	hbl bt grd	46°04'25"	113°15'48"	2503	bt	74.0	0.9	94	0.69
WG04-112	micaeous quartzite	46°03'26"	113°14'43"	2646	ms	56.9	0.7	81	0.34
					bt	52.8	0.7	100	0.63
WG04-052	q di	46°05'09"	113°13'46"	2754	bt	64.1	1.0	88	1.43
WG04-033	dacite dike	46°04'29"	113°10'50"	2583	bt	48.5	0.6	94	0.99
WG04-109	two mica gr	46°02'35"	113°10'43"	2878	ms	48.0	0.6	87	1.75
					bt	47.6	0.6	100	1.60
WG04-101	coarse two mica gr	46°03'39"	113°10'01"	3073	ms	49.6	0.6	78	0.34
					bt	49.2	0.9	93	1.25
WG04-100	pegmatitic dike	46°03'36"	113°09'52"	2927	ms	50.4	0.8	95	2.63
ME-6	coarse two mica gr	46°02'25"	113°10'15"	2732	ms	51.5	1.2	79	0.31
					bt	48.6	1.0	95	1.74
Ug-1	deformed q di sill	46°04'32"	113°08'55"	2610	bt	50.5	0.8	92	0.10
					hb	^U 91.3	1.0	60	0.61
WG04-103 [†]	mylonitic quartzite	46°01'16"	113°10'04"	2524	ms	^{EP} 47.3	1.1	80	0.91
WG04-092	bt gr	46°03'34"	113°08'25"	2896	bt	47.1	0.7	78	3.01
WG04-089	aluminous leuco-gr	46°02'56"	113°08'18"	2646	ms	45.5	0.6	100	1.43
WG04-138	mylonitic quartzite	46°03'37"	113°06'14"	3098	ms	46.1	0.6	99	0.19
DF02-116a	mylonitic two mica gr	46°05'29"	113°02'05"	2573	ms	40.5	2.0	65	2.21
					bt	39.6	2.3	70	1.36
					bt	^{TF} 40.7	0.7	100	-
DF02-120	mylonitic biotite gr	46°03'25"	113°01'38"	2229	bt	^{TF} 38.5	0.7	100	-

Table 6-2. Continued.

Sample	J value	Comments
SL-38 [†]	0.0038300	
	0.0038500	extraneous argon
	0.0038450	
WG04-114	0.0005150	
WG04-112	0.0005140	
	0.0005140	
WG04-052	0.0005145	
WG04-033	0.0005150	
WG04-109	0.0005140	
	0.0005140	
WG04-101	0.0005150	
	0.0005150	
WG04-100	0.0005150	
ME-6	0.0064000	
	0.0064000	
Ug-1	0.0038590	
	0.0038500	extraneous argon
WG04-103 [†]	0.0005145	
WG04-092	0.0005150	
WG04-089	0.0005140	thin garnet bearing sheet
WG04-138	0.0005150	Short Peak mylonite
DF02-116a	0.0038000	Clear Creek mylonite
	0.0037650	
	0.0064600	
DF02-120	0.0064770	Mill Creek mylonite

Table 6-2. Continued.

Sample	Rock type	Latitude	Longitude	Elevation (m)	Mineral	Age (Ma)	Errors (+/-)	% ³⁹ Ar _p	MSWD _p
Outside the ⁴⁰Ar/³⁹Ar transect									
DF02-118a	mylonitic bt gr	46°11'49"	112°59'11"	-	bt	38.8	1.6	72	0.82
DF02-118b	mylonitic bt g	46°11'49"	112°59'11"	-	bt	42.4	1.6	100	1.03
DF02-121	gr	-	-	-	bt	55.3	2.8	83	0.84
DF02-119a	two mica gr	46°16'42"	112°57'53"	-	ms	^{EP} 68.3	2.3	98	4.14
					bt	^{EP} 66.2	1.2	81	2.23
DF02-113 [†]	rhyolite tuff	46°01'11"	112°59'03"	-	bt	53.7	1.4	66	0.71
DF02-114	bt hbl gr	46°04'24"	112°56'22"	-	bt	76.3	1.1	95	0.57

Table 6-2. Continued.

Sample	J value	Comments
DF02-118a	0.0038100	Lost Creek mylonite
DF02-118b	0.0038540	Lost Creek mylonite
DF02-121	0.0038500	
DF02-119a	0.0038540	Racetrack Creek
	0.0038540	
DF02-113 [†]	0.0037650	upper plate, lower LCV
DF02-114	0.0038770	from upper plate

Note: grd = granodiorite, q di = quartz diorite, gr = granite, q = quartz, bt = biotite, ms = muscovite, hbl = hornblende, kfs = K-feldspar, † = previously dated by other workers, LT = low temperature plateau, TF = single grain total fusion cooling age, EP = error plateau, u = unreliable cooling age, % ³⁹Ar_p = percent of ³⁹Ar used in weighted plateau age calculation, and MSWD_p = mean standard weighted deviates for plateau cooling age. All cooling age are reported in 2 sigma error.

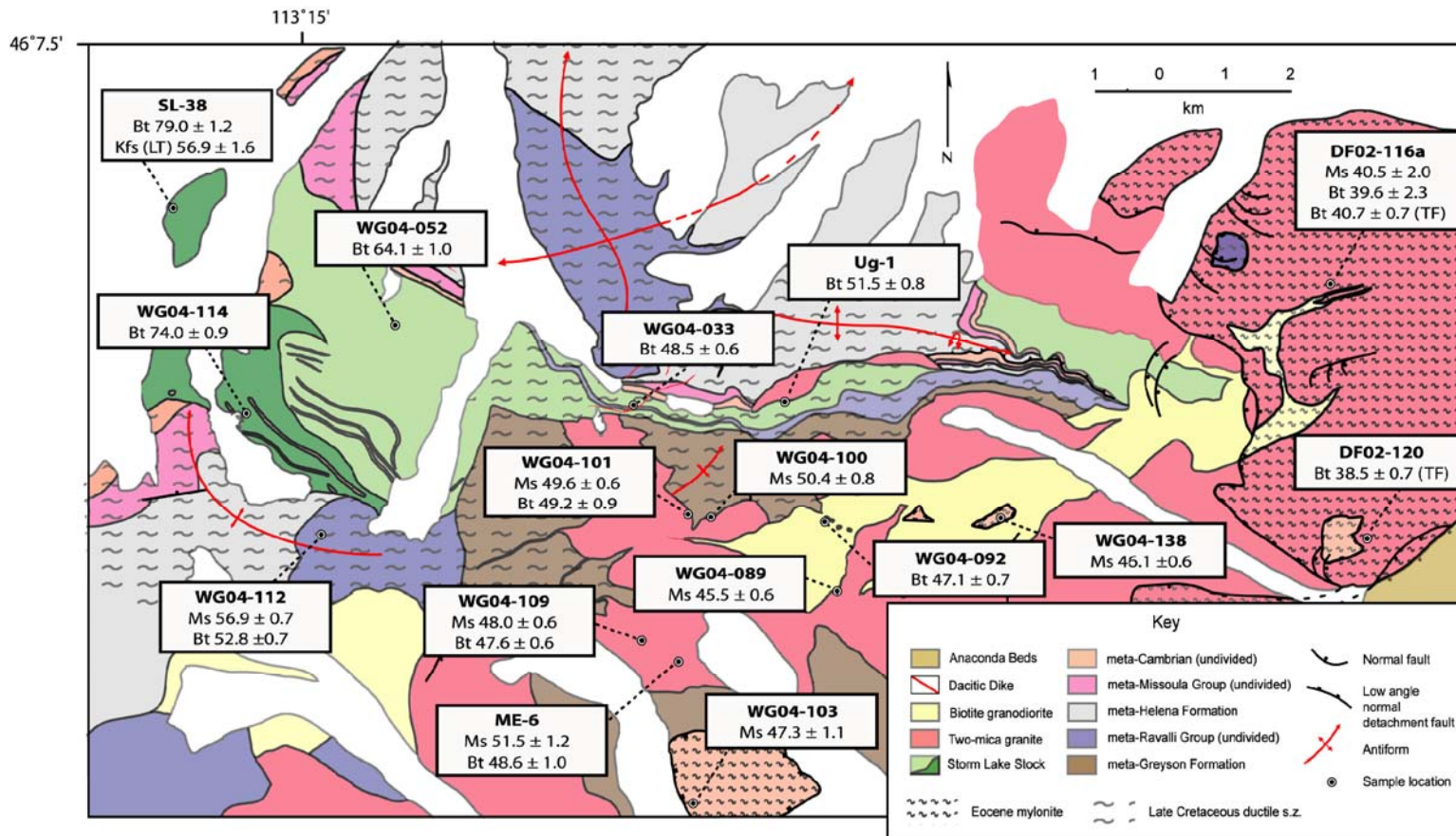


Figure 6-2. Geologic sketch map showing mineral cooling ages from samples collected along the ACC lower plate transect using $^{40}\text{Ar}/^{39}\text{Ar}$ thermochronology. Mineral cooling age errors are two sigma.

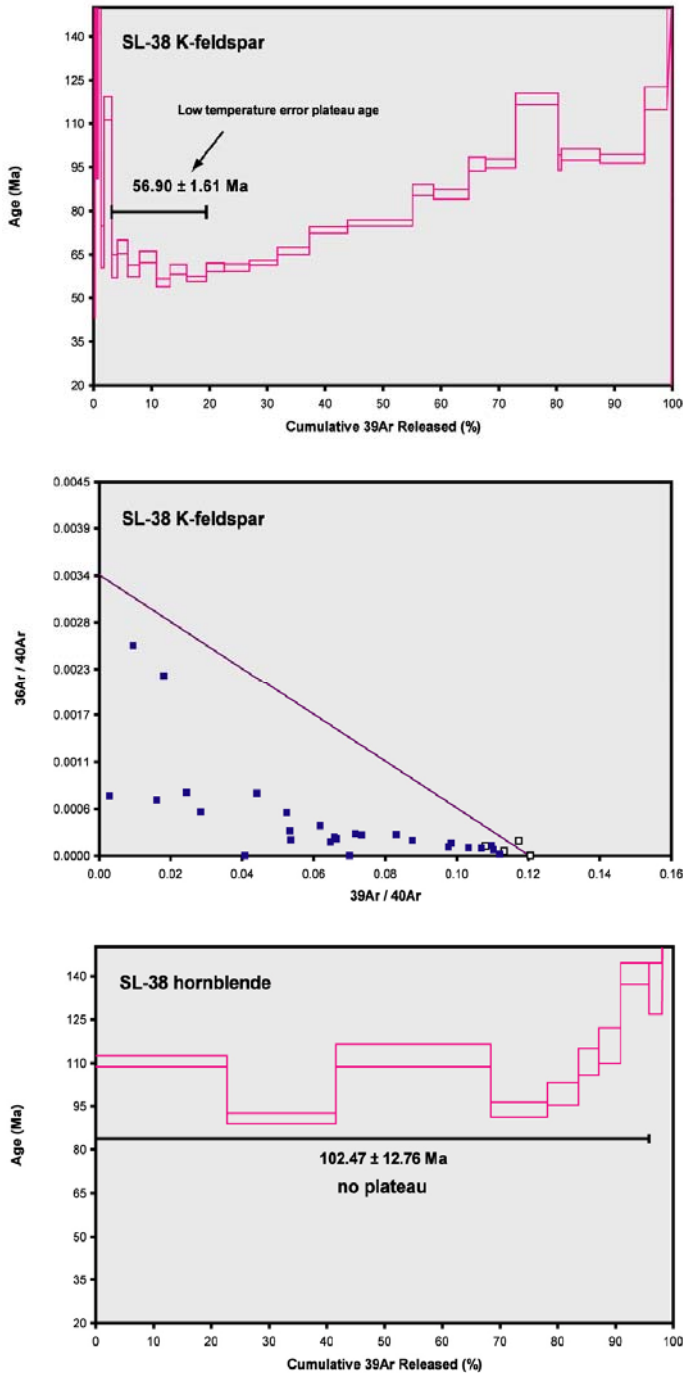


Figure 6-3. $^{40}\text{Ar}/^{39}\text{Ar}$ mineral age spectra obtained for samples collected from the Anaconda metamorphic core complex using $^{40}\text{Ar}/^{39}\text{Ar}$ thermochronology. All ages are weighted plateau cooling ages calculated from three or more contiguous heating steps with $>50\%$ total ^{39}Ar gas released unless otherwise specified. Error plateau ages were calculated from noncontiguous heating steps and/or less than 50% total ^{39}Ar gas released. All ages are reported with two sigma errors. Thickness of age plateaus corresponds to the two sigma errors for the cooling age calculated for that particular heating step.

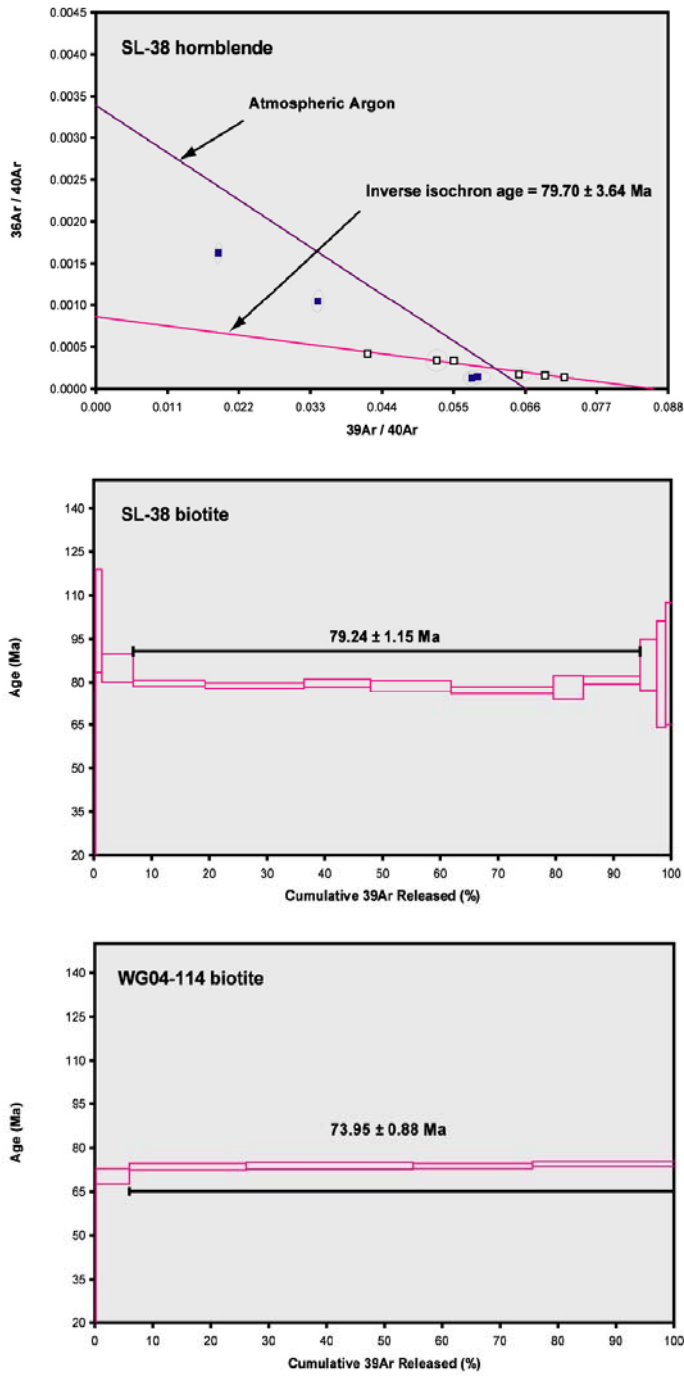


Figure 6-3. Continued.

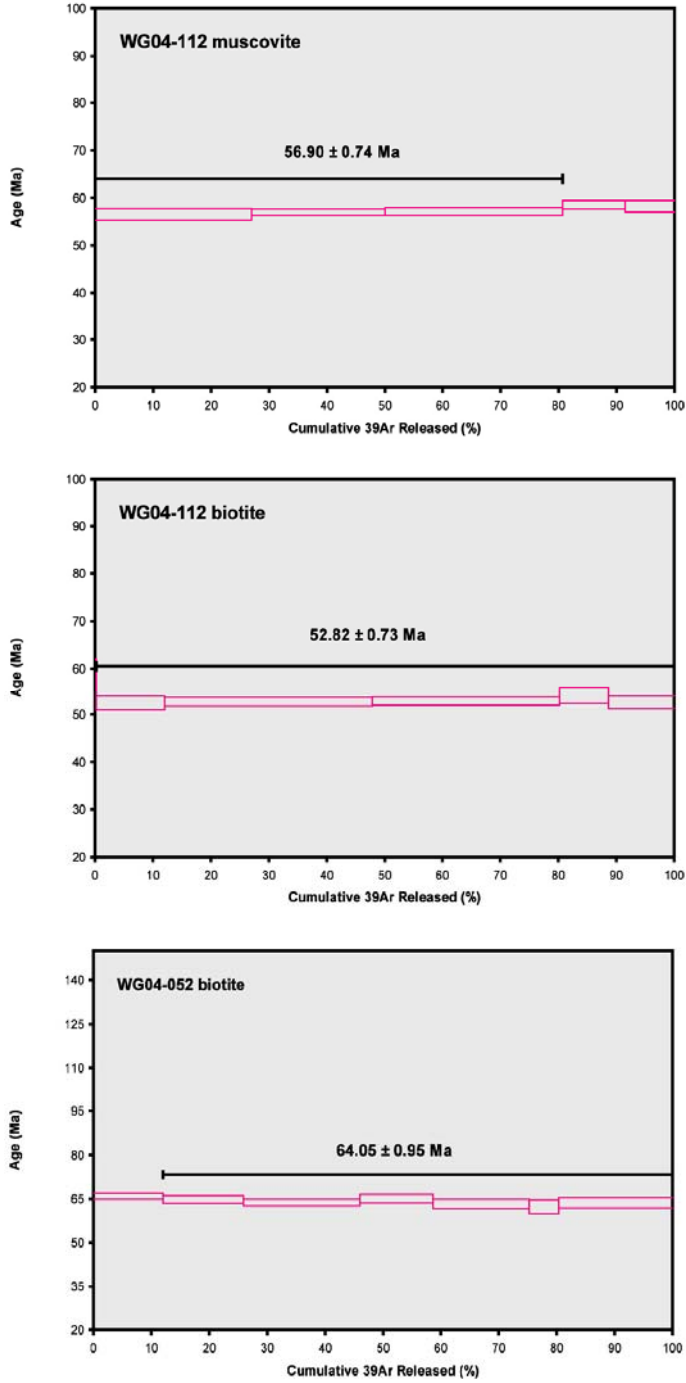


Figure 6-3. Continued

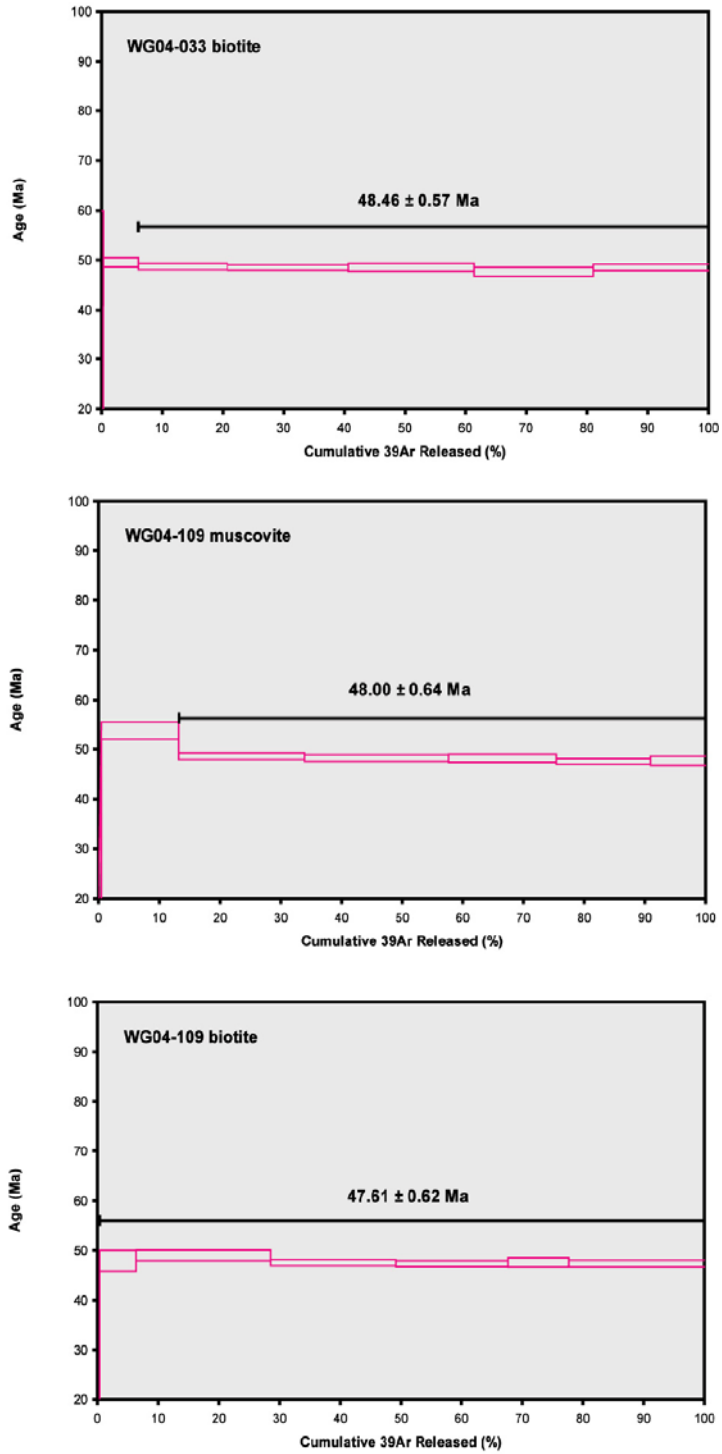


Figure 6-3. Continued.

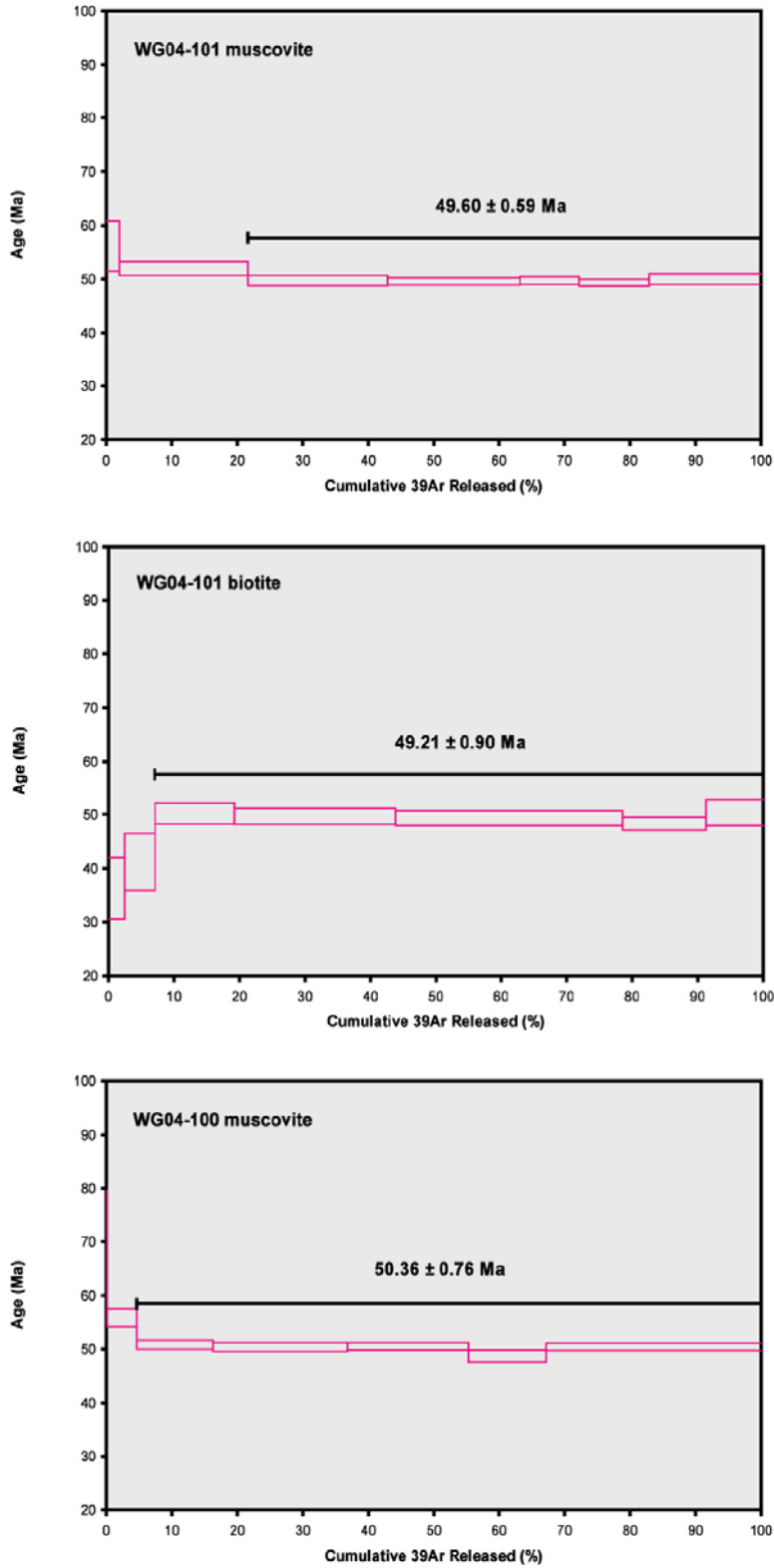


Figure 6-3. Continued.

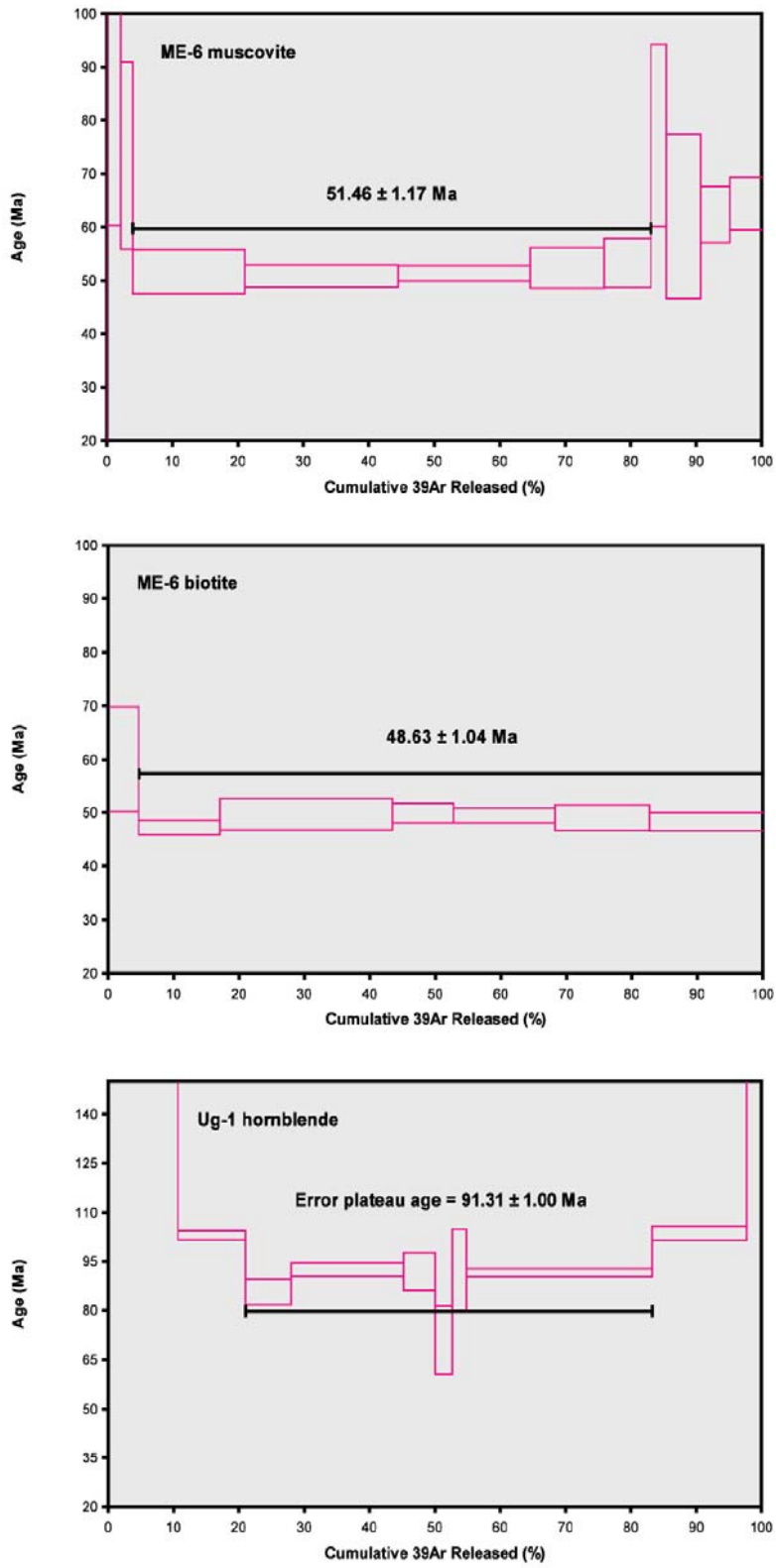


Figure 6-3. Continued.

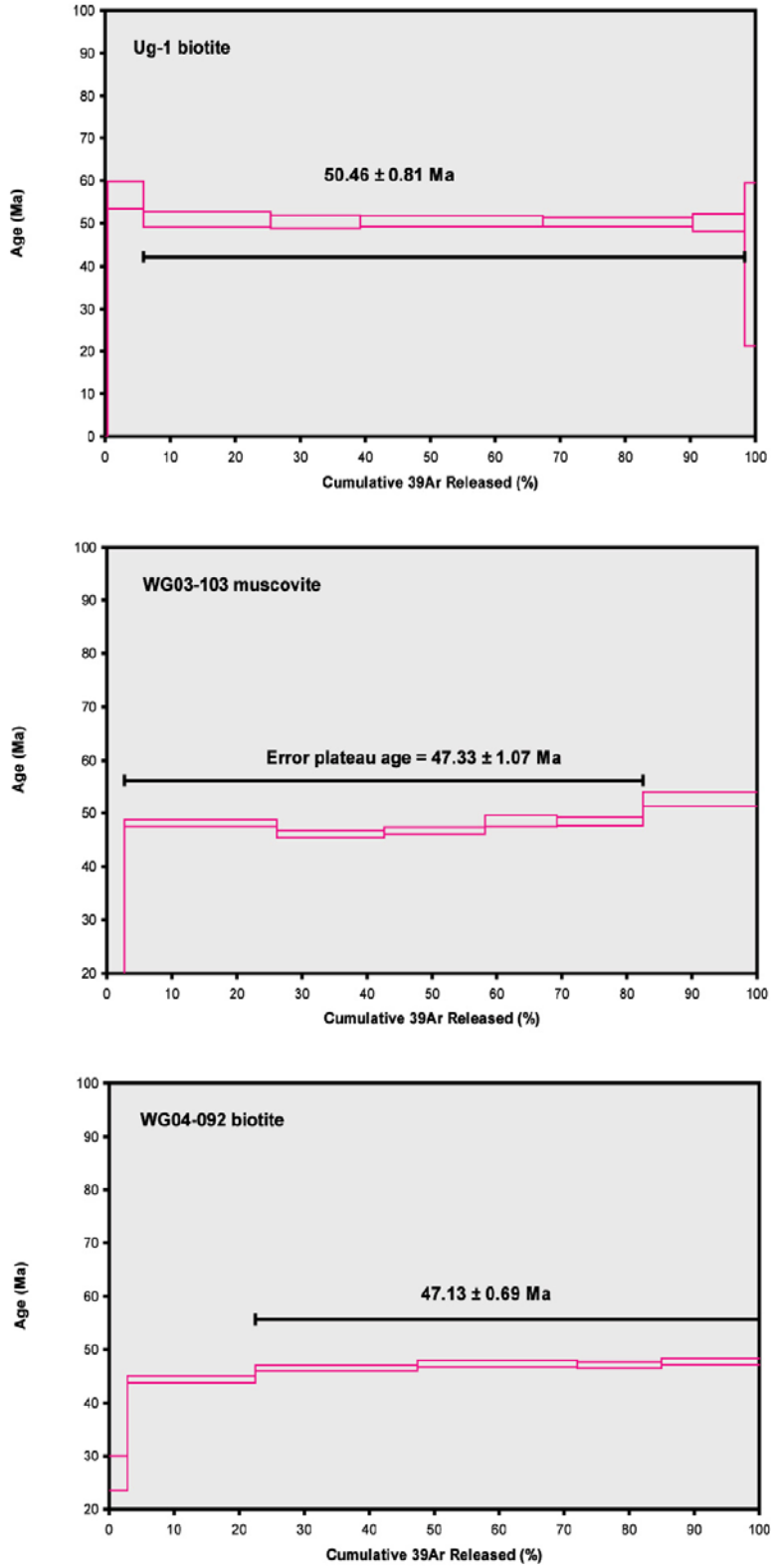


Figure 6-3. Continued.

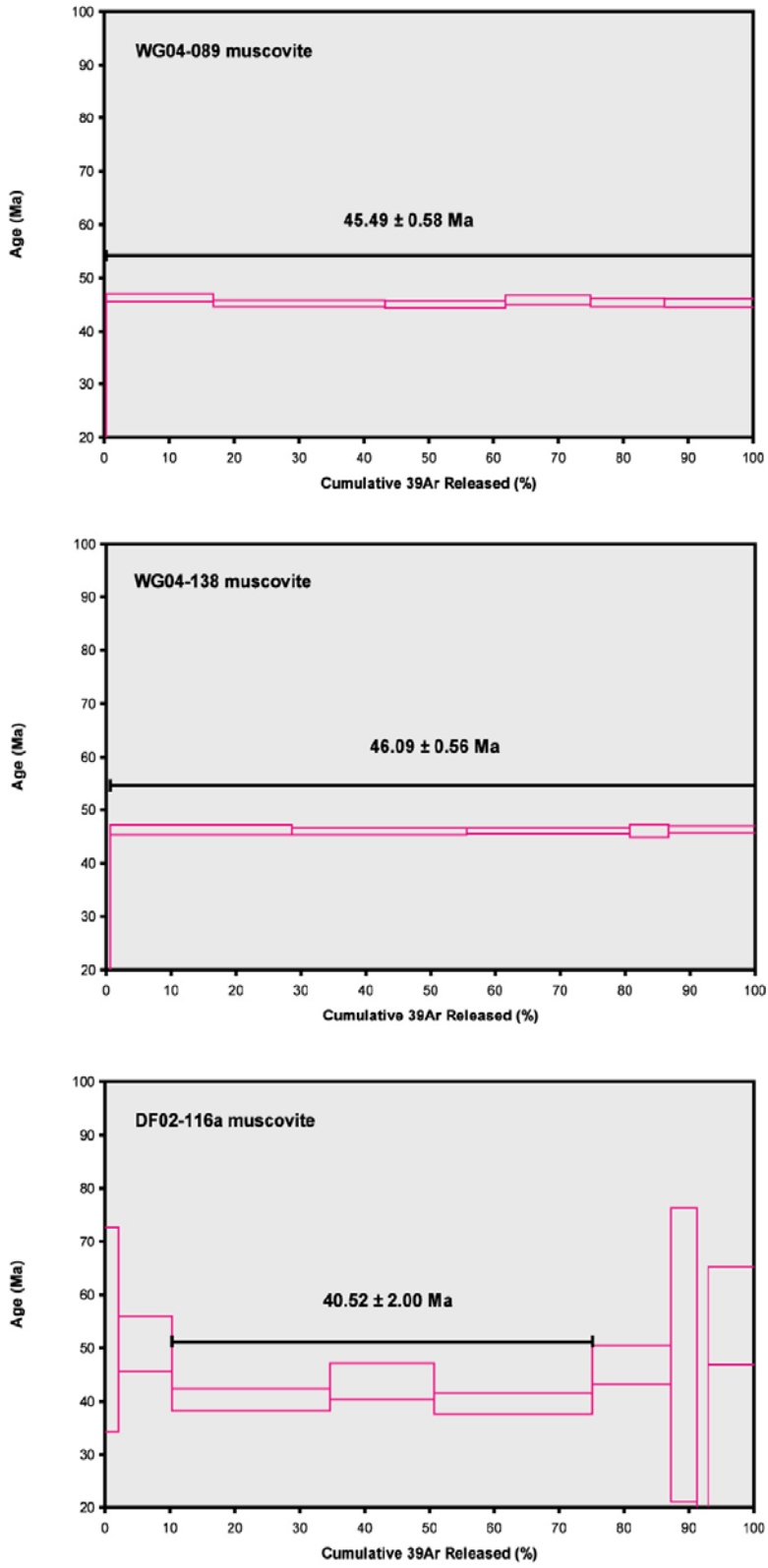


Figure 6-3. Continued.

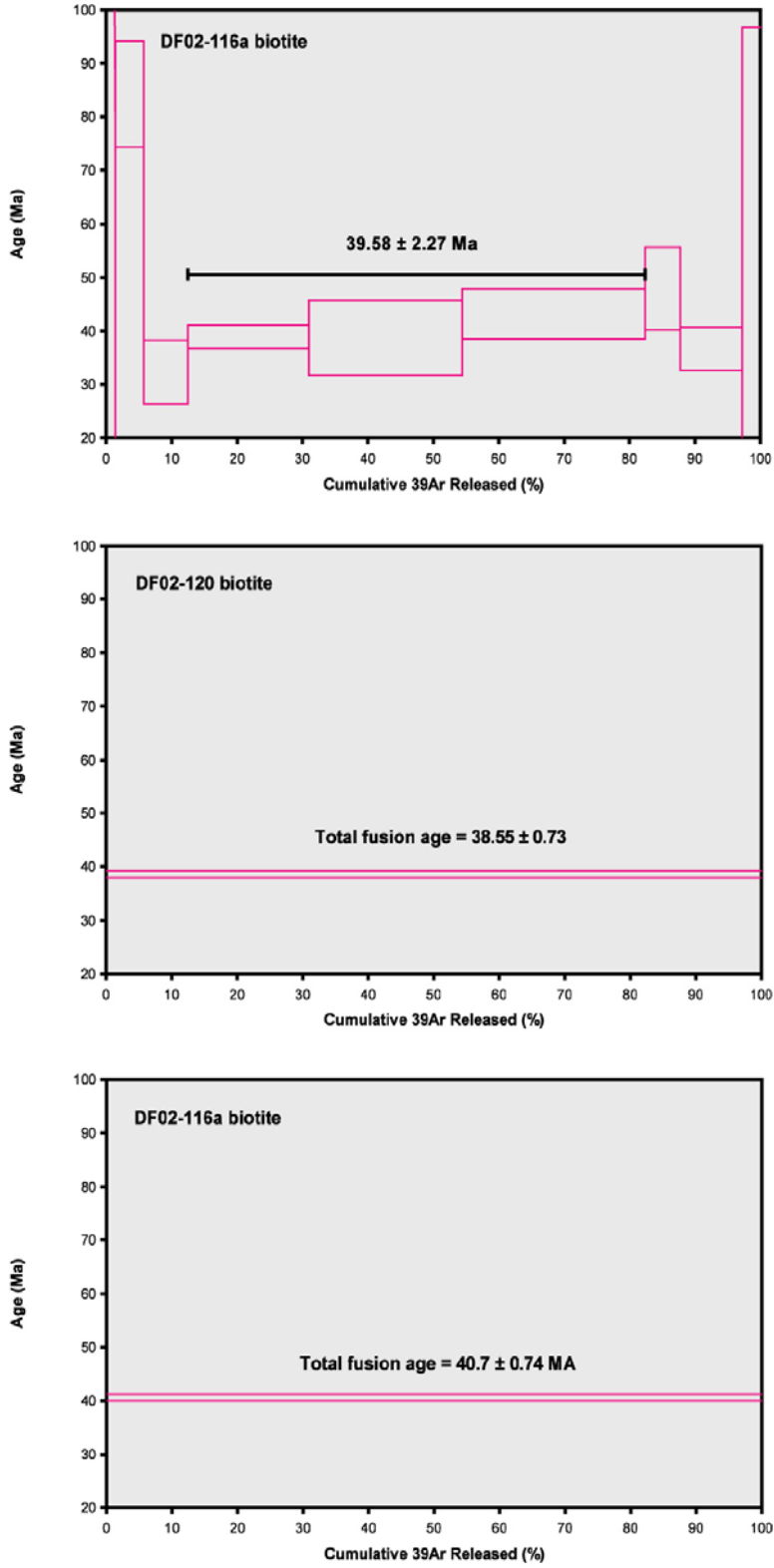


Figure 6-3. Continued.

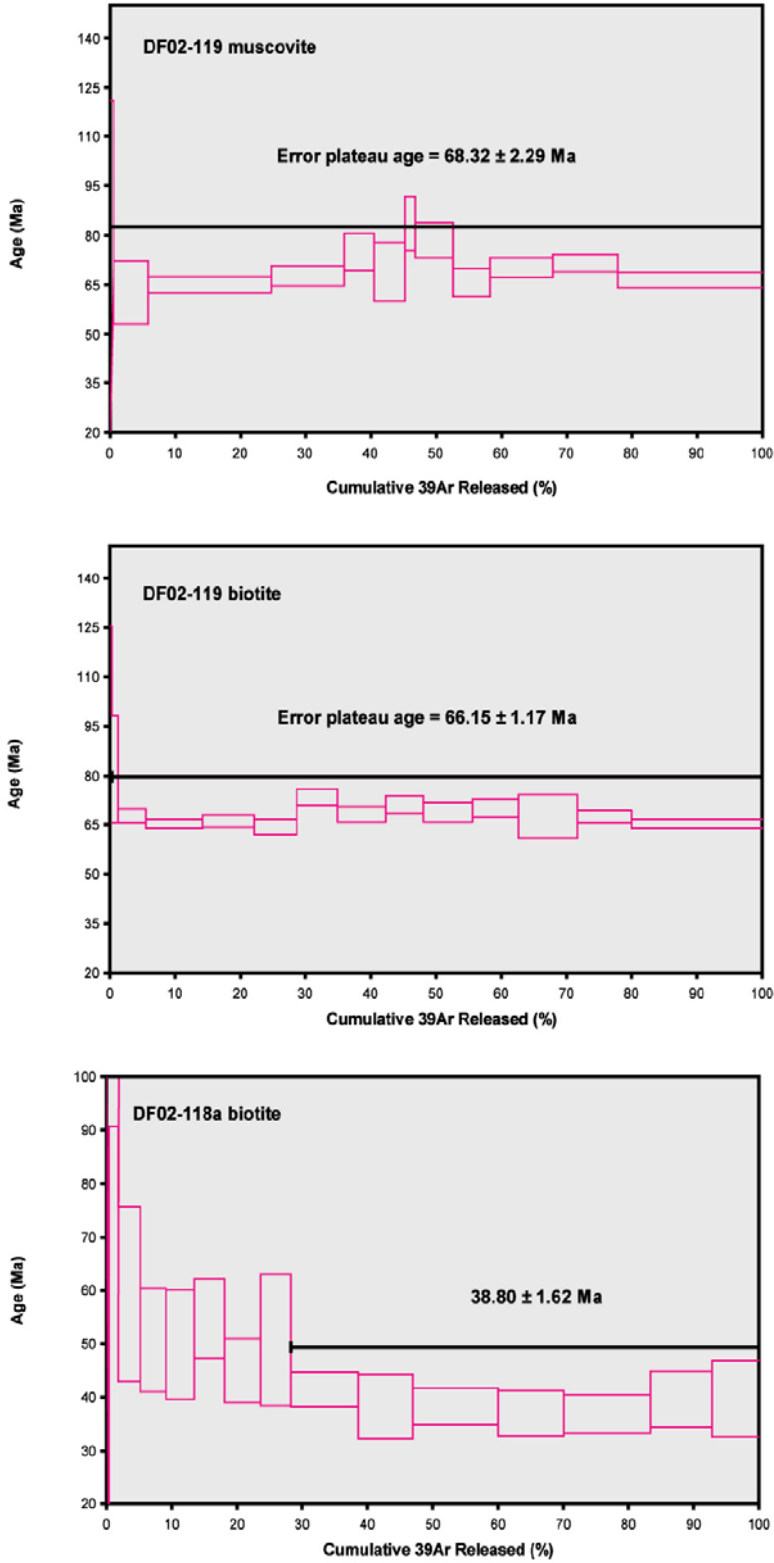


Figure 6-3. Continued.

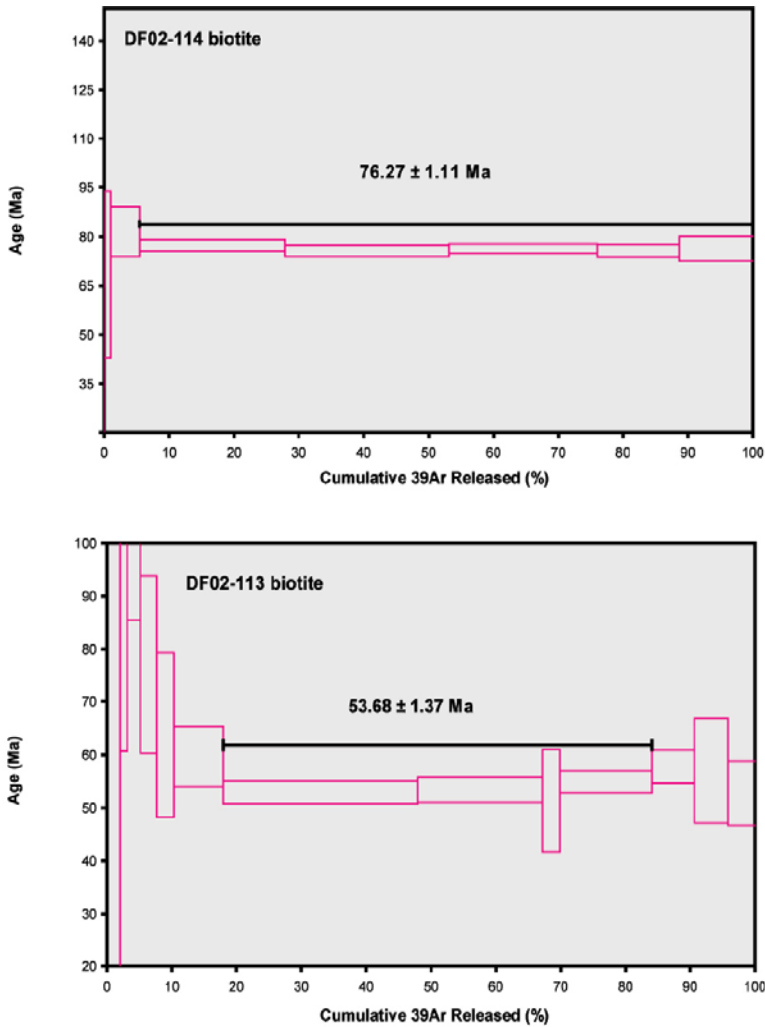


Figure 6-3. Continued.

temperatures from ~200-250°C (lower temperature closure) to ~350°C (high temperature closure); the variation in Ar closure temperature for K-feldspar arise from the presence of multiple sized Ar diffusion domains within its crystalline structure (e.g., Lovera et al., 1989; Foster et. al., 1990).

Because of the differences in the Ar closure temperature between K-bearing minerals cooling histories can be derived from single rock samples containing more than one of these minerals. Note, however, that Ar closure temperature for any given K-bearing mineral is a function of lithostatic pressure, Ar diffusion domain size, and

especially cooling rate (dT/dt) (Lister and Baldwin, 1996). Therefore, these factors must be taken into account when estimating Ar closure temperatures and using cooling ages obtained from K-Ar or $^{40}\text{Ar}/^{39}\text{Ar}$ thermochronology to constrain the cooling histories of exhumed rocks. In this study, the Ar closure temperatures (T_c) for biotite, muscovite, and hornblende were calculated using the following formula from Harrison and McDougall (1999):

$$T_c = (E/R) / \ln[(A R T_c^2 (D_0/r^2)) / (E(dT/dt))] \quad (6-1)$$

where E is the diffusion activation energy, R is the gas constant (1.987 cal/mol-K), A is the diffusion geometry coefficient, D_0 is the frequency factor, r^2 is the effective diffusion domain radius, and dT/dt is the estimated cooling rate. The diffusion parameters for muscovite and hornblende used in equation X were taken from Lister and Baldwin (1996). The diffusion parameters for biotite are from Harrison et al. (1985). The diffusion parameters are summarized in Table 6-3. The cooling rates for both biotite and muscovite (dT/dt) are estimated to be $\geq 100^\circ\text{C}/\text{Ma}$ because biotite and muscovite cooling ages from two two-mica granite samples in the central study area (WG04-101 and WG04-109) are essentially equal (well within analytical error, Table 3). Therefore, a cooling rate of $100^\circ\text{C}/\text{Ma}$ was used in the biotite and muscovite closure temperature calculations here. A cooling rate of $100^\circ\text{C}/\text{Ma}$ was also applied to the hornblende closure temperature calculation. For biotite $T_c = 343 \pm 20^\circ\text{C}$, for muscovite $T_c = 390 \pm 20^\circ\text{C}$, and for hornblende $T_c = 545 \pm 20^\circ\text{C}$. The $\pm 20^\circ\text{C}$ error was applied to these calculations to estimate uncertainties in the diffusion parameters used and in Ar closure temperatures at pressures of 0-5 kbar (see Fig. 2a, p. 88, Lister and Baldwin, 1996). The closure temperature of K-feldspar was not calculated here and is taken to be $\sim 200\text{-}250^\circ\text{C}$ for

lower temperature closure and $\sim 350^\circ\text{C}$ for high temperature Ar closure. Below the results of the $^{40}\text{Ar}/^{39}\text{Ar}$ thermochronology from this study are summarized by mineral type. When a cooling age is reported here for a given mineral the age corresponds to the Ar closure temperatures calculated or estimated here.

Biotite

Laser step-heating experiments and data reduction from eleven biotite separates across the lower plate $^{40}\text{Ar}/^{39}\text{Ar}$ transect resulted in mostly well-defined, flat-shaped weighted age plateaus (Figure 6-3).¹ In every experiment, incremental heating steps were highly radiogenic (i.e., very low $^{36}\text{Ar}/^{40}\text{Ar}$ ratios). In most cases the highly radiogenic steps clustered low on the inverse isochrons, but within error of atmospheric Ar ($^{36}\text{Ar}/^{40}\text{Ar}_i = 3.38 \times 10^{-3}$). Therefore, regression of these heating steps produced unrealistic regressions on inverse isochron diagrams, hence poorly defining the initial values of $^{36}\text{Ar}/^{40}\text{Ar}$ in the biotites. Nonetheless, in all but one of the analyses the inverse isochron ages are within error of the weighted plateau ages (Table X). This is because most incremental heating steps used in the age calculations yielded $^{36}\text{Ar}/^{40}\text{Ar}_i$ ratios within error or very close to atmospheric $^{36}\text{Ar}/^{40}\text{Ar}_i$. However, the weighted plateau ages calculated from the heating experiments are considered the most reliable and preferred over inverse isochron ages.

Apparent biotite weighted plateau ages define a lateral age gradient across the ACC lower plate, where biotite cooling ages young in a ESE direction along the $^{40}\text{Ar}/^{39}\text{Ar}$ transect (Table 2, Fig. 3). In the westernmost transect biotite from the SLS yielded

¹ The definition or criterion used to define a $^{40}\text{Ar}/^{39}\text{Ar}$ age “plateau” is not uniquely defined in the literature (e.g., see McDougall and Harrison, 1999). However, in this study a reliable age plateau is considered to be any age plateau consisting of ≥ 50 total percent ^{39}Ar released from three or more contiguous heating steps; the contiguous steps must be within 2σ error as well.

weighted plateau ages ranging from 79-64 Ma. Biotite from sample SL-38 (2311 m), a granodiorite sampled from the SLS, yielded a flat age plateau over 78 percent of the total ^{39}Ar gas released corresponding to a cooling age of 79.0 ± 1.1 Ma (MSWD = 2.02). The higher MSWD for this age calculation is due to the presence of a small amount of excess Ar in the first and last few heating steps of the experiment. However, the plateau age is considered robust with these anomalous steps omitted. Notably, the biotite cooling age from SL-38 is concordant with a K-Ar biotite cooling age of 78.7 ± 1.6 Ma from E1048, a sample collected from the same outcrop by Wallace et al. (1992, see Table 1). Biotite from WG04-114, another granodiorite sampled from the SLS near the eastern shore of Storm Lake (2503 m) gave a plateau age of 74.0 ± 0.9 Ma (94% total ^{39}Ar gas, MSWD = 0.69). In addition, biotite from sample WG04-052, a quartz diorite from the SLS, yielded a substantially younger weighted plateau age of 64.1 ± 1 Ma (88 % ^{39}Ar gas, MSWD = 1.43). This sample was collected from a ridge top (2754 m) just east of and overlooking the Fourmile Lakes Basin along the western part of the transect (Appendix D).

Biotite cooling ages abruptly young east and south of the SLS. Biotite from WG04-112, a micaceous quartzite gneiss sampled south of the SLS in the upper Twin Lakes Creek drainage yielded a flat age plateau over 100 percent ^{39}Ar gas release and a cooling age of 52.8 ± 0.7 Ma (MSWD = 0.63). East of Lake of the Isle, in the center of the transect, biotite from two samples yield weighted plateau ages near 50 Ma. Biotite from a highly deformed hornblende-biotite quartz diorite sill (Ug-1) gave a plateau age of 50.5 ± 0.8 Ma over 92 percent total ^{39}Ar gas released (MSWD = 0.10). Biotite from an undeformed coarse-grained two-mica granite (WG04-101) sampled along the continental divide (3073 m) yielded an age plateau showing slight Ar loss over the first two heating

steps. However, with these steps excluded a cooling age of 49.2 ± 0.9 Ma was calculated over the remaining 93 percent of the total ^{39}Ar gas released (MSWD = 1.25). An aphanitic porphyritic dacite dike sampled near the Lake of the Isle yielded a slightly younger biotite plateau age of 48.5 ± 0.6 over 94 percent of its ^{39}Ar gas (MSWD = 0.99). This dacite dike crosscuts the foliated quartz diorite sill and highly deformed metasedimentary strata in central LISZ. In addition, the dacite dike and others like it crosscut an undated medium-grained two-mica granite pluton south of the Lake of the Isle (Appendix D).

Two samples of undeformed coarse-grained two-mica granite (similar to WG04-101) collected south of the central transect on the southeastern flank of Mt. Evans yielded biotite cooling ages of ~ 48 Ma. WG04-109 (2878 m) gave a cooling age of 47.6 ± 0.6 Ma over 100 percent of its ^{39}Ar gas release (MSWD = 1.6). Biotite from ME-6 sampled nearby but down slope (2732 m) of WG04-109 yielded a flat age plateau over 95 percent the total ^{39}Ar gas released and a similar cooling age of 48.6 ± 1.0 Ma. Wallace et al. (1992) reports a K-Ar biotite cooling age of 48.5 ± 1 for two-mica granite sampled from the same outcrop as WG04-109.

Eastward along the transect an undeformed biotite granodiorite (WG04-092) was sampled from a steep cliff just below the continental divide (2896 m) on the eastern side of Tenmile Lakes Basin. Biotite from this sample yielded a plateau indicative of some mild Ar loss over the first 2 steps. However, a cooling age of 47.1 ± 0.7 (MSWD = 3.01) was calculated from the remaining 78 percent ^{39}Ar gas of the experiment defining a flat plateau.

Step heating experiments carried out on biotite from the greenschist facies two-mica granite mylonite (DF02-116a) from upper Clear Creek yielded a U-shaped age plateau indicating the presence of some excess Ar. However, three contiguous steps are within two sigma error and yielded a weighted plateau age of 39.6 ± 2.3 Ma over 70 percent of the total ^{39}Ar gas release (MSWD = 1.36). A total fusion age of 41.7 ± 3.2 Ma was calculated from the same analysis. The larger error associated with the plateau age for DF02-116a is due to low Ar yields from the incremental heating steps (0.002-0.4 V ^{40}Ar). Note a separate total fusion analysis of a single biotite grain from DF02-116a yielded a cooling age of 40.7 ± 0.7 Ma, within error of the weighted plateau and total fusion ages from the first analysis. These data indicate that DF02-116a cooled below the biotite closure temperature by about 40 Ma. No step-heating experiments conducted on DF02-120, the greenschist facies biotite granite mylonite from Mill Creek. However, a total fusion analysis of a single biotite grain from this sample yielded a cooling age of 38.6 ± 0.7 Ma, slightly younger than the biotite total fusion age from DF02-116a.

Muscovite

Muscovite separates from nine different rock samples collected from the ACC lower plate underwent in-vacuo laser step-heating $^{40}\text{Ar}/^{39}\text{Ar}$ analyses. Note five of these muscovite analyses are paired with biotite analyses from the same samples (Table 2). As in the biotites, the analyses of muscovite resulted in largely well-defined, flat-shaped age spectra with highly radiogenic incremental heating steps. Thus, inverse isochrons from the muscovite Ar data are also characterized by clustered data points near atmospheric Ar, poor $^{36}\text{Ar}/^{40}\text{Ar}_i$ regressions and inadequate $^{36}\text{Ar}/^{40}\text{Ar}_i$ estimations. Therefore, the weighed plateau ages for muscovites are considered most reliable and preferred over inverse isochron ages.

Apparent muscovite plateau ages generally young in an ESE direction across the ACC lower plate, similar to the lateral age pattern revealed from biotite cooling ages. In the western transect muscovite from WG04-112 gave a plateau age of 56.9 ± 0.7 over 81 percent of the total ^{39}Ar gas released (MSWD = 0.32). Muscovite of sample WG04-101 from the central transect yielded a flat age plateau over 78 percent of the total ^{39}Ar gas released and a cooling age of 49.6 ± 0.6 Ma (MSWD = 0.34). In addition, muscovite from WG04-100 (2927 m), a pegmatitic dike sampled nearby WG04-101 yielded an indistinguishable plateau age of 50.4 ± 0.8 Ma (95 % ^{39}Ar gas, MSWD = 2.63).

South of the central transect, muscovite from samples WG04-109 and ME-6 gave plateau ages ranging from ~ 48 -51 Ma. WG04-109 yielded a well-constrained muscovite plateau age of 48.0 ± 0.64 (87% total ^{39}Ar gas, MSWD = 1.75). However, muscovite from ME-6 collected less than 1 km to the southeast of the WG04-109 sample locality gave a slightly older weighted plateau age of 51.5 ± 1.2 Ma over 79 % of the total ^{39}Ar gas released (MSWD = 0.31). Note the age plateau for muscovite from ME-6 is U-shaped indicating the presence of some excess Ar in the first and last few heating steps of the experiment. However, the plateau age quoted here is reliable when the six heating steps with anomalous Ar are excluded. An inverse isochron from the analyses of the ME-6 muscovite shows that the five remaining contiguous heating steps used in the age calculation lie on a well-defined regression within error of atmospheric $^{36}\text{Ar}/^{40}\text{Ar}_i$ (Fig X).

Muscovite from WG04-103 (2524 m), a muscovite-bearing mylonitic quartzite, gave a weighted plateau age of 48.1 ± 0.6 Ma over 80% ^{39}Ar gas release (MSWD = 0.70). This sample was collected from a large mylonitic quartzite outcrop along the

eastern side of the Sullivan Creek drainage, 2 km south of the ME-6 sample locality (Fig X). O'Neill et al. (2004) report a slightly younger muscovite plateau age of 47.2 ± 0.3 Ma (quoted as 2σ error here) from a sample (ME-1) collected from the same locality (85 % ^{39}Ar gas release, no MSWD reported). The slight difference in these cooling ages can be explained by a small amount of excess Ar in the WG04-103 muscovite as indicated by the inverse isochron, where three heating steps used in the age calculation fall below atmospheric $^{36}\text{Ar}/^{40}\text{Ar}_i$ (i.e., have slight excess ^{40}Ar). However, because the data points are clustered on the inverse isochron diagram the excess Ar cannot be accurately quantified and subsequently corrected for.

A thin (< 0.5 m) garnet-bearing leucogranite vein was sampled from the biotite granodiorite in the upper Tenmile Creek drainage along the eastern transect. The vein trends NE, roughly parallel to the nearby contact between the biotite granodiorite and porphyritic two-mica granite (Appendix D). In some places the leucogranite vein strikes parallel to a 1-2 m thick foliated zone in the biotite granodiorite. However, the vein can also be seen crosscutting this foliation; therefore it post-dates emplacement of the biotite granodiorite. Analyses of muscovite from sample WG04-089 (2646 m) gave a very flat age plateau corresponding to cooling age of 45.5 ± 0.6 Ma over 100 percent of the total ^{39}Ar gas released (MSWD = 1.43). Notably, this cooling age apparently ~ 1.6 m.y. younger than the biotite cooling age obtained from WG04-092 located 1 km to the north and $\sim 4-6$ m.y. younger than muscovite cooling ages obtained from the porphyritic two-mica granite just ~ 2.5 km to the west.

WG04-138 was collected from a mylonitic muscovite-bearing quartzite unit near the summit of Short Peak (3098 m) on the continental divide between the Tenmile Creek

and Mill Creek drainages. The mylonitic quartzite that outcrops at Short Peak is essentially identical to the mylonitic quartzite exposed in the Sullivan Creek drainage (i.e., WG04-103). Muscovite from WG04-138 yielded a cooling age of 46.1 ± 0.6 Ma over five contiguous heating steps and 99 percent of the total ^{39}Ar gas released (MSWD = 0.19).

As in the biotites, muscovite from the easternmost transect gave the youngest cooling ages. Muscovite from DF02-116a, the Clear Creek two-mica granite mylonite, yielded a slightly U-shaped age plateau indicating some excess Ar in the sample. However, three contiguous heating steps from a flat part of the U-trough lie within 2σ error and were used to calculate a weighted plateau age of 40.5 ± 2.0 Ma (65% ^{39}Ar gas, MSWD = 2.21). The inverse isochron diagram plotted from these data indicates the three heating steps used in the age calculation are within error of atmospheric $^{36}\text{Ar}/^{40}\text{Ar}_i$, therefore excluding the excess ^{40}Ar (Fig X). The cooling age of DF02-116a indicates that the Clear Creek two-mica granite mylonite cooled below the muscovite closure by about 40 Ma.

Hornblende

Hornblende separates from two samples were analyzed by furnace step-heating to provide higher temperature age constraints for parts of the ACC lower plate. In particular, hornblende from SL-38 was analyzed to better constrain the cooling history for the SLS granodiorite in the westernmost transect. In addition, hornblende from the sample Ug-1, the deformed quartz diorite sill, was analyzed to provide higher temperature age constraints in the central transect. A hornblende cooling age from this sill could be used to further constrain the cooling history of the LISZ and to assess the

extent of heating from mylonitization and emplacement of younger granitoids near this part of the lower plate.

Unlike biotite and muscovite, step-heating experiments performed on these two hornblende separates resulted discordant and saddle-shaped age spectra. The age spectrum for the SL-38 hornblende is highly discordant, where the first four heating steps of the experiment alternate between ~ 110 and ~ 90 Ma then ages steadily climb to ~ 183 Ma at the last step. This type of step-heating pattern in hornblendes is attributed abundant excess Ar in the sample (e.g., Richards and McDougall, 1990). K/Ca ratios from the sample anomalously high (0.8-1.1) over the first two heating steps of the experiment (800 and 900°C) suggesting the SL-38 hornblende contains K-bearing mineral inclusions. Such inclusions could account for the excess Ar or “inherited” Ar (Kelley, 2002) in the first two heating steps of the experiment. However, K-bearing mineral inclusions can not account for the apparent excess Ar in the remaining heating steps because all give very low K/Ca ratios (<0.1).

Despite the obvious presence of excess Ar in the SL-38 hornblende some useful information can be extracted from the results of this experiment. The SL-38 hornblende yielded a total fusion age of 108.8 ± 1.7 Ma, about 30 Ma older than the biotite cooling age from the same sample. Wallace et al. (1992) report a similar spread between hornblende and biotite K-Ar cooling ages for the SLS granodiorite sampled from the same locality (~ 37 Ma difference). The apparent difference in these cooling ages imply slow cooling of SLS granodiorite, on the order of $< 10^\circ\text{C}/\text{Ma}$. However, removal of the now documented excess Ar in SLS hornblende would result in a more realistic hornblende cooling age and a more rapid cooling rate. Regression of four heating steps

on an inverse isochron diagram can roughly quantify some of the excess Ar in the SL-38 hornblende ($^{36}\text{Ar}/^{40}\text{Ar}_i$ of 1165 ± 140 , Fig X). The inverse isochron age calculated from this regression is 80.5 ± 7 Ma. This cooling age is within error of the biotite weighted plateau age of SL-38 suggesting rapid cooling ($\sim 200^\circ\text{C}/\text{Ma}$) of the SLS granodiorite at ~ 79 Ma rather than slow cooling over ≥ 30 Ma.

The Ug-1 hornblende yielded a strongly saddle-shaped age spectrum where the first and last few heating steps of the experiment gave anomalously old cooling ages (~ 330 - 460 Ma). Ages from the steps between these ranged from ~ 180 - 70 Ma. This hornblende age spectrum is indicative of abundant excess Ar as well. However, unlike hornblende from SL-38, all heating steps from this experiment yielded low K/Ca ratios (< 0.02). Thus, the apparent excess Ar in the Ug-1 hornblende is not likely derived from K-bearing mineral inclusions. One possible source for excess Ar in this sample is Ar uptake during a reheating event. Harrison and McDougall (1980) report age spectra with anomalously high ages in early heating steps from amphiboles sampled within the contact aureole adjacent of a Cretaceous intrusion. They attribute the anomalously old ages in parts of the age spectra to excess Ar incorporated into grain margins during reheating by the neighboring intrusion. The Ug-1 sample was collected < 100 m from the contact with a younger two-mica granite intrusion (Fig X). Thus, reheating by the two-mica granite intrusion may have allowed excess Ar to be incorporated into the Ug-1 hornblende. The fact that biotite from Ug-1 reports an Eocene cooling age (50.5 ± 0.8 Ma) suggests temperatures were at least high enough to practically reset Ar in biotite.

Unfortunately, the excess Ar in the Ug-1 hornblende could not be quantified and corrected for using an inverse isochron diagram. Most heating steps reported $^{36}\text{Ar}/^{40}\text{Ar}$

values ≤ 0 , lying along the x-axis of the diagram. The low $^{36}\text{Ar}/^{40}\text{Ar}_i$ ratios in the Ug-1 hornblende are the result of very high radiogenic (high ^{40}Ar) and low ^{36}Ar yields over most of the heating steps. Thus, a realistic $^{36}\text{Ar}/^{40}\text{Ar}_i$ ratio needed to correct for excess Ar could not be obtained from the data. Therefore, the total fusion age of 113.3 ± 1.4 Ma from the analysis of Ug-1 hornblende is considered geologically unsound because of abundant uncharacterized excess Ar. Note also, this total fusion age is ~ 38 Ma older than the U-Pb zircon crystallization age obtained for the same sample further exemplifying its unreliability (see U-Pb geochronology results).

K-feldspar

One K-feldspar separate from SL-38 underwent furnace step-heating and $^{40}\text{Ar}/^{36}\text{Ar}$ analysis. Cooling age constraints from the SL-38 K-feldspar were desired to be used in conjunction with the U-Pb zircon, hornblende and biotite data from the same sample to provide an in depth cooling history for the SLS granodiorite. Vacuo step-heating experiments of K-feldspars have shown K-feldspar is characterized by multiple Ar diffusion domains of different sizes, therefore having different Ar closure temperatures (e.g., see Lovera et al., 1989). The Ar closure temperature for K-feldspars typically ranges from ~ 200 - 250°C for the smaller diffusion domains to ~ 350 - 400°C in larger domains. Therefore, modeling of Ar data obtained from step-heating analyses of K-feldspars can be used to produce time-temperature curves that often span several million years (Lovera, 1992; Lovera et al., 2002). A single K-feldspar step-heating analysis and modeling can often reveal a detailed cooling history for a given rock sample in itself (e.g., Richter et al., 1991).

Furnace step-heating of the SL-38 K-feldspar produced an age spectrum characterized by anomalously old cooling ages over the first few percent ^{39}Ar released

then ages that rapidly drop to ~ 65-55 Ma for the next 30% cumulative ^{39}Ar release. The cooling ages then gradually climbed to near 100 Ma with one anomalous step yielding a cooling age of ~ 118 Ma. Thereafter, cooling ages abruptly rise to > 300 Ma over the last few percent cumulative ^{39}Ar released (Fig. 3). The gradual increase in apparent cooling ages over much of cumulative ^{39}Ar released is common in many step-heating experiments of K-feldspars. Such an age gradient reflects release of Ar from diffusion domains with different Ar closure temperatures with progressive heating of the sample (Lovera et al., 1989; Harrison et al., 1991). However, the anomalously old cooling ages of the first and last few percent cumulative ^{39}Ar released from the SL-38 K-feldspar are unmistakably due to the presence of excess Ar (McDougall and Harrison, 1999). Harrison and McDougall (1981) attribute such “saddle-shaped” K-feldspar age spectra to excess Ar trapped in cation sites and anion vacancies in the near-surface crystal lattice of K-feldspar at temperature < 350°C (see Foster et al., 1990 for a review).

An inverse isochron diagram from the step-heating experiment of SL-38 K-feldspar shows that virtually all steps released have abundant excess Ar (i.e., all but two heats yielded $^{36}\text{Ar}/^{40}\text{Ar}_i$ ratios of < 3.38×10^{-3}). In fact, the last 50% cumulative ^{39}Ar release from the experiment yielded unreasonable ages, older than the U-Pb zircon crystallization age for WG04-114, another SLS granodiorite sample. Therefore, the age spectrum for the SL-38 K-feldspar is largely unreliable and unsuitable for detailed K-feldspar modeling. Thus, a detailed cooling curve is obtained for the SL-38 K-feldspar. However, some useful time-temperature constraints can be deduced from the lower temperature portion of this step-heating experiment.

The heating steps over 2-20 percent cumulative ^{39}Ar released during the step heating experiment define “saw tooth” pattern where older cooling ages alternate with slightly younger cooling ages. These alternating steps correspond to the isothermal heating steps employed in the step-heating schedule of the SL-38 K-feldspar (550-750°C). Heating steps that yield slightly younger cooling ages are from the second fraction of Ar gas analyzed at each temperature, and vice versa. Harrison et al. (1994) demonstrated that the excess ^{40}Ar in the older steps of this saw tooth pattern is strongly correlated with Cl probably derived from fluid inclusions in K-feldspars (i.e., a strong linear relationship between $^{40}\text{Ar}/\text{K}$ and Cl/K ratios). This excess ^{40}Ar is often released from fluid inclusions during low temperature steps of the experiment creating this common discordant saw tooth pattern. Therefore, by discarding the first of each isothermal heating step the Cl-correlated excess ^{40}Ar is avoided and useful time-temperature constraints can be deduced from the low temperature (< 800°C) portions of K-feldspar step-heating experiments. Following this strategy, four Cl-corrected excess Ar steps were removed from eight steps in the low temperature portion of the age spectra. The four remaining steps were used to calculate an error plateau age of 56.9 ± 1.61 Ma. Note the four steps used in this age calculation lie close to atmospheric Ar $^{36}\text{Ar}/^{40}\text{Ar}_i$ on the inverse isochron diagram (Fig X); effectively avoiding the excess Ar apparent in other steps. These results suggest that SL-38 cooled below $\sim 200\text{-}250^\circ\text{C}$ (approximate low temperature closure for K-feldspar) by about 57 Ma. This also indicates that the SLS in the westernmost transect was not reheated above $\sim 200\text{-}250^\circ\text{C}$ during the Eocene.

$^{40}\text{Ar}/^{39}\text{Ar}$ Thermochronology From Outside the Lower Plate Transect

As noted above, four samples were collected for $^{40}\text{Ar}/^{39}\text{Ar}$ thermochronology from areas outside the transect across the northeastern Anaconda-Pintlar Range (Table 2).

Two samples were collected from the LVC sequence within the ACC upper plate. DF02-113, a crystal-lithic rhyolitic tuff, was collected from the Deerlodge Valley, southeast of the eastern transect. Biotite from this sample yielded a weighted plateau age of 53.7 ± 1.4 Ma (66% ^{39}Ar gas, MSWD = 0.71). Note this biotite age is slightly older than the biotite age of 51.4 ± 0.4 Ma reported for a sample collected from the same outcrop (Isoplatov, 1997). A large, isolated granodiorite block was sampled (DF02-114) from within the LVC field, northeast of the DF02-113 sample locality. This granodiorite is a medium grained biotite-hornblende bearing granodiorite similar to the SLS and other granodiorite intrusions in the ACC lower plate. Biotite from DF02-114 yielded a weighted plateau age of 76.3 ± 1.1 Ma over 95% ^{39}Ar gas release (MSWD = 0.57). Notably, this biotite cooling age is similar to that of WG04-114 (74.0 ± 0.9 Ma), the SLS sample from the westernmost transect.

The two remaining samples were collected from ACC lower plate exposures directly north of the easternmost transect in the Flint Creek Range. DF02-118a was collected from an outcrop of mylonitic biotite granite along Lost Creek, in the southernmost Flint Creek Range. Biotite from this sample gave a weighted plateau age of 38.8 ± 1.62 (72% ^{39}Ar gas, MSWD = 0.82). This biotite cooling age is within analytical error of the biotite cooling age from DF02-120 (total fusion age = 38.5 ± 0.7 Ma), the mylonitic biotite granite from Mill Creek located directly to the south. DF02-119a was collected from two-mica granite of the Mt. Powell Batholith (granodiorite) on the eastern flank of the Flint Creek Range. Biotite and muscovite from this sample yielded slightly discordant plateaus. However, useful age information can be deduced from the results. The muscovite plateau of DF02-119a is characterized by four

anomalous steps near the middle of the experiment (Fig. 3). With these steps removed an error plateau age of 68.1 ± 2.77 Ma was calculated from the remaining steps (55% ^{39}Ar gas, MSWD = 4.33). The biotite plateau of DF02-119a is a slightly convex-up shaped, where the first and last few steps of the experiments resulted in slightly younger ages. By excluding these steps, a weighted plateau age of 68.8 ± 1.40 Ma was calculated over 45% of the ^{39}Ar gas release, corresponding to six contiguous steps from the middle of the experiment (Fig. 3). Note these mica cooling ages are slightly older than those reported for the Mt. Powell Batholith (~ 61.5 - 59.7 Ma) by Martin et al. (1989).

CHAPTER 7 DISCUSSION

Origin of the Lake of the Isle Shear Zone

Field observations (Chapter 3) indicate that at least two phases of high grade metamorphism have affected the Lake of the Isle shear zone (LISZ): (1) an early higher pressure event shown by fresh and relict kyanite in the Lower Belt Greyson Formation-equivalent (Kalakay et al., 2003) and pelitic upper Ravalli Group-equivalent metasedimentary strata and (2) a later lower pressure and high temperature upper-amphibolite facies event that created sillimanite-bearing assemblages which overprint the earlier higher pressure assemblage in some areas. Localized anatexis (in pelitic strata) and significant ductile attenuation of Belt and Middle Cambrian-equivalent apparently accompanied the later upper-amphibolite facies metamorphic event (Chapter 3). Here, new age constraints obtained from U-Pb geochronology are discussed for upper-amphibolite facies metamorphism and the associated localized anatexis and ductile deformation in the LISZ. In addition, pressure-temperature constraints obtained by conventional thermobarometry for the upper-amphibolite facies metamorphism are discussed in context of the PT history of the LISZ. Together, these constraints, combined with field observation, are used to provide a kinematic history for the LISZ. The age and pressure-temperature constraints obtained for upper-amphibolite facies metamorphism in the LISZ are also used in a later section as a proxy for estimating the maximum amount of exhumation in the ACC facilitated by extension during the Eocene (see below).

Age Constraints

The most direct age constraint for upper-amphibolite facies metamorphism, local anatexis, and ductile deformation of meta-Belt and meta-Cambrian metasedimentary strata in the LISZ would be a U-Pb zircon crystallization age from granitic leucosome sample WG05-02. However, all the zircons analyzed from this sample are interpreted to be Proterozoic and Archean zircons inherited from the protolith (meta-Greyson) that have undergone variable lead loss (Chapter 4). Despite the lack of relevant age information obtained from the leucosome zircons the U-Pb zircon ages obtained from the undeformed Storm Lake Stock (SLS) granodiorite and the deformed quartz diorite sill, combined with some important field observations, provide substantial age constraints for upper amphibolite facies metamorphism and the related events in the LISZ. Field relationships are summarized below, followed by a discussion of the U-Pb ages obtained from these intrusions and implications for the age of the upper-amphibolite facies metamorphism, local anatexis, and ductile deformation in the LISZ.

In the central and eastern parts of the LISZ, the deformed quartz diorite sill exhibits a solid-state foliation concordant with the transposed metamorphic foliation in the adjacent metasedimentary strata (Chapter 3, also see Appendix B and D). This relationship indicates the emplacement of the quartz diorite sill either (1) predated high grade metamorphism and ductile deformation in the LISZ or (2) was synchronous with these events. In the western LISZ, the undeformed SLS granodiorite clearly cross-cuts deformed upper-amphibolite-grade meta-Belt and meta-Cambrian metasedimentary strata. In addition, the undeformed quartz diorite of the SLS (not dated in this study) cross-cuts these deformed metasedimentary strata; the contact between these two intrusions shows the quartz diorite phase to be earliest (Appendix B and F). Granitic

leucosome is commonly observed in the meta-Greyson pelitic paragneiss and often found in boudin neck pressure shadows between the boudins. The longer axes of the boudins are oriented parallel to the metamorphic foliation in the metasedimentary country rock and deformed quartz diorite sill indicating local anatexis in the meta-Greyson was synchronous with ductile deformation in the LISZ (Chapter 3). Together, these field observations indicate the following relative order of events in the LISZ: (1) emplacement of the quartz diorite sill before or synchronous with (2) upper-amphibolite facies metamorphism, local anatexis in the meta-Greyson pelitic paragneiss, and ductile deformation of metasedimentary strata followed by (3) emplacement of the SLS quartz diorite and then (4) the emplacement of the SLS granodiorite.

$^{206}\text{Pb} / ^{238}\text{U}$ weighted mean zircon ages obtained from the deformed quartz diorite sill and SLS granodiorite phase are 75.0 ± 0.8 and 74.6 ± 0.8 , respectively (2σ errors, Chapter 4). The concordance of these crystallization ages indicate the quartz diorite sill and SLS granodiorite were emplaced into the LISZ at a very similar time. Because of the cross-cutting field relationships described above, the SLS quartz diorite in the western LISZ must have been emplaced at a similar time, presumably during the short time interval between emplacement of the quartz diorite sill and the SLS granodiorite.

Because the $^{206}\text{Pb} / ^{238}\text{U}$ weighted mean zircon ages of the deformed quartz diorite sill and undeformed SLS granodiorite are within analytical error it is not likely that the emplacement of the quartz diorite sill significantly predated upper-amphibolite facies metamorphism, local anatexis, and ductile deformation in the LISZ. Instead, emplacement of the quartz diorite sill was probably synchronous with some stage of these events. The outcrop pattern of migmatites within pelitic Greyson Formation-equivalent

paragneiss adjacent to the quartz diorite sill in the central LISZ supports this interpretation (Appendix F). The migmatites only occur directly adjacent to the sill (≤ 0.5 km) which indicates the emplacement of the sill provided a thermal pulse causing localized anatexis and more significant ductile attenuation of adjacent meta-Belt and meta-Cambrian metasedimentary strata (see below). Because the quartz diorite sill exhibits a solid-state foliation that is concordant to the metamorphic foliation in the adjacent metasedimentary strata, ductile deformation must have continued for at least some time after emplacement of the sill.

Emplacement of the undeformed SLS quartz diorite, followed by the emplacement of the SLS granodiorite, must have occurred immediately after ductile deformation had ceased in the LISZ because these two intrusions cross-cut the deformed metasedimentary strata. The thermal effects of these intrusions on metasedimentary strata in the western LISZ has not yet been determined. However, a biotite cooling age of 74.0 ± 0.9 Ma from near the center of the SLS granodiorite pluton (WG04-114) show this intrusion, and at least the western LISZ, rapidly cooled to temperature less than $\sim 350^\circ\text{C}$ by about 74 Ma (Chapter 6). Upper-amphibolite facies metamorphism and synchronous ductile deformation had ceased before ~ 74 Ma, at least in the western LISZ.

In summary, the U-Pb geochronology, $^{40}\text{Ar}/^{39}\text{Ar}$ thermochronology, and field relationships summarized here show upper-amphibolite facies metamorphism, local anatexis in the meta-Greyson pelitic paragneiss, and ductile attenuation in the LISZ occurred from ~ 75 -74 Ma. More constraints may be obtained for the duration of these events by: (1) Use catholuminescence imaging (CL) to identify magmatic rims on the WG05-02 leucosome zircons from the migmatitic pelitic Greyson Formation-equivalent

paragneiss. If thin magmatic rims are present, then employ a higher resolution (<30 μm) beam (e.g., SHRIMP) to obtain U-Pb isotopic data and ages from the rims. (2) Separate and date metamorphic zircon and/or titanite from the attenuated upper-amphibolite facies metasedimentary strata in the LISZ using U-Pb geochronology (e.g., Dziggel, et al., 2005).

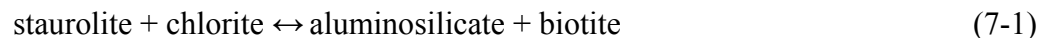
Pressure-temperature History

Relict and fresh kyanite-bearing assemblages in some parts of the LISZ indicate earlier higher pressure metamorphism prior to the lower pressure, high temperature metamorphism at ~75-74 Ma (Chapter 3). The earlier higher pressure metamorphism in the LISZ may have followed a “Barrovian-style” clockwise PT path related to tectonic loading during emplacement of the Sapphire thrust slab in the Late Cretaceous. Peak pressures associated with the early metamorphism were probably no more than ~7-8 kbar, based on a reconstructed thickness of ~20-25 km for the Sapphire thrust slab in the Late Cretaceous (Sears and Hendrix, 2004, see cross sections in their Fig. 2 and 4) and that the LISZ was probably near the base of the Sapphire thrust slab (Wallace et al., 1992). Although this may be a viable hypothesis, the age and extent of earlier higher pressure metamorphism in the LISZ is currently unknown. Therefore, only the pressure-temperature history of the LISZ during the later lower pressure and high temperature metamorphism is further discussed.

The thermobarometric data obtained from the LISZ in this study (Chapter 5), combined with field relationships and metamorphic petrology, indicate the metasedimentary strata in the LISZ underwent prograde isobaric heating during the low pressure, high temperature metamorphic event at ~75-74 Ma. Peak metamorphic conditions during this metamorphism were at the upper-amphibolite facies at ~3.2-5.3

kbar and ~750-825°C (Chapter 5). The marked increase in metamorphic grade within the Meta-Greyson pelitic metasedimentary strata towards the center of the LISZ, and the contact with the deformed quartz diorite sill, indicates the thermal peak during this metamorphic event is directly related to a heat from emplacement of the sill at ~75-74 Ma. Therefore, the mineral/textural zones and zone boundaries mapped in the Greyson Formation-equivalent pelitic strata were correlated with specific divariant fields and invariant metamorphic reactions in PT space (Table 3-1, Fig. 3-16). Combining these empirical constraints with the best pressure-temperature estimate obtained from the thermobarometry of this study (Chapter 4), a PT path can be constructed for the LISZ during the later low pressure, high temperature metamorphism.

Figure 7-1 displays a phase diagram for the KFMASH chemical system representative of pelitic rocks along with the peak pressure-temperature estimate for sample ME-231, select labeled divariant fields and univariant reactions, and the proposed isobaric PT path (Path A) for the LISZ during the low pressure, high temperature metamorphism. At distances greater than ~1 km from the deformed quartz diorite sill contact, within mineral/texture zone 1, the Meta-Greyson pelitic schist contains; primary muscovite, abundant coarse-grained biotite, garnet and K-feldspar porphyroblasts, and fine-grained sillimanite fibrolite. This assemblage corresponds to divariant field 1 (D1) in Figure 7-1, immediately up temperature of the reaction



which is responsible for the appearance of aluminosilicate with heating during prograde metamorphism (Spear, 1993); the type of aluminosilicate polymorph produced across reaction 7-1 is solely dependent on the pressure (Fig. 7-1).

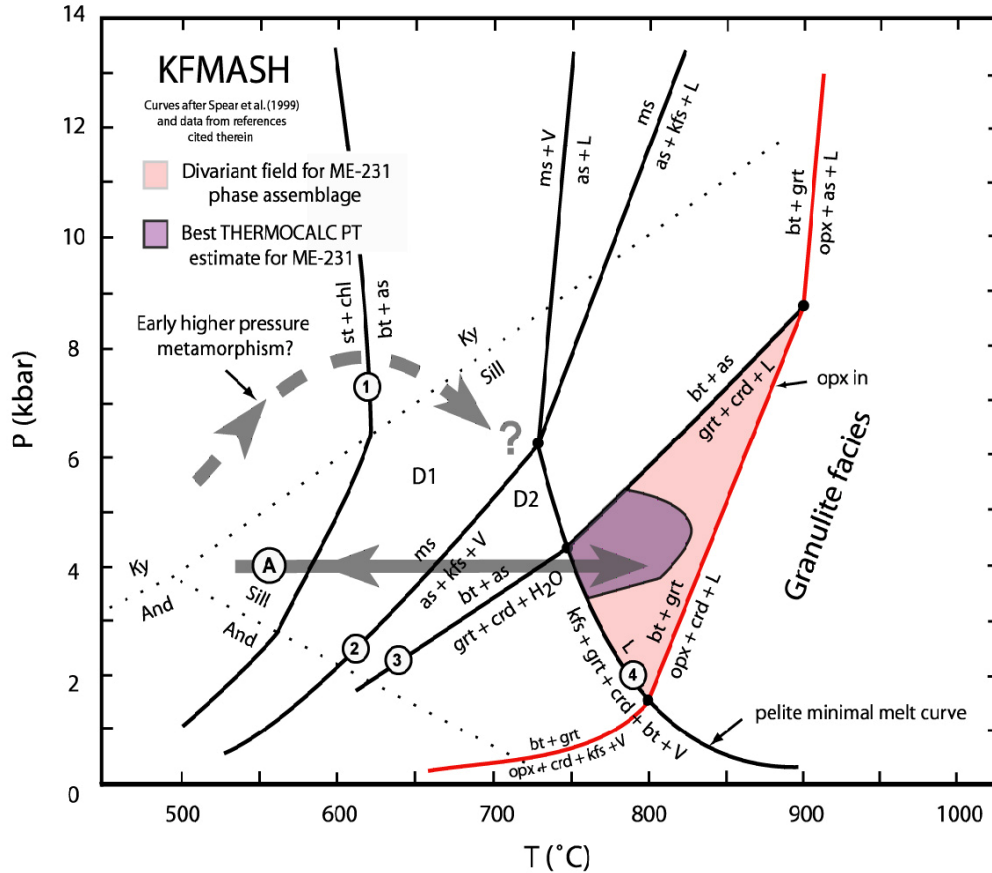


Figure 7-1. Phase diagram showing the Late Cretaceous PT history of the Lake of the Isle shear zone (LISZ). The numbered univariant reactions and divariant fields (D1 and D2) are discussed in the text. Path A represent the isobaric PT path proposed for the LISZ during lower pressure high temperature metamorphism associated with the emplacement of the quartz diorite sill. The dashed PT path corresponds to the poorly constrained earlier higher pressure metamorphic event that may have been associated with tectonic loading during emplacement of the Sapphire thrust plate (see text).

Closer to the deformed quartzdiorite sill, at distances between ~ 1 -0.5 km, the Meta-Greyson pelitic schist lie in mineral/textural zone 2 and contains; relatively coarser-grained sillimanite fibrolite mats, K-feldspar, garnet, abundant biotite and lack primary muscovite suggesting these rocks passed through the muscovite-out dehydration reaction

$$\text{muscovite} \leftrightarrow \text{aluminosilicate} + \text{K-feldspar} + \text{H}_2\text{O}_{\text{vapor}} \quad (7-2)$$

during prograde heating and fall in divariant field 2 (D2) in Figure 7-1. Still closer to the deformed quartz diorite sill contact, at distances of ≤ 0.5 km, the Meta-Greyson pelitic

schist grades to highly deformed paragneiss and corresponds to mineral/texture zone 1 with an upper-amphibolite facies assemblage comprised of; thick relatively coarser-grained sillimanite fibrolite mats, less abundant and altered biotite, large sigmoidal-shaped K-feldspar and cordierite porphyroblasts, large garnet porphyroblasts, common granite leucosome, and lack primary muscovite. Note that the granitic leucosome can be seen cross-cutting garnet porphyroblasts and within cordierite pressure shadows in thin section (Fig. 3-15). Together, these features indicate that the meta-Greyson pelitic paragneiss directly adjacent to the deformed quartz diorite sill (≤ 0.5 km), within mineral/texture zone 1, passed through the reactions



during prograde metamorphism. Note reaction 7-4, the pelite minimal melting reaction, requires the presence of a vapor phase to produce a melt phase (Spear et al., 1999). Some vapor phase would have been necessary to cause anatexis of the meta-Greyson pelitic paragneiss near the quartz diorite sill at near peak temperature conditions during metamorphism. One possible vapor source could be H_2O produced by the dehydration of biotite as reaction 7-3 was crossed immediately before crossing reaction 7-4 or 7-2, see Fig. 7-1). Passage through reaction 7-3 and 7-4 with production of granitic leucosome during anatexis is consistent with the pressure-temperature estimate of ~ 3.2 - 5.3 kbar, ~ 750 - 825°C obtained for sample ME-231, the meta-Greyson migmatitic paragneiss sample located ~ 0.4 km from the contact with the deformed quartz diorite sill.

Following the thermal peak in upper-amphibolite facies metamorphism, the Meta-Greyson pelitic schist and paragneiss most likely underwent isobaric cooling following

the prograde path in reverse. Upon cooling, and passing through reaction 7-4 in reverse, all leucosome melt present would have crystallized and any H₂O release associated with crystallization of the leucosome would have ceased on the low temperature side of reaction 7-4; at these temperatures most free H₂O would have likely been expelled to shallower depths (Spear et al., 1999). The absence of a significant quantity of vapor during further cooling would have prohibited the prograde reactions 7-2 and 7-3 from operating in reverse. Therefore, no retrograde muscovite would be produced as reaction 7-2 was crossed during cooling. This is consistent with the absence of muscovite in the Greyson Formation-equivalent pelitic migmatitic paragneiss located directly adjacent to the deformed quartz diorite sill. The presence of fine-grained sillimanite fibrolite in large cordierite porphyroblast also supports the reversal of reaction 7-3 during isobaric cooling (Table 3-1, Fig. 7-1).

Kinematic Interpretation

The new U-Pb geochronology, thermobarometry, and field observations show that low pressure, high temperature metamorphism in the LISZ occurred synchronous with emplacement the quartz diorite sill at ~75-74 Ma. The low pressure, high temperature apparently posted higher pressure kyanite-zone metamorphism event in the LISZ; the origin of the earlier metamorphism is not yet constrained. Field observations (Chapter 3) show that ductile attenuation of metasedimentary strata in the LISZ accompanied the upper-amphibolite facies metamorphism and localized anatexis. The most convincing line of evidence for the coincidence of these events is the common occurrence of granitic leucosome within pressure shadows between flattened mesoscopic boudins in the intensely deformed meta-Greyson pelitic paragneiss adjacent to the deformed quartz diorite sill (Fig. 3-9). Emplacement of the granodiorite and quartz diorite phases of the

SLS must have postdated the ductile deformation because these intrusions are undeformed and obliquely cross-cut the ductile metamorphic fabrics in the metasedimentary strata.

Strain localization and ductile attenuation of metasedimentary strata in the LISZ

Low pressure, high temperature metamorphism associated with emplacement of the quartz diorite sill into the LISZ at ~75-74 Ma resulted in a thermal anomaly that surrounded the deformed quartz diorite sill. This is shown by the marked changes in metamorphic assemblages and textures in the metamorphosed Greyson Formation perpendicular to the contact with the sill (see Table 3-1 and Fig. 3-16). The thermal anomaly surrounding the sill apparently localized ductile attenuation of Belt and Middle Cambrian-equivalent metasedimentary strata within the LISZ, as the degree of ductile strain (attenuation) increases towards the sill contact in the center of the LISZ. The thermally induced ductile strain gradient is indicated by the marked change in the geometry of mesoscopic folds and boudins towards the sill; folds are increasing isoclinal and recumbent and boudins are progressively flattened towards the sill contact and the center of the LISZ (Chapter 3). The marked change in the geometry of mesoscopic structures towards the sill and center of the LISZ (and attenuation) is the result of major fabric transposition under ductile flow which rotated, stretched, and flattened the mesoscopic structures into an orientation parallel to the metamorphic foliation or gneissic banding in the host metasedimentary strata and the contact with the quartz diorite sill (e.g., Davis and Reynolds, p. 453). Therefore, ductile attenuation of Belt and Middle Cambrian-equivalent metasedimentary strata in the LISZ was facilitated by a reduction rheology (rock strength) caused to the thermal pulse related to emplacement of the quartz diorite sill at ~75-74 Ma.

Strain classification

The transposition of structures and fabrics and attenuation of the Belt and Middle Cambrian metasedimentary strata in the LISZ was accommodated predominately by pure shear and plane (flattening) coaxial strain (e.g., Passchier et al., 1993, p. 16). The predominance of plane coaxial strain in the LISZ is indicated by the widespread occurrence of symmetric porphyroblasts shear indicators. However, documentation of asymmetric porphyroblasts showing a left lateral sense of shear indicate in some areas ductile deformation was accommodated, at least in part, by localized left lateral simple shear and noncoaxial strain (Chapter 3). These areas probably represent small-scale sinistral shear zones but the significance of these structures has not yet been determined. It is possible these smaller shear zones accommodated differential strain in the LISZ.

Structural Interpretation

In the central part of the LISZ, near the Lake of the Isle, Lower Belt Meta-Greyson schist and paragneiss are juxtaposed with the Middle Cambrian-equivalent strata separated only by the deformed quartz diorite sill. To the west, towards Storm Lake, progressively younger Belt-equivalent metasedimentary strata in the south are juxtaposed with the Middle Cambrian-equivalent metasedimentary strata to the north. However, in the western LISZ, the undeformed SLS (Storm Lake Stock) granodiorite and quartz diorite intrude the shear zone and separate these juxtaposed metasedimentary strata by a significant distance (see geologic map, Appendix D). The fact the apparent offset between Belt and Middle Cambrian metasedimentary across the LISZ progressively decreases to the west permits the shear zone to be interpreted as a fault which cuts up section towards the west. In the central LISZ, the juxtaposition of the Lower Belt Meta-Greyson with Middle Cambrian-equivalent strata indicates an enormous amount of offset.

In the west the entire metamorphosed Ravalli Group to Middle Cambrian section is apparently repeated but separated by the voluminous SLS.

The structure is complex in the eastern LISZ. Here, the LISZ consists of the Mill Creek nappe, a km-scale east-verging recumbent fold originally mapped by Emmons and Calkins (1913) and then in more detail by Heise (1983). The Mill Creek nappe folds the metamorphosed and attenuated Helena Formation through meta-Cambrian section and is cored by a thrust fault which places the Helena Formation over the metamorphosed Middle Cambrian Silver Hill Formation (Appendix F). Presently, it cannot be shown the LISZ is a thrust or normal fault structure. However, the Late Cretaceous age of the LISZ and the fact that several plutons have intruded into the structure (similar to many thrust faults elsewhere in the Sapphire thrust plate) combined with thrust fault structure in the Mill Creek drainage suggest the entire LISZ is a thrust fault.

Eocene Exhumation and Cooling History of the Anaconda Metamorphic Core Complex defined by $^{40}\text{Ar}/^{39}\text{Ar}$ Thermochronology

The $^{40}\text{Ar}/^{39}\text{Ar}$ thermochronological data set obtained from rock samples collected across the ACC lower plate in the current study area define a lateral cooling age gradient, where cooling ages young progressively to the ESE across the lower plate. Individual mineral cooling ages and transect sample localities are shown in Figure 7-2 plotted on a simplified geologic sketch map. In addition, mica cooling ages (muscovite and biotite) have been contoured in Figure 7-3 to clearly illustrate the lateral cooling age gradient across the exposed ACC lower plate rocks. The presence of the lateral cooling age gradient and the fact that cooling ages young in same direction as tectonic transport (detachment) of the upper plate (ESE, 110-100°, as defined by stretching lineations and kinematic indicators in the greenschist mylonites, Kalakay et al., 2003) indicates the

dominate mechanism for vertical exhumation and cooling of the ACC lower plate was tectonic unroofing, not erosion (Foster et al., 1990; McGrew and Snee, 1994; Foster and John, 1999).

Thermochronological data obtained by $^{40}\text{Ar}/^{39}\text{Ar}$ thermochronology in this study are discussed below in the context of the tectonic exhumation and cooling of the ACC lower plate. In particular, the new thermochronological data combined with previous thermochronology and geochronology provide constraints on: (1) the thermal history of the ACC lower plate, (2) the onset and duration of extension in the ACC, (3) the slip rate and geometry of the bounding normal detachment fault, and (4) the magnitude of offset facilitated by the bounding detachment fault since the onset of extension.

Lower Plate Cooling History

The cooling history of the ACC lower plate exposed in the current study area is now defined from the late Cretaceous to the Eocene by new $^{40}\text{Ar}/^{39}\text{Ar}$ thermochronological data, U-Pb geochronology, and thermobarometric data obtained in this study combined with previous thermochronology and U-Pb geochronology. All relevant data has been compiled and summarized in Figure 7-4 which displays a temperature (y-axis) vs. time (x-axis) cooling diagram for the ACC lower plate. The temperature-time cooling diagram contains fields representing the approximate range in temperature and age for magmatic and metamorphic events recorded by the ACC lower plate since late Cretaceous time. In addition, cooling curves have been constructed for major intrusions emplaced into the ACC lower plate and for different regions of the ACC lower plate “country rock.”

During the late Cretaceous much of the ACC lower plate was at temperatures in

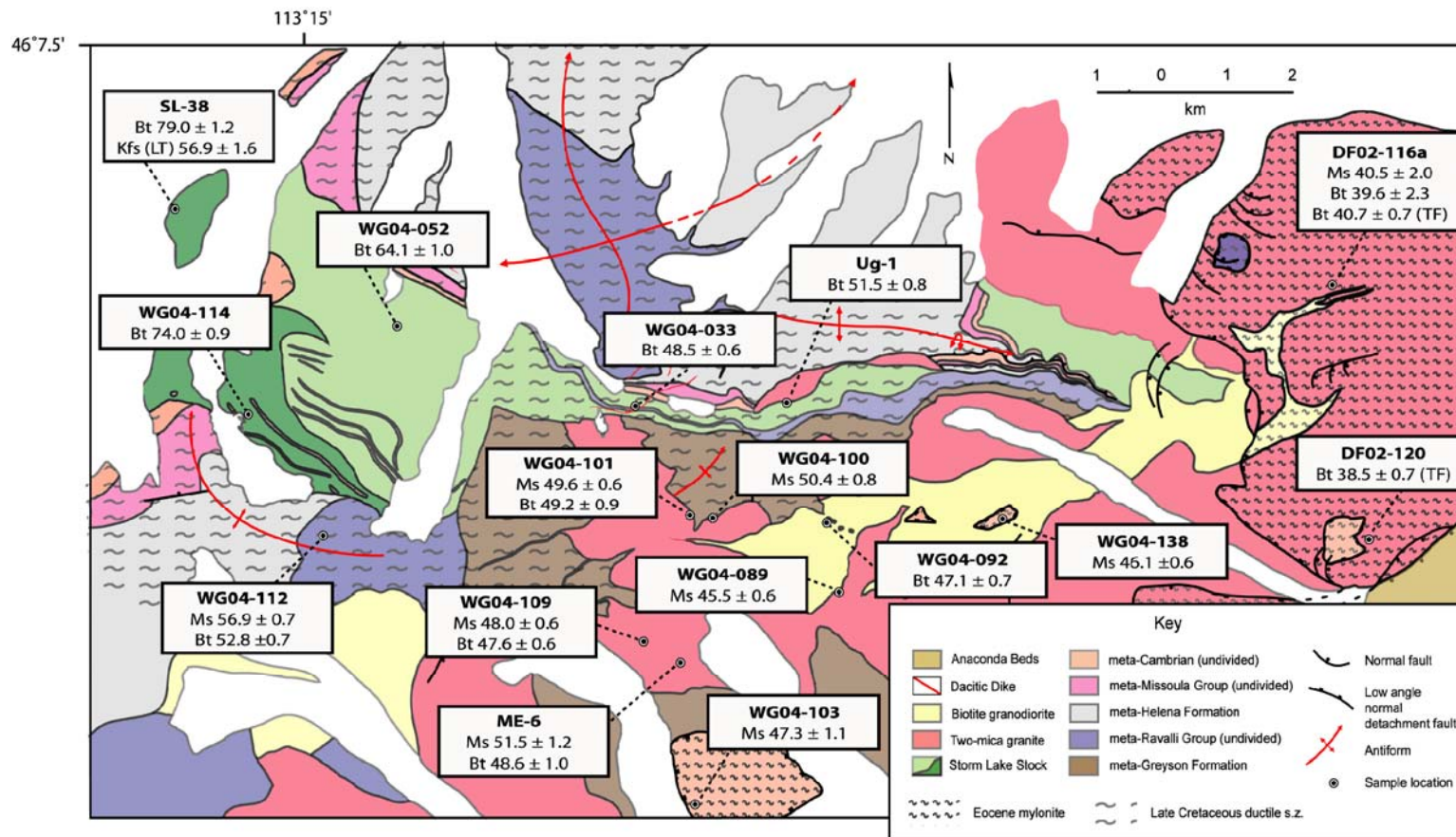


Figure 7-2. Geologic sketch map showing the mineral cooling ages obtained by $^{40}\text{Ar}/^{39}\text{Ar}$ thermochronology from samples collected along the ACC lower plate transect in this study. Mineral cooling ages are reported with two sigma error.

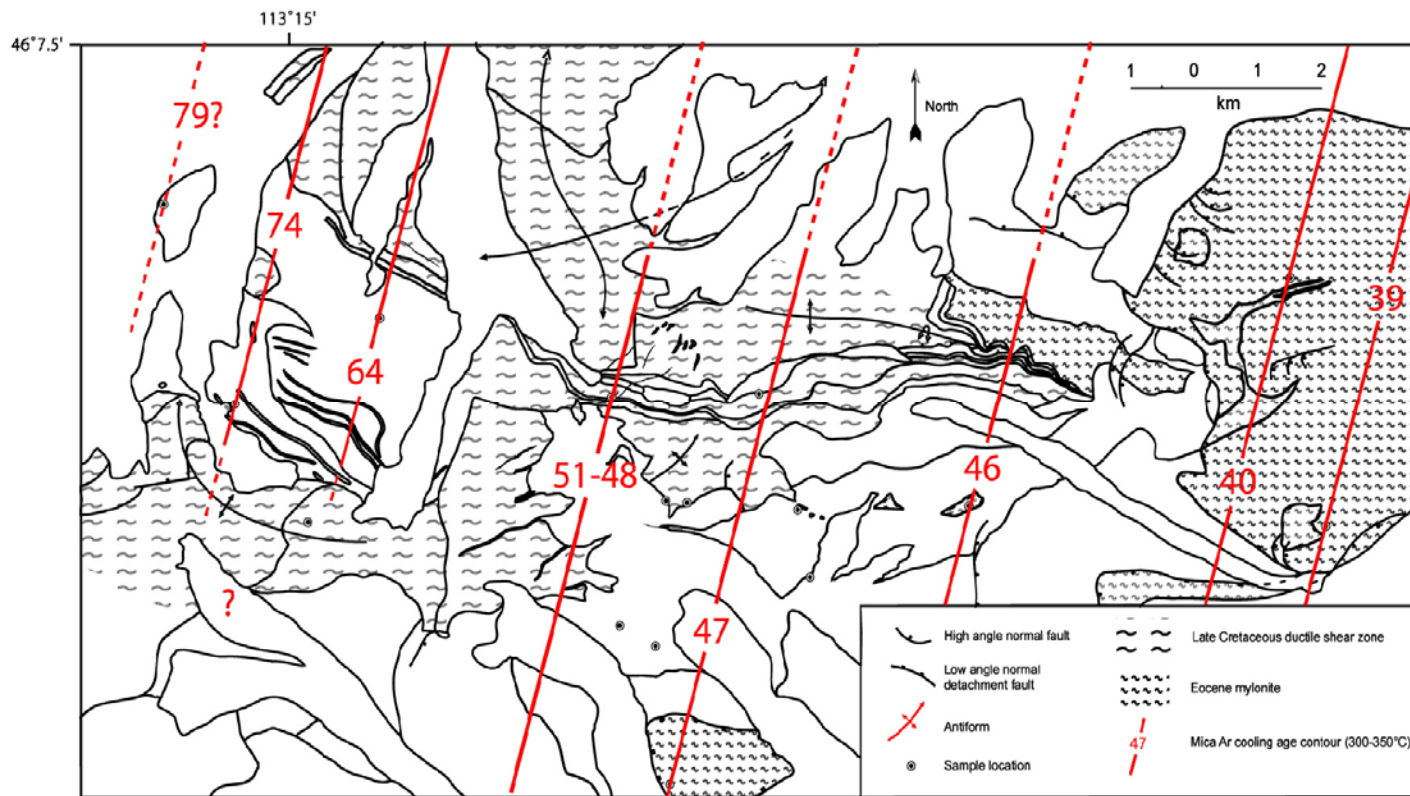


Figure 7-3. Mica cooling age contour map constructed from biotite and muscovite cooling ages obtained $^{40}\text{Ar}^{39}\text{Ar}$ thermochronology from samples collected along the ACC lower plate transect in this study. Mica cooling ages young to the east across the footwall, consistent with top-to-the-east-southeast Eocene unroofing of the lower plate (see text for details).

excess of ~600-700°C. Thermobarometric data obtained from migmatitic meta-Greyson pelitic gneiss in the LISZ indicates peak metamorphic temperatures reached ~750-850°C during upper-amphibolite facies metamorphism which occurred no later than ~74-76 Ma (see Chapter 5). Previous pressure-temperature estimates from other regions of the ACC lower plate (e.g., the Flint Creek and southern Anaconda-Pintlar Ranges) suggest similar metamorphic temperatures at this time (see Chapter 5). Emplacement of the several voluminous batholiths, stocks, and plutons at ~80-65 Ma (e.g., the Flint Creek plutons, Storm Lake Stock, and Boulder and Pioneer Batholiths, see Fig. 2-2 and 2-4) maintained high temperatures in the ACC lower plate during the late Cretaceous (Fig. 7-4).

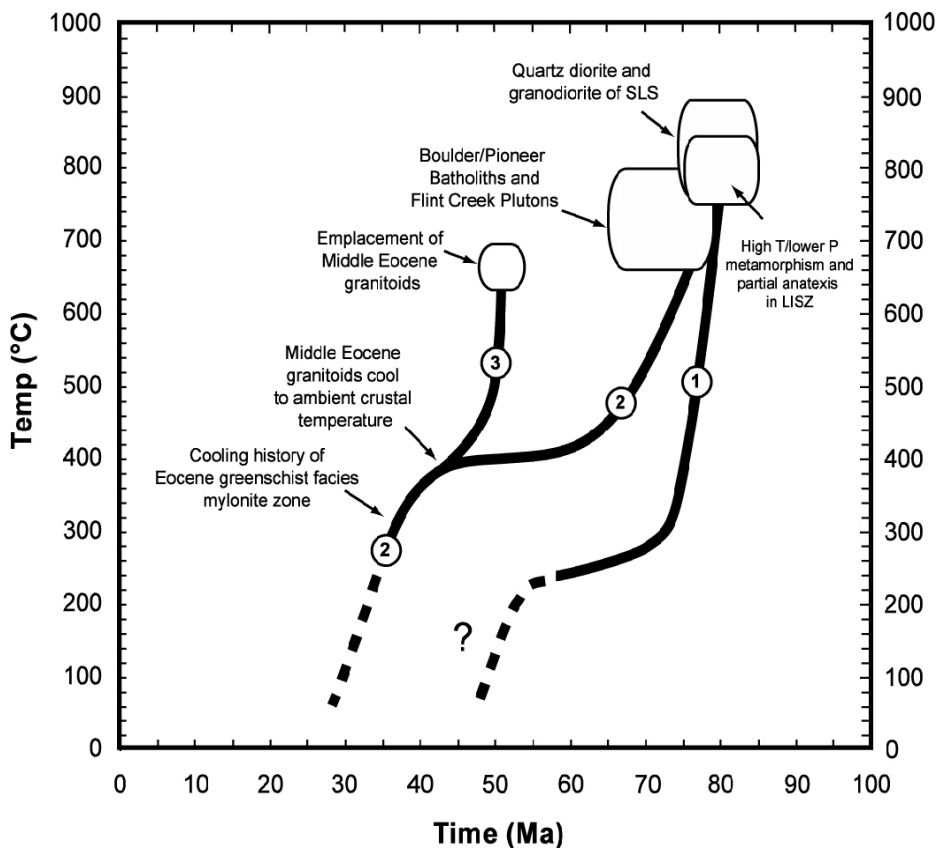


Figure 7-4. Temperature-time cooling diagram showing the cooling history of the ACC lower plate. The diagram was constructed from the new and previous thermochronology, geochronology, and thermobarometry from the ACC lower plate.

The ACC lower plate underwent rapid cooling immediately following upper-amphibolite facies metamorphism in the LISZ and emplacement of voluminous intrusions during in the late Cretaceous. However, the lateral gradient in mica cooling ages now documented across the exhumed lower plate within the current study area (Fig. 7-2 2 and 3) indicates the eastern and western parts of the ACC lower plate underwent substantially different cooling histories upon tectonic exhumation. The difference in cooling history, at least from the middle Eocene on, is due to tectonic exhumation of the lower plate along the east-dipping detachment (i.e., the eastern ACC lower was down-dip and deeper [and warmer] than the western ACC lower during extension). In addition, the eastern (deeper) part of the ACC lower plate was intruded by granites and granodiorite plutons in the early to middle Eocene time causing its cooling history to substantially differ from the western (shallower) part of the ACC lower plate.

The cooling history of the western lower plate is now defined by geochronology and thermochronology from the Storm Lake Stock (cooling curve 1, Fig. 7-4). Following emplacement of the quartz diorite and granodiorite phases of the SLS at ~75-74 Ma (see Chapter 4) the western lower plate cooled very rapidly to less than ~350°C by ~74 Ma based on a well defined biotite cooling age from the SLS granodiorite (see Chapter 6). The ~350°C closure temperature for this biotite was calculated for rapidly cooled sample. Subsequent to ~74 Ma, however, cooling of the SLS and western ACC lower plate was slower. A low-temperature error plateau obtained from laser step-heating of K-feldspar from the SLS granodiorite gave a $^{40}\text{Ar}/^{39}\text{Ar}$ cooling age of ~57 Ma indicating the western lower plate most likely remained above ~250-200°C until ~57 Ma. After ~57 Ma, the low temperature history of the western part of the ACC lower plate cannot be further

constrained with low-temperature thermochronological data such as apatite fission track or U-Th/He cooling ages.

The eastern part of the ACC lower plate slower following upper-amphibolite facies metamorphism and emplacement of late Cretaceous intrusions compared to the western part of the lower plate (cooling curve 2, Fig. 7-4). Presumably, the eastern ACC lower plate initially cooled slower following the late Cretaceous thermal maximum because this part of the lower plate was at deeper and therefore at higher ambient temperatures during this time. At ~53-47 Ma two-mica and biotite granites and granodiorite plutons intruded the eastern (deeper) part of ACC lower plate based on $^{206}\text{Pb}/^{238}\text{U}$ zircon crystallization ages (Foster et al., 2006a). These intrusions most likely cooled rapidly at first because the elevated geothermal gradient in the ACC lower plate during the late Cretaceous (~40-50°C/km) had since decayed, probably to ~25-30 °C/km (cooling curve 3, Fig 7-4). However, biotite and muscovite from these intrusions gave cooling ages of ~40-39 Ma indicating the intrusions, and the eastern lower plate country rock, remained above ~350-400°C before this time. Muscovite and biotite cooling ages from these intrusions are within error indicating the onset of rapid cooling ($\geq 125^\circ\text{C}/\text{Ma}$) at ~40-39 Ma most likely due to a change in the detachment geometry in the upper crust (see below).

The cooling history of the eastern lower plate within the current study area cannot be further constrained at this time without lower thermochronological data (e.g., apatite fission track or U-Th/He cooling ages). Foster and Raza (2002) report apatite fission track cooling ages from the eastern part of the Chief Joseph Batholith in the southern Anaconda-Pintlar Range. These cooling ages range from ~40-30 (younging approximately west to east) and record the time at which the Chief Joseph Batholith

cooled below $\sim 120\text{-}90^\circ\text{C}$ within the shallow crust (Reiners et al., 2005). These low temperature thermochronological data approximate the low temperature cooling history of the eastern ACC lower plate, at least in the southern part of the exposed lower plate (dashed part of cooling curve 2, fig 7-4).

Constraints on the Timing of the Onset of Extension

The timing of the onset of extension in fault-bound metamorphic core complexes can be constrained using lower plate $^{40}\text{Ar}/^{39}\text{Ar}$ thermochronology in two ways. One strategy is to document the timing of accelerated cooling of the lower plate, which presumably commences at the onset of rapid extension; lower plate rocks cool relatively slow prior to extension and then quickly during rapid extension as they are uplifted towards the surface (e.g., Foster and John, 1999; other references?). This method, referred to as the “accelerated cooling method” here, requires temperature information from individual lower plate rock samples prior to, during and after the onset of rapid extension therefore spanning a wide range of temperature and time (e.g., U-Pb zircon crystallization ages, hornblende, mica, K-feldspar and apatite fission-track cooling ages, ranging $\sim 750\text{-}100^\circ\text{C}$, their respective closure temperatures). Following this approach, mineral cooling ages, sometimes from multiple lower plate samples, are typically plotted on a temperature (y-axis) vs. time (x-axis) diagram and cooling curves are fit to the data. A sharp increase (or break) in the slope of the cooling curve for the samples marks the time at which exhumation began, causing rapid cooling (Foster and John, 1999).

Another way to constrain the timing of the onset of extension in metamorphic core complexes using lower plate $^{40}\text{Ar}/^{39}\text{Ar}$ thermochronology is to document the position of preserved or “quenched” palaeoisotherms within the exhumed lower plate (Foster et al., 1993; Foster and John, 1999). In particular, the position of the palaeoisotherm

representing the base of the partial retention zone (PRZ) for a given temperature sensitive mineral system can be used to estimate the age of the onset of extension (Foster and John, 1999). This approach is referred to as the “PRZ method” here. The PRZ refers to a zone (or range of depths) within a vertical column of crust where heating, due to the geothermal gradient, causes the daughter product for a given radiogenic decay scheme to be only partly retained by its host mineral (Stockli, 2005). This occurs because temperatures within the PRZ progressively approach the closure temperature of a given mineral with increasing depth (e.g., the Ar closure temperatures of K-bearing minerals). Above the PRZ, in the case of the K-Ar system, K-bearing minerals record cooling ages unaffected by heating from the geothermal gradient at a given time, presumably related to earlier cooling events. Within the range of depths defining the PRZ, cooling ages from K-bearing minerals are considered “mixed” ages because some amount of ^{40}Ar is not retained during radiogenic decay of ^{40}K due to heating with increasing depth (Foster and John, 1999). However below the PRZ, K-bearing minerals are effectively “zero aged” because at these depths the crust is too warm to retain any ^{40}Ar produced by radiogenic decay. Only when these deeper rocks are rapidly uplifted through the PRZ will K-bearing minerals within the rocks acquire cooling ages. Thus, at the onset of extension, for example in metamorphic core complexes, rocks at the base of the PRZ are uplifted along detachment faults through the PRZ and record cooling ages that correspond the age of the onset extension. Rocks at deeper crustal levels (i.e., significantly below the base of the PRZ) will record cooling ages progressively younger than the onset of extension because these deeper rocks are uplifted through the PRZ at progressively later times (Foster and John, 1999; Stockli, 2005).

To estimate the timing of the onset of extension in metamorphic core complexes using the PRZ method as described here the following steps must be taken. (1) A suite of rock samples should be collected along a lower plate transect in the direction of slip on the bounding detachment fault system(s). Therefore, the samples collected along the transect will young in the slip direction and represent once progressively deeper rocks (i.e., increasing paleodepths), given that the lower plate rocks were exhumed by tectonic unroofing (Foster and John, 1999; Stockli, 2005). (2) A cooling age (y-axis) vs. distance in slip direction (x-axis) diagram is then constructed from cooling ages obtained from thermochronology; the distance in slip direction corresponds to the relative positions of the rock samples along a chosen lower plate transect line. A curve is then fit to the cooling age data for a given mineral system. (3) The base of the PRZ for a given temperature sensitive mineral system can then be identified by locating an inflection point defined by a dramatic change in the slope of the cooling age curve in the direction of slip. The inflection point is usually marked by a change from sub-vertical to sub-horizontal slope of the curve in the slip direction. (4) A horizontal line is then passed through the inflection point and will intersect the y-axis at the age of the onset of extension. A cooling age from a rock sample that falls along this line is equal to the age of the onset of extension because it was at the base of the PRZ. Rock samples that fall below the line record cooling ages after the onset of extension because they were below the base of the PRZ prior to extension. Most rock samples above this line represent lower plate rocks that were within the PRZ prior to the onset of extension and record mixed cooling ages. However, the oldest rock samples near the top of the diagram can represent cooler, shallower rocks that were above the PRZ before extension began. Note

also a vertical line passed through the inflection point in the age vs. distance in slip direction diagram will intersect the x-axis at the distance along the lower plate transect line representing the base of the exhumed PRZ (Foster and John, 1999).

In this study, the PRZ method was utilized to constrain the timing of the onset extension and exhumation of the ACC lower plate. The accelerated cooling method could not be employed because the thermochronological data obtained from individual lower plate samples do not span the temperature-time range needed to employ this method (i.e., from pre-to-syn-to-post-extensional temperatures). Below, the PRZ method is applied to the mica cooling ages obtained along the ACC lower plate transect in the current study area.

Figure 7-5a displays an age vs. distance in slip direction diagram constructed from muscovite and biotite cooling ages obtained from lower plate rock samples using $^{40}\text{Ar}/^{39}\text{Ar}$ thermochronology. In addition, Figure 7-5b shows a simplified geologic stretch map of the exhumed ACC lower plate in the current study area with rock sample localities and the chosen transect line (oriented at 105° , the average slip direction on the detachment). Rock samples adjacent to the transect line were projected orthogonally back to the line defining their distances in slip direction as shown along the x-axis in Figure 7-5a. Horizontal (distance) error bars for each rock sample are ± 1 km. It is common practice to apply distance in slip direction error on these types of plots to account for errors associated with sample projections and variability in elevation (i.e., paleodepth) between transect rock samples (Foster et al., 1993; Brichau et al., 2005). Vertical error bars represent errors in individual mica cooling ages. The distance in slip direction and age error bars in Figure 5a represent 2σ errors (95% confidence interval).

Both muscovite and biotite cooling ages progressively young across the ACC lower plate to the ESE, in the direction of slip on the detachment fault system (Fig. 7-1, 7-2, and 7-5a). This trend in cooling ages is consistent with the interpretation that rock samples collected in the direction of slip across exhumed lower plates represent increasing paleodepths (e.g., Fitzgerald, et al., 1991; Foster et al., 1993; Lee, 1993, Foster and John, 1999). Therefore, these thermochronological data can be used to constrain the position of the exhumed PRZ for micas and the age of the onset of extension in the ACC. At a distance of ~4-5 km along the lower plate transect mica cooling ages drop from Late Cretaceous (≥ 74 Ma) to middle Eocene cooling ages (≤ 53 Ma). Further to the ESE, in the direction of slip, mica cooling age more gradually decrease to ~39 Ma. The marked change in slope of the mica cooling age curve defines the position of the palaeoisotherm that corresponds to the base of the exhumed PRZ for micas (Fig. 7-2 5a, b). The top of mica PRZ is constrained to be just ESE of (or slighter deeper in paleodepth than) WG04-114, a rock sample collected from the SLS granodiorite (Fig 7-5a, b). This sample yielded a biotite cooling age of 74.0 ± 0.9 Ma and a zircon $^{206}\text{Pb}/^{238}\text{U}$ weighted mean age of 75.6 ± 1.1 (Chapter 4). The concordance of these ages indicates the SLS granodiorite underwent rapidly post-magmatic cooling after emplacement into cooler, shallow crust above the mica PRZ. Therefore, samples WG04-052 and WG04-112 lie within the exhumed mica PRZ (Fig. 7-5a, b). A horizontal line passed through the mica cooling age inflection point intersects the y-axis at ~53 Ma, the age of the onset of extension in the ACC and initial exhumation of the lower plate (Fig. 7-5a).

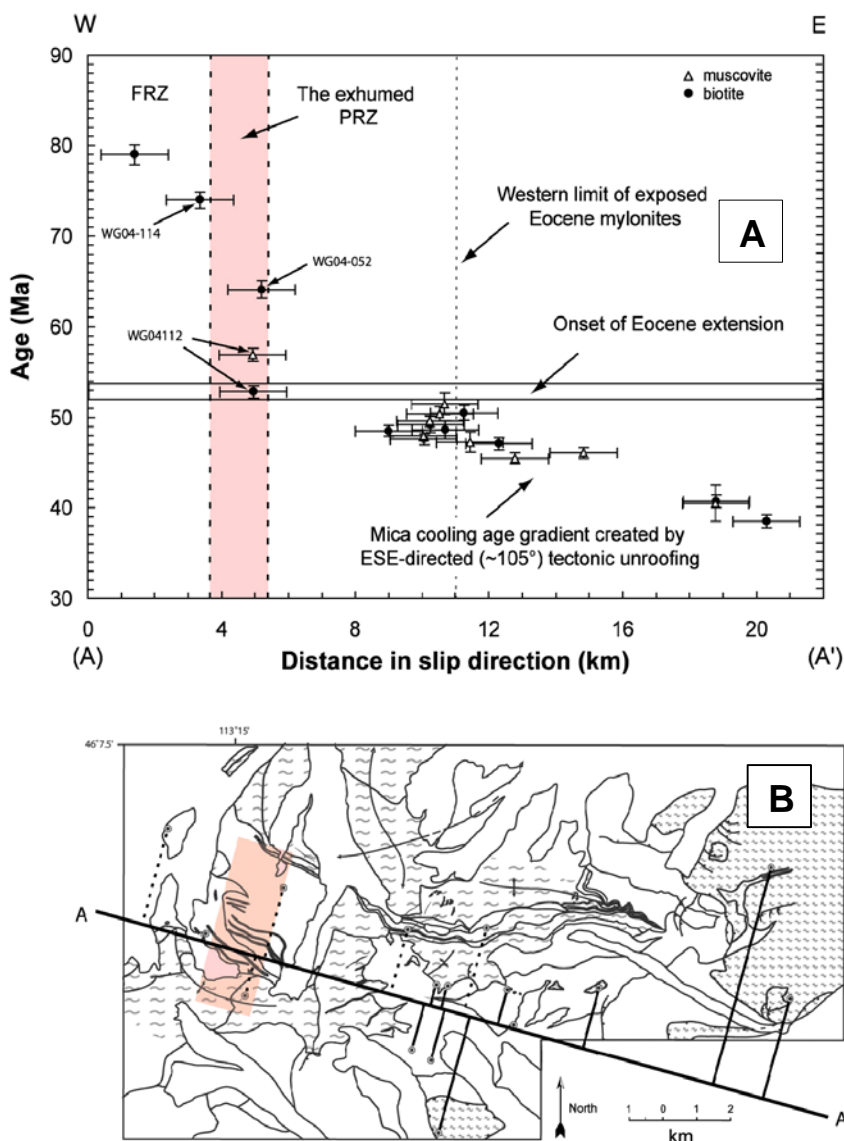


Figure 7-5. Age vs. distance in slip direction diagram and lower plate transect sketch map. A) The age vs. slip rate direction diagram was constructed by projecting samples back to a defined transect line which has been oriented parallel to the average slip direction on the detachment (105°). PRZ = partial Ar retention zone for micas. B) The lower plate transect sketch map shows the sample projections used to construct the age vs. slip rate direction diagram. Samples projected back to the transect line with dashed lines were not used in subsequent slip rate calculations.

Constraints on the Duration of Extension

The duration of extension and tectonic exhumation of the ACC are now largely constrained by lower plate mica cooling ages obtained here and by $^{206}\text{Pb}/^{238}\text{U}$ zircon

crystallization ages from the granitoid mylonites sampled from the greenschist facies mylonitic shear zone in the easternmost study area ($^{206}\text{Pb}/^{238}\text{U}$ zircon ages from Foster et al., 2006a). These data indicate that extension, causing exhumation and cooling of the ACC lower plate, began at ~ 53 Ma within the mylonitic shear zone, presumably at mid-crustal depths. Extension in the ACC, facilitated by ductile flow in the mylonitic shear zone and by brittle detachment at shallower crustal levels, continued until ~ 40 - 39 Ma based the cooling ages of mica from the greenschist facies mylonites. These mica cooling ages record the time when the eastern part of the shear zone was exhumed upwards through the brittle-ductile transition (at ~ 300 - 350°C) therefore causing ductile deformation to cease.

O'Neill et al. (2004) report a cooling age of 47.2 ± 0.3 Ma (given with 2σ error here) from a single muscovite porphyroclast extracted from a sample of mylonitic micaeous quartzite in the Sullivan Creek drainage within the southern part of the current study area. In this study, a similar cooling age of 47.3 ± 1.1 Ma was obtained from a fraction of muscovite porphyroclasts extracted from a sample collected at the O'Neill et al. (2004) sample site. These cooling ages most likely record recrystallization (or neocrystallization) of the pre-existing muscovite porphyroclasts within the quartzite at or just below the closure temperature of muscovite in the latest stages of ductile deformation under greenschist facies conditions (Dunlap, 1997; Foster, et al., in press). Thus, ductile deformation apparently ceased much earlier in this part of the mylonitic shear zone. The differences in age of ductile deformation in these two part of the shear zone is consistent with ESE directed tectonic unroofing of the ACC lower plate. Because this part of the mylonitic shear zone lies west (and was previously up-dip on the detachment) of the

shear zone exposed in the Mill and Clear Creek drainages it would have been exhumed through the brittle-ductile transition at an earlier time during extension. Apatite fission track cooling ages from the southern Anaconda-Pintlar Range reported by Foster and Raza (2002) indicate that extension, exhumation, and cooling of the ACC lower plate continued until ~30-25 Ma, at least in the south.

Constraints on the Detachment Slip Rate

Thermochronological data from rock samples collected along lower plate transects in metamorphic core complexes parallel to the direction of tectonic unroofing have also been successfully used to estimate previous slip rates on bounding detachment faults (e.g., Foster et al., 1993; John and Foster, 1993; Foster and John, 1999; Wells et al., 2000; Stockli, 2005). The mica cooling ages obtained from the ACC lower plate transect in this study may be used to estimate the slip rate on the bounding detachment fault. In order to make realistic and meaningful slip rate estimates from these thermochronological data some important assumptions must be made. (1) Vertical exhumation and cooling of the ACC lower plate during the time interval over which the slip rate is estimated must have been due to tectonic unroofing (i.e., uplift by displacement along the detachment), not erosion. (2) Isotherms of the syn-extensional geothermal gradient must have remained approximately horizontal and stable over the time interval used to estimate a slip rate for the detachment (Ketchum, 1996; Foster and John, 1999; Stockli, 2005).

In the case of the ACC lower plate, the first assumption is most likely valid. As noted above, the presence of a lateral thermal gradient across the ACC lower plate defined by the ESE younging trend in mica cooling ages precludes any major contributions of erosion to the exhumation of the ACC lower plate; this holds true for at least the time interval in which the previously “zero” aged lower plate micas were

uplifted and cooled below their Ar closure temperatures (from ~51-39 Ma). The second assumption, a stable syn-extensional geothermal gradient, is also probably valid for the ACC but requires more discussion here. One potential cause for an unstable geothermal thermal gradient during extension in metamorphic core complexes is heat advection. For example, when deeper and warmer rocks are rapidly uplifted along a detachment fault they are placed directly adjacent to relatively shallow and cooler rocks. As a result, heat from the previously deeper rocks will advect into the surrounding shallower, cooler rocks (i.e., cooling of the deep rocks does not keep the pace with tectonic uplift, House and Hodges, 1994; Scott et al., 1998). Consequently, a lateral thermal gradient is created across the detachment fault possibly resulting in an unstable geothermal gradient during extension characterized by non-horizontal isotherms. Although two-dimensional conductive cooling models show that heat advection occurs, the same models suggest the heat advection dissipates rapidly, probably in less than a few million years after the onset of extension (Ketchum, 1996; Carter et al., 2006). Thereafter, a stable syn-extensional geothermal gradient is restored (Foster and John, 1999). Thus, the complications related to heat advection from initial exhumation of deeper, warmer rocks can be avoided when making detachment fault slip rate estimates by using rock samples with mineral cooling ages at least a few million years younger than the onset of extension (Stockli, 2005). In the case of the ACC, the previously “zero” aged mica cooling ages appropriate for the slip rate estimates are ≥ 2 Ma younger than the onset of extension at ~53 Ma. The potential pitfalls associated with advection of heat in the early stages of extension are effectively avoided by using these thermochronological data to estimate a slip rate.

Another possible cause for an unstable syn-extensional geothermal gradient, resulting in unrealistic slip rate estimates, is heating caused by emplacement of voluminous intrusions into the active detachment fault zone (Ehlers, 2005; Stockli, 2005). This is a valid concern and should always be addressed because syn-kinematic intrusions are common in metamorphic core complexes (e.g., Lister and Baldwin, 1993; Foster et al., 2001). Therefore, it is necessary to provide some age constraints on the emplacement of intrusions within the exhumed lower plates of metamorphic core complexes when making slip rate estimates using lower plate transect thermochronological data (Stockli, 2005). However, three lines of evidence indicate the Eocene granitoid intrusions within the ACC lower plate were emplaced during the early phases of extension and therefore should not interfere with the slip rate estimates made here. (1) There is no evidence for radial mica cooling age patterns within or surrounding any of the intrusions (i.e., the mica cooling ages young to the ESE, the direction of tectonic unroofing). A radial pattern in cooling ages would be expected if one or more of the intrusions were emplaced after the country rock and other intrusions had cooled below mica Ar closure temperatures due to tectonic unroofing (e.g., John and Foster, 1993). (2) The youngest intrusion (as indicated by cross-cutting relationships in the field), porphyritic two-mica granite, yielded mica cooling ages of ~51-48 Ma. These cooling ages indicate that the other intrusions must have been emplaced earlier, probably earlier than ~51-50 Ma. (3) Zircon populations from biotite granodiorite and biotite granite overprinted by greenschist facies mylonitic fabrics within the eastern exposed mylonite zone yielded $^{206}\text{Pb}/^{238}\text{U}$ weighted mean ages 53.0 ± 1.2 and 47.1 ± 0.8 Ma (2σ errors), respectively (Foster et al., 2006a). The emplacement of biotite granodiorite is interpreted to have occurred at the onset of

extension or just slightly before. The younger $^{206}\text{Pb}/^{238}\text{U}$ weighted mean age for the biotite granite should be considered a minimum age of emplacement because several zircons analyzed from this sample gave $^{206}\text{Pb}/^{238}\text{U}$ ages of ~53-50 Ma, indicating incorporation of zircon material the age of the granodiorite. Thus, these two intrusions and other intrusions within the ACC lower were most likely emplaced 0-3 Ma after the onset of extension in the ACC. By ~50 Ma the syn-extensional geothermal gradient would have been restabilized. Therefore, realistic slip rates estimates can be made from the lower plate micas that were effectively “zero” aged prior to the onset of extension at ~53 Ma.

Slip rate estimates were made using both biotite and muscovite cooling ages separately to compare results from the two different isotopic systems. To make these slip rate estimates, the mica cooling ages and errors (as presented in Figure 7-5a, both age and ± 1 km distance errors) were first imported into the computer program Isoplot v. 3.09a (see Ludwig, 1991) where straight lines were fit to the thermochronological data using least-squares regressions. In Isoplot, the least-squares regressions (using Isoplot regression mode 1) are made with the original algorithms of York (1969) and the error propagation and correlation between the thermochronological data points follow that of Titterton and Halliday (1979; see Isoplot user’s manual, p. 21, Ludwig, 2003). Note the biotite cooling age from WG04-033, a sample collected from a aphanitic porphyritic dacite dike, was excluded from the least-squares regression and subsequent slip rate estimate made from the biotite thermochronological data. This dacite dike and several others in the central part of the current study area were emplaced relatively late and their

cooling histories may be significantly different from the country rock and therefore should not be included in the slip rate estimate.

Figure 7-6 shows the results from the Isoplot least-squares regressions made from both the biotite and muscovite thermochronological data. For biotite, the regression slope (m) = -1.07 ± 0.34 and for muscovite $m = -1.15 \pm 0.62$ (regression slope errors are 2σ). Slip rate estimates for the detachment were made from these least-squares regressions by taking the inverse of the absolute values of the regression slopes and their errors (e.g., see Foster and John, 1999; Brichau, et al., 2005). The slip rate estimates for the detachment are shown in Figure 6 as well. For biotite, the calculated slip rate = $0.93 + 0.44 / - 0.23$ km/Myr (or cm/yr) and for muscovite = $0.87 + 1.09 / - 0.31$ km/Myr (slip rate errors are 2σ). The asymmetry of the slip rate errors is derived from adding and then subtracting the regression slope errors from the regression slopes.

Despite the larger positive error associated with muscovite slip rate estimate, the closeness the mica derived slip rates indicate the slip rate estimates for the detachment made here are most likely realistic (i.e., the two separate isotopic systems give virtually the same slip rate). The larger positive error of the muscovite slip rate is the result of some scatter in the muscovite cooling ages at ~10-11 km in the slip direction and a relatively large error (± 2.3 Ma) in the muscovite cooling age from sample DF02-116 at ~19 km, mylonitic two-mica granite sampled from upper Clear Creek in the east (Fig. 7-2 5a). Together, the muscovite and biotite slip rate estimates correspond to an average slip rate = $0.90 + 0.59 / - 0.19$ km/Myr for the detachment (a range of 1.5-0.71 km/Myr). It is important to note that these slip rates estimates are time-averaged, meaning that slip

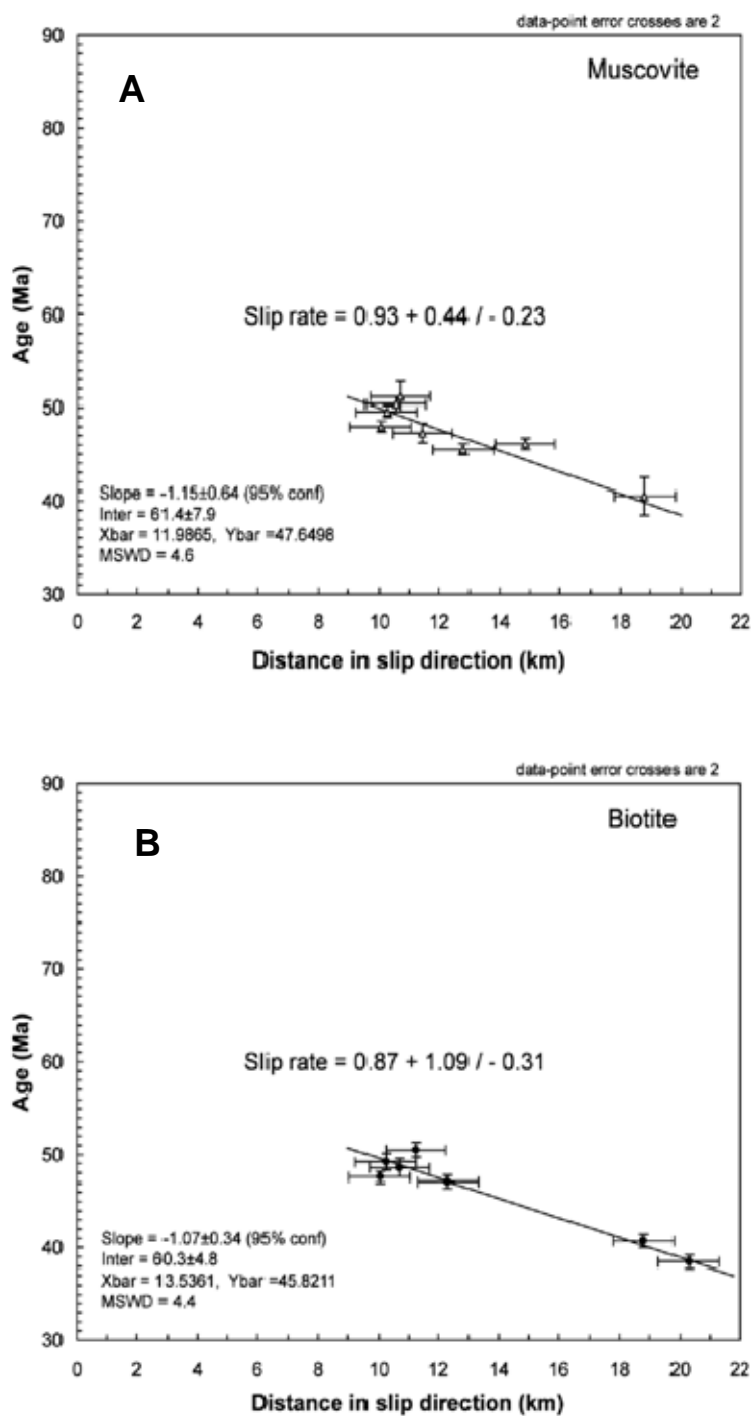


Figure 7-6. Slip rate calculations. A) Slip rate calculated from muscovite cooling ages. B) Slip rate calculated from biotite cooling ages (see text).

along the detachment is averaged over the time interval from ~51-39 Ma, the range of cooling ages used in the slip rate estimates. Therefore, these slip rate estimates do not

account for increases or decreases in slip along the detachment during the time period from ~51-39 Ma (Foster and John, 1999; Stockli, 2005).

Original Detachment Geometries

For over two decades now, considerable controversy has been focused on the original geometries of low-angle normal detachment faults (i.e., the dip of the fault in the earliest phases of extension) that bound metamorphic core complexes (see Wernicke, 1992, 1995 or Carney and Janecke, 2005 for a review). The basis of the a debate is whether these complex-bounding low-angle normal detachment faults originated within the brittle upper crust with shallow ($\leq 30^\circ$) dips, as many are presently observed in the field, or with steeper ($\geq 45^\circ$ or even $\geq 60^\circ$) dips; the latter implies some subsequent tectonic mechanism must alter the original steep fault geometries. There is a generally consensus, however, among most workers that regardless the dip of fault in the brittle upper crust, normal faults become sub-horizontal at mid-crustal depths due to interaction with the brittle-ductile transition which acts as a crustal-scale stress guide (e.g., Lister and Davis, 1989).

At one end of the debate, Andersonian fault mechanic purists (e.g., Anderson, 1951) argue that normal faults, such as low-angle detachment faults, cannot form originally with shallow dips in the brittle upper crust because the orientation of the maximum principle stress axes (approximately vertical) during extension will not allow such faults to slip. Fault models such as the “rolling hinge” or “domino-style” models have been employed to explain the present-day low-angle orientation of many complex-bounding normal detachment faults (e.g., Spencer, 1984; Wernicke and Axen, 1988; Buck, 1988; Wernicke, 1992; Brady et al., 2000). These two models hold that normal

faults originally form within the brittle upper crust with steep dips and then are rotated to shallower dips later in their evolutions. The rolling hinge model calls for the rotation of steeply dipping detachments at their shallower crustal reaches by isostatic rebound of the lower plate upon its vertical exhumation. The isostatic rebound is thought to be caused by unroofing of the lower plate itself and in some cases, buoyant forces created from syn-kinematic intrusions (Wernicke and Axen, 1988; Lister and Baldwin, 1993). According to the domino-style model, older, steeper normal faults become inactive and then rotated to more gentle dips by a younger generation(s) of synthetic normal faults (see Brady, 2000 or Carney and Janecke, 2005 for a review of these models). An overwhelming proportion of current seismic data indicates that active normal faults are slipping with steep dips ($>30^\circ$, Wernicke, 1995) suggesting a steeper dip origin for normal faults in the upper brittle crust is most geologically plausible; these seismic data support the rolling-hinge and domino-style models for steep-then-shallow dip normal fault evolution.

On the other hand, several workers provide strong evidence for a low-angle, or shallow dip ($\leq 30^\circ$) origin for normal faults in the brittle upper crust. These workers use thermochronology (see example below in this study), structural reconstructions, and stratigraphic reconstructions to argue for a shallow dip origin of normal detachment faults that bound several major metamorphic core complexes in the western United States (e.g., John, 1987; Davis, 1988; Foster et al., 1990; Scott and Lister, 1992; John and Foster, 1993; Dokka, 1993; Carney and Janecke, 2005). In addition, relatively recent seismic data document active low-angle normal faulting in the juvenile metamorphic core complexes of the D'Entrecasteaux Islands, Papua New Guinea indicating an original shallow dip origin for low-angle detachment normal faults is also geologically viable in

nature (Abers, 1991; Abers et al., 1997; Abers, 2001). The apparent lack of evidence for shallow dipping active normal faults in many previous seismic studies may simply be because slip on low-angle normal faults is less frequent in most current tectonic environments and as a result less recorded (Abers, 1991; Wernicke, 1995). Therefore at present, it appears that normal detachment faults bounding many metamorphic core complexes could have originated in the brittle upper crust with steep or with shallow dips as most are now observed in the field.

Constraints on the Original Detachment Geometry

Apparent mineral cooling ages obtained from rock samples collected across the exhumed lower plates of metamorphic core complexes parallel to the direction of tectonic unroofing have also been utilized to estimate the original geometries (i.e., the fault dip) of the bounding detachment normal faults (e.g., Foster et al., 1990; John and Foster, 1993; Dokka, 1993; Stockli, 2005). Typically, cooling ages from multiple temperature sensitive mineral systems (e.g., micas, K-feldspar, and apatite) are plotted on a single age vs. distance in slip direction diagram as the one described above. Given enough thermochronological data, the positions of more than one palaeoisotherm (e.g., the base of the mica PRZ and apatite partial annealing zone, the PAZ) can be identified from inflection points on the diagram (Foster and John, 1999). If the geothermal gradient at the start of extension is known or can be estimated then paleodepths to the identified palaeoisotherms can be calculated. The original dip of the detachment normal fault is then simply found by the difference in the paleodepth between the palaeoisotherms (rise) divided by the distance between the palaeoisotherms in the direction of slip (run). Often, a paleodepth (y-axis) vs. distance in slip direction (x-axis) diagram is constructed from this information and the original dip of detachment fault is measured directly from the

diagram (e.g., Foster and John, 1999). The original dip of the detachment fault can also be determined by the relationship: $\text{dip (in degrees)} = \sin^{-1} (z / h)$, where z is difference in paleodepth between palaeoisotherms and h is the inferred length of the detachment fault measured along a sloped line connecting the palaeoisotherms on the paleodepth vs. distance in slip direction diagram (Dokka, 1993). The above methodology for constraining the original dip of normal detachment faults can be used provided that: (1) cooling of the lower plate was due to tectonic exhumation from below a single detachment fault system, (2) any significant lateral variations in the geothermal gradient can be ruled out, (3) two or more well spaced palaeoisotherm can be identified across the exhumed lower plate from the available thermochronological data, and (4) the geothermal gradient is known or can be calculated for the time the fault dip is to be calculated (Foster and John, 1999).

In the case of the ACC, the first two conditions are met. There is no evidence for more than one generation of normal detachment faults being responsible for the exhumation and cooling of the lower plate. Seismic imaging of the detachment fault zone just east of the current study area and industry wells reveals a single planar zone mylonite zone dipping to the east at $\sim 20^\circ$ with no evidence for any major intervening structures (Vejmelek and Smithson, 1995, see their Fig. 7-2 2). Also, there is no evidence for a secondary detachment within the lower plate. This is indicated by a relatively smooth change from older to younger cooling ages across the lower plate (besides the change in cooling ages across the base the mica PRZ, Fig. 7-5a). If any intervening structures were present, such as a secondary detachment fault, then an abrupt change in mineral cooling would be seen across the lower plate (e.g., Stockli, 2005). In

addition, the presence of a significant lateral thermal gradient at ~53 Ma is unlikely. Intrusions that were emplaced by ~53 Ma would have ponded below the brittle/ductile transition because this zone acts a barrier to rising magmas (Lister and Baldwin, 1993).

The third condition is partially met. The positions of two palaeoisotherms within the ACC lower plate have been defined by mica thermochronological data obtained in this study. These palaeoisotherms are the top and bottom boundaries of the mica PRZ. The temperature of the top of the PRZ for biotite and muscovite is ~200°C and the temperature of the bottom of the PRZ for biotite and muscovite is ~325°C and 375°C, respectively. These temperatures were approximated from the thermal modeling of Lister and Baldwin (1996, see their Figures 9 and 10, p. 97-98). These two palaeoisotherms may be used to estimate the dip of the segment of the detachment that exhumed the westernmost lower plate. However, another palaeoisotherm(s) from the eastern exposures of the lower plate would help to provide more complete constraints on the detachment geometry. A geothermal gradient at the onset of extension in the ACC (~53 Ma) cannot be estimated from the tilted upper plate due of the lack of the necessary upper plate thermochronology. In addition, the ACC upper plate is pervasively shattered by high-angle brittle normal faults making its inappropriate for estimating a paleogeothermal gradient for the ACC at the start of extension (e.g., Foster and John, 1999; Stockli, 2005).

Despite these apparent short comings, important limits can be placed on the geometry of the detachment fault at ~53 Ma with the thermochronological data obtained in this study. First, the position of another paleoisotherm can be approximated in the easternmost exposure of the lower plate within the greenschist facies mylonite zone. This paleoisotherm can be used to more completely constrain the original geometry of the

detachment. Because the granitoid mylonites of this mylonite zone formed as a result of ductile deformation at lower to middle greenschist facies conditions (as indicated by their mineral assemblages and metamorphic textures, see descriptions above) they could not have been subjected to temperatures greater than $\sim 400^{\circ}\text{C}$ (Spear, 1993). In addition, because the micas within these mylonites were effectively “zero” aged until $\sim 40\text{-}39$ Ma they were at least at 350°C , and more likely $>375^{\circ}\text{C}$ when extension began at ~ 53 Ma (Lister and Baldwin, 1996). Therefore, as a conservative approximation, a paleoisotherm representing a temperature of $\sim 400^{\circ}\text{C}$ can be placed within the greenschist mylonite zone in the easternmost exposures of the lower plate. The $\sim 400^{\circ}\text{C}$ palaeoisotherm was placed at the sample locality of DF02-116a. This sample was collected from mylonitic two-mica granite at the head of Clear Creek structurally high within the greenschist mylonite zone (2573 m). Presumably, the greenschist mylonites at the sample locality of DF02-116a and vicinity were closest to the base of the detachment fault plane at 53 Ma. The $\sim 400^{\circ}\text{C}$ paleoisotherm approximated here and those representing the top and bottom of the biotite PRZ (at $\sim 200^{\circ}\text{C}$ and $\sim 325^{\circ}\text{C}$, respectively) are contoured on a simplified geological sketch map of the exhumed ACC lower plate in Figure 7-7.

Using the three palaeoisotherms identified across the ACC lower plate and a range of paleogeothermal gradients a set of possible original faults geometries can be calculated for the Anaconda detachment at ~ 53 Ma. Figure 7-8 displays a distance in slip direction (x-axis) vs. paleodepth (y-axis) diagram where the original geometry of the detachment has been reconstructed using paleogeothermal gradients of $50^{\circ}\text{C}/\text{km}$, $35^{\circ}\text{C}/\text{km}$, $30^{\circ}\text{C}/\text{km}$, and $25^{\circ}\text{C}/\text{km}$. For each paleogeothermal gradient the paleodepths of samples WG04-114, WG04-052, and DF02-120, representing the 200°C , 325°C , and 400°C

paleoisotherms, respectively, were calculated simply by dividing the paleoisotherm temperatures by the paleogeothermal gradients. Lines connecting the palaeoisotherms (and samples locations) for each paleogeothermal gradient define the shape of the detachment at the onset of extension in the ACC at ~53 Ma. Note the paleoisotherms, as defined by the sample localities of WG04-114, WG05-052, and DF02-114, must have been positioned structural beneath the detachment fault at ~53 Ma (i.e., within the lower plate). Therefore, the actual detachment fault plane must have been slightly shallower than as depicted in Figure 7-8. However, because erosion is considered to be relatively minor across the ACC lower plate the detachment was probably not more than ~1 km above the paleodepths indicated in Figure 7-8.

Notably, all four reconstructions reveal a listric shaped (curved) fault geometry for the Anaconda detachment at ~53 Ma (Fig. 7-8). The listric nature of the detachment is defined by a marked break in the fault dip at 5.2 km in the slip direction which corresponds to the ~325°C palaeoisotherm, the bottom of the biotite PRZ, and the sample locality of WG04-052. West of (structurally above) this location, the detachment must have been steep because the minimum difference in temperature between samples WG04-114 and WG04-052 was ~125°C and these two samples are separated by a distance of only 1.9 km in the slip direction. However, east of (structurally beneath) this location the dip of the detachment must have been much shallower because the difference in temperature between WG04-052 and DF02-120 was not more than ~75°C and these two samples are separated by a distance of 13.6 km in the slip direction (Fig. 7-8).

The significant decrease in the apparent dip of the detachment at 5.2 km (the base of the biotite PRZ, WG04-052 sample locality), defining the listric shape of the fault, is

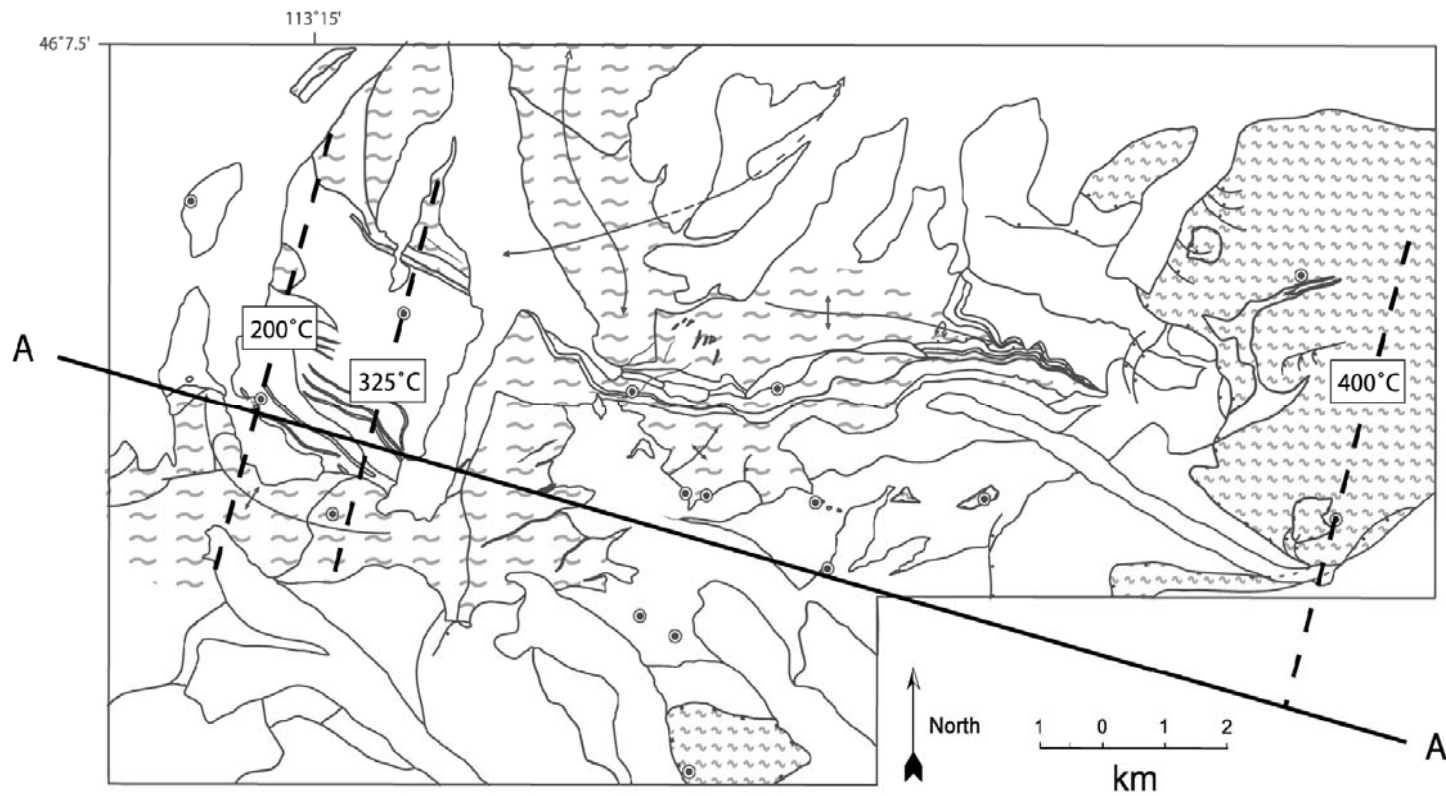


Figure 7-7. Paleoisotherm contour map. Paleoisotherms refer to estimated temperatures of the ACC lower plate directly beneath the detachment at the onset of extension at ~53 Ma. The 200°C and 325°C paleoisotherms represent the top and bottom of the biotite partial retention zone for biotite. The 400°C isotherm was estimated from the metamorphic grade of the greenschist mylonites in the eastern lower plate (see text).

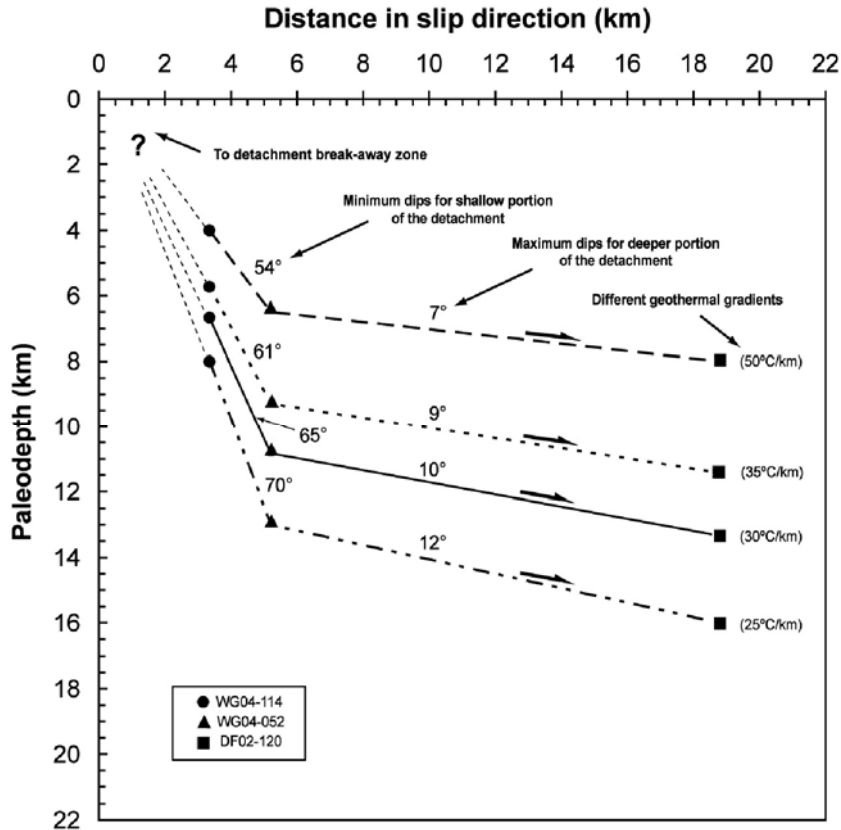


Figure 7-8. Distance in slip direction vs. paleodepth diagram showing geometries for the detachment at the onset of extension at ~53 Ma. Each reconstruction was made with a different geothermal gradient to show the range of possible geometries. Regardless of the geothermal gradient chosen, all the reconstructions indicate the detachment was strongly listric shaped at ~53 Ma with a steep upper crustal portion and a sub-horizontal middle crustal portion (see text).

consistent with deeper portion of the fault entering the brittle-ductile transition (BDT, at ~300-350°C) with increasing depth to the east (Lister and Davis, 1989). Within the BDT, the yield strength of the brittle upper crust is at a maximum (yield strength increases with depth without substantial pore fluid pressure present) just above the weaker, warmer, and more ductile lower crust. Therefore, when detachment normal faulting occurs at the BDT, detachments must form with shallow dips to accommodate the strain

incompatibility between the brittlely deforming upper crust and plastically deforming lower crust separated by the BDT (Lister and Davis, 1989).

The shallowest reconstructed detachment fault dip was obtained with a paleogeothermal gradient of $50^{\circ}\text{C}/\text{km}$ (Fig. 7-8). In this fault reconstruction, above the base of the biotite PRZ within the brittle upper crust, the reconstructed fault dip is 54° . Below the base of the PRZ (within the BDT and slightly below), the fault dip is sub-horizontal at 7° . Note that the $50^{\circ}\text{C}/\text{km}$ reconstruction made here is not viable because a geothermal gradient of $\sim 50^{\circ}\text{C}/\text{km}$ was in place during upper-amphibolite facies metamorphism ($\sim 700\text{-}800^{\circ}\text{C}$) in this part of the lower plate during the late Cretaceous (i.e., within the LISZ, see thermobarometric constraints, this study). However, mylonites exhumed along the detachment were deformed under lower to middle greenschist facies conditions ($\sim 350\text{-}400^{\circ}\text{C}$ maximum temperatures). Nonetheless, the $50^{\circ}\text{C}/\text{km}$ fault reconstruction is presented to show the absolute minimal dips for the detachment fault in the brittle and ductile parts of the crust. The detachment fault dips obtained from the fault reconstructions using the $35^{\circ}\text{C}/\text{km}$, $30^{\circ}\text{C}/\text{km}$, and $25^{\circ}\text{C}/\text{km}$ paleogeothermal gradients are probably more realistic because they are typical of rapidly extending the crust today (e.g., Sags et al., 200?) and middle Tertiary metamorphic core complexes in the Colorado River extensional corridor (e.g., Foster et al., 1991; Fitzgerald, et al., 1991). These reconstructions show the detachment dipping at 61° and 65° in the upper brittle crust and at 9° and 10° within the BDT and below for the $35^{\circ}\text{C}/\text{km}$ and $30^{\circ}\text{C}/\text{km}$ paleogeothermal gradients, respectively (Fig. 7-8). The fault geometry reconstruction made with the $25^{\circ}\text{C}/\text{km}$ paleogeothermal gradient give maximum values of dip possible

for the detachment at ~53 Ma. With a paleogeothermal gradient 25°C/km the dip of the detachment is 70° in the brittle upper crust and 12° within the BDT and below.

The fault dip reconstructions made here show that the shallower portion of the detachment fault formed in the brittle upper crust at ~53 Ma probably with an original dip of ~61-65°. A detachment dip in this range for the brittle upper crust is in good agreement with Andersonian fault mechanics which states that during extension the maximum principle stress axes (σ_1) are oriented at 90° and brittle normal faults should form with dips >60° (Anderson, 1951). Within the BDT and slightly below, however, σ_1 can become rotated substantially from vertical due the influence of the crustal-scale stress guide created by the high yield strength of the BDT. As a result, detachment faults form with sub-horizontal dips at these depths (Lister and Davis, 1989). Therefore, dips estimates of 9-10° made here for the deeper portion of the detachment fault are certainly reasonable.

Magnitude of Offset on the Detachment

The magnitude of offset across a given fault depends on the fault geometry, slip rate, and duration of slip on the fault (Scott et al., 1998). Therefore, the amount of offset (including both vertical and horizontal displacement) across a fault can be estimated provided these aspects of the fault can be accurately estimated. With the constraints on the geometry, slip rate, and duration of slip constraints summarized above the magnitude of offset on the Anaconda detachment can be estimated for the time interval of ~53-40 Ma. In order to estimate the offset across the detachment during this time three assumptions are made: (1) the slip rate on the detachment between ~51-40 Ma can also be applied to slip on the fault between 53-51 Ma, 2) the geometry of the detachment did

not change significantly between ~53-40 Ma, and 3) the geothermal gradient remained approximately stable from ~53-40 Ma.

Figure 7-9 shows a reconstruction diagram for the detachment fault geometry at ~53 Ma with the paleoisotherms representing temperatures of 200°C, 325°C, and 400°C assuming a paleogeothermal gradient of 35°C/km. The amount of vertical exhumation and horizontal displacement facilitated by the detachment from ~53-40 Ma can be calculated by moving a point along the fault surface for 13 Myr at the estimated slip rate and then measuring the displacement directly from the diagram. The amount of vertical and horizontal displacement on the detachment has been calculated for the range of possible slip rates on the detachment between 53-40 Ma (average slip rate = 0.90 ± 0.59 / $- 0.19$ km/Myr, 1.49-0.71 km/Myr). If rock “X”, representing the DF02-120 greenschist facies biotite granite mylonite, is displaced along the detachment at a slip rate of 0.71 km/Myr for 13 Myr, the total amount of vertical and horizontal displacement = 1.75 km and 8.75 km, respectively. Using the average slip rate of 0.90 km/Myr the total vertical and horizontal displacement across the detachment = 2.0 km and 11.6 km, respectively. Furthermore, if rock X is displaced along the detachment at a slip rate of 1.49 km/Myr then the total vertical and horizontal displacement from ~53-40 Ma = 7.3 km and 16.1 km, respectively (Fig. 7-9).

These calculations indicate the possible range of vertical and horizontal displacement on the detachment from ~53-40 Ma is 1.75-7.3 km and 8.75-16.1 km, respectively. The range of possible displacement along the detachment during this time interval is large because of the large errors on the slip rate estimate. However, because the greenschist facies mylonites cooled rapidly ($\geq 125^\circ\text{C}/\text{Ma}$) they had probably just

passed upwards into the steeper portion of the detachment by ~40 Ma. This would require a minimum of 2.4 km and 13.8 km of vertical and horizontal displacement, respectively, on the detachment from ~53-40 Ma.

Note the constraints on the magnitude of offset on the Anaconda detachment made here are only for vertical and horizontal displacement of the now exhumed greenschist mylonites during the time interval of ~53-40 Ma. During this time, the greenschist mylonites were uplifted to crustal depths above the brittle-ductile transition. These constraints do not take into account the continued vertical and horizontal displacement of the mylonites into the brittle upper-crust and towards the surface, presumably from ~40-30 Ma (see constraints on the duration of extension above). Another way to constrain the amount of horizontal displacement on the detachment, which does take into account extension from ~53-30 Ma is to reconstruct the upper plate to the lower plate using a structural “pinning point.” Figure 7-10 displays a geologic map of the ACC showing the Anaconda detachment, which separates the lower plate (to the west) from the upper plate (to the east). Two intrusions are highlighted here: 1) the SLS granodiorite exposed in the ACC lower plate labeled “A” and 2) a detached granodiorite block in the upper plate labeled “B.” These two intrusions share very similar mineralogies and textures. In addition, a sample from the SLS granodiorite (WG04-114) and the detached upper plate granodiorite (DF02-114) gave very similar biotite $^{40}\text{Ar}/^{39}\text{Ar}$ cooling ages (74.0 ± 0.9 and 76.3 ± 1.1 Ma, respectively, Table 6-2). Furthermore, the major and trace element compositions of these two samples suggest the two intrusions are related by fractional crystallization and/or assimilation (AFC, Appendix D). These similarities suggest the two intrusions were originally part of the same intrusive body prior to the onset of

extension in the ACC at ~53 Ma. The fact that the detached upper plate granodiorite block lies to the ESE of the SLS granodiorite (the approximate extension direction, Chapter 3) supports its origin as part of the SLS granodiorite as well. Reconstructing the SLS granodiorite and detached upper plate granodiorite indicates ~25-28 km of horizontal displacement was facilitated on the Anaconda detachment from ~53-30 Ma (Fig. 7-10). Note if the the Anaconda detachment slipped at the average slip rate calculated above (0.9 km/Myr) from ~53-30 Ma then the total displacement would be ~21 km. This estimate of horizontal displacement is similar to the one made using the two granodiorite structural pinning points.

The amount of vertical displacement (total exhumation) facilitated by the Anaconda detachment may be better constrained using the thermobarometric data obtained from the LISZ in this study. Because the LISZ is Late Cretaceous in age (~75-74 Ma, see above and Chapter 4) and it lies structurally beneath the Eocene greenschist facies mylonite zone in the eastern ACC (Chapter 3) the pressure-temperature estimate from the LISZ can be used to constrain the maximum amount of exhumation. The pressure-temperature estimate for sample ME-231, meta-Greyson pelitic paragneiss from the LISZ, gave upper-amphibolite facies pressures and temperatures of ~3.2-5.3 kbar and 750-825°C (Chapter 5). These pressures correspond to crustal depths of ~10-16 km, assuming an increase in pressure of 0.33/km depth. Therefore, a maximum of 16 km of vertical displacement (total exhumation) was facilitated by the Anaconda detachment after ~53 Ma, assuming no extension occurred between the late Cretaceous (~75-74 Ma) and middle Eocene time. The maximum total vertical displacement estimate made here (based on thermobarometry) is consistent with the detachment reconstruction shown in

figure 7-9. Based on this detachment reconstruction (using a geothermal gradient = 35°C/km) the greenschist mylonites now exposed in the eastern ACC were exhumed from a crustal depth of ~13 km, near the brittle-ductile transition.

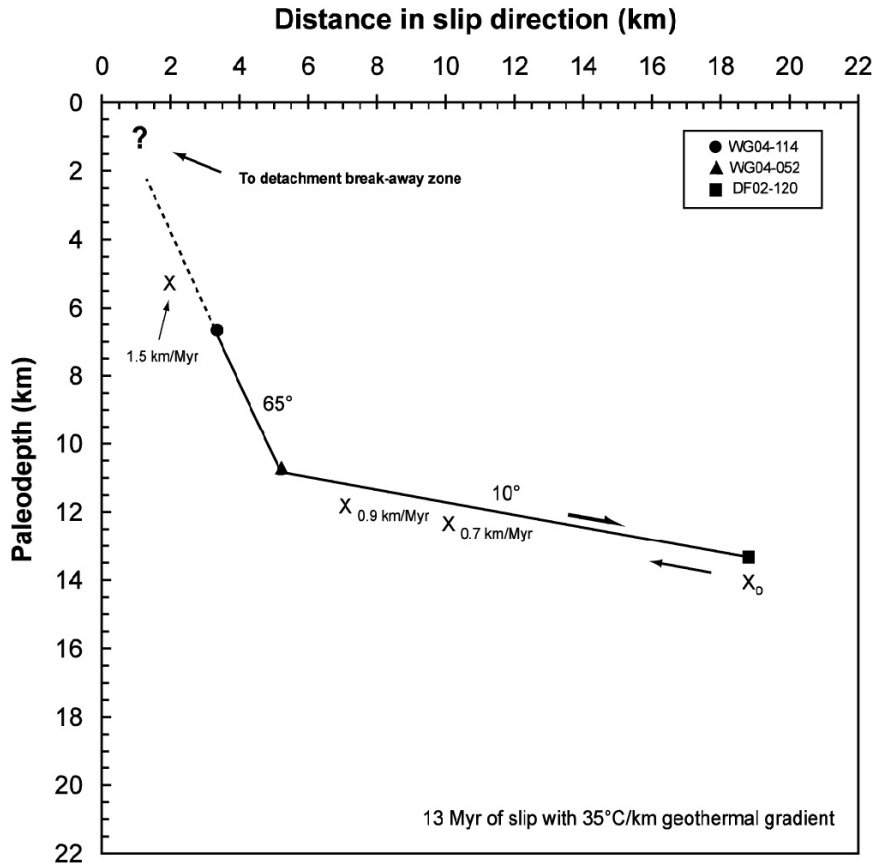


Figure 7-9. Distance in slip direction vs. paleodepth diagram showing magnitude of offset on the detachment with variable slip rate from ~53-40 Ma with a geothermal gradient of 35°C/km. Rock "X" represents the greenschist mylonites now exposed at the surface in the eastern ACC lower plate (see text).

Chapter 8 CONCLUSIONS

Age and Pressure-temperature Constraints on High Grade Metamorphism in the ACC lower plate: Origin of the Lake of the Isle Shear Zone

Thermobarometric data obtained from the attenuated Lower Belt Greyson migmatitic paragneiss, within the Lake of the Isle shear zone (LISZ) in the ACC lower plate, show that anatexis occurred at uppermost-amphibolite facies pressure-temperatures conditions at ~3.2-5.3 kbar and 750-825°C (Chapter 5). Granitic leucosome found within pressure shadows between boudins shows that ductile deformation accompanied this metamorphism (Chapter 3). U-Pb zircon crystallization ages from the deformed quartz diorite sill in the LISZ and the Storm Lake Stock (SLS) granodiorite which cross-cuts the LISZ indicate that uppermost-amphibolite facies metamorphism and ductile deformation in the LISZ occurred at ~75-74 Ma (Chapter 4). The meta-Greyson migmatitic paragneiss, located directly beneath the greenschist mylonite zone and brittle detachment in the ACC, are not the result of decompressional anatexis during exhumation of the ACC lower plate in the Eocene (as in the BCC to the west, e.g., House et al., 1997; Foster et al., 2001). Rather, the meta-Greyson migmatites were formed during anatexis related to the emplacement of the quartz diorite sill in the Late Cretaceous in the LISZ, most likely in a compressional tectonic setting.

Exhumation and Cooling History of the Middle Eocene Anaconda Metamorphic Core Complex:

The thermochronological data set obtained from the Anaconda metamorphic core complex (ACC) lower plate transect in this study provides several constraints on the

exhumation and cooling history of the ACC during the Eocene: (1) The age of the onset of extension in the ACC is indicated to be ~53 Ma by the marked break in the slope of the cooling age curve on the age vs. distance diagram constructed from the lower plate mica cooling ages (Fig. 7-5). This thermochronology-based age constraint is in good agreement with the one U-Pb zircon crystallization age of 53 ± 0.6 Ma from mylonitic granodiorite within the greenschist facies mylonitic shear zone (Foster et al., 2006a). Thus, the onset of extension in the ACC is now well constrained and confirmed to be at ~53 Ma, coincident with the onset of extension in the BCC to the west (Foster et al., 2001, 2006a). Furthermore, (2) the cooling ages from micas in the greenschist facies mylonites in the eastern study area show that extension in the ACC continued until at least ~40-39 Ma. These cooling ages record the time at which ductile deformation ceased in the exposed part of the greenschist mylonitic shear zone and do not take into account their continued uplift into the brittle upper crust. However, apatite fission track ages from the southern Anaconda-Pintlar Range (Foster and Raza, 2002), suggest brittle extension in the ACC continued to ~30 Ma. Thus, extension in the ACC likely spanned from ~53-30 Ma, the synchronous with extension in the BCC to the west (Foster et al., 2001; Foster and Raza, 2002). (3) The lateral cooling age gradient, defined by mica cooling ages that progressively young to the east across the ACC lower plate, confirms that tectonic unroofing of the lower plate occurred by top-to-the-east-southeast directed detachment of the upper plate from ~53-39 Ma; this is consistent with the extension direction suggested by the mineral stretching lineations in the greenschist mylonites (102-108°, Kalakay et al., 2003). (4) Thermochronological data from the lower plate show the original Anaconda detachment (at ~53 Ma) was an east-dipping listric-shaped normal

fault with a steeply dipping ($54\text{-}70^\circ$) portion in the brittle upper crust and a low-angle ($\sim 7\text{-}12^\circ$), sub-horizontal portion in the middle crust near the brittle-ductile transition (Chapter 7). The ACC lower plate was exhumed along a single east-dipping mylonitic shear zone and brittle detachment system during the Eocene synthetic to the east-dipping detachment in the BCC to the west. The original geometry of the Bitterroot detachment cannot be constrained to such detail due to deeper erosion of the detachment zone (D. Foster, per comm.).

(5) Thermochronological data obtained in this study were also used to constrain the slip rate on the ACC detachment. These data show that between $\sim 53\text{-}40$ Ma, the time-averaged slip rate on the detachment was ~ 0.9 km/Myr. Currently, slip rates have not been constrained for detachments in any other metamorphic core complex north of the Snake River Plain (SRP). Thus, no comparison can be made with these core complexes, including the BCC at this time. However, the slip rate for the ACC detachment is significantly low compared to detachment time-averaged slip rates of $\sim 3.0\text{-}7.0$ km/Myr from middle Tertiary metamorphic core complexes in the Colorado extensional corridor of the southwestern United States (e.g., Foster and John, 1999). Therefore, the rates of extension in middle Eocene metamorphic core complexes north of the (SRP) may have been much slower, at least initially, compared to later extension in the middle Tertiary metamorphic core complexes to the south. To fully compare the rates of extension in these separate regions slip rates are needed for later brittle extension in the ACC (i.e., during the $\sim 40\text{-}30$ Ma time interval) and slip rates are needed for the other core complexes north of the SRP. Low temperature thermochronological data (e.g., apatite

fission-track and (U-Th)/He apatite cooling ages) can be used to constrain this later lower temperature brittle extension (e.g., Stockli, 2005).

(6) Constraints have been placed on the amount of offset on the ACC detachment using the thermochronological data set obtained in this study. These data show that a minimum of 13.8 km and 2.4 km of horizontal displacement and vertical exhumation, respectively, occurred along the detachment between ~53-40 Ma. However, this amount of offset on would have exhumed the greenschist mylonites to crustal depths only just above the brittle-ductile transition which was probably at a depth of ~10-12 km (assuming a geothermal gradient of 35°C/km, Fig. 7-9). These estimates of offset do not account for uplift of the mylonites in the brittle upper crust, presumably with continued brittle extension and exhumation of the greenschist mylonites through the shallower crust from ~40-30 Ma. Major and trace element geochemistry from similar Late Cretaceous granodiorite intrusions from the lower plate and the detached upper plate suggest they are related by fractional crystallization (with minor assimilation, AFC, Appendix D) and originally part of the same pluton (the SLS). Reconstructing these granodiorite intrusions shows the ACC detachment accommodated ~25-28 km of displacement after the onset of extension at ~53 Ma. Interestingly, if a slip rate of ~0.9 km/M.y. is assumed for the Anaconda detachment from ~53-30 Ma then ~22 km offset was accommodated along the detachment during this time interval. This is similar to the displacement estimate made by reconstructing the granodiorites from the lower and upper plates indicating a displacement estimate on the order of ~22-28 km is realistic.

(7) Thermobarometric data from the LISZ show that upper amphibolite facies metamorphism in the Late Cretaceous occurred at ~3.2-5.3 kbar, which corresponds to

depths of ~10-16 km depths (0.33 kbar/km) for the shear zone at ~75-74 Ma (see above). Therefore, a minimum of ~10 km of vertical exhumation was facilitated along the ACC detachment during the Eocene. This estimate is consistent with the exposed Eocene mylonites being of lower to middle greenschist facies and located near the brittle-ductile transition (at a depth of ~10-12 km, assuming a 35°C/km geothermal gradient) at the onset of extension.

The conclusions summarized above show several aspects of Eocene extension in the ACC are remarkably similar to extension in the BCC located to the west. However, the data obtained in this study show important differences between these core complexes which include: (1) Extension in the ACC was accompanied by greenschist facies metamorphism and not by upper-amphibolite facies metamorphism and decompression anatexis as in the BCC. (2) Therefore, total (vertical) exhumation in the ACC ($\leq 10-16$ km) is much less than in the BCC, which is estimated to be ~20-25 based on thermobarometric data from early to middle Eocene migmatites in the eastern lower plate. In addition, (3) Displacement in the ACC (~22-28 km) is approximately half the displacement in the BCC, which is ~40-50 km based on based on reconstructions of Cretaceous dioritic plutons in the detached upper plate with similar aged dioritic plutons in western BCC lower plate (Foster et al., 2006a).

The similarities (and differences) in the timing and kinematics of extension between the ACC and BCC permit the proposed tectonic model for Eocene extension south of the Lewis and Clark line (e.g., O'Neill et al., 2004). These two metamorphic core complex therefore represent one continuous and integrated extensional system which accommodated large-scale crustal extension (~60-75 km of eastward displacement) south

of the Lewis and Clark line from ~53-30 Ma. Both of the metamorphic core complexes were exhumed along single separate, but synthetic, east-dipping detachments. In addition, the thermochronological from this study show the Anaconda detachment was sub-horizontal near the brittle-ductile transition and therefore does not likely merge with the Bitterroot detachment at depth. Therefore, a “nested” position for the Anaconda detachment with respect to the Bitterroot detachment is geologically plausible.

Regional Tectonic Context

The results from this study show that synchronous exhumation of the BCC and ACC accommodated large-scale extension south of the LCL beginning in the Eocene at ~53 Ma. The onset of extension in the BCC and ACC was coincident with the onset of extension in metamorphic core complexes north of the LCL in northeastern Idaho and eastern Washington (the Priest River, Kettle, and Okanagan), southern British Columbia (the Shuswap) and within the LCL (the Clearwater). Extension in all these metamorphic core complexes began during the time interval of ~54-52 Ma (Foster et al., 2006a, and references cited therein). These metamorphic core complexes formed in the previously thickest parts of the Sevier hinterland immediately following the end crustal shortening in the foreland fold-and-thrust belt directly to the east. The early extension in these metamorphic core complexes was accompanied by voluminous back-arc Kamloops-Colville-Challis-Absaroka (KCCA) magmatism; this magmatism was concentrated in regions where the Eocene extension was most intense (Armstrong and Ward, 1992; Morris et al., 2000; Breitsprecher et al., 2003; Foster et al., 2001).

Exhumation of metamorphic core complexes in southern British Columbia and the northwestern United States was linked regional dextral transtension along major dextral strike-slip fault zones during the Eocene. In southern British Columbia, extension in the

Shuswap metamorphic core complex was linked to dextral strike-slip motion along the approximately margin-parallel northern Rocky Mountain trench and Yalakom-Ross Lake fault zones (Price and Carmichael, 1986; Foster et al., 2006a). In the northwestern United States, regional dextral transtension along the northwest-west trending Lewis and Clark line drove extension and exhumation of metamorphic core complexes during the Eocene (Foster et al., 2006a). Eocene extension in metamorphic core complexes to the north of the LCL was directed approximately E-W (e.g., Shuswap metamorphic core complex) and ENE-WSW (e.g., Priest River metamorphic core complex). South of the LCL, Eocene extension was directed to the ESE in the BCC and ACC, approximately parallel to the strike of the LCL. Therefore, the LCL apparently served as a regional accommodation zone between E-W and ENE-WSW directed extension to the north of the line and ESE directed extension to the south within the BCC and ACC (Foster et al., 2006a).

Regional dextral transtension, exhumation of metamorphic core complexes, and large-scale crustal extension along major strike-slip faults zones in southern British Columbia and the northwestern United States during the Eocene was most likely driven by changes in plate boundary forces along the western margin of the North American Plate. Plate reconstructions show the angle of convergence between the North American and Pacific Ocean basin plates became increasingly oblique beginning in the early to middle Eocene, coincident onset of large-scale extension and exhumation of the metamorphism core complexes southern British Columbia and the northwestern United States (Haeussler et al., 2003). An increase in the obliquely of convergence (increasing right-lateral convergence with time) would have created traction along the western

margin of the North American Plate driving dextral transtension and extension inboard of the plate boundary during the Eocene (Breitsprecher et al., 2003).

Plate reconstructions also indicate the presence of a slab window (a gap between subducting plates) beneath the North American Cordillera of southern British Columbia and the northwestern United States during the early to middle Eocene (Thorkelson and Taylor and 1989; Breitsprecher et al., 2003; Haeussler et al., 2003). The approximate orthogonal subduction of the Kula-Farallon ridge (or the Resurrection-Farallon ridge, e.g., Haussler et al., 2003) during the Eocene would have created the slab window. The presence of a slab window beneath the North American Cordillera of southern British Columbia and the northwestern United States at this time is consistent with voluminous Eocene KCCA magmatism in the back arc region (Breitsprecher et al., 2003). The back-arc KCCA magmatism may have been the result asthenosphere upwelling through the slab window and subsequent partial melting of the lithosphere (Foster et al., 2006a). Heating and partial melting of the lithosphere above a slab window may have caused thermal weakening of the lithosphere which may have also helped to facilitate large-scale extension and exhumation of metamorphic core complexes in southern British Columbia and the northwestern United States beginning in the early to middle Eocene (Breitsprecher et al., 2003).

APPENDIX A METHODOLOGIES

Field Mapping and Sampling Methods

Prior to this study a detailed, accurate map of the geology from Storm Lake to the Mill Creek area of the Anaconda-Pintlar Range was not available. Thus, production of such a map was necessary to work out the complex structures exposed in the ACC lower plate. Mapping these structures in detail was essential in understanding the deformational history of the lower plate rocks. Furthermore, this mapping was needed to determine spatial relationships between rock samples collected for the analytical work of this study (i.e., $^{40}\text{Ar}/^{39}\text{Ar}$ thermochronology, U-Pb geochronology, thermobarometry, and major and trace element geochemistry and modeling).

The geology of the ACC lower plate exposed east of Storm Lake was mapped during multiple transects made by foot over a five week and one week period during the summers of 2004 and 2005, respectively. During the transects, unit contacts were hand drawn on several 1:15000 scale topographic base maps created from the Storm Lake, Mt. Evans, and Mt. Haggin 7.5 minute quadrangles. In addition, one hundred structural data points were collected along the mapping transects. These include strike-and-dip measurements on metamorphic foliations, unit contacts, fault surfaces, joints, and cleavage. Lineation measurements made included mesoscopic fold hinges, slickenlines on fault surfaces, and limited stretching or mineral lineations on foliation surfaces. The hand drawn geologic maps were then digitally drafted into one continuous 1:24000 scale geologic map using Adobe Illustrator© version 10. The mapping of Heise (1983) was

added to the easternmost map area in the Mount. Haggin area. In addition, some mapping of Emmons and Calkins (1914) and Kalakay *et al.* (unpublished mapping) were added to fill gaps in the final map.

The rock samples analyzed in this study were collected during transects made while mapping in the summers of 2004 and 2005 with the exception of samples ME-6, ME-231, SL-38, Ug-1, DF02-113, DF02-114, DF02-116a, DF02-117a, DF02-118a and b, and DF02-120. Samples ME-6, ME-231, SL-38 and Ug-1 were collected by Tom Kalakay during the summer of 2002. DF02 samples were collected by David Foster in summer 2002.

$^{40}\text{Ar}/^{39}\text{Ar}$ Thermochronology Methods

Sample Preparation and Irradiation

In preparation for $^{40}\text{Ar}/^{39}\text{Ar}$ thermochronology, thin sections were made from select rock samples collected during the summer of 2004. Billets were cut from these samples and sent to Petrographic International for the thin section preparation. The thin sections were necessary to inspect the quality of mineral phases in the rock samples to be used in $^{40}\text{Ar}/^{39}\text{Ar}$ analyses. Only rock samples which exhibited fresh and unaltered micas, k-feldspars and hornblendes were used for the analyses $^{40}\text{Ar}/^{39}\text{Ar}$ analyses.

The selected samples were then crushed and milled into a medium to fine-grained size using a Sturtevant rock Jaw Crusher and Bico Pulverizer type UA disk mill, respectively. Each disk milled samples was then dry sieved in a stack of (from top down) 30, 40, 50, 60, 80 and 100 mesh sieves. The 40 and 50 mesh fractions were kept for further separation of biotite, muscovite and k-feldspar. However, in the case of hornblende, 60 and 80 mesh fractions were kept for further separation. This was done to avoid inclusion-rich hornblendes in some rock samples as observed in thin section.

The sieved rock samples were then processed with Tetrabromoethane (TBE) and Methylene Iodine (MI) heavy liquids (densities of 2.96 and 3.33 g/cm³, respectively) to separate the micas, k-feldspars and hornblendes based on densities. These separates were rinsed with ethanol (for TBE) and acetone (for MI) 2-3 times following heavy liquid separation. A Frantz magnetic separator Model L-1 was then used to separate the biotite and hornblende from non-magnetic phases. Only the most magnetic biotite and hornblende Frantz separates were kept to avoid inclusion-rich minerals. All mineral separates were then hand picked under a binocular microscope for better refinement using standard picking tools (i.e., nylon brushes, Pyrex[®] glass dishes and wax weighing paper). Some hand-picked biotite separates were given an ultrasonic bath in dionized H₂O for approximately fifteen minutes to remove any altered materials.

The cleansed, hand-picked mineral separates along with GA1550 biotite flux monitors (98.79 ± 0.5 Ma, see Reene et al., 1998) were then individually packaged in aluminum foil (~ 10 mg for mineral separate, 1 mg for flux monitors) and sealed in a quartz glass tube by melting the ends of the tube. The mineral separates and flux monitors were irradiated for 2 hrs in a 1.1 MW TRIGA MARK II research nuclear reactor at the Oregon State University Radiation Center. For a more detailed description of these facilities and irradiation methods see http://ne.oregonstate.edu/facilities/radiation_center/. Note micas, k-feldspar and hornblende from the DF02, Ug-1 and SL-38 samples underwent the same sample preparation and irradiation as described above. However, these samples were irradiated in an earlier irradiation batch for ten hours rather than two and no thin sections were made available.

$^{40}\text{Ar}/^{39}\text{Ar}$ Analytical Instrumentation and Procedures

The $^{40}\text{Ar}/^{39}\text{Ar}$ analyses were carried out in the noble gas laboratory at the Department of Geological Sciences, University of Florida. A combination of both laser ablation and furnace step-heating techniques were utilized to extract Ar gas from mineral separates. Micas were step-heated by both laser ablation and furnace, where k-feldspar and hornblende separates underwent furnace step-heating only. Laser ablation step-heating of mica separates was facilitated by a water-cooled New Wave Research model MIR10 30W CO₂ laser. During laser step-heating the New Wave laser was manually controlled using LAS (laser ablation software) version 1.3.0.1 by New Wave Research. Mica separates were ablated a total of 5-15 steps under a 1750 μm continuous wavelength focused laser beam at 2-5.5% power. A final laser fusing-step was employed at 10-12% power. The step-heating schedule used for laser ablation varied and was adjusted accordingly to maximize Ar gas output for the mineral separates. A water-cooled double-vacuum resistively heated furnace was used to step-heat k-feldspar and hornblende separates. The furnace step-heating analyses were controlled manually using LabSpec version 3.1 by LabView.

Ar gas extracted from laser and furnace step-heating was transferred by vacuumed lines to a getters trap for 5-10 min to remove volatiles. The cleansed Ar gas was subsequently analyzed in a gas-sourced Mass Analyzer Products Model 215-50 mass spectrometer equipped a filament for gas ionization and a magnetic sector mass discriminator followed by a single faraday collector to measure the isotopic abundances of ^{36}Ar , ^{37}Ar , $^{38}\text{Ar}^*$, ^{39}Ar , and ^{40}Ar . Cold laser blanks were typically analyzed at the beginning of each analytical session and every five steps after. The laser blanks were

made by closing the cleansed laser chamber for two min and then passing the blank gas to the mass spectrometer just as a sample. Heated furnace blanks were made by closing and heating the empty furnace to 750°C, 1000°C and 1100°C prior to sample step-heating. Data files produced from the argon gas and blank analyses were then imported into the program ArArCALC version 2.2 by Koppers (2002) for data regression and $^{40}\text{Ar}/^{39}\text{Ar}$ cooling age calculations. ArArCALC uses Excel[®] by Microsoft to plot argon data tables, age plateaus and isochrons. ArArCALC was also used to calculate J-values from total fusion analyses of the GA1550 biotite flux monitors. These J-values were then applied to $^{40}\text{Ar}/^{39}\text{Ar}$ cooling age calculations.

Thermobarometry

In preparation for thermobarometry, two polished thin sections were prepared from ME-231, migmatitic pelitic cordierite gneiss sampled from the central LISZ. These thin sections were then carbon coated using a PAC-1 PELCO carbon coater Model 9500. The elemental oxide weight percent data needed for the ME-231 thermobarometry were acquired using by electron microprobe analyses at the Department of Earth Sciences, Florida International University (FIU). The polished and coated thin sections were then analyzed at FIU using a JOEL Model 8900R Superprobe electron microprobe. The JOEL Superprobe uses five two-crystal wavelength-dispersion spectrometry (WDS) spectrometers and one electron-dispersion spectrometry (EDS) detector to measure mineral compositions and for back-scatter imaging, respectively. Before these analyses, the JOEL Superprobe was calibrated using in-house mineral standards to measure Na, Mg, Al, Si, K, Ti, Ca, Cr, Mn and Fe compositions in ME-231 mineral phase. For a list of the FIU in house mineral standards see http://www.fiu.edu/~emlab/Inst_EPMA_standards.html. Note these analyses were

carried out with the JOEL Superprobe with the beam current set to 20 nA and an accelerating voltage of 15 kV.

The compositions of garnet, biotite, plagioclase and cordierite were measured in order to calculate phase equilibria and average PT estimates for the ME-231 mineral assemblage. Care was taken only to analyze the most euhedral and clearest mineral grains. Back-scatter imaging allowed fractures and suspicious areas to be avoided. Rim-core-rim spot transects were made across larger intact positions of garnet and cordierite porphyroblasts. In addition, several fine-grained biotite and plagioclase grains were analyzed from the ME-231 matrix. Inclusions were rare in garnet and cordierite porphyroblasts and only a few small biotite inclusions were measured.

The selected elemental oxide weight percents from the electron microprobe analyses were subsequently imported into the program AX by Holland and Powell (2000) to calculation of cation unit formulas (with ferric iron estimations) and mineral end-member activities. Mineral end member activities were then imported into the program THERMOCALC version 3.2 by Powell *et al.* (1998) for average PT calculations for the mineral assemblage of ME-231. Pressure-temperature calculations were also made using the program Geothermobarometry (GTB) v 2.1 by Spear and Kohn (1999). The details of thermodynamic calculations made using the programs AX, THERMOCALC, and GTB are described in the thermobarometry results section.

U-Pb Geochronology

Sample Preparation

In preparation for zircon U-Pb analyses, several kilograms of samples WG04-114, Ug-1 and WG05-02 were first crushed to gravel-sized particles using a Sturtevant rock Jaw Crusher. This rock material was then passed through a Bico Pulverizer type UA disk

mill several times until all material fell through a dry 425 μm (40 mesh size) sieve. The < 40 mesh rock fractions were then passed over an inclined water table twice for density separation. The heavy water table fractions underwent further density separation using Tetrabromoethane (TBE) and Methylene Iodine (MI) heavy liquids (densities of 2.96 and 3.33 g/cm^3 , respectively). The MI sink fractions were kept and run through a Frantz isodynamic magnetic separator model L-1 to remove the remaining unwanted magnetic minerals. Each fraction was passed through the Frantz separator several times at a setting of 1.5 volts. For each run, the Frantz trough tilt was decreased until the least magnetic fraction of zircons was obtained (at 0-1°). Individual zircons were subsequently hand-picked from the non-magnetic Frantz fractions using a binocular microscope and standard picking tools (i.e., nylon brushes, Pyrex[®] glass dishes and wax weighing paper). Care was taken to pick the clearest, most euhedral and inclusion-free zircons. In addition, smaller zircons (< 300 μm) were targeted over larger ones to avoid possible inherited cores that if dated would not represent crystallization ages of interest.

In preparation for laser ablation, the individual hand-picked zircon fractions were mounted on separate pieces of adhesive Buehler Meta-Kleer mold base along with several large fragment of FC-1 zircons, the ~1100 Ma external zircon standard chosen for the U-Pb analyses (in house $^{207}\text{Pb} / ^{206}\text{Pb}$ age = 1086.9 ± 5.3 , $^{207}\text{Pb} / ^{235}\text{U}$ age = 1091.5 ± 13.4 , and $^{206}\text{Pb} / ^{238}\text{U}$ age = 1096.7 ± 21.7 Ma). Each unknown and FC-1 pair was then surrounded by a 2.5 cm diameter plastic ring mold and a 5-to-1 mixture of Buehler Epoxicure resin and hardener was poured over the zircons. After hardening, the epoxy zircon mounts were ground down to an even, flat surface and wet-polished using a Buehler Ecomet 6 variable speed grinder and polisher with 600, 800 and then 1200 grit

disks. Each zircon mount was ground and polished to expose an equatorial section of the zircons for laser ablation. The polished zircon mounts were cleaned using sterile Chem-wipes and 2-propanol just prior to loading into the laser ablation chamber.

LA-MC-ICP-MS Instrumentation

Zircon *U-Pb* isotopic data were acquired in this study using laser ablation multi-collector inductively coupled plasma mass spectrometry (LA-MC-ICP-MS). The mass spectrometer employed is a Nu Plasma multi-collector plasma source mass spectrometer produced by Nu-Instruments installed on site at the Department of Geological Sciences, University of Florida. The Nu Plasma mass spectrometer is configured in a standard Nier-Johnson geometry consisting of a plasma torch with focal lens (cones) followed by a 35 cm radius electrostatic analyzer (ESA), a 25 cm radius laminated electromagnet and variable dispersion zoom lenses. These devices are followed by a detector array comprised of 12 sapphire/ceramic Faraday collectors and 3 ion counters mounted on a single fixed mop plate with electron suppressors. The ion counters are comprised of three discrete dynode electron multipliers and a retardation filter to measure isotopic abundances with higher sensitivity than Faraday collectors (for more details see <http://www.nu-ins.com/npdetail.html>). The Nu Plasma mass spectrometer is configured to measure ^{238}U and ^{235}U abundances on Faraday collectors EX-H and H6, respectively and ^{207}Pb , ^{206}Pb and ^{204}Pb abundances on ion counters IC0, IC1, and IC2, respectively. The Nu Plasma mass spectrometer is coupled to a Nu-Instruments DSN 100 desolvation nebuliser. In this study, the DSN 100 was used to introduce a U-Pb calibration solution to the mass spectrometer prior to the analyses (see below). A more detailed description of this Nu Instrument equipment is provided by Simonetti et al. (2005). The Nu Plasma

mass spectrometer has also been coupled with a New Wave 213 nm ultraviolet laser manufactured by Merchantek Products for ablating the solid geologic samples in this study.

LA-MC-ICP-MS Analytical Protocol

All laser ablations in this study were carried out in the presence of a helium carrier gas. The helium carrier gas was introduced directly into the ablation chamber using external Tygon[®] silicon tubing where it mixes with the ablated sample and aids in its transportation to the plasma torch. Use of helium as a carrier gas during single-spot laser ablation analyses has been shown to reduce within-run Pb-U elemental fractionation and increase instrument sensitivity, both desired results (Simonetti et al., 2005). In addition, argon gas was subsequently mixed with the helium and ablated sample mixture just prior to the plasma torch using Tygon[®] tubing and a plastic Y-connector. The argon gas aids in the sample transportation and reacts with a radio frequency coil in the plasma torch box to produce the high temperature plasma needed to ionize the ablated sample (Thomas, 2001).

Prior to each analytical session the Nu Plasma ion counters were calibrated to ensure accurate isotope abundance measurements and proper sensitivity. To achieve this calibration a solution of SRM 3164 U (25 ppb) and SRM 981 Pb (1 ppb) was aspirated into the Nu Plasma mass spectrometer using the DSN 100. The abundances of ²⁰⁴Pb, ²⁰⁶Pb and ²⁰⁷Pb were then measured on the ion counters for a minimum of 1 hour to ensure proper calibration and to warm up the Nu Plasma mass spectrometer. After the ion counter calibration the DSN 100 was disconnected from the Nu Plasma mass spectrometer.

Prior to data acquisition the helium and argon gas flows, laser settings, and Nu-Plasma instrument parameters were carefully tuned to maximize the signal intensities. A standard zircon and an unknown zircon were ablated separately for ~ 60 s while these parameters were adjusted to obtain the best settings. In every analytical session, the best results were obtained with the helium and argon gas flow rates set to 0.6-0.7 L/min and 1.05 L/min, respectively. In addition, best results were obtained with a laser setting of 50-60% power, a 2-4 Hz pulse frequency and a laser spot size of 30-60 μm . Note that all the standard and unknown zircons were ablated under the same gas and laser settings throughout each analytical session as determined at the beginning of the session.

Isotopic data were acquired during the analyses using Time Resolved Analysis (TRA) software provided by Nu-Instruments. Before the ablation of each zircon a 30 s on-peak zero was determined on the blank He and Ar gases with closed laser shutter. This zero is used for on-line correction for isobaric interferences, particularly from ^{204}Hg which is largely derived from the argon gas. Following blank acquisitions individual zircons underwent spot analyses for ~30-60 seconds. The analyses of unknown zircons were “bracketed” by analyzing an FC-1 standard zircon for every 2-6 unknown zircons. These standard zircon analyses were later used to correct raw unknown zircon isotopic analyses (see below). An important feature of the TRA is that it allows the analyst to choose the desired portion (or time) from each analysis used in the subsequent isotopic abundance and ratio calculations. This feature allows the omission of 1) slight spikes in ^{204}Pb over the first few seconds during some of the analyses and 2) Pb-U elemental fractional near the end of each ablation related to deepening of the ablation pit (see Kosler and Sylvester, 2003).

U-Pb Data Reduction and Common Lead Correction

Raw isotopic data obtained from the LA-MC-ICP-MS analyses and TRA software were imported into a Microsoft Excel[®] spreadsheet where they were corrected for instrumental drift (change in instrument sensitivity with time) and isotopic fractionation.

The raw isotopic data were corrected for instrumental drift using the formula:

$$R(\text{sam})_{\text{meas}} \times (1 - \text{Cor}_{\text{fac}} \times (P/N)) \quad (\text{A-1})$$

where $R(\text{sam})_{\text{meas}}$ is the raw isotopic ratio for the sample and Cor_{fac} is a correction factor derived from taking the difference between the measured isotopic ratios of the two standards which “bracket” the measured isotopic ratios of the unknowns (standard 2 minus standard 1) and then dividing this value by the measured isotopic ratio of the first standard (standard 1). P is the number of the bracketed unknowns and N is the number of intervals between the unknowns and bracketing standards (e.g., five unknowns bracketed between two standards would be numbered 1, 2, 3, 4, and 5 and have 6 intervals). This equation was applied to each set of unknown bracketed between pairs of standards analyses for a given analytical session. The drift corrected unknown zircon isotopic ratios were then corrected for isotopic fractionation using the following equation:

$$R(\text{sam})_{\text{true}} = R(\text{sam})_{\text{meas}} \times [R(\text{std})_{\text{true}} / R(\text{std})_{\text{meas}}] \quad (\text{A-2})$$

where $R(\text{sam})_{\text{true}}$ is the drift and fractionation corrected unknown ratio and $R(\text{sam})_{\text{meas}}$ and $R(\text{std})_{\text{meas}}$ are the raw isotopic ratios of the unknown and standard zircons, respectively. $R(\text{std})_{\text{meas}}$ is the raw isotopic ratio of the first standard measured during the analytical session. $R(\text{std})_{\text{true}}$ is the true isotopic ratio of the external standard zircon determined by a separate isotopic analyses; the $R(\text{std})_{\text{true}}$ values for the standard FC-1 zircons have been determined by ID-TIMS analyses ($^{207}\text{Pb} / ^{206}\text{Pb} = 0.0762$, $^{207}\text{Pb} / ^{235}\text{U} =$

1.9428 and $^{206}\text{Pb} / ^{238}\text{U} = 0.1850$, Paces and Miller, 1993). This “standard-sample-standard” correction for drift and isotopic fractionation is different from the “Tl-doping” correction employed in many previous LA-MC-ICP-MS studies. Recent work has shown this method is equally effective given the external standard is well characterized, as is FC-1 zircon standard (e.g., Paces and Miller, 1993; Simonetti et al., 2005; Jackson et al., 2004; Jeffries et al., 2003).

Error propagation used follows that of Horstwood et al. (2003) where analytical errors of the unknown zircon analyses are combined with errors from the analyses of the standard FC-1 zircons by

$$(\sigma_c / C)^2 = (\sigma_{mA} / A)^2 + (\sigma_B / B)^2 \quad (\text{A-3})$$

where A is the raw unknown zircon isotopic ratio and σ_{mA} is the error of the mean of the analysis. B is the raw standard FC-1 zircon isotopic ratio and σ_B is the standard deviation of all the standard FC-1 zircon analyses for a given analytical session. C is the drift and mass bias corrected unknown zircon ratio and σ_c is propagated error for the unknown zircon analyses of interest. Error correlation factors were approximated between isotopic ratios simply by dividing their individual propagated errors. For example, an error correlation factor between the $^{206}\text{Pb} / ^{238}\text{U}$ and $^{207}\text{Pb} / ^{235}\text{U}$ error is obtained by dividing the $^{206}\text{Pb} / ^{238}\text{U}$ error by the $^{207}\text{Pb} / ^{235}\text{U}$ error (e.g., Horstwood et al., 2003).

The drift and mass bias corrected isotopic ratios and propagated errors were imported into Isoplot version 3.09a by Ludwig (2004) where Tera-Wasserburg type and traditional concordia diagrams were constructed for zircon analyses of the two granitoid samples (WG04-114 and Ug-1) and the leucosome sample WG05-02, respectively. $^{206}\text{Pb} / ^{238}\text{U}$ weighted mean age plots were also constructed for the granitoid samples. Note

however, that isotopic data plotted on Tera-Wasserburg concordia diagrams are not corrected for common lead. However, individual $^{207}\text{Pb} / ^{235}\text{U}$ and $^{206}\text{Pb} / ^{238}\text{U}$ ages were calculated from both common lead corrected and uncorrected data for comparison. For these data, the common lead correction was carried out using the “207 method” as outlined in Kosler and Sylvester (2000), where common ^{206}Pb is estimated using measured $^{207}\text{Pb} / ^{206}\text{Pb}$ ratios; the 207 method assumes concordance. For the leucosome sample, $^{207}\text{Pb} / ^{235}\text{U}$ and $^{206}\text{Pb} / ^{238}\text{U}$ ratios were corrected for common lead using measured ^{204}Pb as described by Williams (1998). Note the common lead isotopic ratios used in both correction methods were approximated using the two-stage lead evolution model of Stacey and Kramers (1975). Furthermore, individual $^{207}\text{Pb} / ^{206}\text{Pb}$ ages were estimated from the uncorrected isotopic data of sample WG05-02 by interpolating between known $^{207}\text{Pb} / ^{206}\text{Pb}$ ratios and ages in Table 18.3 of Faure (1986). A probability density plot was made for the $^{207}\text{Pb} / ^{206}\text{Pb}$ ages using Isoplot.

Major and Trace Element Geochemistry

Clean, representative portions of samples DF02-114, WG04-114 and Ug-1 were first crushed to gravel-sized particles using a Sturtevant rock Jaw Crusher. These fractions were then reduced to coarse sand using a Progressive Exploration Products “mini” Jaw Crusher model 150. The coarse sand fractions were then loaded into individual sealed ceramic cylinders along with two small ceramic powering balls. The sealed ceramic cases were then shaken in a Spex model 8000 mixer/mill for 30-60 minutes to create homogenized whole-rock powders from the samples.

The whole-rock powders were subsequently sent to Acme Analytical Laboratories Ltd (Vancouver, B.C.) where both major and trace element analyses were carried out. In preparation for the analyses, the whole rock powders were first dissolved using a 4-acid

digestion. Then major and trace element data were acquired using ICP-MS (inductively coupled plasma mass spectrometry). For details of the Acme ICP-MS analytical procedures see <http://www.acmelab.com/cfm/index.cfm?It=100&Id=1>.

APPENDIX B
ACC LOWER PLATE LITHOLOGIC UNIT DESCRIPTIONS AND DISTRIBUTION

General Statement

Lower plate rock units mapped in the current study area fall into three distinct age categories: 1) Metasedimentary strata correlated with the Mesoproterozoic Belt Supergroup and Middle Cambrian formations, 2) Late Cretaceous intermediate-composition intrusive rocks and 3) Middle Eocene intermediate-to-felsic-composition intrusive rocks. Notably, all Belt Supergroup and Middle Cambrian correlated metasedimentary strata in the study area have been subjected to middle to upper-amphibolite grade metamorphism. In some areas, pronounced ductile deformation and tectonic attenuation of the metasedimentary strata accompanied this metamorphism (e.g., within the Lake of the Isle shear zone). In addition, in the easternmost part of the study area intrusive rock units were deformed under greenschist facies conditions (e.g., mylonitic granitoids of the Anaconda mylonite). For simplicity, the details of such metamorphism and deformation are described and discussed in later sections. Here, general lithologic descriptions, distinguishing characteristics and overall distribution of the mapped rock units are given to provide a “metamorphic-stratigraphic” framework for Belt Supergroup and Middle Cambrian correlated metasedimentary strata and basic descriptions for the Late Cretaceous to Eocene intrusive rocks.

Belt Supergroup and Middle Cambrian Metasedimentary Strata Correlation

All metasedimentary strata exposed in the study area were originally mapped, described and correlated with the Belt Supergroup (then, the Belt Series) and Middle

Cambrian section by Emmons and Calkins (1913). Much later, mapping and correlations made by Lonn et al. (2003) largely agree with the early work, although Lonn et al. (2003) use more current Belt nomenclature for this region (see Winston and Link, 1992 for a review and history of the Belt nomenclature). However, one difference is that Lonn et al. (2003) group the Middle Cambrian formations into one undivided group, unlike Emmons and Calkins (1913) who mapped and correlated with individual formations. In this study, Belt correlation follows that of Lonn et al. (2003), while Middle Cambrian-equivalent metasedimentary strata are mapped and correlated with individual formations as Emmons and Calkins (1913). Metamorphosed Belt Supergroup units mapped include (from old to young) the Greyson Formation, Ravalli Group, Helena Formation, and Missoula Group. Middle Cambrian-equivalent metasedimentary strata mapped include (from old to young) the Flathead, Silver Hill, and Hasmark Formations.

Belt Supergroup-equivalent Metasedimentary Strata

Pelitic Schist and Migmatitic Paragneiss

The structurally lowest metasedimentary rock unit exposed in the study area is largely comprised of a distinct reddish-brown to dark-brown or dark-grey schist correlated with the lower-Belt Greyson Formation. Because of its dark color, this schist unit is easily distinguished in the field, especially where in contact with relatively lighter-colored intrusive rocks. In general, the schist is fairly massive (and highly schistose), medium-grained containing abundant biotite with less (in decreasing abundance) garnet + sillimanite + quartz + plagioclase + K-feldspar ± muscovite. Excellent exposures of this rock unit are found along the walls of Sullivan Creek and in the uppermost Tenmile Creek drainage. Exposures in the Tenmile Creek headwall are characterized by alternating garnet-rich (smaller garnets 1-4 mm in diameter) and quartzofeldspathic

horizons. Individual garnet-rich horizons range in thickness from a few millimeters to a several centimeters.

In the central mapping area, north of the continental divide the schist grades to cordierite-bearing paragneiss. Good exposures of the paragneiss are found in several glacially polished outcrops southwest of the Lake of the Isle and in the uppermost reaches of East Fork of the Twin Lakes Creek drainage. At these localities, the paragneiss is characterized by abundant sillimanite giving some outcrops a distinct battleship-grey hue. Mineral phases subordinate to sillimanite include (in decreasing abundance) biotite + garnet + K-feldspar + quartz + plagioclase + cordierite. Note several outcrops of the paragneiss are migmatitic and show evidence for partial anatexis (melting) during severe ductile deformation. These outcrops are characterized by boudinaged quartzite-rich horizons, mesoscopic (nearly isoclinal) folds and transposed planar foliations; where granitic leucosome is found in boudin necks or as concordant, thin elongate pods within the transposed fabrics .

Biotite Quartzite Paragneiss

A prominent mica-rich quartzite unit overlies the Greyson-correlated schist and paragneiss and is correlated with the Ravalli Group strata. The contact between these two units is observed only along the continental divide on the western flank of Mount Howe, where pelitic horizons of the Greyson gradually grade to more and more quartzite of the Ravalli. In most places, the meta-Ravalli Group strata consist of medium-grey to dark-grey or dark-blue medium-grained quartzite paragneisses. These quartzite paragneiss are comprised of more or less pure quartzite horizons that alternate with more pelitic (or schistose) horizons consisting of variable amounts of biotite (commonly

chloritized) + K-feldspar + quartz + plagioclase ± sillimanite. Individual horizons (gneissic bands) range in thickness from a few millimeters to several meters in some places. These quartzite gneisses are also characterized by common mesoscopic-scale folds, small-scale to outcrop-scale shear bands (mm to 10's of m thick) and rare boudins. Interestingly, some Ravalli outcrops preserve less deformed horizons with relic cross-bedding between highly deformed horizons; suggesting strain was distributed heterogeneously at some levels.

The upper ~100-200 m section of the metamorphosed Ravalli Group is distinctively more pelitic than lower sections. The best exposure of the pelitic section is found adjacent to a small unnamed lake southeast of Storm Lake in the uppermost Twin Lakes Creek drainage. This pelitic horizon was also documented by both Emmons and Calkins (1913) and Lonn et al. (2003); the latter suggest correlation with the Saint Regis Formation of the uppermost Ravalli Group. Notably, Lonn et al. (2003) document kyanite in this upper pelitic horizon. Limited fresh kyanite was found at this locality but only seen in thin section (see description of the LISZ above). However, pseudomorphs resembling both kyanite and garnet are abundant in the more pelitic horizons of the uppermost Ravalli Group at this locality.

Calc-silicate Paragneiss

Above the Ravalli Group lies a thick sequence of deformed, largely calc-silicate paragneiss correlated with the Helena Formation (eastern equivalent to the Wallace Formation, both part of the Middle Belt Carbonate; Winston and Link, 1992). The calc-silicate paragneiss is typically a dense, fine-grained and strongly layered rock. Light-tan to light-grey more silicic horizons comprised of calcite + quartz + chlorite alternate with

pale-green to greenish-grey horizons mostly comprised of diopside + calcite (sometimes dolomitized) + tremolite (often highly altered) ± actinolite + quartz ± chlorite. These alternating horizons commonly range in thickness from a few millimeters to a few centimeters. In addition, some minor quartzite and biotite-rich schist horizons (usually ~1-5 cm thick) are found near the base of the metamorphosed Helena Formation, where the quartzite horizons are commonly boudinaged. Excellent exposure of the metamorphosed Helena Formation are found along the pack trail on the eastern flank of Mount Tiny and along the prominent ridge line west of Mount Haggin. Notably, the Mount Tiny exposures are characterized by a distinct cleavage that cuts the metamorphic foliation at a moderate angle (usually $\geq 35^\circ$). This cleavage-foliation relationship geometrically resembles that of sedimentary cross-bedding. Also note mesoscopic-scale folds are very common in the metamorphosed Helena Formation exposures along the eastern flank of Mount Tiny, some exhibiting sheath-fold geometries.

Calc-silicate Paragneiss and Biotite Schist

Metasedimentary strata above the metamorphosed Helena Formation and below the Middle Cambrian section are correlated with the uppermost Belt Missoula Group. The Missoula group is typically subdivided into several formations in other parts of western Montana (e.g., Snowslip, Shepard, Mt. Shields, Bonner, McNamara, Garnet Range and Pilcher Formations). However, in the current study area not all formations are expected to be present due to the progressively down-cutting Cambrian unconformity in this region (Winston and Link, 1993 and references cited therein). In addition, because the Missoula Group strata present have undergone high grade metamorphism and intense deformation this division is impractical and virtually impossible.

Metasedimentary strata mapped as the Missoula Group are mostly comprised of calc-silicate paragneiss similar, in many aspects, to the underlying calc-silicate gneiss of the metamorphosed Helena Formation. However, the Missoula Group calc-silicate gneiss is generally more diopside-rich, commonly contains chlorite and typically outcrops in a distinctively darker green hue. In addition, the calc-silicate gneiss of the Missoula Group contains more interlayered schistose horizons than calc-silicate gneiss of the Helena Formation. The Missoula Group calc-silicate gneiss is well exposed along northwestern shore of Storm Lake where it comprises the eastern limb of an antiformal structure. Here, the calc-silicate gneiss exhibits profound ductile deformation and is characterized by extensive “chocolate tablet-style” boudinage of the more silicic horizons. Note some metamorphosed Missoula Group strata are comprised of schist and micaceous quartzite horizons, particularly near the bottom of the section. These horizons are usually characterized by alternating biotite schist and biotite-rich quartzite horizons, where individual horizons usually range from 1 mm up to 50 cm in thickness. Some outcrops expose distinct blocky-shaped quartzite boudins.

Middle Cambrian-equivalent Metasedimentary Strata

Micaceous Quartzite, Locally Mylonitic

A thin quartzite unit overlies the metasedimentary strata correlated with the Missoula Group and is correlated with the Middle Cambrian Flathead Formation. Outside the study area, the Flathead Formation is comprised of clean quartzite sandstone and interpreted to represent the first major flooding surface to encroach on western Montana during the middle Cambrian transgression (Winston and Link, 1993). However, within the study area, the Flathead Formation is highly metamorphosed and recrystallized to a coarse-grained, vitreous, and white to light-pink or tan pure quartzite. Major

outcrops of the metamorphosed Flathead Formation are found directly west of Storm Lake on the western limb of an antiformal structure and on the eastern walls of the Sullivan Creek drainage in the southern study area. Notably, the Sullivan Creek exposure is strongly mylonitic and characterized by elongate quartz ribbons (up to ~ 1.5 cm in length) and abundant muscovite-fish, both comprising an east-southeast trending lineation. Lonn et al. (2003) and O'Neill et al. (2004) interpret the Sullivan Creek quartzite to be a detached slab of metamorphosed and deformed Flathead Formation brought down against the Greyson schist (i.e., a younger-on-older normal detachment). A similar structural relationship was documented at Short Peak, northeast of Sullivan Creek along the continental divide. Here, two smaller detached slabs of mylonitic quartzite correlated with the Flathead Formation rests on biotite granodiorite.

Pelitic Garnet-biotite Schist

In many places, a thin tan to light-brown colored schist unit overlies the Flathead Formation correlated quartzite and is correlated with the Middle Cambrian Silver Hill Formation. The Silver Hill schist is generally fine to medium-grained containing abundant biotite defining a moderately defined foliation with lesser K-feldspar + quartz + plagioclase ± sillimanite. Small garnets ($\leq 1-3$ mm in diameter) are also common in some horizons. In addition, the uppermost horizons of the Silver Hill schist are calcareous and effervesce in HCL. Good exposures of the Silver Hill schist can be found in the uppermost East Fork of the Twin Lakes Creek drainage and directly west of Storm Lake. Note at the Twin Lakes Creek locality the Silver Hill schist and other Middle Cambrian equivalent metasedimentary strata are folded into a tight, upright isoclinal antiform.

White Marble, Locally Dolomitic

The structurally highest metasedimentary unit mapped in the study area consists of a thin, coarse-grained white to light-grey locally dolomitic marble unit correlated with the Middle Cambrian Hasmark Formation. In several locations, this Hasmark marble can be found directly overlying the Flathead and Silver Hill correlated metasedimentary strata, comprising a complete, yet metamorphosed and highly deformed Cambrian marine transgressive sequence. Good exposures of the sequence are found on the southern flank of Mount Haggin within a large overturned nappe and on the walls of the Fourmile Basin Lakes drainage. The Hasmark marble is also common as thin, but laterally extensive septa within the Storm Lake Stock. These marble septa are typically ≤ 10 m across but often extend for 100's to 1000's m through the intrusion. The uppermost Fourmile Basin Lakes drainage provides the most spectacular exposures of the marble septa. Here, several septa together define a west-northwest verging fold intruded by quartz diorite of the Storm Lake Stock

Late Cretaceous Intrusions

The Storm Lake Stock

The Storm Lake Stock (SLS) is an intermediate composite-type pluton that mostly outcrops over a ~ 5 km² area within the western LISZ, in the northeastern Anaconda-Pintlar Range, adjacent to Storm and Twin Lakes. The pluton was originally mapped by Emmons and Calkins (1913) who describe the SLS as undeformed medium-to-fine-grained basic (mafic) granodiorite and quartz-bearing diorite. Later, Wallace et al. (1992) described the pluton as being composed of several different phases including: quartz diorite, tonalite, granodiorite, quartz monzodiorite, and diorite. They refer to the pluton as the Stock of Storm Lake because of its size (or volume) and composite nature.

Although some compositional variations were observed as described by Wallace et al. (1992), these variations are generally on the small scale. Therefore, here the SLS is subdivided into only two main phases: a granodiorite and quartz diorite phase. This subdivision (similar to the division made by Emmons and Calkins, 1913) was made because these two phases are by far the most voluminous and their distinction is important to later discussions involving the development of LISZ. The SLS granodiorite is was emplaced later than the quartz diorite phase. The age relationship was observed in the uppermost Fourmile Basin Lakes drainage where the granodiorite phase contains several stopped blocks of the quartz diorite phase. Documentation of this age relationship is important to later discussions concerning the evolution of the LISZ.

The granodiorite phase of the SLS was previously dated by Wallace et al. (1992) using the K-Ar method who report hornblende and biotite cooling ages of 116.4 ± 4.6 and 78.7 ± 1.6 Ma, respectively. They attribute the anomalously old hornblende cooling age to extraneous argon and suggest a late Cretaceous age for the SLS granodiorite based on the biotite cooling age. In this study, two samples were collected from the SLS granodiorite for $^{40}\text{Ar}/^{39}\text{Ar}$ analyses to provide better age constrains. In addition, U-Pb zircon analyses were carried out on one of the samples to provide a crystallization age for the SLS granodiorite phase. The SLS quartz diorite phase was sampled for $^{40}\text{Ar}/^{39}\text{Ar}$ and U-Pb zircon analyses. The SLS quartz diorite phase had not been dated prior to this study.

Storm Lake Stock Granodiorite

The SLS granodiorite partly surrounds Storm Lake and lies west of the quartz diorite phase within the western LISZ. Several scattered outcrops, mostly along the

eastern shores of Storm Lake, provide good exposures of this phase. In this area, the SLS granodiorite is an undeformed medium-grained, salt-and-pepper, grey-colored rock comprised of the major mineral phases (in decreasing abundance) plagioclase, quartz, biotite, hornblende and K-feldspar. In thin section, typical SLS granodiorite (sample WG04-114) is characterized by abundant subhedral to euhedral plagioclase phenocrysts ranging up to ~ 3-4 mm in length, often with well-developed albite twinning. Most of these plagioclase phenocrysts have a “peppered” appearance due to abundant fine-grained mineral inclusions. Biotite and hornblende phenocrysts commonly range up to ~ 2-3 mm in length and some larger hornblendes are twinned. Notably, most biotite and hornblende phenocrysts are anhedral in form, having irregular or “ratty” grain boundaries. K-feldspar and quartz are generally present as relatively small (≤ 1.5 mm) phenocrysts. Accessory mineral phases identified in thin section include (in decreasing abundance) magnetite, apatite, zircon and titanite. These phases are found as small inclusions within the phenocrysts phases.

Several good exposures express the relationship between the SLS granodiorite and highly deformed Belt Supergroup/middle Cambrian-correlated metasedimentary strata in the western LISZ. Immediately west-northwest of the Storm Lake dam (north end of the lake) the undeformed granodiorite phase obliquely crosscuts deformed calc-silicate gneiss, quartzite and schist on the northern tip of an antiformal structure. These strata are correlated with the Missoula Group, Flathead and Silver Hill Formations, respectively (see descriptions above). A similar relationship can be observed at the divide between Storm and Twin Lakes Creek drainages, ~2 km southwest of Storm Lake. At this locality, the granodiorite cuts orthogonally across a well-developed metamorphic

foliation in deformed biotite quartzite and calc-silicate gneiss (Ravalli Group and Helena Formation equivalents, respectively) on the northeastern limb of the same antiform structure. In addition, the SLS granodiorite contains abundant thin, elongate septa of deformed white marble correlated with the middle Cambrian Hasmark Formation. These septa are exposed on the eastern shores of Storm Lake and to the southeast along the northeastern wall of the upper Storm Lake drainage. A few of the most extensive Hasmark septa within the SLS granodiorite were mapped and are shown in .

Storm Lake Stock Quartz diorite

A quartz diorite phase comprises most of the eastern SLS and is mainly exposed over a broad area in the upper Fourmile Basin Lakes and upper Twin Lakes Creek drainages. Here, the SLS quartz diorite is an undeformed medium-to-coarse-grained grey-colored rock somewhat similar looking in outcrop to the SLS granodiorite (i.e., grey, salt-and-pepper appearance). However, the quartz diorite is typically more coarse-grained and contains more plagioclase and hornblende; plagioclase and hornblende comprise over 70 % of the rock at many exposures. Other major mineral phases found in the quartz diorite include (in decreasing abundance) biotite, quartz and K-feldspar. A thin section of the SLS quartz diorite (sample WG04-052 from upper Fourmile Basin Lakes drainage) exhibits abundant large euhedral plagioclase phenocrysts ranging in size up to ~ 4-5 mm in longest dimension. Most plagioclase phenocrysts in thin section display a prominent albite twinning. Hornblende is present as large, sometimes elongate phenocrysts up to ~ 5-7 mm in length. Biotite is observed often as lath-shaped phenocrysts ranging up to 3-4 mm in length. Notably, the hornblende and biotite of the quartz diorite are subhedral-euhedral in crystal form, therefore having a more defined

form than hornblende and biotite of the SLS granodiorite. K-feldspar and quartz are present as relatively small phenocrysts up to ~ 2-3 mm in diameter and some K-feldspar phenocrysts exhibit tartan twinning. In addition, myrmekitic worm-like intergrowths of quartz and K-feldspar are commonly found on plagioclase phenocryst rims adjacent to K-feldspar. Accessory mineral phases identified in the SLS quartz diorite and their relative abundances are similar to those of the SLS granodiorite phase (i.e., in decreasing abundance: magnetite, apatite, zircon and titanite).

Exposures along the western walls of the Fourmile Lakes Basin drainage, just above several small lakes express the relationship between the SLS quartz diorite and the LISZ in the western study area. At this locality, the undeformed SLS quartz diorite clearly crosscuts highly deformed metasedimentary strata correlated with the upper Belt Missoula Group and the middle Cambrian section. Emmons and Calkins (1913) document this same crosscutting relationship. In addition, in the uppermost Fourmile Basin drainage along the east-northeast facing headwall, several Hasmark marble septa together outline a northwest verging fold. Emplacement of the undeformed SLS quartz diorite clearly post-dates folding of the septa.

The Deformed Quartz Diorite Sill

East of the widespread exposures of quartz diorite within upper Fourmile Basin and Twin Lakes drainages, a deformed narrow (≤ 1 km thick) quartz diorite sill was mapped. The quartz diorite sill is emplaced within steeply dipping, strongly metamorphosed and deformed Belt Supergroup/middle Cambrian-correlated metasedimentary strata in the central and eastern LISZ and can be traced eastward to the base of Mount Haggin. Unlike the exposures of undeformed quartz diorite in the west, the quartz diorite sill exhibits a well-developed solid-state foliation concordant with the metamorphic foliation within the

adjacent Belt and middle Cambrian-equivalent metasedimentary country rocks in the LISZ. The foliation in the quartz diorite sill is defined by the parallel alignment of elongate hornblende “clots,” flattened plagioclase and K-feldspar phenocrysts, and quartz ribbons (all \leq 4-5 cm in length). Some larger (\sim .5 to 1 cm diameter) plagioclase phenocrysts exhibit symmetric and asymmetric sigmoidal geometries as well. The foliated SLS quartz diorite sill is well-exposed along the southern side of the upper East Fork of the Twin Lakes drainage (east-northeast of the Lake of the Isle) and in the upper reaches of the Mill Creek drainage. At the upper East Fork of the Twin Lakes drainage exposure, the sill contains thin (\leq 5 m thick) septa of biotite-rich quartzite gneiss and calc-silicate gneiss; the latter resembles calc-silicate gneiss of metamorphosed Missoula Group.

In the eastern study area, a fairly large isolated pluton also comprised of quartz diorite is exposed on Mount Haggin. The quartz diorite on Mount Haggin crosscuts highly deformed and metamorphosed metasedimentary strata correlated with the upper Belt Supergroup and middle Cambrian section along the upper limb of a large, east-verging recumbent nappe structure (Heise, 1983). Therefore, the quartz diorite intrusion on Mount Haggin shows the same relationship with the deformed and metamorphosed metasedimentary wall rocks as the quartz diorite of Fourmile Basin Lake drainage in the west. However, the quartz diorite on Mount Haggin is deformed and overprinted by a mylonitic fabric in some places, presumably the same fabric that overprints the granitoids in the mylonite zone to the east (Heise, per comm.).

Eocene Intrusions

The central, eastern, and southern parts of the study area, in the northeastern Anaconda-Pintlar Range, are characterized by highly voluminous Eocene intrusive rocks.

In this region, four major intrusive phases were identified and mapped as separate units. These intrusive rock units include: medium-grained biotite granite, medium-to-coarse-grained two-mica (biotite and muscovite) granite, biotite granodiorite, and porphyritic two-mica granite. A number of northeast-trending dacite dikes were also mapped in the central part of the study area. Crosscutting relationships observed in the field indicate the following order of emplacement for the mapped intrusive units, from oldest to youngest: biotite granite \geq two-mica granite $>$ biotite granodiorite $>$ porphyritic two-mica granite \geq dacite dikes. These subdivisions and relative ages agree with the early work of Emmons and Calkins (1913). However, they also describe and map a porphyritic biotite granite phase, placing this unit between the biotite granodiorite and porphyritic two-mica granite in relative age (see their manuscript for a very complete assessment of the intrusive rocks of the northeastern Anaconda-Pintlar Range). Here, relatively basic descriptions are provided for the different intrusive units mapped in the current study area; emphasis is placed on distinctive characteristics and general spatial distribution of the rock units throughout the study area. Note the biotite and two-mica granite in the easternmost study area have greenschist mylonite fabrics (i.e., within the Anaconda mylonite). The characteristics of the greenschist mylonite fabrics are described in a later section.

Biotite Granite

Biotite-bearing granite outcrops over a large area within the southeastern portion of the study area, reaching from the Tenmile Creek drainage to the upper Clear Creek drainage within the Anaconda mylonite. When not mylonitized, the biotite granite is typically a fabric-less medium-grained rock largely comprised of (in decreasing

abundance) quartz + K-feldspar + plagioclase + biotite. Quartz typically forms anhedral to subhedral phenocrysts ranging in diameter up to ~3-4 mm. Plagioclase is similar in size to quartz, but usually subhedral to euhedral. Plagioclase commonly exhibits albite twinning in thin section. In addition, K-feldspar exhibit tartan twinning in thin section and some phenocrysts range up to ~8 mm in longest dimension. Individual lath-shaped biotites are usually ~1-3 mm in length and often found in randomly oriented clusters with other biotite laths.

At high elevations (e.g., along the northwest-trending ridge that separates the Tenmile and Mill Creek drainages) the biotite granite is highly chloritized, but lacks a well-developed mylonitic fabric. At these high elevation outcrops the biotite granite also exhibits a pervasive green hue and is brittlely fractured; presumably because high elevations approach the previous detachment level. On the eastern side of the Mill Creek drainage, within the mylonitic biotite granite, a slab of coarse white-pink quartzite is juxtaposed with the biotite granite along a low-angle detachment fault. This quartzite has been correlated with the middle Cambrian Flathead Formation by Emmons and Calkins (1913). However, without any adjacent metasedimentary units present it is difficult to confidently make such a correlation.

Two-mica Granite

Medium-grained two-mica granite is the most voluminous intrusive rock type mapped within the study area. This rock type outcrops in several places: north and east of Mount Haggin, including the upper Clear Creek drainage, the upper Mill Creek drainage, a large glacial creek south of the Lake of the Isle, and along the northwest-trending ridge that separates the Sullivan and Seymour Lakes Creek drainages in the

southwestern study area. The exposures north and east of Mount Haggin are mostly mylonitic. The non-mylonitic two-mica granite is remarkably similar to the biotite granite in both texture and mineralogy; the only difference is the presence of muscovite and sometimes slightly more abundant quartz and K-feldspar in the two-mica granite. In thin section, muscovite is found as randomly oriented, sometimes clustered, lath-shaped crystals similar in size to usually more abundant biotite laths (~1-3 mm laths). Biotite is sometimes chloritic. Notably, in a thin section of one two-mica granite sample (WG04-043), quartz and K-feldspar show substantial deformation, which could not be detected at hand sample or outcrop scale. In this thin section, quartz exhibits strongly developed undulatory extinction and is sometimes characterized by multiple subgrains with serrated grain boundaries within (i.e., grain boundary migration). In addition, K-feldspar is highly fractured sometimes exhibiting a complex, anastomosing pattern of fine-grained fractures.

Biotite Granodiorite

A medium-grained biotite granodiorite comprises a west-dipping tabular sheet-like intrusion that stretches from the upper Tenmile Creek drainage, across Mill Creek into the upper Clear Creek drainage. In addition, a large pluton in the Seymour Lakes Creek drainage in the southwestern part of the study area is comprised of a similar biotite granodiorite (Lonn et al., 2003). In the upper Clear Creek drainage the biotite granodiorite narrows to a “finger-like” extrusion that extends into the two-mica granite and is strongly mylonitic. However, elsewhere the biotite granodiorite is observed to be non-mylonitic and mostly comprised of (in decreasing abundance) quartz + plagioclase + K-feldspar + biotite ± hornblende (rare).

Similar to the biotite granite, the biotite granodiorite is observed to be brittlely fractured and mildly to moderately chloritized at some high elevations exposures. In particular, along the northwest-trending ridge which separates the Tenmile and Mill Creek drainages (southwest of Short Peak) the biotite granodiorite is cut by several closely spaced (~5-30 m apart) high angle brittle faults. Individual fault blocks are moderately chloritized and the degree of chloritization generally increases towards the faults within individual fault-bound blocks.

Porphyritic Two-mica Granite

A porphyritic two-mica granite pluton was mapped in the upper Twelvemile and Tenmile Creek drainages. This intrusion was originally mapped and referred to as the Twelvemile Batholith by Emmons and Calkins (1913). Mineralogically, the porphyritic two-mica granite is very similar to the to medium-grained two-mica granite and contains (in decreasing abundance) quartz + K-feldspar + plagioclase + biotite + muscovite. K-feldspar is commonly more abundant than plagioclase feldspar and biotite is usually more abundant than muscovite. In addition, some exposures exhibit very large tabular K-feldspar phenocrysts ranging up to ~3-4 cm in longest dimension and quartz phenocrysts up to ~1-1.5 cm in diameter; the larger K-feldspar and quartz phenocrysts are often concentrated in clusters and surrounded by relatively finer-grained quartz, K-feldspar, plagioclase, biotite and muscovite. In the upper Tenmile Creek drainage several thin (typically $\leq 1-5$ m) aplite dikes extend from the main body of the porphyritic two-mica granite pluton. These aplite dikes are solely comprised of (in decreasing abundance) K-feldspar + quartz + muscovite. Muscovite is very coarse-grained in within these dikes

(sometimes up to ~1-1.5 cm flakes). Some aplite dikes trend to the north while others trend east or northeast.

Northeast-trending Dacite Dikes

Numerous thin (~1-5 m thick) medium to dark-grey dacite dikes cut through the central part of study area and predominantly trend to the northeast. These dacite dikes are characterized by aphanitic porphyritic texture. In thin section, plagioclase phenocrysts are usually subhedral to euhedral in crystal form and ~2-10 mm in diameter; many exhibit albite twinning and concentric zoning patterns. Some plagioclase phenocrysts are highly angular and apparent fragments of original whole plagioclase phenocrysts. Quartz is present as less abundant sub-rounded to rounded phenocrysts usually ~1-2 mm in diameter. Markedly, some quartz phenocrysts exhibit well-developed undulatory extinction and internal subgrains with serrated grain boundaries. Biotite is common as small (~1 mm by 2 mm) lath-shaped phenocrysts dispersed among the larger plagioclase and quartz phenocrysts; some biotite laths are moderately chloritic. These phenocrysts phases are separated by a very fine-grained matrix comprised mostly of plagioclase with lesser quartz and biotite.

Although not shown on the map in Appendix E, these dikes are especially concentrated within the metamorphosed Greyson Formation (pelitic schist and migmatitic paragneiss) in the area north of Mount Evans and south of the Lake of the Isle (see the mapping of Emmons and Calkins, 1913 and Lonn et al., 2003). Most of the dacite dikes mapped in this study trend to the northeast and cut across the Belt and middle Cambrian-equivalent metasedimentary strata in the LISZ at high angle. Just to the northeast of the Lake of the Isle the dacite dikes crosscuts the deformed quartz diorite sill, the

metamorphosed middle Cambrian section, and calc-silicate and biotite quartzite paragneisses correlated with the metamorphosed Helena Formation and Ravalli Group, respectively. One mapped dacite dike crosscuts the western part of a two-mica granite pluton south of the Lake of the Isle. Note the dacite dikes mapped in this study area are likely the northern continuation of the extensive NE-trending middle Eocene dike swarm in the southwestern Anaconda-Pintlar Range and the Chief Joseph Batholith documented by previous workers (e.g., Desmarais, 1983; Hyndman et al., 1988; Wallace et al., 1992).

APPENDIX C
DESCRIPTION OF SAMPLE ME-231

ME-231 was chosen for the thermobarometry of this study. This sample was taken from one of several large outcrops exposing highly deformed migmatitic pelitic paragneiss (metamorphosed Greyson Fm., Lower Belt) near the Lake of the Isle, in the central part of the LISZ (Appendix F). ME-231 bears an assemblage of (in increasing relative abundance) cordierite + garnet + K-feldspar + albite + biotite + quartz + sillimanite; this upper-amphibolite facies assemblage is ideal for calculation of several mineral phase equilibria used in conventional thermobarometry in pelitic rocks (e.g., Spear, 1993). The outcrop from which ME-231 was taken also contains abundant granitic leucosome commonly found in boudin neck pressure shadows; this is consistent with the interpretation of insitu partial anatexis occurred during ductile deformation in the central LISZ. Furthermore, the migmatitic pelitic paragneiss here are the most intensely deformed and highly metamorphosed exposed in the LISZ. Therefore, PT estimates calculated from the equilibrium phase assemblage of ME-231 most likely represent peak pressure and temperature conditions (or closest to peak PT possible) associated with upper-amphibolite facies metamorphism and ductile deformation of Belt and middle Cambrian-equivalent metasedimentary strata in the LISZ.

More specifically, the outcrop from which ME-231 was collected is characterized by highly transposed, planar metamorphic fabrics. Abundant sillimanite mats and lesser biotite are conspicuous and define a planar sub-vertical to vertical foliation in outcrop (and many other outcrops in the central LISZ). Quartzite-rich horizons alternate with

pelitic horizons. The quartzite-rich horizons are moderately to highly flattened and often boudinaged to thin (≤ 10 cm thick) elongate blocky to ellipsoid boudins. The longer axes of these boudins are usually oriented parallel to the steep transposed and planar foliation in outcrop. These quartzite-rich horizons are also found folded into elongate mesoscopic-scale isoclinal, sometimes rootless folds with hinge lines oriented parallel to the planar fabrics. In addition, light-grey to tan or light-orange colored albite + quartz + k-feldspar bearing leucosome is common in boudin necks (i.e., between individual boudins) and as thin (≤ 5 cm) elongate pods (≤ 0.5 m) within the planar fabrics of the outcrop.

In thin section, sample ME-231 exhibits a pervasive metamorphic foliation comprised of aligned fresh sillimanite fibrolite mats on a less abundant light-brown biotite substrate (i.e., epitaxial sillimanite). The individual sillimanite fibrolite and biotite layers of this foliation are commonly ≤ 2 mm thick and generally spaced by ~ 4 to 8 mm. Thin, elongate (≤ 1.5 mm long) ilmenite ribbons are commonly associated with sillimanite fibrolite mats, with their long axes parallel to fibrolite mats and the overall orientation of the foliation in ME-231 (see photomicrographs of ME-231 in the description of LISZ above).

The sillimanite-biotite foliation of ME-231 encases a population of garnet, cordierite and K-feldspar porphyroblasts. All of these porphyroblasts show a “pre-tectonic” relationship to the foliation where the foliation wraps (or bent) around individual porphyroblasts (Yardley, 1999, p. 171). Because of this relationship, pressure shadows filled with fine-grained quartz, albite and K-feldspar are commonly associated with the larger porphyroblasts (mostly garnet and cordierite) in ME-231.

The garnet porphyroblasts of ME-231 are typically anhedral to subhedral-dodecahedrons and mostly range from ~1 to 10 mm in diameter. A few larger garnets are tabular-shaped with their longer axes oriented parallel to the sillimanite-biotite foliation. Note all garnet porphyroblasts are slightly to moderately fractured, where fractures are oriented near 90° to the encasing sillimanite-biotite foliation. In addition, some garnets exhibit minor embayments along grain boundaries.

Cordierite in ME-231 is common as large, slightly flattened sigma-type porphyroblasts ranging from ~ 4 to 12 mm in diameter. These sigmoidal-shaped cordierites are symmetric or slightly asymmetric; many having tails sub-parallel to the sillimanite-biotite foliation described above. K-feldspar is found as moderately to highly flattened, elongate asymmetric porphyroblasts or “ribbons” with large aspect ratios (e.g., ~1-2 mm long by 0.2 mm thick). Some of the most severely flattened K-feldspar porphyroblasts exhibit subgrains and moderate undulatory extinction. In addition, some K-feldspar porphyroblasts in ME-231 have exhibit areas of myrmekitic intergrowths with quartz.

Both garnet and cordierite porphyroblasts in ME-231 contain inclusions suites. Garnets have abundant quartz and rare biotite inclusions, both usually up to ~ 1 mm in diameter. Cordierite porphyroblasts commonly contain several small (≤ 2 mm in diameter) zircon inclusions marked by bright yellow damage halos. A few cordierite porphyroblasts also host small biotite inclusions typically ≤ 5 mm in length. Note both garnet and cordierite porphyroblasts in ME-231 lack albite plagioclase inclusions.

Fine-grained hair-like sillimanite fibrolite inclusions are abundant in both garnet and cordierite porphyroblasts. In the garnets, these inclusions define a preserved internal

sub-planar foliation oriented at high angles (often $\sim 90^\circ$) to the pervasive external sillimanite-biotite foliation. The smallest garnets (~ 1 mm diameter) exhibit hair-like sillimanite fibrolite inclusions as well but the fibrolites are generally arranged in small, circular wreath-like patterns. The diameter of the hair-like “sillimanite wreaths” are commonly about half that of the host garnet. The hair-like sillimanite fibrolites also define a preserved internal foliation in cordierite porphyroblasts, somewhat analogous to that of the larger garnets porphyroblasts. However, the internal foliation in cordierites is commonly wavier and more chaotic, somewhat analogous to the classic syn-tectonic “snowball texture” of garnets described by Spry (1963).

Albite and quartz are common in quartzofeldspathic layers (~ 1 to 8 mm thick) between the sillimanite fibrolite mat-biotite layering of the foliation described above. In the feldspathic layers individual albite and quartz grains are usually fine-grained and anhedral, often ~ 0.1 to 0.8 mm in diameter. Both albite and quartz grains display undulatory extinction, this phenomenon being most intense in the later of the two. The deformed quartz grains often have several subgrains, some exhibiting serrated grain boundaries with respect to other quartz grains. In addition, quartz can be found as thin, highly flattened elongate quartz ribbons often reaching lengths of ~ 4 to 8 mm. More fresh and coarser grained albite, quartz and K-feldspar are also found as thin (~ 1 to 1.5 mm) elongate (up to few cm in length) leucosome lenses or “fingers” between sillimanite-biotite and feldspathic layers of the foliation described above. Individual albite, quartz and K-feldspar grains are typically subhedral to euhedral in shape, ranging in diameter from ~ 0.5 to 1.5 mm. Albite and K-feldspar grains exhibit well-developed albite twinning and tartan twinning, respectively. Furthermore, the individual albite,

quartz and K-feldspar grains of the leucosome fingers do not exhibit undulatory extinction, subgrains or irregular grains boundaries as those described in the quartzofeldspathic layering.

Notably, the placement of the albite + quartz + K-feldspar bearing leucosome viewed in thin sections of ME-231 is very similar to its macroscopic placement in outcrop. In thin section, the leucosome is commonly found in both garnet and cordierite porphyroblast pressure shadows, analogous to the leucosome found within boudin necks pressure shadows in outcrop. In addition, some garnets porphyroblasts display thin fingers, or veinlets, of the leucosome cross-cutting the grains, parallel to the foliation of ME-231. Individual lenses of the leucosome are also found within the sillimanite fibrolite mat-biotite layers as ~1 mm to ~1 cm in length (see photomicrographs in description of LISZ above).

Muscovite is absent from ME-231 except for a few small, rare isolated clusters. These muscovite clusters are characterized by fresh muscovite laths, where individual laths reach ~ 1 mm in length. In all cases, the muscovite crosscuts the sillimanite fibrolite mat-biotite foliation of ME-231 at moderate to high angles. Rare fine-grained muscovite is found along fractures in a few larger garnet and cordierite porphyroblasts. In addition, chlorite mica is absent from ME-231.

APPENDIX D
MAJOR AND TRACE ELEMENT GEOCHEMISTRY

Purpose

Major and trace element analyses were carried out to investigate the genetic relationship between late Cretaceous intrusions found within the ACC. Three samples were chosen for these analyses. DF02-114 was collected from a large medium-to-coarse-grained undeformed granodiorite block in the detached ACC upper plate located ~3 km east of the greenschist facies mylonite zone exposed in the Mill and Clear Creek drainages. Notably, the upper plate granodiorite is similar to the undeformed granodiorite phase of the Storm Lake Stock (SLS) located in the western part of the ACC lower plate (Appendix F). In particular, the upper plate granodiorite sample DF02-114 is similar to WG04-114, a sample collected from the SLS granodiorite. These two granodiorite samples differ only slightly in texture and mineralogy, where DF02-114 is coarser-grained and contains less hornblende, less plagioclase, and more K-feldspar. In addition, these two samples gave similar biotite $^{40}\text{Ar}/^{39}\text{Ar}$ cooling ages; DF04-114 and WG04-114 gave biotite $^{40}\text{Ar}/^{39}\text{Ar}$ cooling ages of 76.3 ± 1.1 Ma and 74.0 ± 0.9 Ma, respectively (Chapter 6).

The similar mineralogy, texture, and biotite cooling ages of sample DF02-114 and WG04-114 indicate that the upper plate granodiorite and the SLS granodiorite are likely genetically related and originally part of the same pluton. One possibility is the upper plate granodiorite represents a slightly more fractionated and evolved phase of SLS granodiorite emplaced at a shallower depth. This interpretation could account for the

slightly more evolved nature of the upper plate granodiorite (i.e., as the upper plate granodiorite rose from the SLS granodiorite below it fractionated and become more evolved). In addition, emplacement into the shallower (and cooler) crust above the SLS granodiorite could also account for the slightly older biotite cooling age obtained for DF04-114 (i.e., the top of the pluton would have cooled slightly earlier).

It is possible the upper plate granodiorite and the SLS granodiorite were originally part of the same pluton that was emplaced into the ACC lower plate in the late Cretaceous. Subsequently, the shallower part of the pluton (the upper plate granodiorite) was detached and displaced to the east-southeast along the Anaconda detachment during the Eocene. If this relationship is proven plausible then the map distance between the upper plate granodiorite and SLS granodiorite can be used to estimate the amount of horizontal displacement facilitated by the Anaconda detachment since the onset of extension at ~53 Ma. Major and trace element data were also obtained from Ug-1, a sample from the deformed quartz diorite sill emplaced within the attenuated (ductily thinned) Mesoproterozoic and middle Cambrian-equivalent metasedimentary strata in the central and eastern LISZ (Appendix F). These data are needed to test the quartz diorite sill as a possible parent for the upper plate granodiorite (i.e., the upper plate granodiorite could have originated from the quartz diorite sill by fractional crystallization rather than the SLS granodiorite).

Major and Trace Element Analytical Results

Whole rock powders were prepared from samples DF02-114, WG04-114 and Ug-1 using traditional rock crushing and powdering methods and sent to Acme Analytical Laboratories Ltd for ICP-MS (inductively coupled plasma mass spectrometry) major and trace element analyses. Methods for sample preparation are summarized in Appendix A.

See <http://www.acmelab.com/cfm/index.cfm?It=100&Id=1> for Acme ICP-MS analytical procedures.

Major Element Analyses

The results of the major elemental analyses from samples DF02-114, WG04-114 and Ug-1 are reported in Table D-1 and plotted on Harker variation diagrams in Figure D-1. All major element oxides are reported in weight percent. The results show that all three samples are intermediate (55-62 wt % SiO₂) in composition. The upper plate granodiorite DF02-114 is the most evolved, followed by the granodiorite WG04-114, and then the quartz diorite sill Ug-1 (SiO₂ wt % = 64.0, 59.5 and 59.2, respectively). All three samples are high in K₂O (2.27-3.74 wt %) as well falling in the high-K calc-alkaline field of the subalkalic rock classification. In addition, DF02-114, WG04-114 and Ug-1 are very similar in major element composition (also see Table 1). Sample DF02-114 is somewhat similar to Ug-1 and WG04-114 in some major elements, plotting to the right of WG04-114 and Ug-1 on Harker variation diagrams. However, DF02-114 is slightly depleted in Al₂O₃, Fe₂O₃, MgO, and CaO and more enriched in K₂O with respect to Ug-1 and WG04-114.

Trace Element Analyses

The results from trace element analyses are summarized in Table 1 as well. These trace element concentrations are reported in ppm (parts-per-million). Select trace elements concentrations from each sample were also plotted in Figure 2a, which displays an incompatible trace element spider diagram. On the spider diagram the trace elements were plotted from left to right in order of increasing mantle compatibility (e.g., see Rollinson, 1993, p. 144). Trace element concentrations for the average upper and lower crust are also plotted in Figure D-2a for comparison to the unknowns of this study. The

Table D-1. Results from major and trace element analyses

Sample	DF02-114	WG04-114	Ug-1
Rock type	hb bt granodiorite	hb bt granodiorite	q. diorite
<u>Major Elements (wt %)</u>			
SiO ₂	64.01	59.52	59.24
Al ₂ O ₃	15.94	16.26	17.13
Fe ₂ O ₃	4.95	7.13	6.76
MgO	2.17	3.25	3.13
CaO	4.41	5.92	6.15
Na ₂ O	3.04	3.04	3.38
K ₂ O	3.74	2.75	2.27
TiO ₂	0.61	0.83	0.76
P ₂ O ₅	0.17	0.24	0.19
MnO	0.07	0.11	0.11
Cr ₂ O ₃	0.00	0.00	0.00
LOI	0.70	0.70	0.60
TOT/C	0.06	0.04	0.03
TOT/S	0.01	0.01	0.01
Total	99.81	99.76	99.73
<u>Trace Elements (ppm)</u>			
Ba	741.80	787.00	917.90
Be	1.00	2.00	<1
Co	12.20	20.50	19.40
Ni	11.00	29.00	22.00
Sc	11.00	16.00	15.00
Cs	6.80	4.20	1.80
Ga	17.00	19.20	17.80
Hf	6.10	5.50	4.60
Nb	10.70	10.80	8.10
Rb	133.00	111.60	61.40
Sn	2.00	1.00	1.00
Sr	515.00	636.60	470.40
Ta	1.00	0.70	0.70
Th	19.80	8.00	4.30
U	2.40	1.60	1.00
V	99.00	147.00	108.00
W	12.00	6.20	9.60
Zr	203.60	215.70	181.80
Y	21.60	23.10	19.20
La	55.00	28.00	26.60
Ce	112.50	65.40	57.00
Pr	10.27	7.18	5.56
Nd	34.90	29.20	21.80
Sm	5.80	5.30	4.30

Table D-1. Continued.

Sample	DF02-114	WG04-114	Ug-1
Rock type	hb bt granodiorite	hb bt granodiorite	q. diorite
<u>Trace Elements (ppm)</u>			
Eu	1.18	1.39	1.27
Gd	3.77	4.61	3.53
Tb	0.67	0.64	0.57
Dy	3.42	3.81	3.24
Ho	0.78	0.78	0.67
Er	2.13	2.18	1.90
Tm	0.32	0.38	0.31
Yb	1.95	2.05	1.79
Lu	0.37	0.33	0.33
Mo	0.50	1.10	<.1
Cu	14.50	27.30	13.60
Pb	4.10	1.60	1.50
Zn	22.00	71.00	48.00
Ni	7.20	11.80	8.00
As	0.80	0.80	0.70
Cd	<.1	0.10	<.1
Sb	<.1	<.1	<.1
Bi	<.1	<.1	<.1
Ag	<.1	<.1	<.1
Au	0.50	1.00	1.00
Hg	<.01	<.01	0.01
Tl	0.30	0.40	0.30
Se	<.5	<.5	<.5
<u>Major element ratios</u>			
Al ₂ O ₃ / (Na ₂ O+K ₂ O+CaO)	1.42	1.39	1.45
<u>Trace elements ratios</u>			
Zr/Y	9.43	9.34	9.47
Ce/Yb	57.69	31.90	31.84
Note: q = quartz, hb = hornblende, bt = biotite			

average upper and lower crust trace element compositions were taken from Taylor and McLennan (1981) and Weaver and Tarney (1984), respectively. In addition, all trace element data plotted in Figure D-2a were normalized to the primitive mantle trace element concentrations of McDonough et al. (1991).

Overall, samples DF02-114, WG04-114, and Ug-1 yielded trace element concentrations similar to the average upper crust. The trace element trends for the three samples lack pronounced negative rubidium, thorium, uranium, and yttrium anomalies typical of the depleted lower crust. DF02-114 yielded significantly higher thorium, lanthanum, and cerium concentrations than the average upper crust and WG04-114 and Ug-1 gave thorium and uranium concentrations lower than the upper crust. In addition, the rubidium concentration of Ug-1 is lower than rubidium concentration in the average upper crust (Fig. 2a). Rare earth elements (REE) concentrations for samples DF02-114, WG04-114, and Ug-1 are presented in Figure 2b and normalized to the primitive mantle REE concentrations of McDonough et al. (1991). Overall, all three samples are characterized by moderately steep REE trends with negative slopes indicating an enrichment and depletion in the light REE (left) and heavy REE (right), respectively (the Ce/Yb ratios for the three samples ranges from 57.7-31.8). Such patterns are indicative of magma source rocks that contain garnet and/or amphibole which strongly partition heavy REE relative to light REE (Rollinson, 1993). WG04-114 and Ug-1 yielded very similar REE patterns (Fig. 2b). The REE trend for WG04-114 closely mimics the REE trend of Ug-1, lying just above it indicating an overall enrichment the all the REE. The DF02-114 REE pattern is similar to the REE patterns of WG04-114 and Ug-1 over the medium to heavy REE (right to center, Fig. 2b). DF02-114 is more enriched in the light REE. In addition, DF02-114 exhibits a slightly negative anomaly in europium suggesting equilibrium with fractionation of plagioclase (Best and Christiansen, 2001).

The major and trace element data obtained for DF02-114, WG04-114, and Ug-1 suggest these samples could be related by process of fractional crystallization (Rollinson,

1993). In particular, the similar REE patterns of WG04-114 and Ug-1 suggest the SLS granodiorite could have formed by fraction crystallization from the quartz diorite sill. Likewise, these data suggest the upper plate granodiorite (DF02-114) could have fractionated from sources similar the SLS granodiorite or the quartz diorite sill given that the fractionating mineral phases acted enriched the daughter magma in light REE while leaving the heavy REE largely unchanged.

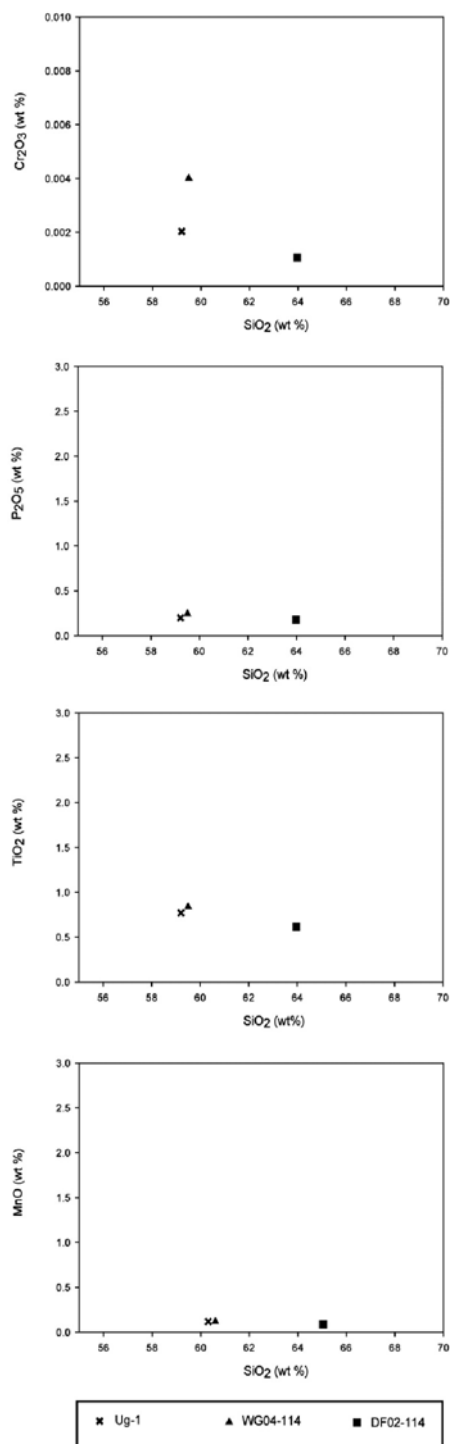


Figure D-1. Major element Harker variation diagrams for samples Ug-1, WG04-114, and DF02-114.

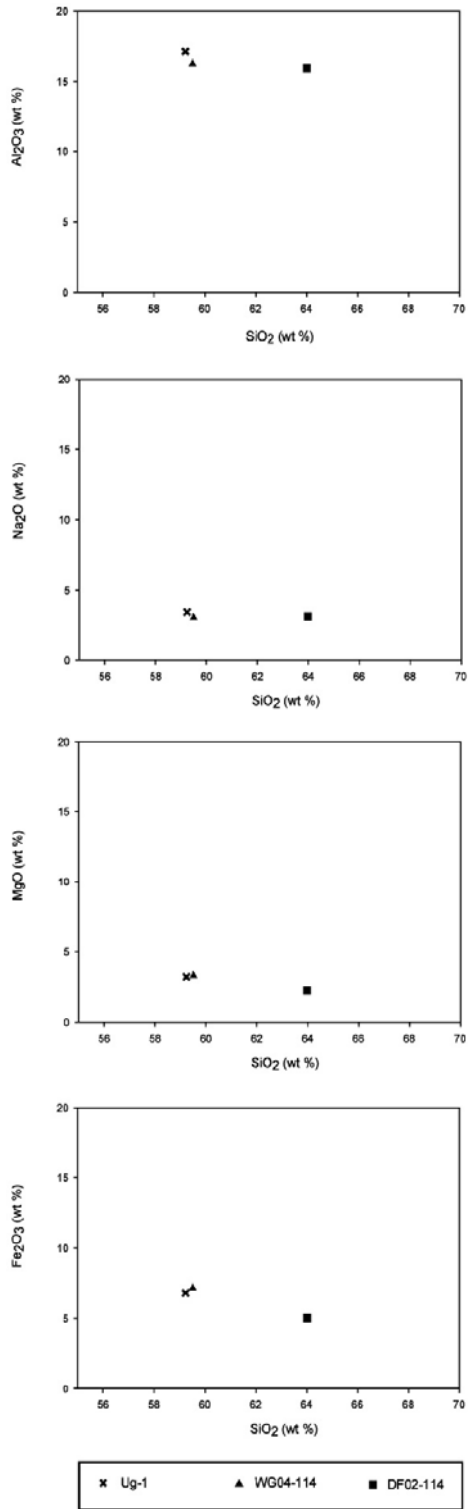


Figure D-1. Continued.

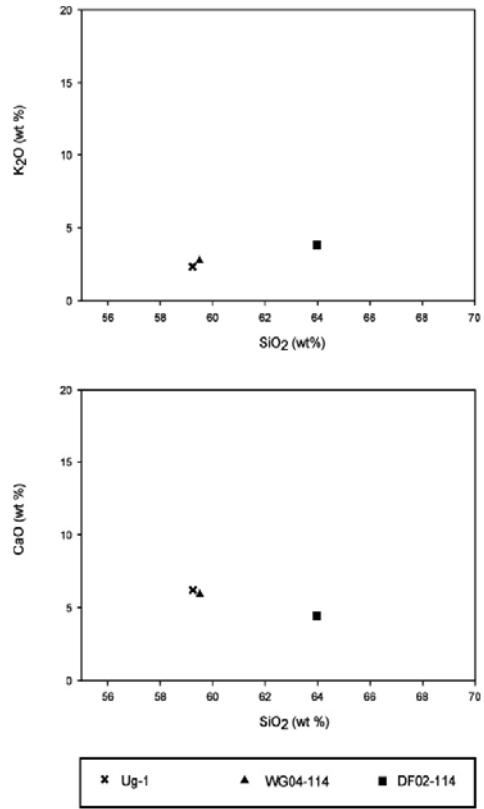


Figure D-1. Continued.

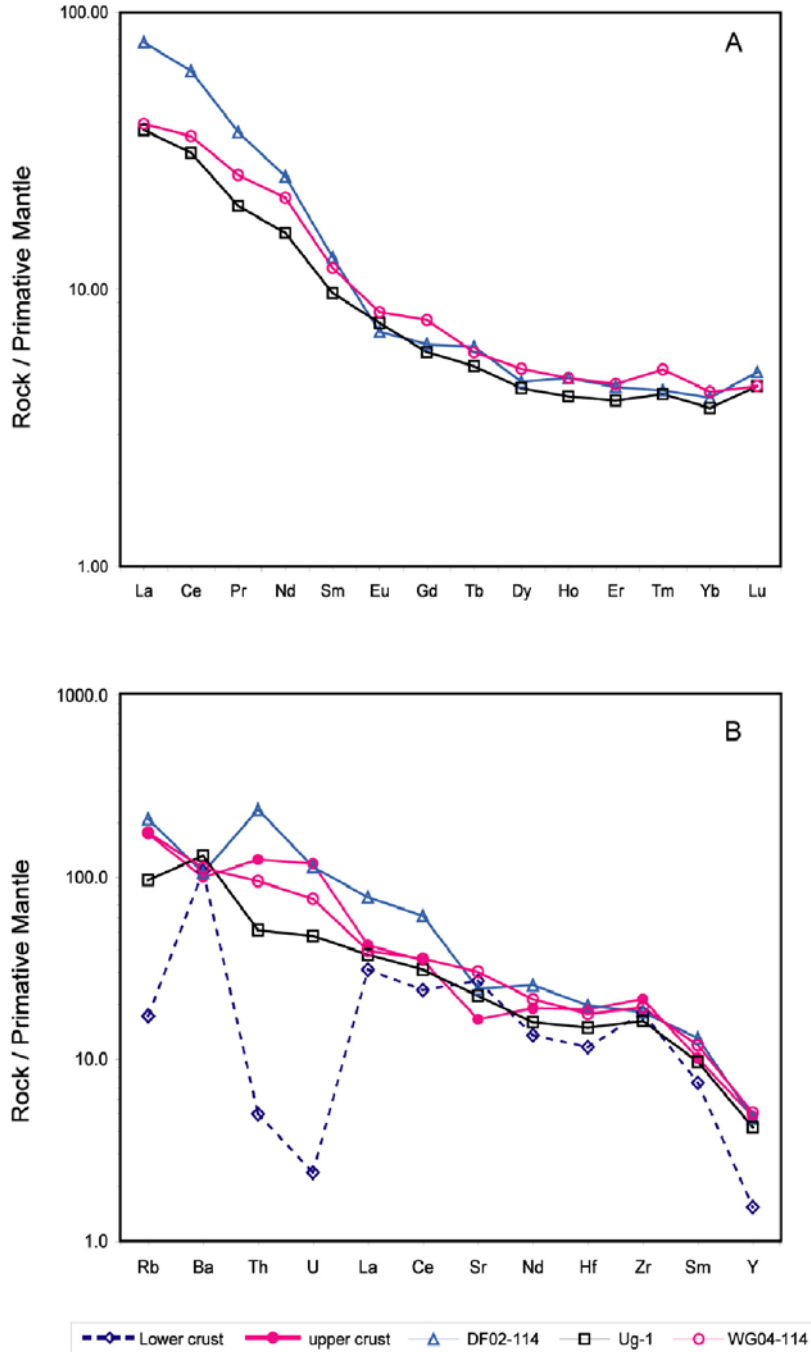


Figure D-2. REE trend and trace element spider diagrams for samples Ug-1, WG04-114, and DF02-114. A) All three samples show enrichment in light REE relative to heavy REE. WG04-114 and Ug-1 show very similar trends in REE while DF02-114 is more enriched in La, Ce, Pr, and Nd. B) All three sample show trace element concentrations largely similar to the average upper crust.

APPENDIX E
THERMOCALC AND AX OUTPUT FILES

AX OUTPUT:

Calculations for P = 4.0 kbar and T = 800°C

g garnet

2-site mixing + Regular solution gammas

Ferric from: Cation Sum = 8 for 12 oxygens

W: py.alm=2.5, gr.py=33, py.andr=73, alm.andr=60, spss.andr=60 kJ

oxide	wt %	cations		activity	±sd	±%
SiO2	36.88	2.934	py	0.0025	0.00111	45
TiO2	0.14	0.009	gr	0.000048	0.0000268	56
Al2O3	21.32	2.000	alm	0.47	0.070	15
Cr2O3	0.16	0.010	spss	0.0000014	0.00000080	59
Fe2O3	2.71	0.162	andr	-	-	-
FeO	35.37	2.353				
MnO	0.50	0.034				
MgO	2.92	0.346				
CaO	1.13	0.097				
Na2O	0.30	0.046				
K2O	0.11	0.011				

Totals 101.56 8.000

bi rim

Al-M1 ordered, site-mixing model + macroscopic RS gammas: (ann, phl, east, obi)

Ferric from: Tet + Oct cation sum = 6.9 for 11 oxygens. Max Ratio = 0.15

SF model parameters: Wpa=9, Wpe=10, Wpo=3, Wao=6, Wae=-1, Woe=10 (kJ)

oxide	wt %	cations		activity	±sd	±%
SiO2	33.76	2.629	phl	0.0088	0.00332	38
TiO2	3.16	0.185	ann	0.090	0.0165	18
Al2O3	19.71	1.810	east	0.015	0.0051	34
Cr2O3	0.24	0.015				
Fe2O3	0.00	0.000				

FeO	24.02	1.565
MnO	0.13	0.009
MgO	5.28	0.612
CaO	0.13	0.011
Na2O	0.40	0.061
K2O	8.20	0.816

Totals	95.04	7.712
--------	-------	-------

fsp plag

Holland & Powell 1992 model 1

Ferric from: all ferric

plag is C1 structure

oxide	wt % cations			activity	±sd	±%
SiO2	59.66	2.679	an	0.47	0.0266	6
TiO2	0.05	0.002	ab	0.65	0.0324	5
Al2O3	24.50	1.297				
Cr2O3	0.08	0.003				
Fe2O3	0.29	0.010				
FeO	0.00	0.000				
MnO	0.05	0.002				
MgO	0.13	0.009				
CaO	7.23	0.348				
Na2O	7.21	0.627				
K2O	0.09	0.005				
Totals	99.31	4.981				

cd rim

2-site Mg-Fe-Mn mixing, anhydrous basis

Ferric from: Cation Sum = 11 for 18 oxygens. Max Ratio = 0.2

WFeMg=1.5, WMgMn=1.5, WFeMn=0 (kJ)

oxide	wt % cations			activity	±sd	±%
SiO2	49.17	5.063	crd	0.31	0.0313	10
TiO2	0.12	0.009	fcrd	0.23	0.0249	11
Al2O3	31.48	3.821	mncrd	-	-	-
Cr2O3	0.15	0.012				
Fe2O3	1.33	0.103				

FeO	9.94	0.856
MnO	0.17	0.014
MgO	6.67	1.023
CaO	0.14	0.015
Na2O	0.35	0.070
K2O	0.09	0.011

Totals 99.61 11.000

THERMOCALC OUTPUT:

Average PT calculation

THERMOCALC 3.21

An independent set of reactions has been calculated

Activities and their uncertainties

	py	gr	alm	phl	ann	east	an	
a	0.00250	4.80e-5	0.470	0.00880	0.0900	0.0150	0.470	
sd(a)/a	0.67228	0.83577	0.15000	0.56674	0.29400	0.51082	0.10000	

	crd	fcrd	q	sill	H2O	
a	0.310	0.230	1.00	1.00	1.00	
sd(a)/a	0.14283	0.17787	0	0		

Independent set of reactions

- 1) $gr + q + 2sill = 3an$
- 2) $2py + 5q + 4sill = 3crd$
- 3) $2alm + 5q + 4sill = 3fcrd$
- 4) $py + east + 3q = phl + crd$
- 5) $alm + east + 3q = ann + crd$

Calculations for the independent set of reactions

(for $a(H_2O) = 1.0$)

	P(T)	sd(P)	a	sd(a)	b	c	ln_K	sd(ln_K)
1	4.7	1.42	25.36	0.59	-0.11333	5.322	7.679	0.888
2	4.2	1.16	-60.65	1.05	-0.05391	10.361	8.469	1.411
3	4.9	0.48	74.95	1.08	-0.10307	11.164	-2.899	0.612
4	4.2	2.57	-40.88	0.52	-0.00976	3.411	4.287	1.027
5	2.3	1.46	3.48	1.06	-0.02315	3.708	1.376	0.625

Average PT (for $a(H_2O) = 1.0$)

Single end-member diagnostic information

avP, avT, sd's, cor, fit are result of doubling the uncertainty on ln a :
 a ln a suspect if any are v different from lsq values.
 e* are ln a residuals normalised to ln a uncertainties :
 large absolute values, say >2.5, point to suspect info.
 hat are the diagonal elements of the hat matrix :
 large values, say >0.45, point to influential data.
 For 95% confidence, fit (= sd(fit)) < 1.61
 however a larger value may be OK - look at the diagnostics!

	avP	sd	avT	sd	cor	fit		
lsq	3.8	0.9	657	88	0.901	1.08		
	P	sd(P)	T	sd(T)	cor	fit	e*	hat
py	2.71	1.32	560	124	0.958	0.90	0.73	0.75
gr	3.76	0.91	657	88	0.895	1.08	0.08	0.07
alm	3.80	0.88	648	88	0.845	1.05	-0.25	0.23
phl	3.87	0.84	661	82	0.899	0.95	-0.90	0.04
ann	4.00	0.86	673	83	0.903	0.81	0.95	0.03
east	3.88	0.85	667	83	0.903	0.97	-0.83	0.03
an	3.76	0.90	657	88	0.899	1.08	-0.03	0.01
crd	4.05	1.01	681	95	0.924	1.03	0.34	0.14
fcrd	3.80	0.85	686	96	0.810	1.01	-0.42	0.63
q	3.77	0.90	657	88	0.901	1.08	0	0
sill	3.77	0.90	657	88	0.901	1.08	0	0

T = 657°C, sd = 88,
 P = 3.8 kbars, sd = 0.9, cor = 0.901, sigfit = 1.08

THERMOCALC 3.21

Pressures calculated over the 750-900°C range

An independent set of reactions has been calculated
 Activities and their uncertainties

	py	gr	alm	phl	ann	east	an	
a	0.00250	4.80e-5	0.470	0.00880	0.0900	0.0150	0.470	
sd(a)/a	0.67228	0.83577	0.15000	0.56674	0.29400	0.51082	0.10000	
	crd	fcrd	q	sill	H2O			
a	0.310	0.230	1.00	1.00	1.00			
sd(a)/a	0.14283	0.17787	0	0				

Independent set of reactions

- 1) gr + q + 2sill = 3an
- 2) 2py + 5q + 4sill = 3crd

- 3) $2alm + 5q + 4sill = 3fcrd$
 4) $py + east + 3q = phl + crd$
 5) $alm + east + 3q = ann + crd$

Calculations for the independent set of reactions
 at $T = 825^{\circ}\text{C}$ (for $a(\text{H}_2\text{O}) = 1.0$)

	P(T)	sd(P)	a	sd(a)	b	c	ln_K	sd(ln_K)
1	5.4	1.53	25.35	0.59	-0.11329	5.314	7.679	0.888
2	4.1	1.26	-58.83	1.05	-0.05522	10.261	8.469	1.411
3	5.8	0.51	76.45	1.08	-0.10410	11.067	-2.899	0.612
4	3.7	2.78	-40.04	0.52	-0.01042	3.377	4.287	1.027
5	2.5	1.58	4.16	1.06	-0.02367	3.677	1.376	0.625

Average pressures (for $a(\text{H}_2\text{O}) = 1.0$)

Single end-member diagnostic information

av, sd, fit are result of doubling the uncertainty on ln a :

a ln a suspect if any are v different from lsq values.

e* are ln a residuals normalised to ln a uncertainties :

large absolute values, say >2.5 , point to suspect info.

hat are the diagonal elements of the hat matrix :

large values, say >0.45 , point to influential data.

For 95% confidence, $\text{fit} (= \text{sd}(\text{fit})) < 1.54$;

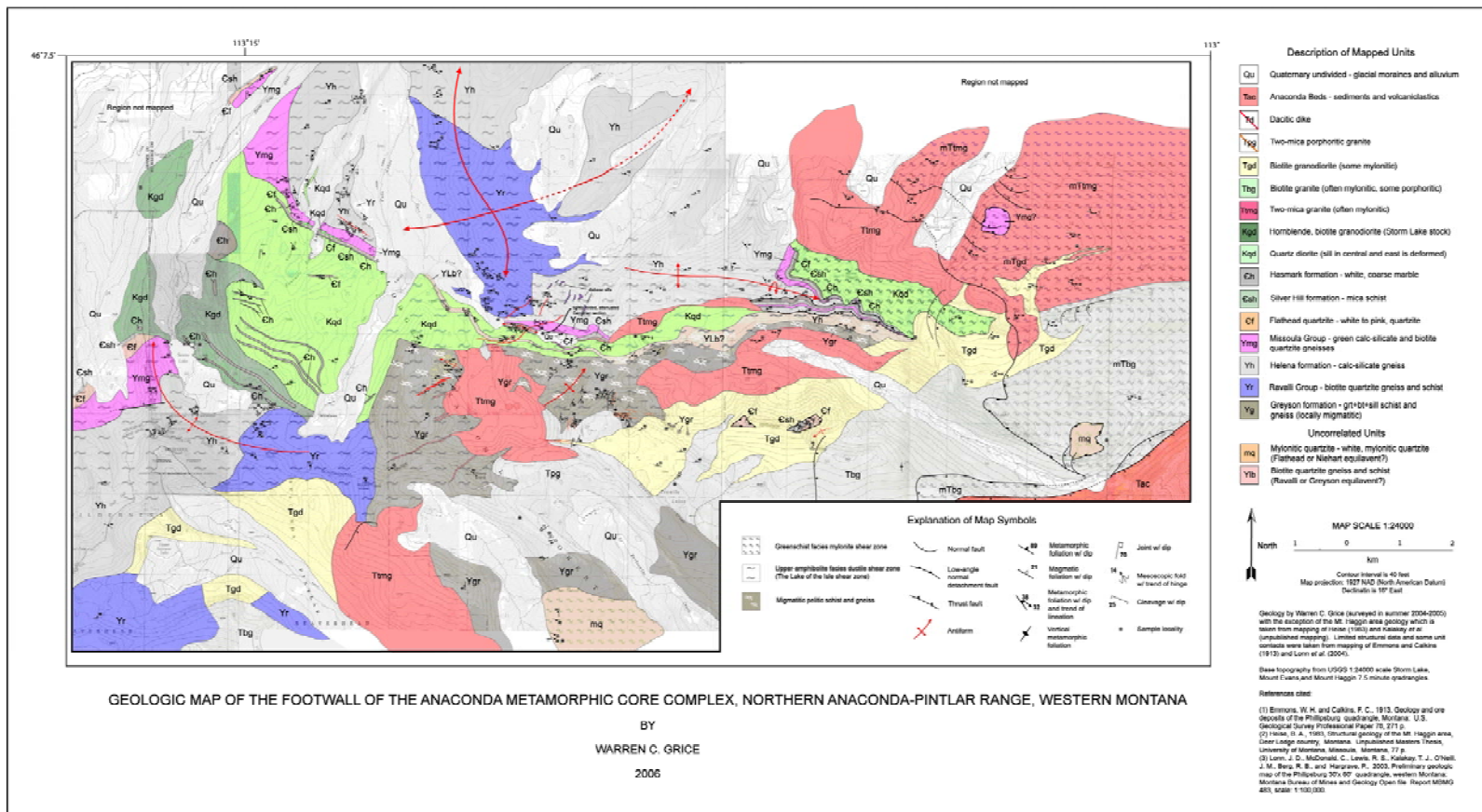
however a larger value may be OK - look at the diagnostics!

	av	sd	fit
lsq	5.33	0.59	1.31

	P	sd	fit	e*	hat	a(obs)	a(calc)
py	5.42	0.59	1.27	0.7	0.09	0.00250	0.00403
gr	5.32	0.60	1.31	-0.1	0.07	4.80e-5	4.42e-5
alm	5.32	0.73	1.31	-0.0	0.21	0.470	0.468
phl	5.42	0.55	1.21	1.0	0.04	0.00880	0.0158
ann	5.46	0.48	1.06	-1.2	0.02	0.0900	0.0632
east	5.37	0.53	1.19	1.2	0.01	0.0150	0.0272
an	5.33	0.59	1.31	0.0	0.01	0.470	0.472
crd	5.50	0.52	1.12	-0.9	0.04	0.310	0.271
fcrd	4.74	0.65	1.08	1.2	0.48	0.230	0.282
q	5.33	0.59	1.31	0	0	1.00	1.00
sill	5.33	0.59	1.31	0	0	1.00	1.00

T°C	750	770	790	810	830	850	870	890	900
av P	4.6	4.8	5.0	5.1	5.3	5.5	5.7	5.9	6.0
sd	0.44	0.47	0.51	0.55	0.59	0.63	0.67	0.71	0.73
sigfit	1.1	1.1	1.2	1.3	1.3	1.4	1.4	1.5	1.5

APPENDIX F
GEOLOGIC MAP OF THE ANACONDA METAMORPHIC CORE COMPLEX
LOWER PLATE



Object F-1. Geologic map of the Anaconda metamorphic core complex lower plate (AMCCfinalmap.pdf, 22 mb).

REFERENCES CITED

- Abers, G. A., 1991, Possible seismogenic shallow-dipping normal faults in the Woodlark-D'Entrecasteaux extensional province, Papua New Guinea: *Geology*, v. 19, p. 1205-1208.
- Abers, G. A., 2001, Evidence for seismogenic normal faults as shallow dips in continental rifts: *Geological Society of America Special Publications*, vol. 187, p. 305-318.
- Abers, G. A., Mutter, C. Z., and Fang, J., 1997, Shallow dips of normal faults during rapid extension: Earthquakes in the Woodlark- D'Entrecasteaux rift system, Papua New Guinea: *Journal of Geophysical Research*, v. 102, p. 15,301-15,317.
- Allmendinger, R. W., 1992, Fold and thrust tectonics of the western United States Cordillera, exclusive of the accreted terranes, In Burchfiel, B. C., Lipman, P., and Zoback, M. L. (eds.), *The Cordilleran Orogen: Conterminous U.S.*: Boulder, Colorado, Geological Society of America, *The Geology of North America*, v. G-3, p. 583-607, 1 plate.
- Allen, J. C., 1966, Structure and Petrology of the Royal Stock, Flint Creek Range, Central-Western Montana: *Geological Society of America Bulletin*, v. 77, p. 291-302.
- Anderson, E.M. 1951. The dynamics of faulting and dyke formation with applications to Britain. Oliver and Boyd, Edinburg.
- Armstrong, R. L., Taubeneck, W. H., and Hales, P. O., 1977, Rb-Sr and K-Ar geochronology of Mesozoic granitic rocks and their Sr isotopic composition, Oregon, Washington, and Idaho: *Geological Society of America Bulletin*, v. 88, p. 397-411.
- Armstrong, R. L., and Ward, P., 1991, Evolving geographic patterns of Cenozoic magmatism in the North American Cordillera: the temporal and spatial association of magmatism and metamorphic core complexes: *Journal of Geophysical Research*, v. 96, p. 13,201-13,224.
- Baken, J. F., 1984, The structural geology and tectonic history of the northern Flint Creek Range, western Montana: Unpublished Master's thesis, Montana State University, Bozeman, Montana, 125 p.

- Best, M. G., and Christiansen, E. H., 2001, *Igneous Petrology*: Best, M. G., and Christiansen, E. H., eds., Blackwell Science, Inc., Malden, Mass, p. 458.
- Bickford, M. E., Chase, R. B., Nelson, B. K., Shuster, R. D., and Arruda, E. C., 1981, U-Pb studies of zircon cores and overgrowths, and monazite: implications for age and petrogenesis of the northeastern Idaho batholith: *Journal of Geology*, v. 89, p. 433-457.
- Bird, P., 2002, Stress direction history of the western United States and Mexico since 85 Ma: *Tectonics*, v. 21, n. 3, 10.1029/2001TC001319.
- Breitsprecher, K., Thorkelson, D. J., Groome, W. G., and Dostal, J., 2003, Geochemical confirmation of the Kula-Farallon slab window beneath the Pacific northwest in Eocene time: *Geology*, v. 31, p. 351-354.
- Brichau, S., Ring, U., Ketcham, R. A., Carter, A., Stockli, and D., Brunel, M., Constraining the long-term evolution of the slip rate for a major extensional fault system in the central Aegean, Greece, using thermochronology: *Earth and Planetary Science Letters*, v. 241, p. 293-306.
- Bond, G. C., Nickeson, P. A. and Kominz, M., A., 1984, Breakup of a supercontinent between 625 Ma and 555 Ma: new evidence and implications for continental histories, *Earth and Planetary Science Letters*, v. 70, p. 325-345.
- Buck, R. W., 1988, Flexural rotation of normal faults: *Tectonics*, v. 7, p. 959-973.
- Buckley, S. N., 1990, Ductile extension in a Late-Cretaceous fold and thrust belt, Granite County, west-central Montana: Unpublished Master's thesis, University of Montana, Missoula, Montana, 42 p.
- Burchfiel, B. C., Cowan, D. S., and Davis, G. A., 1992, Tectonic overview of the Cordilleran orogen in the western U. S., in Burchfiel, B. C., Lipman, P. W., and Zoback, M. L., *The Cordilleran Orogen: conterminous U. S.: The Geology of North America, Volume G-3, Decade of North American Geology*, Geological Society of America, Boulder, p. 407-480.
- Bryan, W. B., 1969, Some applications of linear least squares calculations to petrographic problems: *Eos, Transactions, American Geophysical Union*, v.50, p. 354
- Camilleri, P. A., 1998, Prograde metamorphism, strain evolution, and collapse of footwalls of thick thrust sheets: a case study from the Mesozoic Sevier hinterland U.S.A: *Journal of Structural Geology*, v. 20, p. 1023-1042.
- Carney, S. M., and Janecke, S. U., 2005, Excision and the original low dip of the Miocene-Pliocene Bannock detachment system, SE Idaho: Northern cousin of the Sevier Desert detachment: *Geological Society of America Bulletin*, v. 117, p. 334-353.

- Carter, T. J., Kohn, B. P., Foster, D. A., Gleadow, A. J. W., Woodhead, J. D., 2006, Late-stage evolution of the Chemehuevi and Sacramento detachment faults from apatite (U-Th)/He thermochronology-Evidence for mid-Miocene accelerated slip: *Geological Society of America Bulletin*, v. 118, p. 689-709.
- Coney, P. J., 1980, Cordillera core complexes: An overview, in Crittenden, M.D., Jr. Coney, P.J., and Davis, G. H., eds., *Cordilleran metamorphic core complexes: Geological Society of America Memoir 153*, p. 7-31.
- Coney, P. J. and Harms, T. A., 1984, Cordillera metamorphic core complexes: Cenozoic extensional relics of Mesozoic compression: *Geology*, v. 12, p. 550-54.
- Constenius, K. N., 1996, Late Paleogene extensional collapse of the Cordilleran foreland fold and thrust belt: *Geological Society of America Bulletin*, v. 108, p. 20-39.
- Coyner, S. J., Foster, D. A., Fanning, C. M., 2001, Emplacement chronology of the Paradise Pluton: implications for the development of the Bitterroot metamorphic core complex, Montana/Idaho: *Northwest Geology*, v. 30, p. 10-20.
- Davis, G. H., and Coney, P. J., 1979, Geologic development of the Cordilleran metamorphic core complexes: *Geology*, v. 7, p. 120-174.
- Deer, W. A., Howie, R. A. and Zussman, J, 1992, *An introduction to the rock forming minerals: second edition*, Longman Scientific & Technical, Harlow.
- Desmarais, N. R., 1983, *Geology and geochronology of the Chief Joseph plutonic-metamorphic core complex, Idaho-Montana: Unpublished Ph.D. dissertation*, University of Washington, Seattle, Washington, 125 p.
- Dewey, J. F., 1988, Extensional collapse of orogens: *Tectonics*, v. 7, p. 1123-1139.
- Dziggel, A., Armstrong, R A., Stevens, G., and Nasdala, L., 2005, Growth of zircon and titanite during metamorphism in the granitoid-gneiss terrane south of the Barberton greenstone belt, South Africa: *Mineralogical Magazine*, v. 69, p.1019-1036.
- Dokka, R.K., 1993, The original dip and subsequent modification of a Cordilleran detachment fault: *Geology*, v. 21, p. 711-714.
- Doughty, P. T., and Sheriff, S. D, 1992, Paleomagnetic evidence for an echelon crustal extension and crustal rotations in western Montana and Idaho: *Tectonics*, v. 11, p. 663-671.
- Dunlap, W. J., 1997, Neocrystallization or cooling? $^{40}\text{Ar}/^{39}\text{Ar}$ ages of white micas from low-grade mylonites: *Chemical Geology*, v. 143, p. 181-203.
- Ehlers, T.A., 2005, Crustal thermal processes and the interpretation of thermochronometer data: *Reviews in Mineralogy and Geochemistry*, v. 58, p.315-350.

- Emmons, W. H. and Calkins, F. C., 1913, Geology and ore deposits of the Phillipsburg quadrangle, Montana: U.S. Geological Survey Professional Paper 78, 271 p.
- Emmons, W. H., and Calkins, F. C., 1915, Description of the Philipsburg Quadrangle, Montana: Geological Atlas Folio, Report GF-0196, 26 pp.
- Engebretson, D. C., Cox, A., and Gordon, R. G., 1985, Relative motions between oceanic and continental plates in the Pacific Basin: Geological Society of America Special Paper 206, 59 p.
- Engebretson, D. C., Cox, A., and Thompson, A., 1984, Correlation of plate motions with continental tectonics: Laramide to Basin-Range: *Tectonics*, v. 3, p. 115-119.
- Fayon, A. K., Whitney, D. L., Teyssier, C., Garver, J. I., and Yildirim, D., 2001, Effects of plate convergence obliquity on timing and mechanisms of exhumation of a mid-crustal terrain the Central Anatolian Crystalline Complex: *Earth and Planetary Science Letters*, v. 192, p. 191-205.
- Feeley, T. C., 2003, Origin and tectonic implications of across-strike geochemical variations in the Eocene Absaroka volcanic province, United States: *Journal of Geology*, v. 111, p. 329-346.
- Ferry, J. M., and Spear, F., 1978, Experimental calibration of the partitioning of Fe and Mg between biotite and garnet: *Contributions to Mineralogy and Petrology*, v. 66, pp. 112-117.
- Fillipone, J. A. and Yin, A., 1994, Age and regional tectonic implications of Late Cretaceous thrusting and Eocene extension, Cabinet Mountains, northwest Montana and northern Idaho: *Geological Society of America Bulletin*, v. 106, 1017-1032.
- Flood, R. E., 1975, Relationship of igneous emplacement to deformation history in the Anaconda Range, Montana: *Northwest Geology*, v. 4, p. 9-14.
- Foster, D. A., 2000, Tectonic evolution of the Eocene Bitterroot metamorphic core complex, Montana and Idaho, in Roberts, S. and Winston, D. eds., *Geologic field trips, western Montana and adjacent areas: Rocky Mountain Section of the Geological Society of America*. University of Montana, Missoula, p. 1-29.
- Foster, D.A., 2004, Kinematics of Eocene metamorphic core complexes in the Northern Rocky Mountains: *Geological Society of America Abstracts with Programs*, Rocky Mountain Section meeting, Vol. 36, No. 4, p. 72.
- Foster, D. A., Doughty, P. T., and Kalakay, T. J., 2003, Exhumation and kinematics of Eocene metamorphic core complexes along the Lewis and Clark strike-slip system, *Geological Society of America Abstracts with Programs*, Seattle Annual Meeting, v. 35, p. 195.

- Foster, D. A., Doughty, P. T., Kalakay, T. J., Fanning, M. C., Coyner, S., Grice, W. C., Jr., Vogl, J., 2006a, Kinematics and timing of exhumation of metamorphic core complexes along the Lewis and Clark strike-slip fault zone, western Montana: Geological Society of America Special paper, in press.
- Foster, D. A. and Fanning, C. M., 1997, Geochronology of the Idaho-Bitterroot batholith and Bitterroot metamorphic core complex: magmatism preceding and contemporaneous with extension: Geological Society of America Bulletin, v. 109, p. 379-394.
- Foster, D. A. and John, B. E., 1999, Quantifying tectonic exhumation in an extensional orogen with thermochronology: examples from the southern Basin and Range Province In: Exhumation processes: normal faulting, ductile flow and erosion. Ring U, Brandon, M. T., Lister, G. S., and, Willet, S. D., eds., Geological Society, London, Special Publication, v. 154, p. 343-364.
- Foster, D. A., Gleadow, A. J. W., Reynolds, S. J., Fitzgerald, P. G., 1993, Denudation of metamorphic core complexes and the reconstruction of the transition zone, West Central Arizona: Constraints from apatite fission track thermochronology: Journal of Geophysical Research, v. 98, p. 2167-2185.
- Foster, D. A., T. M. Harrison, C. F. Miller, C. F., and K. A. Howard, 1990, The $^{40}\text{Ar}/^{39}\text{Ar}$ thermochronology of the eastern Mojave Desert, California, and adjacent Arizona with implications for the evolution of metamorphic core complexes: Journal of Geophysical Research v. 95, p. 20,005-20,024.
- Foster, D. A., Miller, C. F., Harrison, T. M. and Hoisch, T. D., 1992, The $^{40}\text{Ar}/^{39}\text{Ar}$ thermochronology and thermobarometry of metamorphism, plutonism, and tectonic denudation in the Old Woman Mountains area, California: Geological Society of America Bulletin, v. 104, p. 176-191.
- Foster, D. A., Mueller, P. A., Heatherington, A. L., Vogl, J., Meert, J., Lewis, R., and Wooden, J. L., 2006b, Configuration of the western margin of the Wyoming Craton: implications for the tectonic and magmatic evolution of the northern Rocky Mountains: Canadian Journal of Earth Sciences, in press.
- Foster, D. A., and Raza, A., 2002, Low-temperature thermochronological record of exhumation of the Bitterroot metamorphic core complex, northern Cordilleran Orogen: Tectonophysics, v. 349, p. 23-36.
- Foster, D. A., Schafer, C., Fanning, M. C., and Hyndman, D. W., 2001, Relationship between crustal partial melting, plutonism, orogeny, and exhumation: Idaho-Bitterroot batholith, Tectonophysics, v. 342, p. 313-350.
- Gessmann, C. K.; Spiering, B.; Raith, M., 1997, Experimental study of the Fe-Mg exchange between garnet and biotite; constraints on the mixing behavior and analysis of the cation-exchange mechanisms: American Mineralogist, v.82, pp.1225-1240.

- Grice, W. C., Jr., Foster, D. A., and Kalakay, T. J., 2005, Quantifying exhumation and cooling of the Eocene Anaconda metamorphic core complex, western Montana: Geological Society of America Abstracts with Programs, v. 37, n.7
- Haeussler, P. J., Bradley, D. C., Wells, R. E., and Miller, M. L., 2003, Life and death of the Resurrection plate: Evidence for its existence and subduction in the northeastern Pacific in Paleocene–Eocene time: Geological Society of America Bulletin, v. 115, no. 7, p. 867–880.
- Hamilton, W. and Myers, W. B., 1974, Nature of the Boulder Batholith of Montana: Geological Society of America Bulletin, v. 85, p. 365-278.
- Harlan, S. S., Geissman, J. W., Lageson, D. R., Snee, L. W., 1988, Paleomagnetic and isotopic dating of thrust-belt deformation along the eastern edge of the Helena salient, northern Crazy Mountain basin, Montana: Geological Society of America Bulletin, v. 100, p. 492-499.
- Harrison, J. E., Griggs, A. B., and Wells, J. D., 1974, Tectonic features of the Precambrian Belt Basin and their influences on post-Belt structures: United States Geological Survey Professional Paper 866, 15 p.
- Hawley, K., 1975, The Racetrack pluton: A newly defined Flint Creek pluton: Northwest Geology, v. 4, p. 1-8.
- Heise, B. A., 1983, Structural geology of the Mt. Haggin area, Deer Lodge country, Montana: Unpublished Master's thesis, University of Montana, Missoula, Montana, 77 p.
- Hill, E.J., S.L. Baldwin, and G.S. Lister, 1995, Magmatism as an essential driving force for formation of active metamorphic core complexes in eastern Papua New Guinea: Journal of Geophysical Research, v. 100, p. 10,441-10,451.
- Hodges, K. V. and Crowley, P. D., 1985, Error estimation and empirical geothermobarometry for pelitic systems, American Mineralogist v. 70, 702–709.
- Hodges, K. V. and Walker, J. D., 1992, Extension in the Cretaceous Sevier orogen, North America Cordillera: Geological Society of America Bulletin, v. 104, p. 560-569.
- Hoffman, P. F., 1988, United Plates of America, the birth of craton: early Proterozoic assembly and growth of Laurentia: Annual Review of Earth and Planetary Sciences, v. 16, p. 543-603.
- Holland, T. J. B, Powell, R., 1998, An internally consistent thermodynamic data set for phases of petrologic interest: Journal of Metamorphic Petrology, v. 16, p. 309-342.
- House, M. A., and Applegate, J. D. R. A., 1993, Age of Tertiary extension in the Bitterroot metamorphic core complex, Montana and Idaho: Geology, v. 21, p. 161-164.

- House, M. A., Bowring, S. A., and Hodges, K. V., 2002, Implications of middle Eocene epizonal plutonism for the unroofing history of the Bitterroot metamorphic core complex, Idaho-Montana: *Geological Society of American Bulletin*, v. 114, p. 448-461.
- House, M. A., and Hodges, K. V., 1994, Limits on the tectonic significance of rapid cooling events in extensional settings: Insights from the Bitterroot metamorphic core complex, Idaho-Montana: *Geology*, v. 22, p. 1007-1010.
- House, M. A., Hodges, K. V., and Bowring, S. A., 1997, Petrological and geochronological constraints on regional metamorphism along the northern border of the Bitterroot batholith: *Journal of Metamorphic Geology*, v. 15, p. 753-764.
- Humphreys, E. D., 1995, Post-Laramide removal of the Farallon slab, western United States: *Geology*, v. 23, p. 987-990.
- Humphreys, E. D., Hessler, E., Dueker, K., Farmer, G. L., Erslev, E. Atwater, T., 2003, How Laramide-age hydration of North American lithosphere by the Farallon slab controlled subsequent activity in the western United States: *International Geology Review*, v. 45, p. 575-595.
- Hyndman, D.W., 1980, Bitterroot dome-Sapphire tectonic block, an example of a plutonic-core gneiss-dome complex with its detached suprastructure: in P.J. Coney, Max Crittenden, Jr., and G.H. Davis, eds., *Cordilleran Metamorphic Core Complexes: Geological Society of America Memoir 153*, p. 427-443.
- Hyndman, D. W., 1981, Controls on source and depth of emplacement of granitic magma: *Geology*, v. 9, p. 244-249.
- Hyndman, D.W., 1984, A petrographic and chemical section through the northern Idaho Batholith: *Journal of Geology*, v. 92, p. 83-102.
- Hyndman, D. W., Alt, D., and Sears, J. W., 1988, Post-Archean metamorphic and tectonic evolution of western Montana and northern Idaho: in Ernst, W. G., ed., *Metamorphism and crustal evolution in western conterminous U.S.*, Rubey v. 7, Englewood Cliffs, New Jersey, Princeton-Hall, p. 332-361.
- Hyndman, D. W., Talbot, J. L., and Chase, R. B., 1975, Boulder Batholith: A result of emplacement of a block detached from the Idaho Batholith infrastructure?: *Geology*, v. 3, p. 401-404.
- Hyndman, D. W. and Myers, S. A., 1988, The transition from amphibolite-facies mylonite to chloritic breccia: a role of the mylonite in formation of Eocene epizonal, Bitterroot dome, Montana. *Geologischche Rundschau*, v. 77, p. 211-226.
- Ispolatov, V.O., 1997, $^{40}\text{Ar}/^{39}\text{Ar}$ geochronology of the Lowland Creek volcanic field and its temporal relations with the other Eocene volcanic areas: Unpublished Masters Thesis: Old Dominion University, Norfolk, VA, 105 p.

- John, B.E., and Foster, D.A., 1993, Structural and thermal constraints on the initiation angle of detachment faulting in the southern Basin and Range: The Chemehuevi Mountains case study: *Geological Society of America Bulletin*, v. 105, p. 1091-1108.
- Johnson, B. J., 2006, Extensional shear zones, granitic melts, and linkage of overstepping normal faults bounding the Shuswap metamorphic core complex, British Columbia: *Geological Society of America Bulletin*, v. 118, p. 366-383.
- Kalakay, T. J., John, B. E., and Lageson, D. R., 2001, Fault-controlled pluton emplacement in the Sevier fold-and-thrust belt of southwest Montana, USA: *Journal of Structural Geology*, v. 23, p. 1151-1165.
- Kalakay, T. J., Foster, D. A., Thomas, R. A., 2003, Geometry, kinematics and timing of extension in the Anaconda extensional terrane, western Montana: *Northwest Geology*, v. 32, p. 124-133.
- Kalakay, T. J., and Lonn, J. D., 2002, Geometric and kinematic relationships between high-temperature and low-temperature faulting in the Anaconda detachment zone, southwest Montana. Programs and Abstracts, Geological Society of America Annual Meeting, Denver, CO.
- Karlstrom, K. E., Ahall, K., Harlan, S. S., Williams, M. L., McLelland, J., Geissman, J. W., 2001, Long-lived (1.8-1.0 Ga) convergent orogen in southern Laurentia, its extensions to Australia and Baltica, and implications for refining Rodinia: *Precambrian Research*, v. 111, p. 5-30.
- Karlstrom, K. E., Williams, M. L., McLelland, Geissman, J. W., Ahall, Karl-Inge, 1999, Refining Rodinia: Geologic Evidence for the Australia-Western U.S. connection in the Proterozoic, *GSA today*, v. 9, no. 10, p. 2-7.
- Kohn, J. M., Spear, F., Retrograde net reaction insurance for pressure-temperature estimates, *Geology*, v. 28, p. 1127-1130.
- Koppers, A.A.P., 2002, ArArCALC, software for Ar-40/Ar-39 age calculations: *Computers and Geosciences*, v 5, pp 605-619.
- Kosler, J., Sylvester, P. J., 2003, Present trends and the future of zircon in geochronology: Laser ablation ICPMS, *Zircon: Reviews in Mineralogy and Geochemistry*, 2003, v. 53 p. 243-271.
- Koziol, A. M., 1989, Recalibration of the garnet-plagioclase-Al₂SiO₅-quartz (GASP) geobarometer and applications to natural parageneses: *EOS*, v. 70, 493.
- Koziol, A. M., and Newton, R. C., 1988, Predetermination of the anorthite breakdown reaction and improvement of the plagioclase – garnet – Al₂SiO₅ – quartz barometer: *American Mineralogist*, v. 73, p. 216-223.

- Lageson, D. R., Schmitt, J. G., Horton, B. K., Kalakay, T. J., and Burton, B. R., 2001, Influence of Late Cretaceous magmatism on the Sevier orogenic wedge, western Montana: *Geology*, v. 29, p. 723-726.
- Lavier, L. L., W. R. Buck & A. B. N. Poliakov, 1999, A self-consistent rolling-hinge model for the evolution of large-offset low-angle normal faults: *Geology*, v. 27, p. 1127-1130.
- Lewis, R. S., 1990, Geologic map of the Dickie Peak Quadrangle, Deer Lodge and Silver Bow Counties, Montana: Montana Bureau of Mines and Geology, geologic map 51.
- Lewis, R., 1998, Geologic map of the Butte 1 by 2 degree quadrangle, scale 1:250,000: Montana Bureau of Mines and Geology, Butte, open file report MBMG 363.
- Lidke, D. J., and Wallace, C. A., 1993, Rocks and structure of the north-central part of the Anaconda Range, Deer Lodge and Granite Counties, Montana: United States Geological Survey Bulletin, 31 p., map scale 1:24000.
- Lister, G. S., and Baldwin, S. L., 1996, Modeling the effect of arbitrary P-T-t histories on argon diffusion in minerals using the MacArgon program for the Apple Macintosh: *Tectonophysics* v. 253, p. 83-109.
- Lister, G. S., and Baldwin, S. L., 1993, Plutonism and the origin of metamorphic core complexes: *Geology*, v. 21, p. 607-610.
- Lister, G. S., and Baldwin, S. L., 1989, The origin of metamorphic core complexes and detachment faults formed during Tertiary continental extension in the northern Colorado River region, U.S.A.: *Journal of Structural Geology*, v. 11, p. 65-94.
- Lister, G. S., and Davis, G. A., 1989, The origin of metamorphic core complexes and detachment faults formed during Tertiary continental extension in the northern Colorado River region, U.S.A.: *Journal of Structural Geology*, v. 11, p. 65-94.
- Liu, M., 2001, Cenozoic extension and magmatism in the North American Cordillera: the role of gravitational collapse: *Tectonophysics*, v. 342, 407-433.
- Lonn, J. D., McDonald, C., Lewis, R. S., Kalakay, T. J., O'Neill, J. M., Berg, R. B., and Hargrave, P., 2003, Preliminary geologic map of the Philipsburg 30'x 60' quadrangle, western Montana: Montana Bureau of Mines and Geology Open file Report MBMG 483, scale: 1:100,000.
- Ludwig K. R., 2004, Users manual for ISOPLOT, a geochemical toolkit for Microsoft Excel (v. 3.09a).

- Lund, K., Aleinikoff, J.N., Kunk, M.J., Unruh, D.M., Zeihen, G.D., Hodges, W.C., du Bray, E.A., and O'Neill, J.M., 2002, SHRIMP U-Pb and $^{40}\text{Ar}/^{39}\text{Ar}$ age constraints for relating plutonism and mineralization in the Boulder Batholith region, Montana: *Economic Geology*, v. 97, p. 241-267.
- McDougall, I., and Harrison, T.M., 1999, *Geochronology and thermochronology by the $^{40}\text{Ar}/^{39}\text{Ar}$ method*, 2nd ed., Oxford, University Press, Oxford, UK
- McGrew, A. J., Peters, M. T. and Wright, J. E., 2000, Thermobarometric constraints on the tectonothermal evolution of the East Humboldt Range metamorphic core complex, Nevada: *Geological Society of America Bulletin*, v. 112, p. 45-60.
- McGrew, A. J., and Snee, L. W., 1994, $^{40}\text{Ar}/^{39}\text{Ar}$ thermochronological constraints on the tectonothermal evolution of the northern East Humboldt Range metamorphic core complex, Nevada: *Tectonophysics*, v. 238, p. 425-450.
- Meert, J. G., Torsvik, T. H., 2003, The making and unmaking of a supercontinent: Rodinia revisited: *Tectonophysics*, v. 375, p. 261-288.
- Morris, G. A., Larson, P. B., and Hooper, P. R., 2000, 'Subduction style' magmatism in a non-subduction setting: the Colville Igneous Complex, NE Washington State, USA: *Journal of Petrology*, v. 41, p. 43-67.
- Mueller, P. A., Heatherington, A. L., Kelly, D. M., Wooden, J. L., Mogk, D. W., 2002, Paleoproterozoic crust within the Great Falls tectonic zone: Implications for the assembly of southern Laurentia: *Geology*, v. 30, p. 127-130.
- Mueller, P. A., Shuster, R. D., D'Arcy, K. A., Heatherington, A. L., Nutman, A. P., and Williams, I. S., 1995, Source of the Northeastern Idaho Batholith: Isotopic evidence for a Paleoproterozoic Terrane in the Northwestern U.S.: *Journal of Geology*, v. 103, p. 63-72.
- Newton, R.C., and Haselton, H.T., 1981, Thermodynamics of the garnet-plagioclase- Al_2SiO_5 -quartz geobarometer: In Newton R.C., ed., *Thermodynamics of Minerals and Melts*: New York (Springer-Verlag), p. 131-147.
- Noel, J. A., 1956, The geology of the east end of the Anaconda Range and adjacent areas, Montana: Unpublished Ph.D. dissertation, Indiana University, Indiana.
- O'Neill, J. M., Lonn, J. D., Kalakay, T. J., 2002, Early Tertiary Anaconda Metamorphic Core Complex, southwestern Montana: *Geological Society of America Abstracts with Programs Rocky Mountain Section Meeting*, Cedar City, Utah, May 2002.
- O'Neill, J. M., Lonn, J. D., Lageson, D. R., and Kunk, M. J., 2004, Early Tertiary Anaconda Metamorphic Core Complex, southwestern Montana, *Canadian Journal of Earth Sciences*, v. 41, 63-72.

- Passchier, C. W., Myers, J. S., and Kroner, A., 1990, Field geology of high-grade gneiss terrains: Springer-Verlag, New York, p. 150.
- Powell, R., Holland, T., 1994, Optimal geothermometry and geobarometry: *American Mineralogist*, v. 79, p. 120-133.
- Price, R. A. and Carmichael, D. M., 1986, Geometric test for late-Cretaceous-Paleogene intracontinental transform faulting in the Canadian Cordillera: *Geology*, v. 14, p. 468-471.
- Richards, J. P., and McDougall, I., 1990, Geochronology of the Porgera gold deposit, Papua New Guinea; resolving the effects of excess argon on K-Ar and $^{40}\text{Ar}/^{39}\text{Ar}$ age estimates for magmatism and mineralization: *Geochimica et Cosmochimica Acta*, v. 54, pp.1397-1415.
- Reiners, P. W., 2005, Zircon (U-Th)/He thermochronology: *Reviews in Mineralogy and Geochemistry*, v. 58, p. 151-179.
- Rey, P., Vanderhaeghe, O., and Teyssier, C., 2001, Gravitational collapse of the continental crust: definition, regime and modes: *Tectonophysics*, v. 342, p. 435-449.
- Reynolds, M. W., and Kleinkoff, M. D., 1987, The Lewis and Clark line, Montana-Idaho: a major intraplate tectonic boundary: *Geological Society of America Abstracts with Programs* 9, p. 1140-1141.
- Rollinson, H., 1993, Using geochemical data: evaluation, presentation, interpretation: New York, Longman Scientific & Technical, p. 352.
- Ross, G. M., Patchett, P. J., Hamilton, M., Heaman, L., Decelles, P. G., Rosenberg, E., Giovanni, M. K., 2005, Evolution of the Cordilleran orogen (southwestern Alberta, Canada) inferred from detrital mineral geochronology, geochemistry, and Nd isotopes in the foreland basin: *Geological Society of America Bulletin*, v. 117, p. 747-763.
- Ross, G. M., Randall, P. R., Winston, D., 1992, Provenance and U-Pb geochronology of the Mesoproterozoic Belt Supergroup (northwestern United States): implications for age of deposition and pre-Panthalassa plate reconstructions: *Earth and Planetary Science Letters*, v. 113, p. 57-76.
- Ross, G. M., and Villeneuve, M., 2003, Provenance of the Mesoproterozoic (1.45 Ga) Belt basin (western North America): Another piece in the pre-Rodinia paleographic puzzle: *Geological Society of America Bulletin*, v. 115, p. 1191-1217.
- Scott, R. J., and Lister, G. S., 1992, Detachment faults: Evidence for a low-angle origin: *Geology*, v. 20, p. 833-836.

- Sears, J. W., and Fritz, W. J., 1998, Cenozoic tilt domains in southwestern Montana: Interference among three generations of extensional fault systems: Geological Society of America Special Paper 323, p. 241-247.
- Sears, J. W., and Hendrix, M. S., 2004, Lewis and Clark line and the rotational origin of the Alberta and Helena Salients, North American Cordillera: Geological Society of America Special Paper 383, p. 173-186.
- Sears, J. W. and Price, R. A., 1978, The Siberian connection: A case for the Precambrian separation of North America and Siberian cratons: *Geology*, v. 6, p. 267-270.
- Sears, J. W. and Price, R. A., 2000, New look at the Siberian connection: No SWEAT: *Geology*, v. 28, p. 423-426.
- Sears, J. W. and Price, R. A., 2003, Tightening the Siberia connection to western Laurentia, *Geological Society of America Bulletin*, v. 115, p. 943-953.
- Shuster, R. D., and Bickford, M. E., 1985, Chemical and isotopic evidence for the petrogenesis of the northeastern Idaho Batholith: *Journal of Geology*, v. 93, p. 727-742.
- Spear, F. S., 1993, *Metamorphic Phase Equilibria and Pressure-Temperature Paths: Monograph*, Mineralogical Society of America, Washington DC, USA, 799 p.
- Spear, F.S., Kohn, M. J., Cheney, J. T., 1999, P-T paths from anatectic pelites: *Contributions to Mineralogy and Petrology*, v.134, pp.17-32.
- Spear, F. S., Selverstone, J; Hickmott, D; Crowley, P; Hodges, K V., 1984, P-T paths from garnet zoning: a new technique for deciphering tectonic processes in crystalline terranes: *Geology*, v. 12, p. 87-90.
- Spencer, J. E., 1984, Role of tectonic denudation in warping and uplifting of low-angle normal faults: *Geology*, v. 12, p. 95-98.
- Spry, A., 1963, The origin and significance of snowball structure in garnet: *Journal of Petrology*, v. 4, p.211-222.
- Stewart, J.H. and Crowell, J.C., 1992, Strike slip tectonics in the cordilleran region of the Western United States, In Burchfiel, B.C., Lipman, P.W., and Zoback, M.L., eds., *The Cordilleran Orogen: Coterminal U.S.*, Volume G-3 Decade of North American Geology (DNAG), Geological Society of America, Boulder Co., p 583-608
- Stockli, D. F., 2005, Application of low-temperature thermochronology to extensional tectonic settings: *Reviews in Mineralogy and Geochemistry*, v. 58, p. 411-448.
- Thorkelson, D. J., and Taylor, R. P., 1989, Cordilleran slab windows: *Geology*, v. 17, p. 833-836.

- Tilling, R. I., Klepper, M. R., and Obradovich, J. D., 1968, K-Ar ages and time span of emplacement of the Boulder Batholith, Montana: *American Journal of Science*, v. 266, p. 671-689.
- Titterton, D. M., and Halliday, A. M., 1979, On the fitting of parallel isochrons and the method of maximum likelihood: *Chemical Geology*, v. 26, pp.183-195.
- Toth, M.I., 1987, Petrology and origin of the Bitterroot lobe of the Idaho batholith: Chapter 2 in T.L. Vallier and H.C. Brooks, eds., *Geology of the Blue Mountains Region of Oregon, Idaho, and Washington: The Idaho Batholith and its Border Zone*: U.S. Geological Survey Professional Paper 1436, p. 9-35.
- Vanderhaeghe, O., and Teyssier, C., 2001, Crustal-scale rheological transitions during late-orogenic collapse: *Tectonophysics* v. 335, p. 211-228.
- Vanderhaeghe, O., and Teyssier, C., 2001, Partial melting and flow in orogens: *Tectonophysics* v. 342, p. 451-472.
- Vanderhaeghe, O., Teyssier, C., McDougall, I., and Dunlap, W. J., 2003, Cooling and exhumation of the Shuswap Metamorphic Core Complex constrained by $^{40}\text{Ar}/^{39}\text{Ar}$ thermochronology: *Geological Society of America Bulletin*, v. 115, p. 200-216.
- Vanderhaeghe, O., Teyssier, C., and Wysoczanski, R., 1999, Structural and geochronological constraints on the role of partial melting during the formation of the Shuswap metamorphic core complex at the latitude of the Thor-Odin dome, British Columbia: *Canadian Journal of Earth Sciences*, v. 36, p. 917-943.
- Van der Pluijm, B., and Marshak, S., 2004, *Earth Structure: Introduction to Structural Geology and Tectonics*, 2nd ed.: W.W. Norton and Company, 656 p.
- Wallace, C. A. and Lidke, D. J., 1993, Rocks and structure of the north-central part of Anaconda Range, Deer Lodge and Granite counties, Montana: U. S. Geological Survey Bulletin, Report B 1993, 31 p.
- Wallace, C. A., Lidke, D. J., and Schmidt, R. G., Faults of the central part of the Lewis and Clark line and fragmentation of the Late Cretaceous foreland basin in west-central Montana: *Geological Society of America Bulletin*, v. 102, p. 1021-1037.
- Wallace, C. A., Lidke, D. J., Elliot, J. E., Desmarais, N. R., Obradovich, D. A., Lopez, D. A., Zarske, S. E., Heise, B. A., Blaskowski, M. J., Loen, J. S., 1992, Geologic map of the Anaconda-Pintler Wilderness and contiguous roadless area, Granite, Deer Lodge, Beaverhead, and Ravalli Counties, Western Montana. U.S. Geological Survey Miscellaneous Field Study Map, MF-1633-C, scale 1:50,000.
- Wells, M. L., 1997, Alternating contraction and extension in the hinterlands of orogenic belts: an example from the Raft Mountains, Utah: *Geological Society of America Bulletin*, v. 109, p. 107-126.

- Wells, M. L., Dallmeyer, R. D., Allmendinger, R. W., 1990, Late Cretaceous extension in the hinterland of the Sevier thrust belt, northwestern Utah and southern Idaho: *Geology*, v. 18, p. 929-933.
- Wells, M.L., Snee, L.W., and Blythe, A.E., 2000, Dating of major normal fault systems using thermochronology: An example from the Raft River detachment, Basin and Range, western United States, *Journal of Geophysical Research*, v. 105, p. 16,303-16,327.
- Weinberg, R. F., Sial, A. N., and Mariano, G., 2004, Close spatial relationship between plutons and shear zones: *Geology*, v. 32, p. 377-380.
- Wernicke, B. P., 1992, Cenozoic extensional tectonics of the U.S. Cordillera, in Burchfiel, B.C., et al., eds., *The Cordilleran orogen: Conterminous U.S.*: Boulder, Colorado, Geological Society of America, *Geology of North America*, v. G-3, p. 553-581.
- Wernicke, B., P., 1995, Low-angle normal faults and seismicity: A review: *Journal of Geophysical Research*, v. 100, p. 20,159-20,174.
- Wernicke, B. P., and Axen, G.J., 1988, On the role of isostasy in the evolution of normal fault systems: *Geology*, v. 16, p. 848-851.
- Williams, I. S., 1998, U-Th-Pb Geochronology by Ion Microprobe, in McKibben, M. A., Shanks III, W. C. and Ridley, W.I., eds., *Applications of microanalytical techniques to understanding mineralizing processes: Reviews in Economic Geology*, v. 7, p. 1-35.
- Winston, D., Belt Supergroup stratigraphic correlation sections, western Montana and adjacent areas: Montana Bureau of Mines and Geology, *Geologic Map 40*, 15 p.
- Winston, D., and Link, P.K., 1993, Middle Proterozoic rocks of Montana, Idaho and Eastern Washington: The Belt Supergroup: in Reed, Jr., J.C., Bickford, M.E, Houston, R.S, Link, P.K., Rankin, R.W., Sims, P. K., and VanSchmus W.R., eds., *Precambrian: Conterminous U.S.*: Boulder, Colorado, Geological Society of America, *The Geology of North America*, v. C-2, p. 487-517.
- Yardley, B. W., 1999, *An introduction to metamorphic petrology*, Pearson Education Limited, Essex, England, 248 p.
- Yin, A. and Oertel, G., 1995, Strain analysis of the Ninemile fault zone, western Montana: insights into multiply deformed regions: *Tectonophysics*, v. 247, p. 133-143.
- York, D., 1969, Least squares fitting of a straight line with correlated errors: *Earth and Planetary Science Letters*, v.5, p.320-324.

BIOGRAPHICAL SKETCH

Warren Grice was born in Macon, GA, in 1979. He graduated from Tattnall Square Academy high school (Macon, GA) in 1998. He received a Bachelor of Science degree in geology (with honors) from Montana State University (Bozeman, MT) in 2002. While attending graduate school at the University of Florida (Gainesville, FL) Warren served as a teaching assistant for several courses in the Department of Geological Sciences and as a research assistant for Dr. David A. Foster. He will receive a master's degree in geology (with high honors) from the University of Florida in August of 2006. Warren will continue to pursue his interests in geology by enrolling in a PhD program in geology or with a career in the industry.